Optimal electrical and thermal energy management of a residential energy hub integrating renewable energy, demand response and energy storage system

By

JUAN SIECKER

Thesis submitted in fulfilment of the requirements for the degree:

Doctor of Engineering in Electrical Engineering

In the Department of Electrical, Electronic and Computer Engineering

Faculty of Engineering, Built Environment and Information Technology

Central University of Technology, Free State

Promoter: Prof. K. Kusakana

Co-Promoter: Dr. B.P. Numbi

December 2022

DECLARATION

I, JUAN SIECKER, student number _____, do hereby declare that this research project, which has been submitted to the Central University of Technology Free State, for the degree: Doctor of Engineering in Electrical Engineering, is my own independent work and complies with the Code of Academic Integrity, as well as other relevant policies, procedures, rules and regulations of the Central University of Technology, Free State.

This project has not been submitted before by any person in fulfilment (or partial fulfilment) of the requirements for the attainment of any qualification.

_____

J. Siecker Date: **2 December 2022**

DEDICATION

This Dissertation is dedicated to the Lord Jesus Christ, my source of inspiration.

ACKNOWLEDGMENTS

Firstly, I would like to thank the almighty God for giving me the strength and ability to complete this work, without Him, none of this would be possible. His guidance and inspiration made it possible to complete this work.

To Professor Kanzumba Kusakana, my supervisor, I am truly thankful for the motivation and guidance that he bestowed upon me. I am also thankful to him for always pushing me to improve and never give up.

To Doctor Bubele Papy Numbi, my co-supervisor, I would like to thank for his outstanding guidance during the course of this research. I am also sincerely thankful for his technical support in completing this work.

I would like to thank my parents, Doctor Adriaan Siecker and Mrs. Christa Siecker, as well as my brother and sister, Rudie Siecker and Marianka Knox, for their support and encouragement.

LIST OF ABBREVIATIONS

ACADO	Automatic Control and Dynamic Optimization
CENERCOR	Central Energy Corporation
COP	Coefficient of Performance
CUT	Central University of Technology
DANN	Dimensionless Artificial Neural Network
DSM	Demand Side Management
EPI	Energy Performance Indicator
ESTWH	Electric Storage Tank Water Heater
GAMS	General Algebraic Modelling System
HT-PEMFC	High Temperature Polymer Electrolyte Membrane Fuel Cell
HWST	Hot Water Storage Tank Temperature
IO	Input-Output
IOT	Internet of Things
IPOPT	Interior Point Optimizer
KPI	Key Performance Indicator
MATLAB	Matrix Laboratory
MPC	Model Predictive Control
NMD	Notified Maximum Demand
PEMFC	Polymer Electrolyte Membrane Fuel Cell
PEMWE	Polymer Electrolyte Membrane Water Electrolyser
PLC	Programmable Logic Controller
POET	Performance, Operation, Equipment and Technology efficiency
PV	Photovoltaic
PV/T	Photovoltaic/thermal
RER	Renewable energy resources

SCADA	Supervisory Control and Data Acquisition
SCIP	Solving Constraint Integer Programs
TOU	Time-of-Use
UPS	Uninterruptable Power Supply
VSD	Variable Speed Drive
WST	Water Storage Tank

ABSTRACT

The energy consumption of residential buildings contributes approximately 42 % towards the total electrical energy production on a global scale. In residential buildings, the energy consumption could be further sub-categorized into the electrical energy required for space heating, space cooling and water heating, which accounts for 61.2 % of the total energy consumption, thereof. These systems utilized in large residential buildings, are vital for the occupants, to meet their thermal comfort needs, with regards to the residential building air temperature and hot water temperature.

Some conventional means of performing space heating and water heating technology, is the boiler type, where hot water is transferred to the various rooms within the residential building and, thereafter, transferred to the spaces in the building, by means of a radiator. Another conventional space heating and water heating technology, is an electric element, which is used predominantly in water heating applications, as well as the wall mounted electric radiators. These conventional technologies are extremely ineffective due to their elementary operating principle.

Therefore, in this study, an air-to-air heat pump was selected, to provide space heating and space cooling to the residential building and an air to water heat pump, which provides hot water to the residential building. This type of technology generally consumes approximately three times less energy, compared to the conventional technologies, whilst performing at similar levels. However, the initial investment of the air-to-air heat pump and air-to-water heat pump type technology is significantly higher in comparison and becomes economically feasible over an extended period. The air-to-air heat pump and air-to-water heat pump could be further improved through various methods, from an operational energy cost and energy efficiency perspective, such as the addition of renewable energy, energy storage systems and effective control techniques, to the residential energy hub, as well as thermal energy recovery. The residential building was integrated with renewable energy,

which in this case is solar photovoltaic (PV) technology and an energy storage technology, known as hydrogen.

Effective energy management techniques, making use of advanced optimization techniques, become essential when it comes to further energy efficiency optimization and operational energy cost minimization of a residential energy hub. Therefore, in this study, various methods to minimize the operational energy costs and improve the energy efficiency of the space heating, space cooling and water heating equipment are applied to a large residential building. These methods, firstly, include the addition of solar PV technology with hydrogen energy storage and, secondly, apply optimization techniques to the large residential building.

The main objective is to minimize the operational energy cost of the utility grid, with respect to the Time-of-Use (TOU) tariff structure, to the electrical load and the polymer electrolyte membrane water electrolyser (PEMWE), which is responsible for producing hydrogen gas. The other main objectives, were to maximize the electrical energy supply to the load produced by the solar PV modules, optimal switching statuses of the air-to-air heat pump and the air to water heat pump. These main objectives outlined, were achieved by making use of the optimization algorithm, known as the OPTI-Toolbox, in the MATLAB software. These optimization problems are known as mixed integer nonlinear optimization problems (MINLP) and are solved using the (solving constrained integer programs) SCIP solver in the optimization toolbox of MATLAB.

The first model was developed for the optimal switching control of an air-to-air heat pump space heating and space cooling system, to provide space heating and space cooling to a large residential building. A mathematical model of the proposed system was developed, after which simulations were conducted to reveal the performance, as well as the economic viability, thereof. A second model was developed, of a hydrogen PEMWE water heating system, after which the optimal control algorithm was applied and simulated. A third model was developed of the residential energy hub integrating renewable energy, demand response and energy storage system. The proposed model was simulated, in terms of its operation to evaluate the performance and the economic feasibility, thereof.

Two baselines were established for the first model, to thoroughly evaluate the performance and economic feasibility of the air-to-air heat pump space heating and space cooling system. One baseline was established, for the second model, to thoroughly evaluate the performance and economic feasibility of the hydrogen PEMWE water heating system. Two baselines were established, for the third and final model, to thoroughly evaluate the performance and economic feasibility of the proposed residential energy hub integrating renewable energy, demand response and energy storage system.

The proposed air-to-air heat pump space heating and space cooling system, depicted a daily operating energy cost saving of 27.63 % and 14.73 %, compared to the first and second baseline, during the selected winter day, respectively. Furthermore, a potential daily operating energy cost saving of 16.91 % and 12.30 %, could be achieved, compared to the first and second baseline, during the selected summer day, respectively.

Additionally, the study focusing on the proposed hydrogen PEMWE water heating system, revealed that the hydrogen PEMWE water heating system, with optimal switching control, produced slightly less hydrogen energy and, in turn less hydrogen, compared to the standard PEMWE system. However, a daily maximum of 67.32 kWh of thermal energy was recovered during summer. Furthermore, by recovering the generated heat from the PEMWE, the time for the membrane to degrade to a thickness of 50 %, could be prolonged by 1.02 years.

Thirdly and finally, the proposed large 270 occupant residential energy hub integrating renewable energy, demand response and energy storage system, revealed a potential break-even point of 5 years, compared to the first baseline, with a potential cost-saving of 5 640 043.28 USD over a 20-year life cycle, was observed. The optimal control case revealed a potential break-even point of 5.74 years compared to the second baseline, with a potential cost-saving of 5 102 634.70 USD, over a 20-year life cycle, was observed. Furthermore, the proposed optimal control model achieved an annual operational grid energy cost-savings of 83.59 % and 82.37 %, compared to the first baseline and second baseline, respectively.

The results of the various proposed models, by applying the proposed optimal control techniques, illustrated that an improved feasibility, in terms of energy efficiency and

economic feasibility of high initial capital investments may be achieved. These operational energy costs and energy efficiency incentives become of great importance when it comes to the national energy grid security and greenhouse gas emissions.

Keywords*:*

Cost minimization; Hydrogen storage; Residential energy hub; Space heating, space cooling and water heating; Thermal energy recovery; Time-based pricing.

TABLE OF CONTENTS

LIST OF FIGURES

LIST OF TABLES

CHAPTER I: INTRODUCTION

1.1 BACKGROUND

Globally, approximately 42 % of the total energy production is consumed by residential buildings [1]. Space heating, space cooling and water heating at a domestic level, contribute 61.2 % towards the total energy consumption [2]. Fossil fuel resources are depleting, and the electrical energy grid capacity demand is increasing, which, in turn, proportionally increases the carbon dioxide (CO_2) emissions. Due to the observed increase in the electrical energy grid capacity demand, various initiatives, such as load shifting, load shedding, load curtailment, peak clipping, notified maximum demand (NMD) penalties and TOU electricity pricing are enforced, to ease the strain imposed upon the electrical energy grid [3]. The operational cost can become quite significant during the high demand regions of the TOU tariff structure. The forecasted increase, with regards to electricity tariffs in South Africa, poses a threat to the operational costs of residential buildings. Therefore, to mitigate the aforementioned risks effective energy management strategies, should be implemented at the large residential buildings scale to conserve energy which, in turn, could contribute to alleviating the burden on the national energy grid.

In Reference [4], the authors have developed a technique for the optimal design and management of hybrid integrated micro-grid systems, integrating renewable energy and energy storage. Considering the integrated system, consisting of solar PV modules, batteries, heat pump and thermal storage systems, of which the main aim was to maximize the storage efficiencies. The developed energy management strategy was applied to a research center near Rome, Italy.

In Reference [5], the authors have developed a hybrid integrated renewable energy system for heating and cooling equipment, which incorporated demand-side management (DSM). The hybrid integrated renewable energy system consisted of photovoltaic-thermal (PV/T), a ground-source heat pump and the effective control, thereof. The aim of the proposed hybrid integrated renewable energy system was to meet the space heating and space cooling loads of

the residential building, as well as the electrical energy requirements from the space heating and space cooling equipment, efficiently.

The author in Reference [6], has developed an energy efficiency strategy, applied to a hybrid integrated system for Hitit University, consisting of a grid-tied solar PV system, gas engine, electrolyser, hydrogen storage and fuel cell. The solar PV modules and the gas engine were used to supply electrical energy to the university, of which the heat generated by the gas engine was used to supply hot water and space heating demands from the residential building.

In Reference [7], the author has developed a hybrid tri-generation system, integrating renewable energy, solar PV modules, wind turbine and steam turbine, driven by biomass fuel for a small-scale farm and residential building. The electrical energy, generated by the solar PV modules, wind turbine and steam turbine, is supplied to the load, of which the excess heat is recovered from the biomass steam boiler and utilized to assist in meeting the heating loads of the small-scale farm and residential building.

A practical example is the Central Energy Corporation (CENERCOR), proposed to whom a residential energy hub integrating renewable energy, demand response and energy storage system. In Fig. 1.1, a schematic overview of the integrated system, proposed by CENERCOR, is illustrated. As can be seen from the schematic below, the integrated system consists of solar photovoltaic (PV) modules, hydrogen electrolyser, hydrogen fuel cell, battery bank and heat pump. The solar PV modules are controlled based on priority, as the first priority is the hydrogen electrolyser for hydrogen production and the second priority is the residential electrical load and, thirdly, the campus mini grid. The hydrogen, which is generated by the electrolyser, is stored and only utilized by the campus mini grid during the high demand periods of the TOU tariff structure. The heat pump is used for the space heating, space cooling and water heating demands from the residential building. Heat generated by the heat pump, is transferred to two separate tanks, known as a domestic hot water (DHW) storage tank and a heating tank required for water heating and space heating, respectively. The heat, which is generated during the operation of the electrolyser, as well as

the fuel cell, is transferred to the central DHW storage tank. Energy is further stored in a battery bank, which is supplied to the electrolyser, when hydrogen is required by the fuel cell.

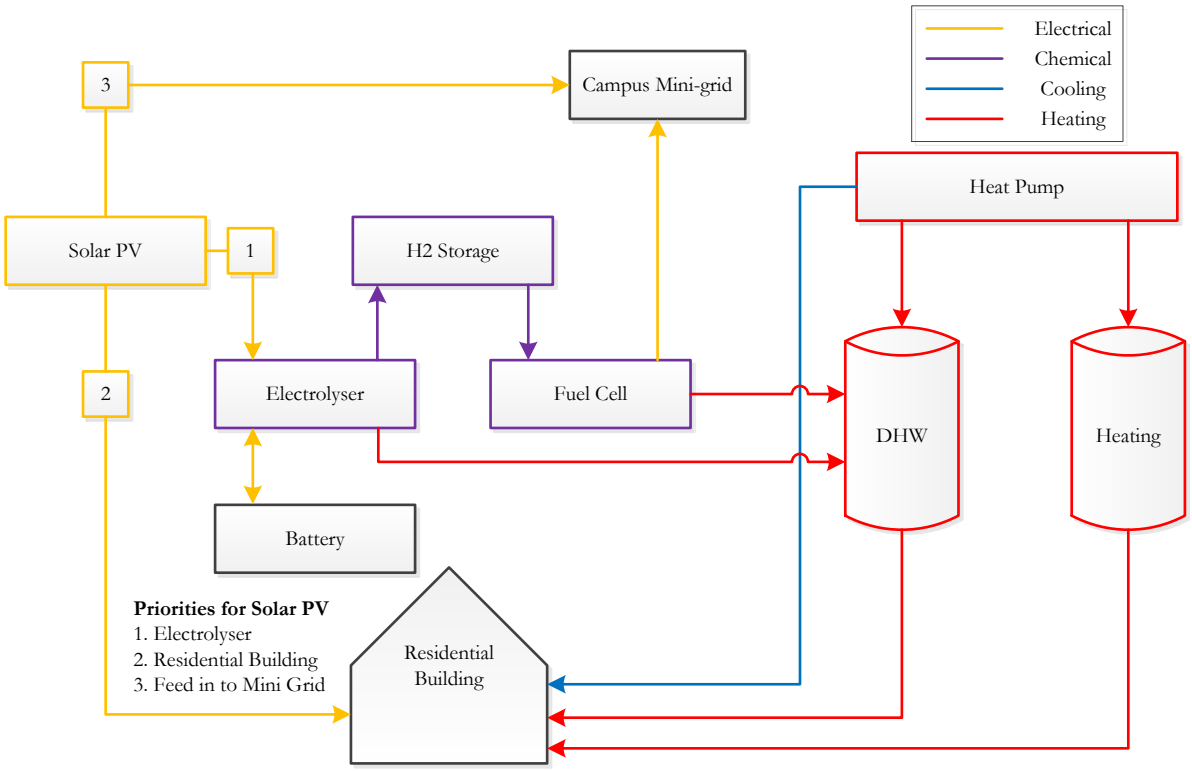

Fig. 1.1: Integrated space heating and water heating system proposed by Cenercor

Based on the proposal presented by CENERCOR, the heat transferred from the electrolyser and fuel cell, are uncontrolled, which means that the majority of the heat generated by the electrolyser and fuel cell are absorbed, leading to a exceptionally low operational efficiency. Another disadvantage is the priority-based control philosophy applied to the solar PV modules, which poses several concerns, such as its inability to be optimally controlled, due to the proposed system being constrained within a rigid control framework. Furthermore, the battery storage becomes of less importance when the solar PV modules are optimally controlled. A further drawback, is that solely one heat pump is used in this setup, as it would become challenging to control the heat pump to meet the space heating, space cooling and water heating demand, based on the TOU tariff structure. Another drawback of the proposed system, is that the hydrogen electrolyser is purely supplied from the solar PV

modules and not from the utility grid, where the utility grid could supply the electrolyser during the low demand regions of the TOU tariff structure.

Therefore, due to the problems identified from the various proposed integrated renewable energy system, the following residential energy hub integrating renewable energy, demand response and energy storage system, is proposed. In Fig. 1.2, a schematic overview of the proposed integrated system is illustrated. Seen below, is the newly proposed integrated system, consisting of solar PV modules, polymer electrolyte membrane water electrolyser (PEMWE), hydrogen storage, polymer electrolyte membrane fuel cell (PEMFC), air-to-air heat pump, air-to-water heat pump and DHW storage tank. The solar PV modules are supplied to the PEMWE and the electrical load. The hydrogen generated by the PEMWE is stored for later use in the hydrogen storage tank, which is supplied to the PEMFC. The PEMFC is used to supply electrical energy to the electrical load, which is further supplied from the utility grid. The utility grid supplies electrical energy to the PEMWE, as well as to the electrical load, which are primarily the air-to-air heat pump and the air-to-water heat pump. The air-to-air heat pump and air-to-water heat pump is supplied by both the utility grid and the integrated renewable energy system. The air-to-air heat pump is purely used to supply space heating and space cooling to the residential building. The air-to-water heat pump is used to supply heat to the DHW storage tank. Due to the nature of the solar PV modules, PEMWE and PEMFC heat is generated during their operation, which could be recovered by the DHW storage tank, alleviating the burden on the air-to-water heat pump.

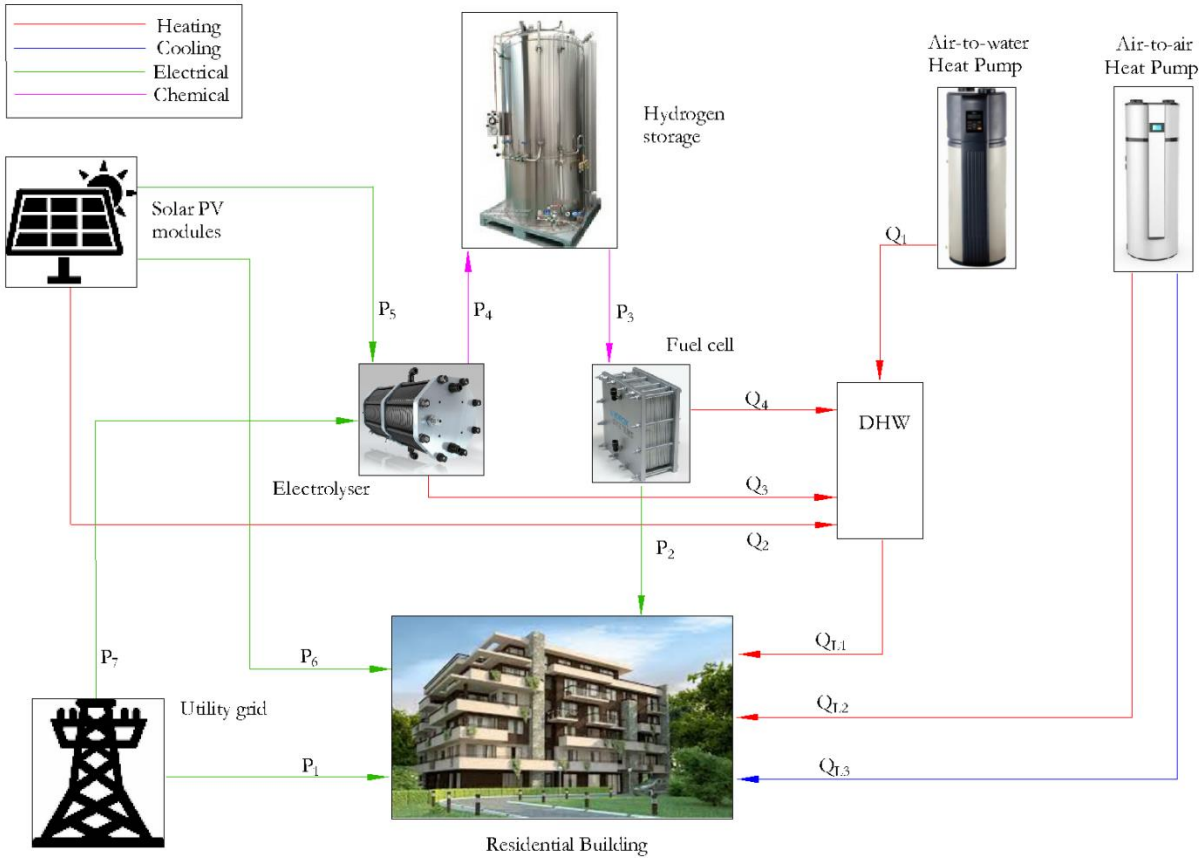

Fig. 1.2: Schematic layout of the proposed residential energy hub integrated with renewable energy

1.2 PROBLEM STATEMENT

From an operational point of view, one of the key challenges experienced by integrated or hybrid systems, for space and water heating, is the power balance that is not easily achievable at minimum cost, between the stochastic demand (heating and cooling loads) and the power generation systems, both submitted to external exogenous variables, such as weather conditions, etc. In literature, as well as the practical example, the performance of such a dynamic operating system is not optimal, due to the following prominent challenges:

- The PV modules, which form part of the integrated system, experience a decrease in the overall efficiency due to heating. There is no provision made for thermal energy

recovery from the PV panel for water heating purposes. This is an important heat source not used.

- The heat pumps in the integrated system consume high amounts of electrical energy, due to the compressor running with a lack of control. This results in higher energy costs, particularly during the high demand regions of the TOU tariff structure.
- The electrolyser, in the integrated system, generates heat during its normal operation. The generated heat is wasted as a byproduct during this operation and is not recuperated, to supply heat to the domestic hot water storage tank. From the literature observed, limited research work has been published, regarding the modeling of generated heat during the charging and discharging operation, as well as utilizing the wasted heat for heating purposes.
- The fuel cell, which forms part of the integrated system, is mainly used to supply electrical energy to the air-to-air heat pump and air-to-water heat pump. Heat generated as a byproduct, is not being recovered.

1.3 OBJECTIVES

This study proposes a hybrid residential energy hub for large residential buildings, integrating renewable energy, demand response and energy storage, by firstly applying the Performance, Operation, Equipment and Technology (POET) concept and, secondly, the optimal control thereof. The aim of the proposed optimal control model applied to the residential energy hub, is to reduce the energy cost, by applying optimal control to space heating, space cooling and water heating integrated system. This may improve the operation efficiency, by reducing the operational cost, whilst preserving certain specific load requirements. Renewable energy systems will be used in tandem with energy storage systems, reducing the strain on the electrical grid. An optimal power dispatch model will be developed, for the sole purpose of reducing the energy costs of the hybrid energy systems. Therefore, the objectives of this study are as follows:

- To review energy efficiency initiatives, applied to integrated energy systems in large residential buildings, for energy cost reductions and energy efficiency improvements.
- To develop a model and simulate the operation of the proposed optimal switching control of an air-to-air heat pump space heating and space cooling system. The simulation results are, thereafter, compared with two baselines. The thermostat-based control of an air-to-air heat pump serves as the first baseline and the timer, with thermostat-based control of an air-to-air heat pump, serves as the second baseline.
- To develop a model and simulate the operation of the proposed optimal switching control of a solid polymer electrolyte membrane water electrolyser (PEMWE) water heating system. The simulation results are, thereafter, compared to a conventional PEMWE system, to evaluate the feasibility of the proposed system.
- To develop a model and simulate the operation of the proposed optimal control of the residential energy hub, integrating renewable energy, demand response and energy storage system. The simulation results are, thereafter, compared to a standard space heating, space cooling and water heating system, which consists of an air-to-water heat pump, for the water heating requirements and an air-to-air heat pump for the space heating and space cooling requirements, to evaluate the feasibility thereof.
- To conduct a techno-economic analysis on the proposed optimal control of the residential energy hub, integrating renewable energy, demand response and energy storage system.

1.4 RESEARCH METHODOLOGY

To achieve the objectives of the study, the methodology is as follows:

1.4.1 Literature review: A comprehensive review of hybrid renewable energy systems connected to space heating, space cooling and water heating systems, by making use of the POET framework. This includes a thorough survey of literature, relating to the

operation and control of renewable energy arrangements with energy storage, space heating, space cooling and water heating equipment. Furthermore, with waste heat recovery techniques applied to each sub-system forming part of the integrated renewable energy system.

1.4.2 Model 1 - Proposed optimal switching control model of an air-to-air heat pump space heating and cooling system

1.4.2.1 System variable identification:

The optimal switching control model of the proposed space heating and space cooling system, consists of an air-to-air heat pump, which is responsible for the space heating and space cooling requirements. Optimal control techniques were applied to the aforementioned model, to achieve various objectives, such as improving the performance, as well as reducing the energy costs subjected to the TOU tariff:

- Independent variables - all the collected input variable data
- Control variable, i.e. decision variable:
  - Switching status of the air-to-air heat pump
- Dependent variables (state variables): The variables influenced by any change in the independent variables and control variables, such as:
  - Residential building temperature

1.4.2.2 Data collection (input variables) and case study:

- Ambient air temperature for the area
- TOU tariff electricity pricing

1.4.2.3 Modelling of the system, as illustrated in Fig. 1.1:

- The model of the proposed system, which includes the space heating, was developed.

- The optimal control algorithm was developed to minimize the operating energy cost of the space heating and space cooling equipment, based on the TOU tariff structure, by making use of the SCIP solver, in the OPTI-Toolbox in MATLAB.
- Each baseline system, as well as the optimal control case study is simulated, using the respective data collected.

1.4.2.4 Simulation:

The proposed model is identified as mixed integer non-linear optimization problems by nature, which forms part of the OPTI-Toolbox in MATLAB. The proposed model is solved using the SCIP solver, due to the fast-solving capabilities which it possesses, as well as seamlessly solving TOU related optimization problems.

- The simulated results include:
  - The optimal switching function of the air-to-air heat pump and the residential building temperature.

1.4.3 Model 2 - Proposed optimal switching control of a solid polymer electrolyte membrane water electrolyser (PEMWE) water heating system.

1.4.3.1 System variable identification:

The optimal switching control model of the proposed PEMWE water heating system, consists of solar PV modules, a PEMWE and a hydrogen storage tank. The PEMWE generates hydrogen from the electrical energy generated from the solar PV modules and, thereafter, is stored in the hydrogen storage tank. Optimal control techniques are applied to the aforementioned model, to achieve various objectives, such as improving the performance and the heat recovery from the PEMWE.

- Independent variables - All of the collected input variable data
- Control variable, i.e. decision variable:
    - Switching status of the PEMWE water heating system
- Dependent variables (state variables): The variables influenced by any change in the independent variables and control variables:
    - Hot water storage tank (HWST) temperature

1.4.3.2 Data collection (input variables) and case study:

- Solar radiation data
- Inlet water temperature supplied to the water heating system
- Ambient air temperature for the area

1.4.3.3 Modelling of the system, illustrated in Fig. 1.1:

- The model of the proposed system, which includes the water heating system, was developed.
- The baseline system and the optimal control case study were simulated, using the respective collected data.

1.4.3.4 Simulation:

The proposed model is identified as a mixed integer non-linear optimization problem by nature, which forms part of the OPTI-Toolbox in MATLAB. The proposed model is solved using the SCIP solver, due to its fast-solving capabilities.

- The simulated results include:
    - The optimal switching function of the air-to-air heat pump and the residential building temperature.

1.4.4 Model 3 - Proposed optimal control of the residential energy hub integrating renewable energy, demand response and energy storage system.

1.4.4.1 System variable identification:

The third system consists of a residential energy hub integrating renewable energy, demand response and energy storage system. Optimal control techniques are applied to the aforementioned model, to achieve various objectives, such as improving the performance and the heat recovery of the equipment, as well as reducing the energy costs subjected to the TOU tariff:

- Independent variables
  - All of the collected input variable data
- Control variable, i.e. decision variable:
  - Power flows between sub-systems of the hybrid system and switching status of the air-to-air heat pump and the air-to-water heat pump.
- Dependent variables (state variables): The variables which are influenced by any change in the independent variables and control variables. These are:
  - State variables: Hydrogen storage level and HWST temperature

1.4.4.2 Data collection (input variables) as well as the case study on the new residence at the Central University of Technology (CUT), Bloemfontein, Free State.

- Solar radiation data
- Hot water demand flow rate
- Inlet water temperature supplied to the water heating system
- Ambient air temperature for the area
- TOU tariff electricity pricing

1.4.4.3 Modelling of the system, as illustrated in Fig. 1.1:

- The final optimal control algorithm is developed to dispatch power efficiently between the sub-systems, forming part of the hybrid integrated system, by making use of the SCIP solver in the OPTI-Toolbox in MATLAB. In addition, the aforementioned algorithm included the space heating and water heating

equipment, with thermal energy recovery supplied solely to the water heating system.

- The two baseline systems, as well as the optimal control case study, are simulated using the respective data collected.

1.4.4.4 Simulation:

The proposed model is identified as a mixed integer non-linear optimization problem by nature, which forms part of the OPTI-Toolbox in MATLAB. The proposed model is solved using the Interior Point Optimizer (IPOPT) non-linear solver, due to its capabilities of solving power dispatch problems, as well as solving TOU related optimization problems efficiently.

- The simulated results include:
  - The optimal power flow of the solar PV, utility grid and the PEMFC power supplied to the electrical load, optimal power flow of the utility grid and the solar PV power supplied to the PEMWE, the hydrogen storage level, residential building temperature, thermal energy recovery of the solar PV modules, PEMWE and PEMFC, as well as the HWST temperature.

The flowchart of the thought processes behind the modelling methodology, for each of the models, is depicted in Fig. 1.1. The first step, regarding the modelling methodology, is to identify the respective input variables, after which realistic initial values are set for each state variable. In the final step, the optimization problem was solved.

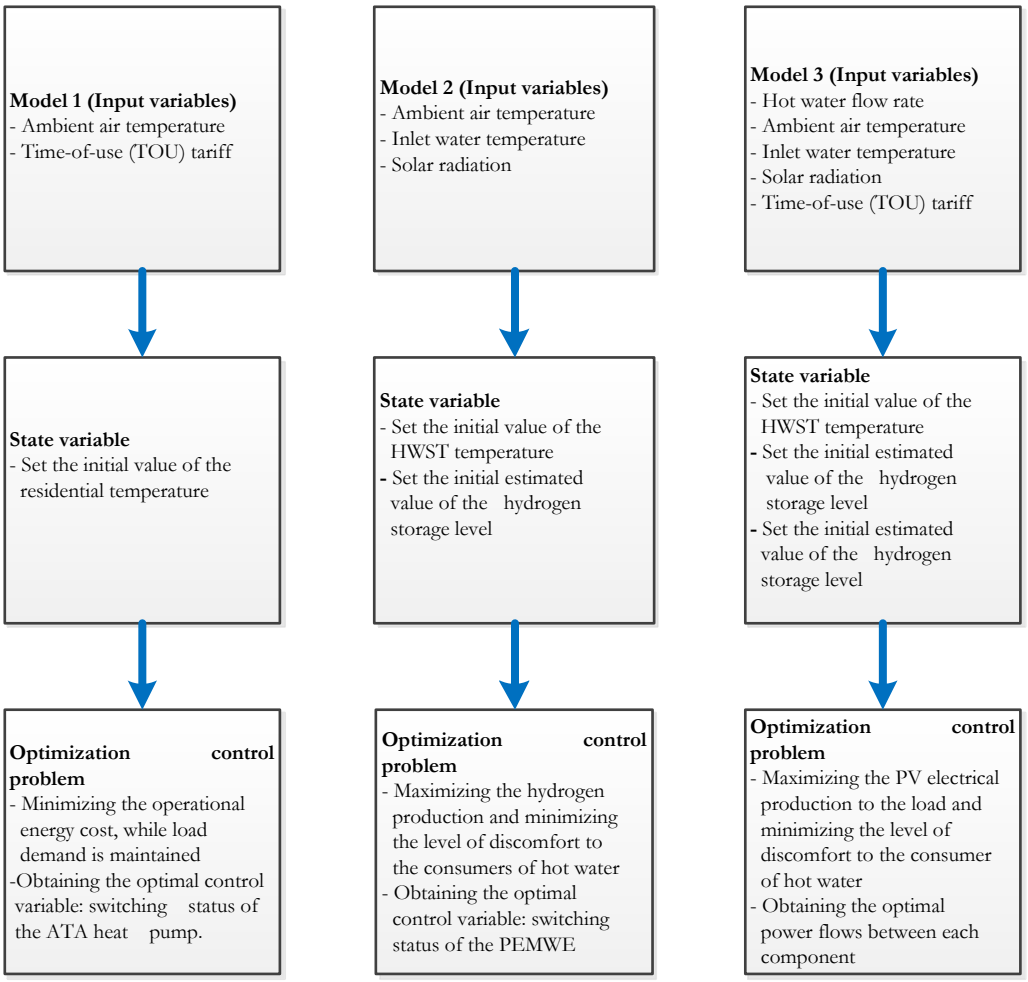

Fig. 1.3: Flowchart of methodology and research design

1.4.5 Techno-economic analysis of the proposed residential energy hub integrating renewable energy, demand response and energy storage system

1.4.5.1 Annual cost-savings analysis:

- The annual utility grid electrical energy cost of the first baseline, second baseline and proposed residential energy hub integrating renewable energy, demand response and energy storage system, are calculated from each simulation result.
- An annual energy cost-savings analysis is conducted on the proposed system, compared to the first baseline.

- An annual energy cost-savings analysis is conducted on the proposed system, compared to the second baseline.

1.4.5.2 Initial capital investments:

- The initial capital investment, forming part of the first baseline, is outlined.
- The initial capital investment, forming part of the second baseline, is outlined.
- The initial capital investment, forming part of the proposed optimal control of the residential energy hub integrating renewable energy, demand response and energy storage system, is outlined.

1.4.5.3 LCC analysis:

- A LCC analysis is conducted on the proposed system, compared to the first baseline, to determine a break-even point.
- A LCC analysis is conducted on the proposed system, compared to the second baseline, to determine a break-even point.

1.5 CONTRIBUTIONS TO KNOWLEDGE

1.5.1 Model 1

The first contribution of the optimal switching control of an air-to-air heat pump, described in detail in Chapter III, was that the electrical energy cost of the air-to-air heat pump was able to be minimized, by avoiding operating the equipment during the peak pricing regions of the TOU tariff structure, whilst ensuring that the level of discomfort of the consumer was minimized; thus, ensuring the temperature set-points were reached, with the least amount of energy consumed.

The second contribution of the proposed model adapted excellently to the various disturbances under which it is exposed to, including building transmission losses, number of occupants present, as well as the number of lights switched on.

1.5.2 Model 2

The first contribution of the comprehensive optimal switching control model of a PEMWE, described in detail in Chapter IV, was a maximized heat recovery from the PEMWE by the HWST, whilst ensuring sufficient hydrogen was produced. The recovered heat was utilized to form part of an integrated water heating system effectively, to minimize the operational energy cost of the main water heating source, such as an air-to-water heat pump.

The second contribution of the optimal control model yielded a prolonged membrane lifespan of the PEMWE, by controlling its operating temperature, which is one of the highest costs in this type of system.

1.5.3 Model 3

The first contribution of the optimal control strategy of a residential energy hub integrating renewable energy, demand response and energy storage system, described in detail in Chapter VI, was the maximized heat recovery from the solar PV modules, PEMWE and PEMFC by the HWST, whilst maximizing the electrical energy supplied from the solar PV modules to the electrical load.

Secondly, the operating energy cost of the utility grid was also minimized, from a power dispatch perspective.

The third contribution yielded a prolonged lifespan of the solar PV modules, PEMWE and PEMFC membranes, by reducing the operating temperature of the equipment through effective cooling.

Social impact:

- The proposed research solutions provide a means to minimize the imposed operating energy costs of the hybrid renewable energy systems connected to space heating, space cooling and water heating systems.

- Furthermore, the proposed research solutions contribute towards energy efficiency improvements, as well as reducing greenhouse gas emissions, by minimizing the operating energy costs, as well its carbon footprint.

1.6 HYPOTHESIS

- The optimal switching control algorithm of the air-to-air heat pump, may substantially reduce the operating energy cost, as well as the energy consumption, thereof.
- The optimal control algorithm of a hybrid renewable energy system, connected to space heating and water heating systems may maximize the heat recovery from the solar PV modules, PEMWE and PEMFC by the HWST, whilst maximizing the electrical energy supplied from the solar PV modules to the electrical load.
- The optimal control model will prolong the membrane lifespan of the PEMWE and PEMFC, as well as prolonging the lifespan of the solar PV modules, by reducing the operating temperature of the equipment through effective cooling, as this equipment is one of the highest costs in this type of system.

1.7 DELIMITATION

The study was conducted with the following delineations:

- The main focus of this study is mainly on large scale residential buildings, due to the extensive load requirements, particularly from the perspective of space heating, space cooling and water heating equipment. However, the energy management techniques applied to the proposed research models, have the potential to be applied to any residential and commercial building with similar technology installed, as seen in Chapter III.

- The study mainly focused on the mathematical model developments and the simulations, thereof.
- In this study, a large residential building in Bloemfontein is considered, as the variable input data was available for this case study. However, the energy management schemes and optimization techniques applied to the case study mentioned above may, in addition, be applied to further large residential buildings, commercial buildings, as well as in healthcare institutions, worldwide.

1.8 PUBLICATIONS DURING THE STUDY

Conference paper(s):

- Siecker Juan, Kusakana Kanzumba, and Numbi Bubele P. "Innovative Energy Management of an Integrated Space and Water Heating System: Case of a Residential Building at CUT." In 2019 Open Innovations (OI), pp. 440-445.
- Siecker Juan, Kusakana Kanzumba, and Numbi Bubele P. "POET Concept for Improving Electrical and Thermal Efficiency of Main Equipment in a Residential Energy Hub." In 2020 8th International Conference on Smart Grid and Clean Energy Technologies (ICSGCE), pp. 52-58.

Journal paper(s):

- Siecker Juan, Kusakana Kanzumba, and Numbi Bubele P. "Optimal switching control of an air-to-air heat pump operating under variable time-based electricity pricing." Energy Reports 8, no. 3 (2022): pp. 995-1 002.
- Siecker Juan, Kusakana Kanzumba, and Numbi Bubele P. "Optimal heat recovery during polymer electrolyte membrane electrolysis." International Journal of Hydrogen Energy 47, no. 76 (2022): pp. 32 692-32 706.

- Siecker Juan, Kusakana Kanzumba, and Numbi Bubele P. "Optimal heat recovery and power dispatch of a proton exchange membrane fuel cell integrated with a renewable energy grid tied hybrid system". (Accepted)

1.9 THESIS LAYOUT

This thesis has been distributed into six Chapters, of which the main research results are presented in Chapters III, IV and V.

Chapter I presents the background related to the study, problem statement and research methodology.

Chapter II presents a comprehensive review of hybrid renewable energy systems connected to space heating, space cooling and water heating systems, by applying the POET framework, including a thorough literature survey, further focusing on the operation and control of renewable energy arrangements with energy storage, space heating, space cooling and water heating equipment.

Chapter III presents the formulation of the optimal switching control model of an air-to-air heat pump providing space heating and space cooling to a residential building. A mathematical model was developed, after which the various constraints and the multi-objective function were developed and defined. Actual and accurate variable input data was used to perform the simulations of this model. Furthermore, a daily economic analysis was conducted, to evaluate the feasibility thereof, by comparing it with two baselines.

Chapter IV presents an optimal switching control model of a solid polymer electrolyte membrane water electrolyser (PEMWE), to obtain optimal heat recovery to a HWST. A similar process to the previous chapter was followed, which involved mathematical model development. The various constraints and multi-objective function were cautiously defined and developed. The simulations were conducted by making use of actual and accurate variable input data. The feasibility of the proposed model was thereafter evaluated, by comparing it to a conventional PEMWE system.

Chapter V presents an optimal control model for a residential energy hub integrating renewable energy, demand response and energy storage system. A comprehensive mathematical model was developed, as well as the multiple constraints to which the integrated system and the various sub-systems are exposed. Furthermore, the multi-objective function was developed and clearly described in this chapter. A thorough economic analysis was conducted to evaluate the feasibility of the proposed optimal control model.

Chapter VI concludes the work of this thesis and proposes recommendations for further possible research.

CHAPTER II: REVIEW ON IMPROVING THE ELECTRICAL AND THERMAL EFFICIENCY OF A RESIDENTIAL ENERGY HUB

2.1 INTRODUCTION

In this chapter, the thermal processes, such as space heating, space cooling and water heating processes in residential buildings and various recent energy management strategies applied to them, are reviewed comprehensively and further discussed. The comprehensive review process is based on the POET framework, which systematically assesses the potential energy efficiency improvements that could be applied to large residential buildings. At each level of the POET framework, the associated results are compared, in terms of the energy savings and the associated effort, which relates to the costs of the initiatives.

This chapter is set out in the following manner: The review justification is presented in Section 2.2. Section 2.3 presents the sustainability of an energy management strategy, based on the POET concept. In Section 2.4, the methodology followed in this chapter is presented. In Section 2.5, the literature containing various energy efficiency improvements applied to the space heating, space cooling and water heating processes in large residential buildings, are outlined and summarized, according to the various levels of which the POET framework is comprised. The key findings of the comprehensive literature reviewed, are presented in Section 2.6.

2.2 REVIEW JUSTIFICATION

The operational energy costs associated with the significant energy consumption of residential buildings, on a global scale and the impact, thereof, may become particularly significant during the high demand regions of the TOU tariff structure. Furthermore, the forecasted increase, with regards to electricity tariffs in South Africa, poses a threat to the

operational costs of residential buildings. These systems should be managed as efficiently as possible, reducing the energy cost, whilst preserving certain specific load requirements.

To reduce the strain that electricity costs pose upon large residential buildings, energy-demanding systems should be effectively managed, to conserve energy. Energy conservation studies and initiatives may be applied to large residential buildings, which could ultimately reduce the strain upon the national energy grid. Therefore, the aim of this chapter is to conduct a comprehensive review, using an effective energy management outline to conserve energy, such as the POET energy efficiency concept, presented by Xiaohua Xia and Jiangfeng Zhang [8].

Energy efficiency comprises of various aspects, which are not clearly defined, posing as a challenge in conducting effective energy management strategies. Therefore, in principle, the POET concept is divided into four pillars: performance, operation, equipment, and technology. The POET framework has yielded successful results, with regards to the energy management of various systems, which resulted in substantial energy cost savings. These include healthcare institutions [9], cruise control of heavy haul trains [8] and conveyor belt systems [10]. However, energy efficiency improvements in residential buildings, specifically, may be a particularly challenging task to accomplish. Thus, the energy management framework is broken up into four levels, which involves ease of implementation related to reward.

The first level, further known as the conceptual level, involves rudimentary energy efficiency methods. At this level, a general energy consumption evaluation is performed, to identify the most dominant energy consumers. These problems, at the conceptual level, are solved by applying the Pareto analysis. The Pareto analysis is referring to the 80/20 principle, which implies that if 20 % of effort is applied, an 80 % return may be achieved, further known as the "low hanging fruits" [11]. At this level, the air-to-air heat pump was selected for space heating and cooling and the air-to-water heat pump is selected for water heating.

The second level, further known as the active level, involves more effort in applying strategies, with less than 80 % return. At this level, additional strategies and accessories were

used to potentially improve the efficiency of the systems. These accessories include variable speed drives (VSD's), soft starters and low-cost timers.

The third level, which is the technical level, involved altering/modifying the design of the existing technology or replacing it with new and more efficient technology. This may improve the efficiency of the systems further, at a greater cost. Furthermore, additional validation of data is required, which may improve the accuracy of the economic feasibility studies. New supplementary renewable energy equipment, such as solar PV modules, a proton exchange membrane (PEM) electrolyser, hydrogen storage vessel and PEM fuel cell, were selected.

The last level, which is known as the engineering level, involves acquiring the validated data obtained at the technical level and applying optimization control techniques to the current preferred technology. Therefore, at this level, which is the last level of this energy management framework, the maximum possible efficiency and, in turn, energy cost savings may be achieved. The supplementary renewable energy equipment has been improved through accessories/modifications applied to them. Furthermore, at this level, optimal control techniques are applied to the equipment individually, as well as in an integrated system.

2.3 SUSTAINABILITY OF AN ENERGY MANAGEMENT STRATEGY, BASED ON THE POET CONCEPT

The sustainability of an energy management framework, in order to improve the efficiency of the system, may be assessed by the following three crucial facets: organizational structure, compatibility of performance indices and engineering support [12].

A well-thought-out organizational structure consistently supports the sustainability of any energy management strategy. The POET efficiencies may be greatly stimulated, to enhance the sustainability of an energy management strategy, by depositing certain rule-sets in place, such as energy policies, regulations, incentives and penalties. An example of this, is the TOU tariff structure, which promotes load shifting from peak times. Energy awareness campaigns,

skills development and training, as well as the appointment of energy managers and energy alerts, are crucial for human sensitization, in order to support energy management strategies [13].

The compatibility of performance indices is generally classified into engineering indices and socio-economic indices. Engineering indices include energy security, energy consumed and further technical indicators. On the other hand, socio-economic indices include environmental impact, labour, energy costs, etc. In several cases, these two types of indices may contradict each other. For example, when an improvement in any engineering indices is observed, deterioration in socio-economic indices is further observed. Sustainability enters the picture, when all of these previously discussed indices yield positive compliance with set-targets [14].

Engineering support provides engineering analysis, modelling and optimization techniques, to be the main drivers of the technical feasibility study of an energy system. This may cause the energy management strategy to possess more reliable solutions, which may, furthermore, drive the energy management strategy to be more sustainable [15].

2.4 REVIEW METHODOLOGY

In this chapter, the POET concept is used to conduct a comprehensive review on the energy efficiency of a residential energy hub. The requirement for such an extensive review has been outlined in the introduction sub-section. This section primarily focuses on how the review was directed, as well as its advantages and disadvantages.

A systemic review process, is followed based on the POET concept, to evaluate the energy efficiency improvements, which may possibly be applied to residential energy hubs. Systemic reviews are commonly used, to provide reliable research to the highest degree. The main purpose of these reviews is to provide current extensive research evidence, which encourages the researcher to pursue all possible avenues, with regards to his/her studies, not restricted to one point of view.

The search strategy to provide extensive research evidence is based on peer-reviewed conferences and journal scientific papers. These published articles were obtained from available online databases, related to improving the electrical and thermal energy efficiency of residential energy hubs. Most recent published articles, where possible, were obtained to conduct this extensive review.

The following are considered, regarding the selection criteria for this study: articles published in English, full-text articles, relevant research topics and publication dates. The major advantage of this study is an extensive evaluation of the possible energy savings and, in turn, energy costs, if the precise energy efficiency actions, obtained from the energy management strategy, are applied.

However, the disadvantage of the POET concept is the challenge of determining an accurate amount of effort, in relation to the return, described by the Pareto Analysis, in the introduction sub-section. Therefore, it is of utmost importance to obtain the most accurate quantitative data, which is used to conduct economic feasibility studies.

2.5 ENERGY EFFICIENCY INITIATIVES BASED ON THE POET ENERGY MANAGEMENT STRATEGY

2.5.1. Conceptual Level

2.5.1.1. Technology Efficiency

Electricity consumption data of residential buildings should be analysed, to identify the largest contributors. Fig. 2.1 presents the average energy consumption of residential buildings in a pie chart format [2]. After observing the chart illustrated below, it is evident that space heating and cooling, are the single largest energy-intensive processes in residential buildings, contributing approximately 47.1 % towards the total energy consumption. Water heating, further known as domestic hot water (DHW), consumes approximately 14.1 % towards the total energy consumption and is the second highest energy consumer in

residential buildings. Cooking may consume approximately 12.4 %, which is slightly above the 10 % threshold. Refrigeration, washing, cleaning, ironing, lighting, audio/video, computer/internet, care person and other equipment, consume significantly less than the 10 % threshold.

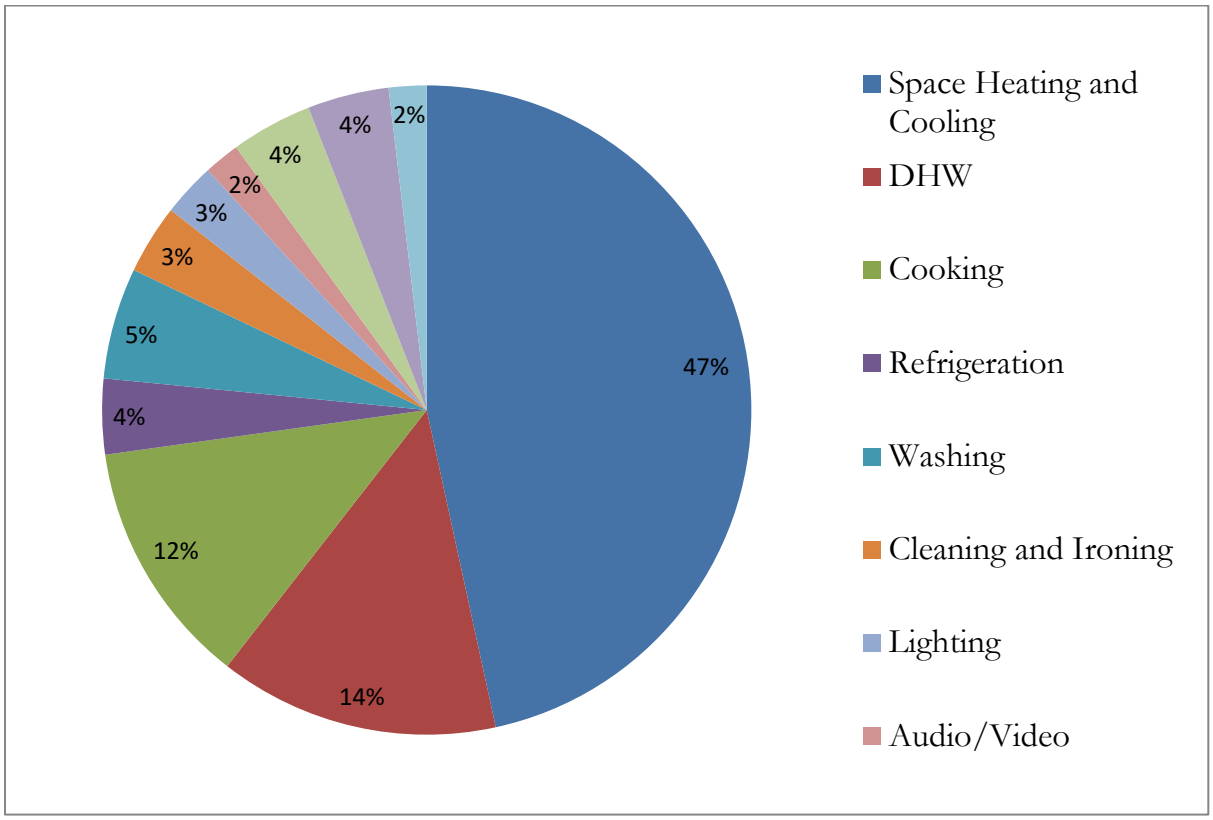

Fig. 2.1: Average electricity consumption of residential buildings

The three largest thermal energy-consuming processes, identified as space heating and cooling, as well as water heating, combined, account for approximately 61.2 % of the total energy consumption. The thermal energy processes are elected, due to the significant energy consumption, which further indicates the most potential, regarding energy efficiency improvements.

2.5.1.2. Equipment Efficiency

Once the major energy consuming processes have been identified, such as the space heating and cooling and water heating, appropriate decisions regarding prioritization and justification of equipment should be made. Improving energy efficiency, at this level, entails the basic operation of each of the equipment required to conserve energy, with regards to space heating and cooling, as well as water heating.

2.5.1.2 a) Space heating and cooling equipment

In this case an air-to-air source heat pump was used, where a refrigerant acts as the evaporating and condensing fluid. The boiling point of the refrigerant is extremely low; thus, heat transfer may occur at ambient fluid temperature. The refrigerant is initially in a low temperature partial liquid/vapour state. The main function of the refrigerant is to transfer heat in the system. Heat from the ambient outside air is absorbed by the Evaporator, where the refrigerant changes from a partial liquid/vapour mixture, into a slightly superheated vapour. The compressor increases the temperature and pressure of the refrigerant vapour, to improve heat transfer. The high pressure and temperature refrigerant vapour is transferred to the condenser unit, where the refrigerant condenses when thermal energy is transferred to the building for space heating. After the condenser phase, the refrigerant is changed to a high pressure and lower temperature vapour. The refrigerant is finally transferred to the expansion/expression valve, which is responsible for changing the refrigerant to a low temperature and pressure partial liquid/vapour mixture. This process, known as the heat pump cycle, as seen from Fig. 2.2, is ready to commence again [16]. For space cooling, a reversing valve is used to reverse this process.

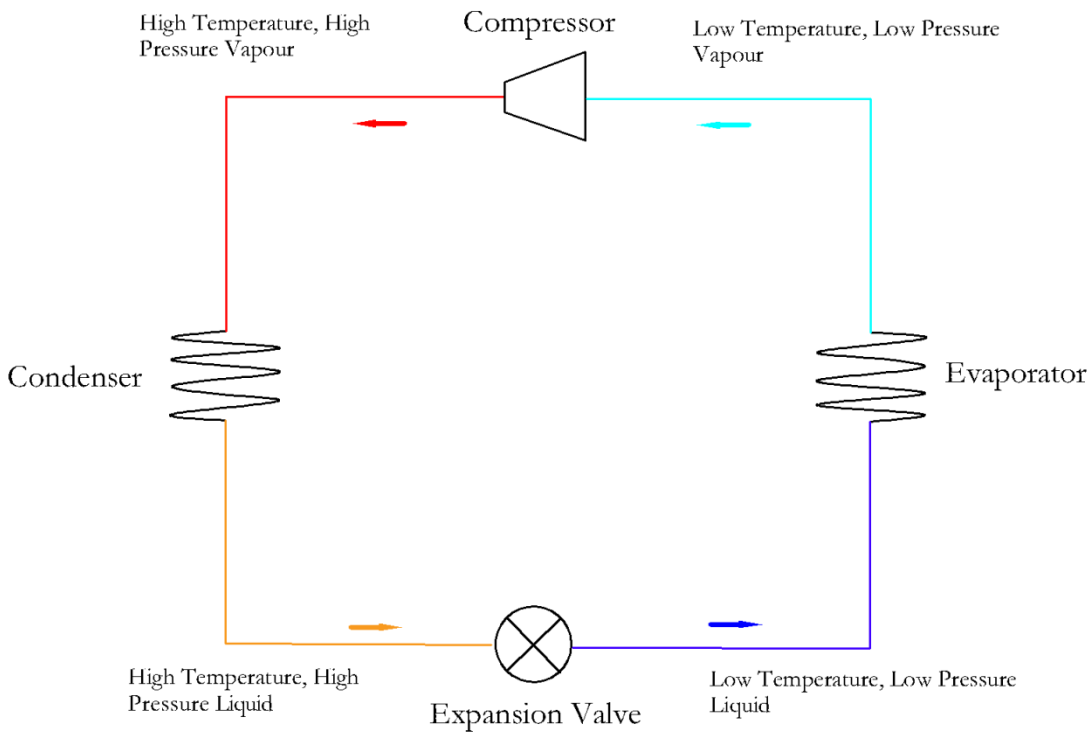

Fig. 2.2: Schematic layout of an air-to-air source heat pump

Heat pumps, at this level, require substantial energy efficiency improvements, with minimum amount of effort. Hence, the following may be considered at the conceptual level, improving the space heating and cooling equipment efficiency:

Building air leakages may be minimised by ensuring appropriate dynamic insulation material for building envelopes, is in order and complies with SANS 10400-XA building regulations [17]. Automatic sliding doors may be used, so that energy is conserved and not wasted to the outside environment.

Energy conservation could be improved by making use of low-cost timers, which may solely be switched on at pre-determined times.

2.5.1.2 b) Water heating equipment

At this level, electric storage tank water heaters (ESTWH) and air-to-water heat pump water heaters are considered. Air-to-water heat pump water heaters offer an energy saving of

approximately 65 %, compared to ESTWHs. Furthermore, the initial investment of air-to-water heat pump water heaters is relatively higher, as compared to ESTWHs [18]. However, an air-to-water heat pump water heater remains the most feasible option when the entirety of the project lifetime is taken into consideration.

Air-to-water heat pump water heaters, operate on the same principle as the air-to-air heat pumps. The heat pump absorbs outside ambient air-to-heat water, as seen in Fig. 2.3, which, in this case, a reversing valve is not required in this setup. The following energy efficiency improvements, at this level, may include the following:

HWST may be subjected to standby losses, which is where thermal energy is lost from the tank to the outside environment. Furthermore, thermal energy is lost from the thermal connecting pipes, due to insufficient piping insulation. Thermal blankets and pipe lagging may be installed, minimizing these effects, which may improve the daily energy efficiency by 21.74 % and 13.04 %, respectively [19].

Low-cost timers may be installed, ensuring that hot water is available at pre-determined times.

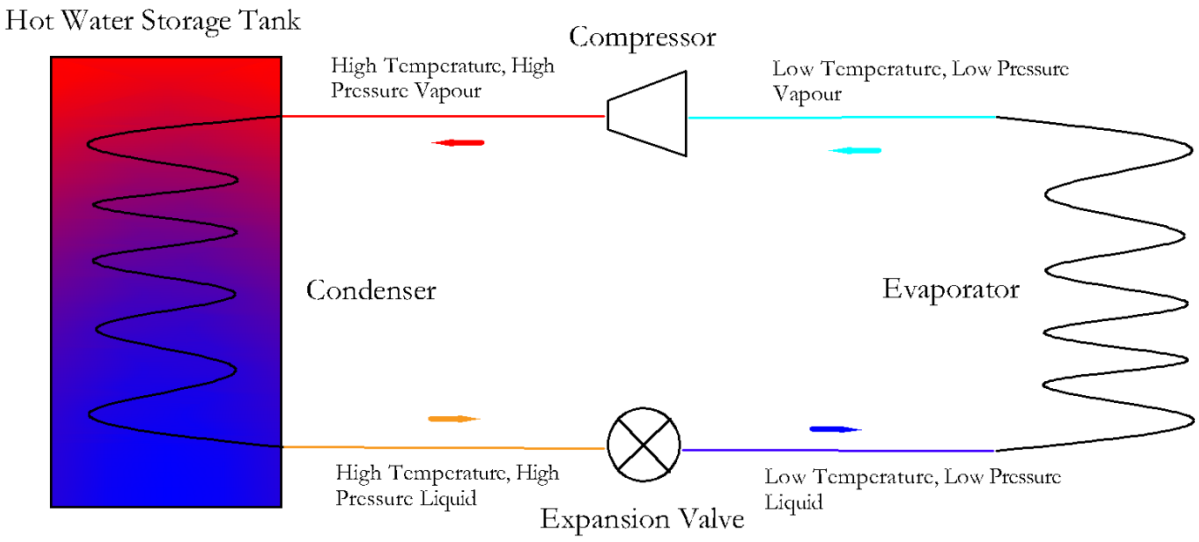

Fig. 2.3: Schematic layout of an air-to-water source heat pump

2.5.1.3. Operation Efficiency

The operation efficiency of a residential building, at this level, requires basic energy management strategies. These energy management strategies may involve basic control techniques, to ensure significant energy efficiency improvements.

2.5.1.3 a) Space heating and cooling equipment

In this case, the operational efficiency, regarding space heating and cooling, may require switching equipment off when not in use and adjusting the temperature set point, to conserve energy.

Space heating and cooling equipment may be switched off when not required to be in operation. Firstly, a study should be conducted to determine at which time intervals occupants are present, which may serve as the estimated load demand. Once the estimated load demand has been established, the low-cost timer may be set up, ensuring sufficient space heating/cooling.

Furthermore, the adjusting of the heating and cooling set-points may result in significant energy efficiency improvements. This was carried out by decreasing the heating set-point and increasing the cooling set-point. According to previous research, if the heating set-point is decreased from 21.1 °C to 20 °C, an energy saving of 34 % may be achieved. Similarly, if the cooling set point is increased from 22.2 °C to 25 °C, an energy saving of 27 %, may be achieved [20].

2.5.1.3 b) Water heating equipment

Water heating equipment may be switched off when not required to be in operation. Once the estimated load demand is established, the low-cost timer may be set up to ensure that sufficient hot water is available during the required intervals.

In addition, if the water temperature set-point is reduced by 10 °C, a possible energy saving of up to 5 %, may be achieved [21].

2.5.1.4. Performance Efficiency

Energy security is regarded as the initial level of performance efficiency, which is one of the key performance indicators (KPI) used for the performance efficiency, known as the energy performance indicator (EPI). Other EPI's may include energy consumption and energy cost.

Enhancements in energy security of a residential building, involve securing the energy supply, without its energy efficiency is meaningless. These may include uninterruptable power supplies (UPS) and generators. In the event of a power failure, UPSs' may solely carry the critical load, until the generator has started up and stabilized. Once the generator has stabilized, it takes over from the UPS, by means of change-over contactors [22]. Whereas, the non-critical load, is solely powered by the generator, in the event of a power failure.

The energy consumption indicator may initially involve a baseline analysis of the energy consumption, which may be followed by setting up energy consumption targets. These targets may be tracked, which may further indicate the energy savings, in terms of energy cost savings. This may create awareness to all stakeholders of the benefits of the energy saving initiatives and, in turn, stimulate energy efficiency as a whole [23].

2.5.2. Active level

At the active level of the energy management strategies, additional equipment/components and software may be required. These energy management strategies may involve more advanced control techniques, compared to that of the conceptual level, in order of ensuring higher energy efficiency improvements. Furthermore, another important facet, at this level, is the validation of further energy efficiency improvements.

2.5.2.1. Technology efficiency

The technology efficiency, at this level, may require intermediate energy monitoring technologies, which may be measured and logged. These technologies may include VSD, soft starters and energy meters. The VSD's and soft starters may have the functionality of indicating the instantaneous readings, such as the power, current, speed, etc [24, 25]. The energy meters could be installed at strategic locations, to measure the various energy-consuming processes, as well as, alerting personnel during any abnormal conditions.

2.5.2.2. Equipment efficiency

At this stage, limited energy management strategies have been applied, which may increase the energy efficiency at the previous level, which is the conceptual level. In this section, basic energy management improvements may be achieved, through the implementation of additional equipment.

2.5.2.2 a) Air-to-air heat pump

At this level, the equipment efficiency, regarding space heating and cooling, may require additional equipment to improve the energy efficiency further, which, hence, may require higher initial investment costs. Therefore, the following are considered at the active level for further energy efficiency improvements, regarding the air-to-air heat pump:

Implementation of VSD's or soft starters on the space heating and cooling equipment fans and compressor, may be considered. The VSD allows the abovementioned components to be controlled, responding to the changing thermal load, as opposed to the ON/OFF control. The soft starters may solely control the inrush current, at every instance when the abovementioned components are switched on. One may observe that VSD's are far more efficient, compared to the soft starters. However, though the VSD's come at a higher cost, compared to the soft starters, the VSD's are elected, due to their flexibility.

2.5.2.2 b) Air-to-water heat pump

In this case, the water heating equipment, such as the air-to-water heat pump water heater, may require the same additional components as those used for the space heating and cooling equipment, at the active level.

2.5.2.3. Operation efficiency

The operation efficiency, at this level, may be improved through the implementation of the previously mentioned additional equipment/components in the equipment efficiency section. Therefore, in this section, control techniques will be discussed, for further energy efficiency improvements.

2.5.2.3 a) Air-to-air heat pump

The operation efficiency may be improved, by reducing the VSD speed at which it operates. The authors in Reference [26], successfully validated a maximum energy saving of 83 %, when the motor speeds were reduced by 60 %. However, these speeds may most likely not satisfy the load requirements, which translates to a significantly lower energy saving.

2.5.2.3 b) Air-to-water heat pump

The operational efficiency of the water heating system may be improved, by adopting the same control techniques as those used for the space heating and cooling equipment, at the active level.

2.5.2.4. Performance efficiency

Initially, at the conceptual level, backup systems were implemented, to ensure energy security.

The reliability improvement of these backup systems, may affect the performance efficiency at this level. A database may be established for all backup systems, to improve the performance efficiency. The database and monitoring systems may contain equipment details, such as diesel storage levels, standby capacity, UPS battery system state of charge (SOC), voltage reading and overall health of the UPS [27, 28].

This data may be useful to determine the overall condition of energy security of the measured equipment, which may indicate whether the equipment should be serviced or replaced.

2.5.3. Technical level

At the technical level of the energy management strategies, new equipment, modifications of existing equipment and automation, may be introduced, further improving energy efficiency.

Additional basic energy management techniques, regarding DSM, may be introduced. Medium to large scale buildings are subjected to the TOU tariff structure, for which the purpose, thereof, is to promote end-users to consume less energy during the high demand regions of the TOU tariff structure. By meritoriously implementing DSM, significant energy savings may be achieved.

2.5.3.1. Technology efficiency

The technology efficiency, at this level, may involve more advanced dashboards for energy monitoring purposes, such as supervisory control and data acquisition (SCADA) software [29]. This software is capable of connecting to field measuring devices, such as

programmable logic controllers (PLC). PLCs may be used, providing real-time data, regarding the energy consumption of various components. These SCADA systems have the functionality of forming a part of the Internet of Things (IOT), which enables the user to have control access from anywhere on earth [28]. Furthermore, the SCADA systems usually have a 'historian', which has the functionality of showing various energy monitoring trends and storing the important history of that data for analysis purposes.

2.5.3.2. Equipment efficiency

At the technical level, the equipment efficiency should be further improved, compared to the previous level, which is the active level. This may be achieved through the implementation of hybrid renewable energy systems. These systems are designed to perform optimally, when the energy consumption is shifted from the high demand regions to the low demand regions of the TOU tariff structure, which is, mostly, achieved through hybrid energy storage systems [30]. At this level, the equipment efficiency, regarding space heating and cooling, may require supplementary renewable energy equipment, to further improve the energy efficiency, which may require even higher initial investment costs. Therefore, the supplementary renewable energy equipment, such as solar PV modules, electrolyser and hydrogen storage vessel, are introduced, and basic energy management improvements are discussed in the following passages. Thereafter, the air-to-water heat pump energy efficiency improvements are discussed.

2.5.3.2 a) Air-to-air heat pump

Additionally, heat pumps, at this level, require substantial energy efficiency improvements, with a substantial amount of effort. Hence, the following may be considered at the technical level, to improve the air-to-air heat pump efficiency:

The authors in Reference [31], have presented a seasonal solar thermal energy storage system for space heating in cold climatic weather conditions, at various locations. The solar

collector area, borehole length, number of boreholes and heat pump capacity, were determined for a typical dwelling for each location. The results have shown that the ground temperatures were stable in each location with solar charging. The coefficient of performance (COP) of the compressor, has shown to be more than 5.8, which shows potential for these systems. It further showed that this type of system may provide more than 93 % of the space heating demands.

In Reference [32], the authors have presented an air-source thermoelectric heat pump system, which may provide both space cooling and water heating, simultaneously. The results of this study indicated that an overall energy efficiency of 90 %, both for space cooling and water heating may be achieved. This validates that thermoelectric heat pumps may be beneficial in daily life, with ambient air as the source of energy.

2.5.3.2 b) Air-to-water heat pump

In this case, the water heating equipment, such as the air-to-water heat pump water heater, may require the same supplementary renewable energy equipment as those being used for the space heating and cooling equipment, at the technical level. However, the following may be considered at the engineering level, to improve the air-to-water heat pump efficiency:

Nannan et al. [33], have built a heat pump water heater test system and a coupling model, containing the vapour-compression-cycle and water heater, with the purpose of analysing the charging and discharging performance. The fixed and variable diameter coil of the heat pump was compared, with regards to its temperature distribution, heat transfer coefficient and the operating efficiency. The results of the charging process, regarding the heat transfer coefficient, as well as the COP, indicated that the variable diameter coil outperformed the fixed diameter coil by 20 % and 10.23 %, respectively. The results of the discharge process, regarding the discharging efficiency and extraction efficiency, indicated that the variable diameter coil outperformed the fixed diameter coil by 7.74 % and 9.7 %, respectively.

In Reference [34], the authors have designed and developed a heat pump water heater, with a frozen type evaporator, where a parallel helical coil type evaporator was used to extract latent heat from the sewage. The data was obtained in the first freezing, melting and second freezing process, at various water temperatures. The results of the developed system, illustrated that it may reduce the required water by more than 90 %, compared to a traditional heat pump water heater. After reviewing the various components, it may be observed that these components could be part of an integrated system for space heating and water heating, where each of the components face problems, which were discussed in the problem statement section.

2.5.3.2 c) PV solar cells

Solar PV solar cells are connected in series and in parallel, which form solar panels. These solar cells comprise of p-type and n-type semiconductor material, which is the positive layer and negative layer, respectively, as seen in Fig. 2.4. During the presence of sunlight, photons are absorbed by the semiconductor atoms, which knock electrons out of its valence band. The released electrons flow from the negative layer to the positive layer, producing an electric current [35].

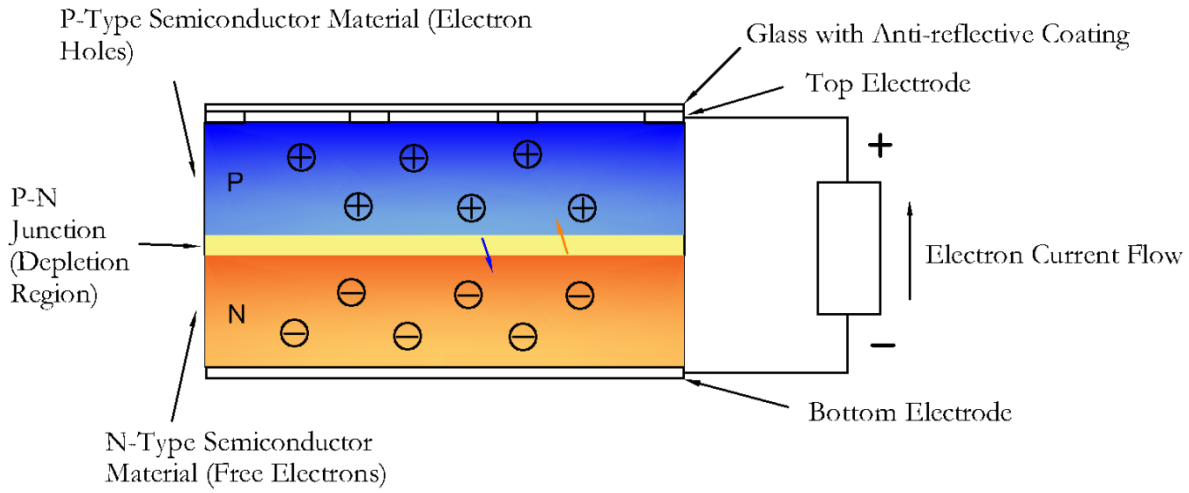

Fig. 2.4: Physical structure of a PV cell

The main purpose of the PV modules is to supply electrical energy to the electrolyser, to produce hydrogen in the gaseous state. Crystalline silicon photovoltaic panels (c-Si PV), behaves flawlessly under high temperature conditions, due to annealing effects, compared to amorphous silicon solar cells (a-Si PV) [36].

2.5.3.2 d) Proton Exchange Membrane (PEM) electrolyser

In Proton Exchange Membrane (PEM) electrolysers, water is supplied at the anode reaction interface through bipolar plates, as seen in Fig. 2.5. When electrical energy is applied, as seen in Eq. (2.1), oxygen and hydrogen are produced at the anode and cathode, respectively [37, 38].

$$H_2O(liquid) + electrical\ energy \rightarrow H_2(\text{gas}) + \frac{1}{2}O_2(gas) \tag{2.1}$$

At the anode side, protons, electrons, and oxygen are produced, as seen from Eq. (2.2). At the cathode side, hydrogen is formed when the electrons and protons recombine, as seen from Eq. (2.3).

$$H_2 0 \rightarrow 2H^+ + 2e^- + \frac{1}{2}O_2(anode) \tag{2.2}$$

$$2H^+ + 2e^- \rightarrow H_2(cathode) \tag{2.3}$$

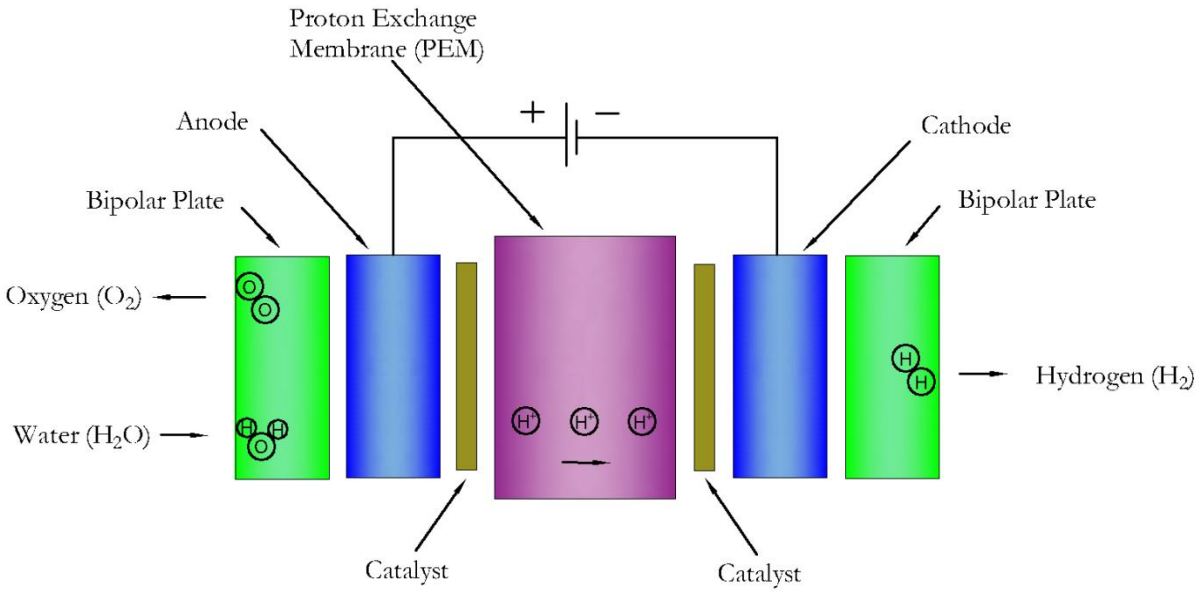

Fig. 2.5: Schematic layout of a Proton Exchange Membrane (PEM) electrolyser

The main purpose of the PEM electrolyser, is to produce gaseous hydrogen, which is stored for on demand requirements. At this level, various energy efficiency improvements have been attempted in recent years.

In Reference [39], the authors of this paper have presented the effect of applying a magnetic field to the PEM electrolyser. The strength of the magnetic field and the flow rate of water, were varied, to study the effect that it has on the performance of the PEM electrolyser. The experimental results achieved a 33 % cell performance improvement, when the magnetic field strength was 1.5 Tesla (T) and the water flow rate was 300 millilitre/per minute (ml/min). The main reason for this improvement is due to the magnetic field causing a pumping effect on the surface of the electrode. This improves the removal of oxygen bubbles and reduces the mass transport polarization, improving the lifespan of the PEM electrolyser.

In Reference [40], the authors have developed an improved design of the PEM electrolyser. This new concept of two plastic frames with integrated mono-polar plates, which form a flexible pocket for the inner cell components, is to improve its heat

management, direct current and media conduction. The capability of the new concept, has been experimentally validated.

The authors in Reference [41], have developed a mathematical model to analyse the performance of a PEM electrolyser and the effect of operating temperature, cathode pressure, membrane thickness, width and height of the channel and current density. The developed model was validated, with valid experimental data, where the results indicated that, when increasing the current density, the voltage of the electrolyser increased, the energy and exergy efficiencies decreased. When the operating temperature of the electrolyser was increased from 313 °K to 353 °K, and the decrease of the cathode pressure from 40 bar to 1 bar, the energy and exergy efficiencies increased between 2 % and 6 % the operating range of the electrolyser.

Rau et al. [42] proposed a solution, which validates that the efficiency of a PV-electrolyser system may be increased, by using a direct connection between a PV module and a PEM electrolyser.

2.5.3.2 e) Proton Exchange Membrane (PEM) fuel cell

In Proton Exchange Membrane (PEM) fuel cells, hydrogen is supplied at the anode reaction interface and oxygen is supplied to the cathode reaction interface, as seen in Fig. 2.6.

$$H_2(gas) + \frac{1}{2}O_2(gas) \rightarrow H_2O(liquid) \tag{2.4}$$

At the anode side, protons and electrons are produced, as seen from Eq. (2.5). At the cathode side, water is formed when electrons, protons and oxygen recombine [43], as seen from Eq. (2.6).

$$H_2 \rightarrow 2H^+ + 2e^- \tag{2.5}$$

$$\frac{1}{2}O_2 + 2H^+ + 2e^- \rightarrow H_2O \qquad (2.6)$$

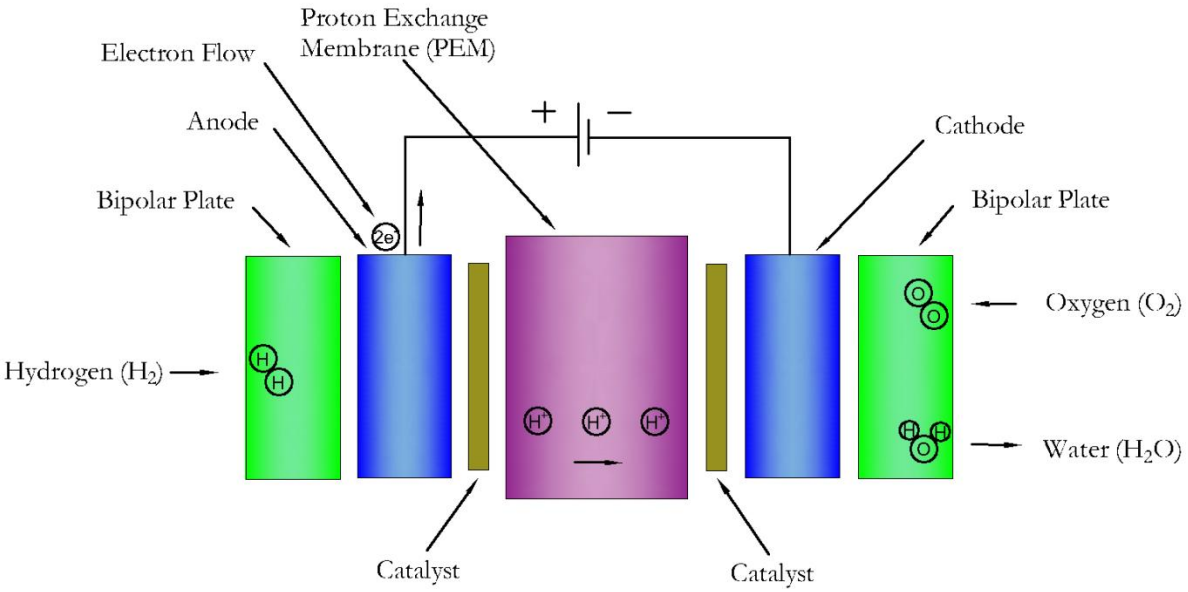

Fig. 2.6: Schematic layout of a Proton Exchange Membrane (PEM) fuel cell

The main purpose of the PEM fuel cell is to produce electrical energy from the hydrogen gas which is supplied from the hydrogen storage vessel. At this level, various energy efficiency improvements have been attempted in recent years.

In Reference [44], the authors have presented an extensive review on various cooling approaches of a fuel cell. Results showed how the operating temperature influenced the performance of the fuel cell, where it may be seen that, by cooling the modules more efficiently, the physical size of the fuel cells may be reduced, as well as the weight, thereof.

The authors in Reference [45], have presented the influence of the exchange current densities, charge transfer coefficients, protonic conduction coefficient and water removal coefficient, that they have on the PEM electrolyser. This was carried out by developing a model, using the ANSYS PEM Fuel Cell Module, after which the simulation results indicated how the activation losses were influenced by the exchange current densities and charge transfer coefficients. The membrane resistance and contact resistance, between the

various components within a fuel cell, contributed towards the ohmic losses. Furthermore, how the concentration losses were influenced by the water removal coefficient.

In Reference [46], the authors have studied the effect of freezing on thermal cycles from 10 °C to 80 °C and further found that the current density reduced from 860 mA/cm^2 to 760 mA/cm^2.

2.5.3.3. Operation efficiency

The operation efficiency, at the technical level, may be improved through the implementation of the previously mentioned supplementary renewable energy equipment, in the equipment efficiency section. Therefore, in this section, control techniques, such as DSM, are discussed for further energy efficiency improvements.

2.5.3.3 a) Air-to-air heat pump

Basic DSM, based on the TOU tariff structure, was carried out through the implementation of the hydrogen storage. Hydrogen was produced through the PEM electrolyser, during off peak periods and converted to electrical energy through the PEM fuel cell, which was used by the air-to-air heat pump, during the peak periods.

Proportional integral (PI) controllers may be implemented, to more accurately control the different zones of heating/cooling, for energy efficiency improvements [47].

2.5.3.3 b) Air-to-water heat pump

Basic DSM, based on the TOU tariff structure, was carried out through the implementation of the hydrogen storage. Hydrogen was produced through the PEMWE, during off peak periods and converted to electrical energy, through the PEMFC, which was used by the air-to-water heat pump, during the peak periods.

Load forecasting may be performed, in order to more accurately set the low-cost timer, for more energy savings [48].

An initiative which ensures that energy usage is monitored more accurately and effectively.

2.5.3.4. Performance efficiency

At the previous level, which is known as the active level, a database was established for all backup systems, which was carried out to improve the performance efficiency. Furthermore, the performance efficiency was monitored, containing various details, as discussed in the active level section.

The advanced energy dashboard, such as the SCADA system, discussed in the technology efficiency section, at this level, is an outstanding tool to measure the performance efficiency of a system. This is achieved by monitoring the energy consumption data, provided by the historian of the SCADA system. Therefore, constant and recent data, regarding the energy consumption, are readily available, which may be used for continuous improvement, by conducting a new baseline analysis, followed by a new target setting. This enables the user to determine more accurate and recent energy savings.

2.5.4. Engineering level

The engineering level, further known as the improvement level, involves more advanced methods to improve energy efficiency. Optimization control techniques may be applied, at this level of the POET concept, which may yield the maximum possible energy efficiency. Therefore, ensuring that energy saving targets, are reached timeously.

2.5.4.1. Technology efficiency

The technology efficiency, at this level, may require additional information, to be included on the energy dashboard, to further improve on it. This may be as basic as a maintenance schedule, which may focus on data analysis, training of personnel and economic analysis, which may be helpful in comparing the planned savings, against the actual savings.

Advanced automation systems, which involve, in this case, dynamic optimal control, should be applied to the major energy consuming processes, such as the space heating and cooling, as well as water heating equipment, to yield maximum energy savings.

2.5.4.2. Equipment efficiency

At this level, the optimal maintenance of the current equipment is attempted to improve the equipment efficiency. As mentioned in the technology efficiency section, at this level, a maintenance strategy should be developed, which requires training of the relevant personnel, to compile a maintenance timetable based on the equipment requirements and specifications.

Furthermore, energy dashboards may be used as a particularly effective tool for the planning and compiling of schedules, based on historic equipment performance. The equipment maintenance frequency should be increased over time, as equipment deteriorates, due to aging.

2.5.4.2 a) Air-to-air heat pump

The equipment efficiency of the space heating and cooling equipment, such as the air-to-air heat pumps, should undergo regular maintenance, which may ensure that the optimal energy efficiency of the air-to-air heat pump, is maintained, which may include the following [49]:

Repairing/replacing of failed sensors, that may provide an energy saving of up to 40 %.

Ensuring that appropriate refrigerant levels are maintained, which may provide a 5 °C – 10 °C saving.

2.5.4.2 b) Air-to-water heat pump

In terms of the air-to-water heat pump maintenance, the following may be considered to maintain optimal energy efficiency [50]:

Thermal blankets could be inspected to ensure that everything is in order.

Pipe lagging and leak inspections may be performed.

2.5.4.2 c) Solar PV modules

At this level, the PV modules may require additional equipment or modification, to further improve the energy efficiency. The PV modules may be modified, such that the heat generated on the surface of the PV module were absorbed through forced water circulation and utilised for water heating applications [51]. The heat gained through forced water circulation, may be transferred to the DHW storage tank, aiding the air-to-water heat pump water heater.

2.5.4.2 d) PEM electrolyser

The PEMWE may require new equipment or modifications, which may further improve the energy efficiency, thereof.

A waste heat recovery system for the PEMWE may be implemented, which may improve its energy efficiency. The optimal operating temperature, ranges from 50 °C – 100 °C [52] and if excess heat is present, it may be removed, by absorbing it through forced water circulation and, in turn, be transferred to the HWST, the same methodology as adopted by the PV modules.

2.5.4.2 e) PEM fuel cell

The new equipment or modifications to further improve the energy efficiency of the PEMFC, may be an exact duplicate of that which is applied to the PEMWE.

2.5.4.3. Operation efficiency

The operation efficiency may be further improved, at this level, by applying various dynamic optimization techniques, which may be applied to the individual equipment. The dynamic optimization techniques may involve, firstly, optimal control techniques. Secondly, it may further involve an optimal power dispatch from the supplementary renewable energy equipment, for supplying and storing of energy, to be dispatched to the loads during the high demand regions of the TOU tariff structure. Thirdly, model predictive control (MPC) may be introduced and applied to the individual equipment. Lastly, all the equipment mentioned, would make up a residential energy hub, integrating renewable energy, demand response and energy storage system. Energy efficiency improvements, related to optimal control, DSM and MPC, are discussed in this sub-section.

MPC is a control method, which possesses the function of predicting the future states of a dynamic process. The controller generates a control vector, to minimise a predefined cost function, subjected to various constraints over a predetermined prediction horizon. The control vector elements are computed for all the sampling intervals, in the prediction horizon. The control algorithm solely applies the first control vector element at the first sampling interval, discarding the remaining control vector elements. Thereafter, the control algorithm computes all the control vector elements again, for the entire prediction horizon and, once more, solely applies the first control vector element at the first sampling interval. This process continues for every subsequent sampling interval, in the prediction horizon [53].

2.5.4.3 a) Air-to-air heat pump

In Reference [54], the author of this paper has presented a new control strategy for a parallel loop hybrid system, with a heat pump and gas fired water heater, in combination. The results of the control strategy, showed to be economically beneficial, ranging from 10 % to 60 %, for space heating applications from -12 °C to 20 °C.

The authors in Reference [55], have developed a transient coupled model, for a variable speed CO_2 direct expansion ground source heat pump, for space heating and cooling of small-scale residential buildings, located in cold climatic weather conditions, such as Canada. The control model rejects optimal heat, by regulating the pressure of the fluid, which allows for the vapour compression cycle to convert from sub-critical to trans-critical. However, the results indicated poor performance, when this system operates at low mass flow rates.

2.5.4.3 b) Air-to-water heat pump

The authors in Reference [56], have developed a heat pump predictive load-shifting controller, where the controller predicts the following day's heating requirements, based on the air temperatures and solar radiation forecasted. The experimental results, indicated more desirable thermal performance of the predictive controller, compared to the simulation results. However, the heat pump was solely in operation during the off-peak region of the TOU tariff, where the performance of the heat pump, under load shift control, was particularly poor.

In Reference [57], the authors have presented an optimal control model of a hybrid heat pump water heater, with an instantaneous shower, powered by means of an integrated renewable energy system. The simulation results indicated a potential cost saving of 23.4 % and 19 L of energy and water, respectively. Furthermore, the excess energy may be fed back into the grid, which may be an additional economic benefit.

Wanjiru et al. [58], have developed an optimal control model of a heat pump and instantaneous water heater, integrated with solar energy, under time-based pricing. The

simulation results yielded a possible power saving of 35 %, with 7.7 kWh energy sold back to the grid and an energy cost saving of 19 %.

2.5.4.3 c) PV modules

The authors in Reference [51], have developed an optimization model of a hybrid PV/T solar system, for domestic hot water applications. Results indicated an improvement in electrical and thermal efficiency, which proved the model to be more economically viable.

In Reference [59], the authors investigated how convection heat transfer and fluid flow, affect the PV module efficiency, where the results of the developed model showed various Reynolds number values in laminar flow, with both optimum plate thickness and length increase in heat transfer.

In Reference [60], the authors have developed a model to extract further energy from solar collectors, by optimizing the fluid flow rate. Results indicated an improvement of 7.82 % extracted energy, where the thermal efficiency decreased between 5.54 % and 7.34 %, when using connecting pipes.

Siecker et al. [61], have developed an optimization model of a hybrid photovoltaic/thermal (PV/T) system, to maximise the electrical output of a PV module and supply hot water to a domestic load. The simulation results indicated a 2.65 % improvement in the electrical efficiency during summer and 5.9 % reduction, during winter. The heat gain, within the hot water storage tank, indicated that it may be utilised by domestic loads.

In Reference [62], the authors have developed a model for a hybrid solar water heater, with an ESTWH. The aim was to reduce the energy cost of heating water, by maximizing the solar water heater utilization and minimizing the switching of the ESTWH, particularly during the high demand region of the TOU tariff structure. The simulation results indicated an energy cost saving of 49 %, in a life cycle of 20 years.

Wu et al. [63], have developed a model to predict the thermal-electrical performance of a heat pipe**.** Results showed that the overall thermal, electrical and exergy efficiency, increased to 63.65 %, 8.45 % and 10.26 %, respectively.

2.5.4.3 d) PEM electrolyser

The authors in Reference [64], proposed a hybrid Photovoltaic/Proton Exchange Membrane Electrolyser. The water temperature of the electrolyser was controlled using fuzzy logic control, to improve its efficiency. The efficiency of the hybrid system, was verified, by maximising the Proton Exchange Membrane Electrolyser hydrogen flow and the PV captured energy.

In Reference [65], the authors have presented a paper to optimally match a PV system with a PEM electrolyser, to maximize the electrical energy transfer and hydrogen production. This was achieved by finding the optimal series-parallel configuration of PV modules and PEM cells. In this study, four 75 W PV modules were used to transfer electrical energy to five 50 W PEM electrolyser stacks. The model predicted a maximum theoretical energy transfer of 94 %, whereas, the experimental results suggested a 95 % energy transfer.

2.5.4.3 e) PEM fuel cell

Lototskyy et al. [66], presented a concept of combined cooling, heating and power energy systems, where solar power is used primarily to supply the electrolyser, which supplies hydrogen to the solid oxide fuel cell. Storage of hydrogen and heat generated, was carried out, by making use of high temperature metal hydrides, as well as low temperature metal hydrides, for superfluous heat management. This was carried out by evaluating the energy balances of the components within the system and the mass, as well as heat transfer modelling. The results indicated that the energy efficiency of the electrolyser and fuel cell modes, is 69.4 % and 72.4 %, respectively. Furthermore, the tri-generation system led to a 36 % improvement, as opposed to the standalone systems.

In Reference [67], the authors have designed a neural network controller, to control the temperature of a 5 kW fuel cell. This controller, initially, learns the pattern of the dynamic power demand, which is the driving force for the fuel cell to produce current. This may influence the temperature of the fuel cell stack, where the change in temperature is

controlled by varying the water-cooling flow rate, through the fuel cell stack. The simulation results showed that the desired temperature set-point is maintained, by using this neural network controller.

The authors in Reference [68], presented the importance of possessing a robust temperature for a PEM fuel cell. In this paper, a model-based characterization of the equilibrium point of an open cathode fuel cell, for appropriate design, is presented. The results indicated the relation between the temperature of the fuel cell, humidification and overall performance. Furthermore, the simulation results validated this robust temperature controller, applied to a nonlinear plant model.

In Reference [69], the authors have proposed an analysis and optimization model for a high temperature proton exchange membrane fuel cell (HT-PEMFC), based on the surrogate model. The surrogate model was developed with samples obtained from the available budget, to conduct the analysis and optimization. The results showed that it affects the cathode stoichiometric ratio of the cell performance more than the anode stoichiometric ratio and that significant nonlinear interactions among the flow channel geometry, are present. The maximum current density and real power, were achieved at a fixed operating voltage, yielding a 10.54 % and 3.93 % improvement, compared to the baseline design, respectively.

The authors in Reference [70], have developed a MPC controller for a fuel cell, powered by renewable energy. In this study, the MPC control algorithm regulating energy sub-system with a supervisory MPC framework is evaluated at various parameters.

2.5.4.3 f) Residential energy hub integrating renewable energy, demand response and energy storage system.

The optimal power dispatch of integrated renewable energy systems, under time-based pricing are discussed in this sub-section. These energy efficiency improvement studies include optimal control of thermal energy storage, hydrogen energy storage, battery storage and demand response, applied to integrated renewable energy systems.

Sichilalu et al. [71], have presented an optimal control technique, to optimize a heat pump water heater, which is supplied from a wind generator-solar photovoltaic-grid. The main objective, was to minimize the energy costs, whilst providing the desired hot water temperature profile, where the results validated this model with a 70.7 % cost reduction achievement.

The authors in Reference [72], have developed an optimal power dispatch model of a grid-tied PV-battery–diesel system, that supplies electrical energy to heat pump water heaters. The battery system was used as the energy storage system during the peak times of the TOU tariff, while the diesel generator was the backup source. The simulation results showed great potential, regarding DSM, which yielded a maximum possible energy cost saving of 68.09 %.

Sichilalu et al. [73], have developed an optimal control model of a grid-tied-PV-fuel cell hybrid system, with the objective of minimizing the energy cost, taking the TOU tariffs into account. This was achieved through the PV modules supplying electrical energy to the electrolyser, storing of the produced hydrogen, for the fuel cell to produce and supply electrical energy to the load demand during the peak times of the TOU tariffs. The simulation results showed that the heat pump water heater, consumed 45.50 kWh under the optimal control conditions, whereas, with a normal thermostat-based controller, it consumed 84 kWh.

In Reference [74], the authors presented a residential energy hub model, in which energy production, conversion and storage were integrated. The electrical, heating and cooling demands are supplied by electricity, natural gas and solar radiation, subjected to a demand response program, which includes load shifting, load curtailing and flexible thermal load modelling. The simulation results validated the feasibility of the proposed model.

The authors in Reference [75], have presented a comprehensive overview of the concepts applied to energy hubs in different sectors, that require energy, such as the residential, commercial and industrial sectors. The energy hub as an integrated energy management system, was evaluated to investigate whether it has the capability of solving the challenges of the major energy consuming processes, in the various sectors. In this study, the focus was

the possible benefits of integrating demand response, distributed energy resources, renewable energy resources, multi-generation systems, energy storage systems and smart energy hub applications.

Jamalzadeh et al. [76], proposed a hybrid interval-stochastic approach, to design an algorithm of an energy hub, where a thermal energy market, thermal demand response and electricity demand response, were considered, in order to minimize operational costs. In this study, a deviation cost was added as a second objective to the average cost objective, with a weighted sum. The simulation results depicted an increase in the average cost, with a decrease in the deviation cost, which confirmed that robust scheduling of an energy hub, system in uncertain conditions, was obtainable.

In Reference [77], the authors presented the optimal control of an energy hub, where it consists of various energy sources and generation to supply electrical, thermal and gas demands. The energy hub, in this study, consisted of wind and solar renewable energy resources, combined heat and power cogeneration, power-to-gas units and a gas-fired generator, in which interdependencies of infrastructures for these energy sources were provided. The energy stability and security of the energy hub, were investigated in this study. The genetic algorithm solver is used to maximize the energy efficiency and minimize the CO_2 emissions. The simulation results of this study, showed an increase in performance when the aforementioned equipment is used in an integrated system.

The authors in Reference [78], proposed a demand response strategy for distribution grid management. The distribution system operator used the various energy hubs at its disposal in a demand response manner, to improve its operation. The aforementioned strategy used a recursive two-level optimization structure, to model the interactions between the distribution system operator and the energy hubs. Electrical and thermal loads were considered with constraints, which may improve the flexibility of the energy hubs. Stochastic optimization was included, to cater for the intermittent wind energy resource. 6-bus and 18-bus test systems were used in this study, where the simulation results with the 6-bus test system, illustrated that the peak loads of the energy hub and distribution grid were reduced by 29 %

and 14 %, respectively. This relates to a 10 % and 14 % operating cost reduction of the energy hub and distribution grid, respectively.

2.5.4.4. Performance efficiency

As discussed at the technical level, an advanced energy dashboard, such as a SCADA system, was introduced to improve the performance efficiency, by monitoring the energy consumption data provided by the historian of the SCADA, to analyse the various EPI's.

At this level, energy supply security and reliability of large residential buildings are important, which poses a problem when unproven optimization techniques are used, where disruption of crucial supply and optimal energy efficiency, may be compromised. Therefore, the optimization model should be validated, through conducting an extensive analysis before implementation occurs. This may be overcome, by using real time simulation hardware and software, which enables the user to validate and simulate the optimization control model, while a physical controller may be tested offline, prior to implementation. In this case, a real time simulator, with analogue and digital input-output (IO) channels, may be used to emulate the behaviour of the process, which may assist with the fine-tuning of the controller, in order to ensure that the system constraints are satisfied [79].

2.6 KEY FINDINGS ON REVIEWED LITERATURE

The POET concept is an effective energy management strategy, for energy efficiency improvements of large-scale residential buildings. Based on the four levels of which the POET comprises, various energy efficiency improvements were proposed. These levels were presented in the sequence of which they were conducted, which includes: the conceptual level, active level, technical level and the engineering level.

As explained previously in this study, the Pareto analysis (80/20 principle), were conducted at the conceptual level, which implies that if 20 % of effort is applied, an 80 % return may be achieved, further known as the "low hanging fruits". At this level, the major

energy consumers were identified, which is the space heating and cooling, as well as water heating equipment. Thereafter, the previously mentioned principle was successfully applied to the air-to-air heat pump and, air-to-water heat pump, which involved low cost and effort initiatives, with high impact on rewards with regards to energy efficiency improvements. Thus, a swift payback period (PBP), was achieved.

The subsequent level, which is the active level, required a higher level of cost and effort to be applied to the space heating and cooling, as well as water heating equipment. At this level, the Pareto analysis was slightly changed from 20/80 to 40/60 and successfully applied to the air-to-air heat pump, for space heating and cooling, as well as air-to-water heat pump for water heating, which implies that, if 40 % of effort is applied, a 60 % return may be achieved, which was achieved at this level.

The third level, known as the technical level, required an even higher level of cost and effort to be applied to the space heating and cooling as well as water heating equipment. At this level, the Pareto analysis was, once again, changed to 60/40, which implies that if 60 % of effort is applied, a 40 % return may be achieved. Therefore, supplementary renewable energy equipment was introduced and successfully applied to the air-to-air heat pump and air-to-water heat pump, at this level, which included solar photovoltaic (PV) modules, a proton exchange membrane (PEM) electrolyser, a hydrogen storage vessel, and a PEM fuel cell. Furthermore, energy efficiency improvements, obeying the 60/40 rule, have been presented and successfully applied to the supplementary renewable energy equipment.

The fourth and last level, known as the engineering level, required an even higher level of effort, compared to the previous level. At this level, the Pareto analysis was, once again, changed to 80/20, which implies that if 80 % of effort is applied, a 20 % return may be achieved. Therefore, modifications were made to the supplementary renewable energy equipment. Forced water circulation was applied to the PV modules, PEM electrolyser and PEM fuel cell, to cool the equipment appropriately, as well as absorb the wasted heat and transfer it to the HWST, reducing the burden on the air-to-water heat pump, for further energy efficiency improvements. Furthermore, the supplementary renewable energy equipment plays a vital role in demand response, DSM and energy storage applied to the air-

to-air heat pump, as well as air-to-water heat pump. Optimal control and DSM techniques were successfully applied to various types of integrated systems.

CHAPTER III: OPTIMAL SWITCHING CONTROL OF AN AIR-TO-AIR HEAT PUMP OPERATING UNDER VARIABLE TIME-BASED ELECTRICITY PRICING

At the offset of this chapter, space heating and space cooling, in residential buildings, and various recent energy management strategies applied to them, are reviewed, followed by identifying the need for the study. Therefore, this chapter further presents the proposed air-to-air heat pump space heating and space cooling system. A mathematical model is developed for the proposed optimal switching control of an air-to-air heat pump space heating and space cooling system, with the main aim of minimizing the operational energy cost subjected to TOU, whilst minimizing the level of discomfort of the occupants, regarding the desired air temperature inside the residential building.

Section 3.1 introduces the chapter, with various relevant reviews on air-to-air heat pumps used for space heating and space cooling. Section 3.2, presents the methodology. Section 3.3, presents the case study description. The simulation results and discussion are presented in Section 3.4. Lastly, in Section 3.5, the conclusion is presented.

3.1 INTRODUCTION

Heat pumps in the space heating and space cooling domain, have gained a wide range of useful applications over the years [80]. In residential buildings, space heating and space cooling, account for approximately 47 % [2] of the total energy consumption, which highlights the need to investigate methods of improving the efficiency, thereof.

Some general means of performing space heating and space cooling, are the boiler type, in which hot water is transferred to the various rooms within the residential building, and thereafter, transferred to the spaces in the building by means of a radiator [81]. A further

method of space heating, is by making use of a wall mounted electric radiator, where it uses an electric element to provide space heating [82]. However, both methods are extremely ineffective, due to their elementary operating principle.

Space heating and space cooling in residential buildings, may be performed, by making use of an air-to-air heat pump, which may be used to improve its operational efficiency, whilst minimizing its operating energy costs.

Few authors have attempted to create a comprehensive optimal control model of an air-to-air heat pump, which includes minimization of the running energy cost, minimization of the level of discomfort to the user, adaptation to exogenous variables, further known as disturbances, such as, the amount of occupants present in the residential building and the amount of lights switched on at each moment in time.

In Reference [83], the authors have developed a dynamic optimization model of an air-source heat pump heating system, in order to reduce energy costs, by making use of the General Algebraic Modelling System (GAMS). The model proposed in this paper, is based on an air-source heat pump, transferring heat to a water pipeline, situated below the building floor, transferring heat to the building. The main objectives were to minimize the energy costs whilst reaching the thermal comfort level of the users, where the simulations results indicated a potential energy cost savings of 16 %.

In Reference [84], the authors have developed a comprehensive model of an air-source heat pump system, with thermal energy storage under varying load shifting scenarios. Data from several households were obtained, to conduct more realistic simulations, where TRANSYS software was used to conduct the simulations. One of the key findings, was that the space heating systems were sensitive when the load shifting techniques were applied.

The authors in Reference [85], developed a dynamic optimization model of an air-source heat pump system, under time-based pricing. The proposed model was based on an air-to-water heat pump, transferring heat to the buffer tank, which is connected to the floor heating water pipeline. The objective function of the algorithm, was to minimize the operation energy cost of the heat pump, under time-based pricing. The simulation results,

illustrated that the hourly optimal scheduling during winter, by adjusting the temperature set-point, based on the meteorological data, showed promising energy costs savings.

In Reference [86], the authors developed an optimal control model of an air-to-water heat pump, which transfers heat to the water pipeline beneath the building floor, which is used for space heating. The sequential quadratic programming solver in the Automatic Control And Dynamic Optimization (ACADO) Toolkit, was used. A Multi-objective function, such as the minimization of the operational energy cost and the maximization of the thermal comfort, was used. The simulation results indicated an energy cost saving up to 4 %, if a 0.5 °C thermal comfort level deviation, which is between the actual building temperature and reference building temperature, is permitted. If the TOU tariff structure is considered, an energy cost savings up to 6 %, may be achieved.

In Reference [87], the authors developed an optimal control strategy, which self-adapts to prevent frosting of air-source heat pumps. This model is based on dimensionless artificial neural network (DANN) correlation model, which was used to analyse the frost formation on the outside heat exchanger. The DANN is improved, by developing a self-adaptive control algorithm, where the simulation results yielded only a 7.55 % difference, compared to the experimental results.

The authors in Reference [88], have developed a novel deep reinforcement learning control algorithm, of which the main focus is to ensure the building temperature is within the desired boundaries, whilst maintaining a minimized energy consumption objective. MPC and rule-based control have been adopted in this study, to compare the performance, thereof. The simulation results yielded the MPC and rule-based control techniques outperformed their model-free counterpart. However, the model-free algorithms, up to this time, still indicated substantial energy cost savings, compared to rule-based algorithms.

After reviewing the literature, it is quite evident that the various authors have developed optimal control algorithms with a multi-objective function, consisting of the minimization of both the energy costs of the heat pump and the level of discomfort. However, the integration of the system disturbances, such as, building transmission losses, the number of occupants present at each moment in time and the number of lights switched on at each

moment in time, are lacking. Therefore, the aim of this study is to propose a comprehensive optimal switching control model of an air-to-air heat pump. The main contributions of this study are as follows:

The electrical energy cost of the air-to-air heat pump is minimized, by taking the TOU tariff structure into account, whilst ensuring the level of discomfort inside the residential building is minimized, such that its temperature set-points are achieved, by ensuring that the air-to-air heat pump is merely switched on to purely meet the temperature set-points and switched off during all of the other instances. Thus, ensuring the temperature set-points are reached, with the least amount of energy consumed. This is achieved, by making use of the SCIP solver, due to this problem being a mixed integer nonlinear optimization problem by nature. Furthermore, this model adapts particularly well to the various disturbances under which it is exposed to, including building transmission losses, number of occupants present at each moment in time and the number of lights switched on at each moment in time. Furthermore, McArthur et al [89], have developed a water source heat pump system, where water is transferred to the radiator units, which are used to provide space heating of the various building rooms, by making use of the genetic algorithm. However, the weakness in their approach, is that the genetic algorithm is stochastic by nature, which means that the results may not be predicted precisely and results may vary significantly. Therefore, in this chapter, a ducted air-to-air heat pump system is developed by making use of the SCIP toolbox, which is deterministic by nature, resulting in particularly accurate and rapid computed results.

3.2 MODEL DEVELOPMENT

3.2.1 Proposed air-to-air heat pump space heating and space cooling system

Fig. 3.1 illustrates the schematic of the proposed space heating and space cooling, to a university residence of 270 students. The air-to-air heat pump uses the vapour compression cycle, to successfully absorb the outside ambient air and transfer the generated heat into the

residential building [16]. Thus, the heat pump serves as the input to the residential building, which is responsible for providing space heating to the residential building. This model ensures that the air-to-air heat pump is controlled, such that the desired temperature set-points are achieved, whilst consuming the least amount of energy. Furthermore, this space heating system may adapt flawlessly to the disturbances of which the residential building is exposed to. These disturbances include the ambient air temperature, the number of occupants present inside the building, during each moment in time, and the amounts of lights that are used during each moment in time. Furthermore, losses experienced by the residential building, is the transmission heat losses, which is through the walls, floor and roof.

3.2.2 Dynamic model of an air-to-air heat pump for space heating and space cooling

In this Section, a mathematical model of this system is developed for simulation purposes, which negates the necessity of conducting physical experiments. The control variable and state variable forming part of the proposed model, are as follows:

- U_A : Discrete switching function of the air-to-air heat pump;
- Ts : Residential building temperature.

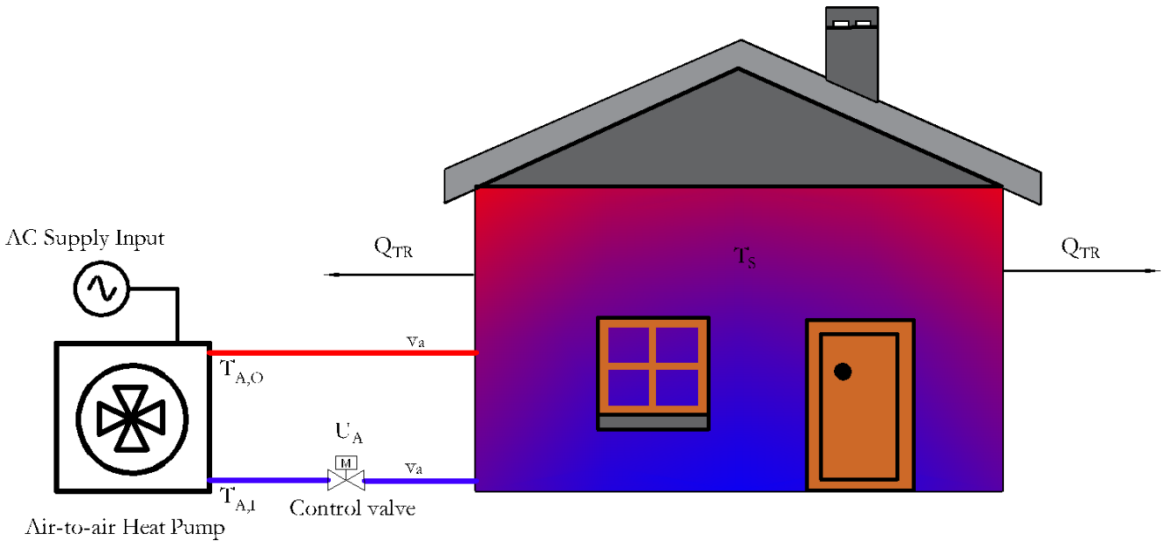

Fig. 3.1: Schematic of the air-to-air heat pump model for space heating and space cooling

The first law of thermodynamics is applied to the space that should be heated, to obtain the energy balance inside the residential building. Eq. (3.1) describes the energy balance equation specifically for space heating. M_a is the mass of the air inside the residential building (kg), C_a is the specific heat capacity of air (J/kg°C) and T_S is the building temperature. Q_{IN} is the useful heat gained by the thermodynamic system [90], Q_{TR} is the transmission heat load [91], i.e. the thermal energy transferred through the building walls, floor, roof, etc, Q_H is the heat load generated from the occupants and Q_L is the heat generated by the lighting inside the building.

$$M_a.C_a.\frac{dT_s}{dt} = Q_{IN} - Q_{TR} + Q_H + Q_L \tag{3.1}$$

The useful heat gain inside the residential building is described in Eq. (3.2). V_a is the volumetric flow rate of the circulation fluid, which is air in this case. ϱ_a is the density of air, $T_{A,O}$ and $T_{A,I}$ are the outlet and inlet temperatures of the air-to-air heat pump.

$$Q_{in} = V_a.\rho_a.C_a.(T_{A,O} - T_{A,I}) \tag{3.2}$$

The transmission heat load of the residential building is described in Eq. (3.3). U_T is the heat transfer coefficient for the transmission load, A_T is the transmission surface area of the building and T_a is the ambient air temperatures.

$$Q_{TR} = U_T.A_T(T_s - T_a) \tag{3.3}$$

The heat load generated from the occupants, is described in Eq. (3.4), by certain factors, such as, P_H, which is the average heat generated by a human being and N_H, the number of occupants present inside the residential building.

$$Q_H = P_H.3600.N_H \tag{3.4}$$

The heat generated by the lighting inside the residential building is determined by Eq. (3.5). P_L is the power rating of the light and N_L is the number of lights switched on.

$$Q_L = P_L.3600.N_L \tag{3.5}$$

By substituting Eqs. (3.2) - (3.5) into Eq. (3.1) yields:

$$M_a.C_a.\frac{dT_s}{dt} = V_a.\rho_a.C_a.(T_{A,O} - T_{A,O}) - U_T.A_T(T_s - T_a) + P_H.3600.N_H + P_L.3600.N_L \tag{3.6}$$

The COP of an air-to-air heat pump is calculated, by making use of Eq. (3.7) [90]. P_A is the rated power of the air-to-air heat pump.

$$COP = \frac{Q_{IN}}{P_A} \tag{3.7}$$

Combining Eq. (3.2) and Eq. (3.7) yield:

$$P_A.COP = V_a.\rho_a.C_a.(T_{A,O} - T_{A,I}) \tag{3.8}$$

Eq. (3.9) can be re-written as follows:

$$(T_{A,O} - T_{A,O}) = \frac{P_A.COP}{V_a.\rho_a.C_a} \tag{3.9}$$

By substituting Eq. (3.9) into Eq. (3.6) yield:

$$M_a.C_a.\frac{dT_s}{dt} = V_a.\rho_a.C_a.\left(\frac{P_A.COP}{V_a.\rho_a.C_a}\right) - U_T.A_T(T_s - T_a) + P_H.3600.N_H + P_L.3600.N_L \tag{3.10}$$

By dividing Eq. (3.10) by M_a and C_a yields:

$$\frac{dT_s}{dt} = \left(\frac{P_A.COP}{M_a.C_a}\right) - T_s.\left(\frac{U_T.A_T}{M_a.C_a}\right) + T_a.\left(\frac{U_T.A_T}{M_a.C_a}\right) + \left(\frac{P_H.3600.N_H}{M_a.C_a}\right) + \left(\frac{P_L.3600.N_L}{M_a.C_a}\right) \tag{3.11}$$

Eq. (3.11) is required to be written in its state space representation, which is illustrated in the following equation: The general state space representation is illustrated in Eq. (3.12), which is necessary to express the previous expression in the state space representation. $\dot{X}(t)$, the state variable, is the residential building temperature, A is known as the state matrix, B is the input matrix and α is the disturbances to the system.

$$\dot{X}(t) = A.X(t) + B.U(t) + \alpha(t) \tag{3.12}$$

Then, applying (3.12) to (3.11), yields:

$$\dot{T}(t) = \left(\frac{P_A.COP}{M_a.C_a}\right).U(t) - T_s.\left(\frac{U_T.A_T}{M_a.C_a}\right) + T_a.\left(\frac{U_T.A_T}{M_a.C_a}\right) + \left(\frac{P_H.3600.N_H}{M_a.C_a}\right) + \left(\frac{P_L.3600.N_L}{M_a.C_a}\right) \tag{3.13}$$

The state matrix, A, is stated in Eq. (3.14), B, the input matrix, is illustrated in Eq. (3.15) and α, the disturbance to the system, is stated in Eq. (3.16).

$$A = -\left(\frac{U_T.A_T}{M_a.C_a}\right) \tag{3.14}$$

$$B = \left(\frac{P_A.COP}{M_a.C_a}\right) \tag{3.15}$$

$$\alpha = T_a.\left(\frac{U_T.A_T}{M_a.C_a}\right) + \left(\frac{P_H.3600.N_H}{M_a.C_a}\right) + \left(\frac{P_L.3600.N_L}{M_a.C_a}\right) \tag{3.16}$$

Such that:

$$\dot{T}(t) = A(t).T_s(t) + B(t).U(t) + \alpha(t) \tag{3.17}$$

3.2.3 Discretized building temperature

Since the numerical approach is easier than the analytical approach, Eq. (3.17) is discretized at each k^{th} sampling interval at a sample period of t_s.

The general discrete formulation of Eq. (3.17), in terms of the k^{th} building temperature, is given in the following equation:

$$T_s(k+1) = \left(1 + t_s.A(k)\right).T(k) + t_s.B(k)U(k) + t_s.\alpha(k) \tag{3.18}$$

Since the state variable, T_{k+1}, should be expressed in terms of its initial value, T_0 and the control variable, $U(t)$, of the initial, T_{k+1}, at each interval, is first derived as:

At the first interval, $k = 0$, which results in the following equation:

$$T_1 = (1 + t_s.A_0).T_0 + t_s.B_0.U_0 + t_s.\alpha_0 \tag{3.19}$$

At the second interval, $k = 1$, which results in the following equation:

$$T_2 = (1 + t_s.A_1).T_1 + t_s.B_1.U_1 + t_s.\alpha_1 \tag{3.20}$$

Furthermore, T_2 from Eq. (3.20) is substituted into Eq. (3.21), such that T_2 in the following equation, after expansion and factorization, becomes:

$$T_2 = (1 + t_s.A_1).(1 + t_s.A_0).T_0 + t_s.\left[(1 + t_s.A_1).B_0.U_0 + B_1.U_1\right] + t_s.\left[(1 + t_s.A_1).\alpha_0 + \alpha_1\right] \tag{3.21}$$

By applying the same principle as Eq. (3.19) – (3.21), at the third interval, $k = 2$, T_3 will be as follows:

$$\begin{aligned} T_3 = (1 + t_s.A_2).(1 + t_s.A_1).(1 + t_s.A_0).T_0 + t_s.\left[(1 + t_s.A_2).(1 + t_s.A_1).B_0.U_0 + (1 + t_s.A_2).B_1.U_1 + B_2.U_2\right] + \\ t_s.\left[(1 + t_s.A_2).(1 + t_s.A_1).\alpha_0 + (1 + t_s.A_2).\alpha_1 + \alpha_2\right], \end{aligned} \tag{3.22}$$

$$\vdots$$

$$T_{k+1} = T_0.\prod_{j=0}^{k}(1 + t_s.A_j) + t_s.\sum_{j=0}^{k}B_j.U_j\prod_{i=j+1}^{k}(1 + t_s.A_i) + t_s.\sum_{j=0}^{k}\alpha_j\prod_{i=j+1}^{k}(1 + t_s.A_i).$$

Here:

T_0 and T_k are the initial and k^{th} building temperature, respectively;

t_s is the sampling time;

U_j is the j^{th} switching status of the air-to-air heat pump, which may either be 1 or 0.

3.2.4 Objective function

The main part of the objective function, described in Eq. (3.23), is to minimize the air-to-air heat pump energy cost, by controlling the switching status of the air-to-air heat pump, $U_A(t)$. C_A is the specific heat capacity of air, ϱ_k is the electricity pricing based on the TOU tariff structure and W_1 is the weighting factor for the cost function.

$$C_A = W_1 . \sum_{k=1}^{N} \left[P_A . p_k(k) . U_A(k) \right] . t_s \tag{3.23}$$

A load profile is obtained, known as the function $F(t)$. This is a function of time and defined as the desired output temperature of the consumer. The thermal comfort level of the consumer is addressed, where the difference between the output temperature $T(t)$ of the hot water storage tank and the desired temperature $F(t)$, should not be excessive. That is, the value of $(T(t)-F(t))^2$ should be minimized. The function $L(t)$ in Eq. (3.24), denotes the thermal discomfort level, which is the second objective function to be minimized [92]. W_2 is the weighting factor the discomfort level minimization function.

$$L(t) = W_2 \sum_{k=1}^{N} \left(T(k) - F(k) \right)^2 . t_s \tag{3.24}$$

Therefore, the final multi-objective function is described in Eq. (3.25), known as J_e.

$$J_e = W_1 . \sum_{k=1}^{N} P_A . p_k(k) . U_A(k) . t_s + W_2 \sum_{k=1}^{N} \left(T(k) - F(k) \right)^2 . t_s \tag{3.25}$$

3.2.5 Constraints

The discrete switching function of the air-to-air heat pump, U_A, which is used to switch the circulating fluid pump, may either be 1 or 0. This is illustrated below:

$$U_A \in \{0,1\} \tag{3.26}$$

The control variable may either be 1 or 0, which is the upper bound and lower bound of the switch. This is shown in the following equation:

$$lb \leq x \leq ub \tag{3.27}$$

3.2.6 Proposed optimization solver

The objective function, as shown in Eq. (3.25), is a non-linear function with an integer-binary control variable that should be solved, in order to obtain the optimal switching status of the air-to-air heat pump. This problem is a mixed integer nonlinear optimization problem (MINLP) and may be solved using the SCIP solver in the optimization toolbox of MATLAB [93]. The main reasons for using SCIP as the solver, are due to its fast-solving capabilities and that it may solve non-linear optimization problems, by controlling a binary integer decision variable, which is required to switch the air-to-air heat pump.

3.3 CASE STUDY DESCRIPTION

In this Section, the optimal switching control of the air-to-air heat pump is simulated using the SCIP solver, in the optimization toolbox of MATLAB. The main objective is to maximize the space heating and space cooling thermal comfort level of the occupants and whilst minimizing the running energy cost of the air-to-air heat pump under time-based pricing.

A case study is conducted using meteorological data obtained at the University of Free State, Bloemfontein, South Africa, on an air-to-air heat pump [94]. The air-to-air heat pump is used to perform space heating and space cooling to a University residence for 270 students. The main objective is to maximize the space heating and space cooling thermal comfort level of the occupants, whilst minimizing the running energy cost of the air-to-air heat pump under time-based pricing. The sampling time, ts = 30 minutes, is implemented, to simplify the simulations.

3.3.1 Data presentation

Table 3.1 shows the parameters of a typical University residential building, with a capacity of 270 students, to be heated and cooled [95]. As the dimensions of the residential building is not known. Therefore, the dimensions per room are taken as 4 m x 3 m x 2.3 m, which is multiplied, to obtain the volume per room, calculating to 27.6 m^3. The calculated volume is further multiplied with the 270 rooms, to obtain a total volume of 7 452 m^3, illustrated in Table 3.1. The total surface area is calculated as stipulated in Table 3.1.

Table 3.1: University residential building parameters

Parameters	**Symbol**	**Value**	**Unit**
Room height	H_r	2.3	m
Building volume	V_B	7 452	m^3
Walls and roof surface area	A_T	15 174	m^2
Heat transfer coefficient for transmission losses	U_T	8	W/m^2K
Air density	ϱ_a	1.2929	kg/m^3
Building air mass	M_a	9 634.69	kg

There are 810 lights, each rated at 15 W installed in the residential building [96]. The number of lights switched on during the day and when the occupants are present inside the residential building, are illustrated in Figs. 3.2 and 3.3, respectively.

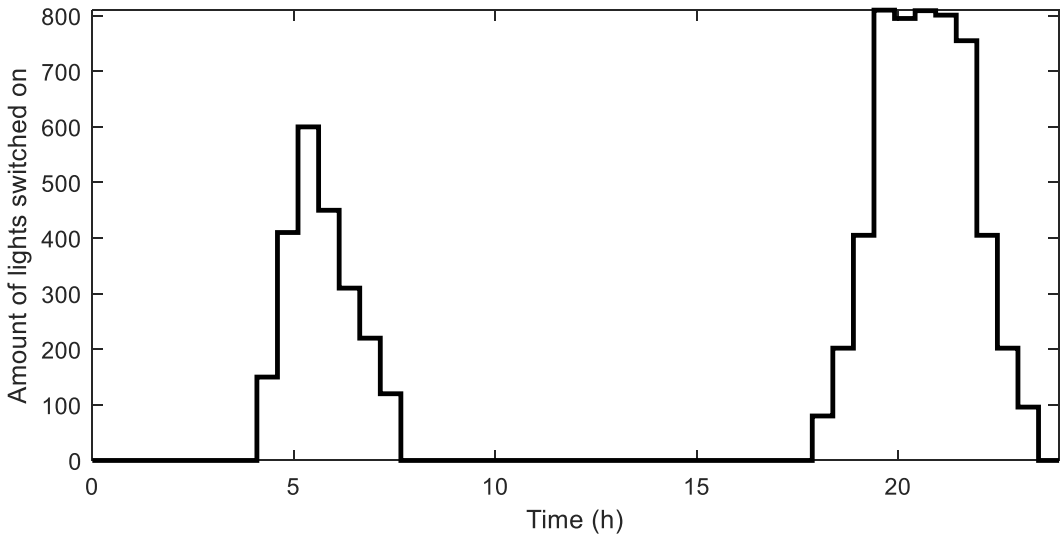

Fig. 3.2: The number of lights switched on

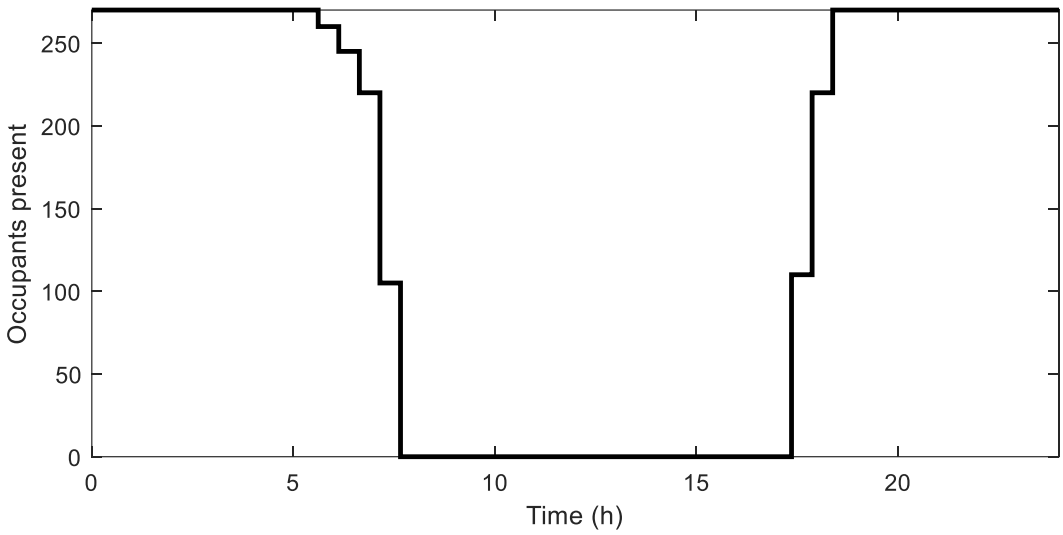

Fig. 3.3: The number of occupants present in the residential building

In this study, optimal system sizing is not conducted, as this does not form part of the main focus of the study. However, sizing of the air-to-air heat pump required for space heating and space cooling, is conducted to a certain level. Firstly, the total heating/cooling load should be determined. The first heating load is the heat generated from human beings, which is, on average 100 W [97]. Therefore, the total heat generated from human beings is calculated as 27 kW. The second heating load is the heat that is generated from lights. Each light generates, on average, 15 W and an assumption was made that each room has 3 lights, of which the total heating load from the lighting, is calculated as 12.15 kW. Each occupant is assumed to have a laptop computer, where the heat generated per laptop is, on average, 100 W, which the total heating load from the laptops is calculated as 27 kW. The final and most dominant heat load is the transmission load, which is the heat transferred through the building walls, floor and roof.

The average transmission load during summer is calculated by making use of Eq. (3.3), in Section 3.2.2 and the data is provided in Table 3.1, which is calculated to be 364.18 kW. For the case to determine the load to be cooled, the sum of the human being heating load, lighting heating load, laptop heating load and the transmission load is taken, which is calculated to be 430.33 kW.

The average transmission load during winter, is further calculated, by making use of Eq. (3.3), in Section 3.2.2 and the data is provided in Table 3.1, which is calculated to be 568.11 kW. For the case to determine the load to be heated, the sum of the human being heating load, lighting heating load and laptop heating load, is deducted from the transmission load, due to these loads contributing towards heating the residential building, which is calculated to be 501.96 kW.

Therefore, by making use of the load calculated to be cooled and heated, the air-to-air heat pump parameters are selected to satisfy these loads, which is shown in Table 3.2 [98].

Table 3.2: Air-to-air heat pump parameters

Parameters	**Symbol**	**Value**	**Unit**
Electrical Power – Cooling	$P_{A,C}$	145.9	kW
Thermal Power –Cooling	$P_{QA,C}$	433.9	kW
COP - Cooling	COP_C	2.97	-
Electrical Power – Heating	$P_{A,H}$	139.01	kW
Thermal Power – Heating	$P_{QA,H}$	503.2	kW
COP - Heating	COP_H	3.62	-

In Figs. 3.4 and 3.5, the ambient temperature in degrees Celsius for the winter and summer cases, are illustrated. The ambient air temperatures have been retrieved from the radiometric station situated at the University of Free State, Bloemfontein (latitude: -29.11°, longitude: 26.185° and elevation: 1491m), forming part of the South African Universities Radiometric Network (SAURAN) [94].

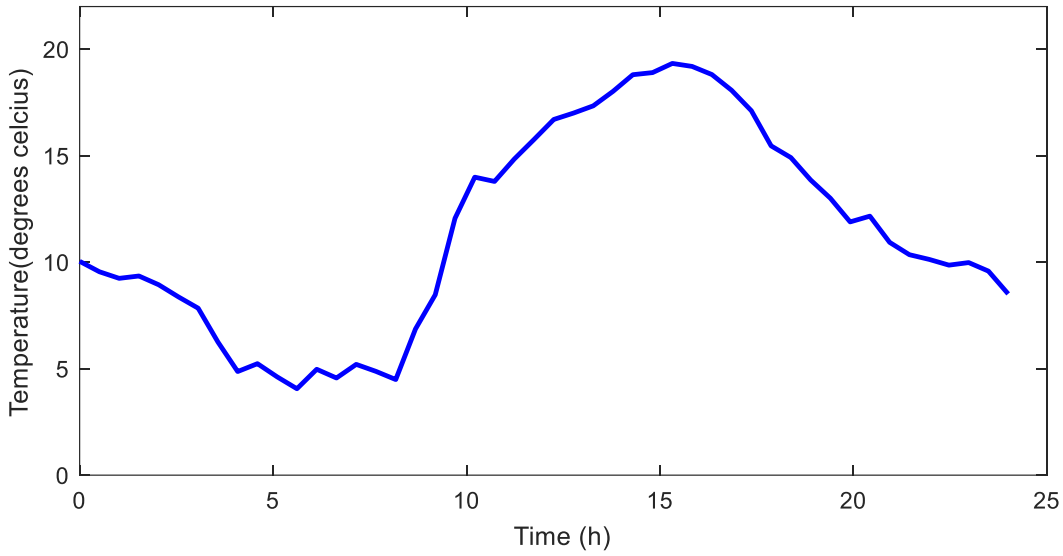

Fig. 3.4: Ambient air temperature during winter

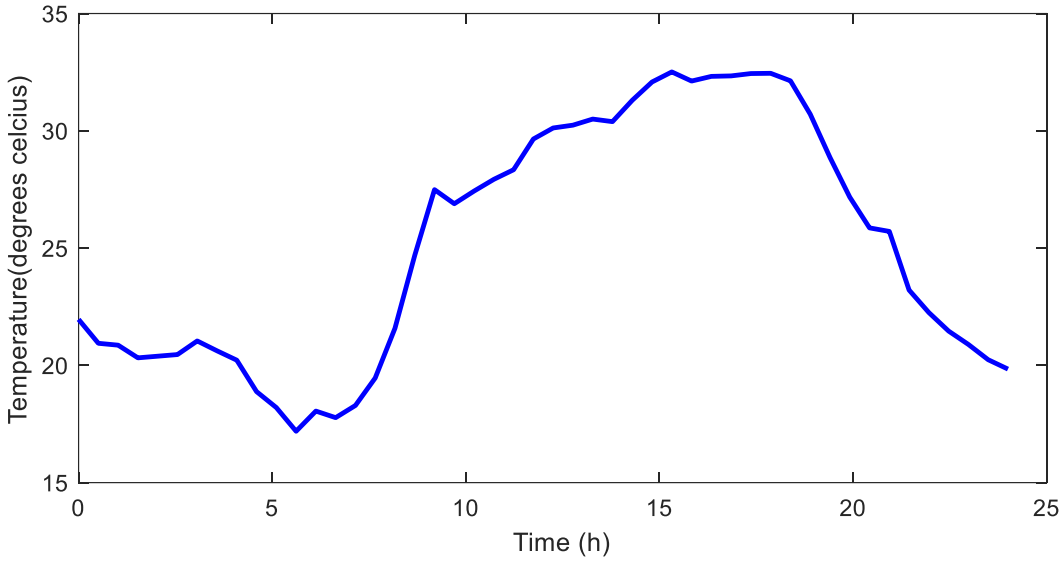

Fig. 3.5: Ambient air temperature during summer

Fig. 3.6 illustrates the TOU tariff during a typical winter day (high demand season), where electricity costs in USD/kWh, with respect to the various pricing regions are presented. The electricity cost, with respect to the various pricing regions, have been retrieved from Centlec, which is the energy utility situated in Bloemfontein, Free State [99].

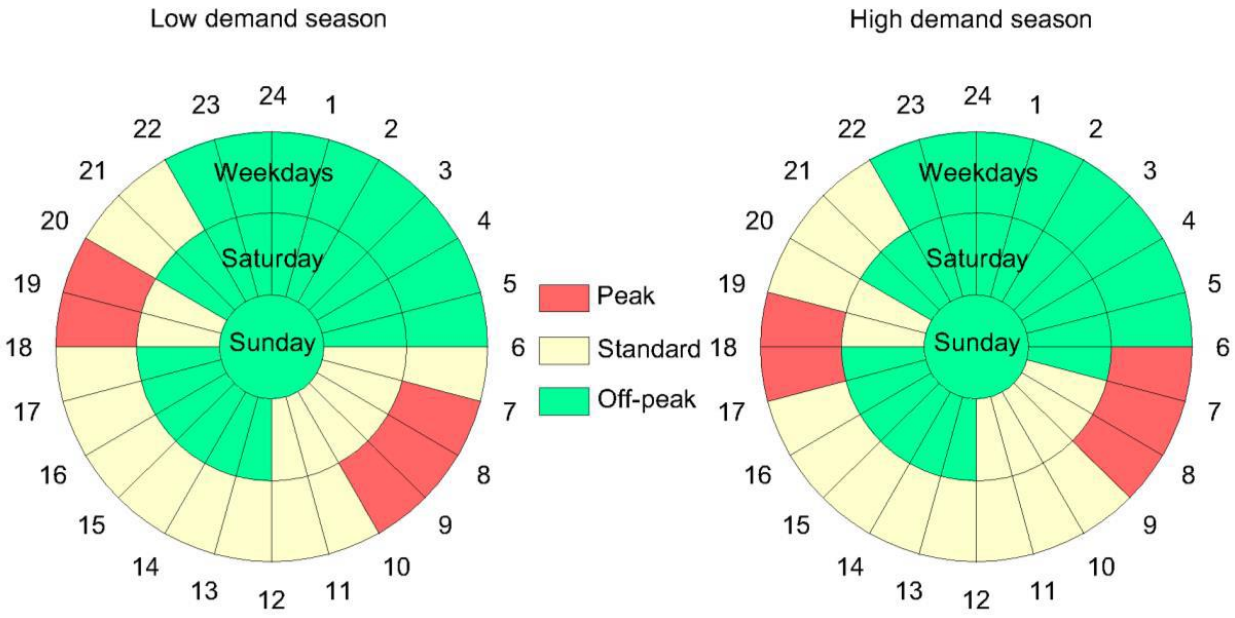

Fig. 3.6: Time of use Periods [100]

The space heating and space cooling demand profiles, during winter and summer, are illustrated in Figs. 3.7 and 3.8, respectively. This figure represents a typical University residential building, with a capacity of 270 students, to be heated and cooled. The desired building temperature is 22 °C at 6:00, which is when the occupants wake up and get ready for classes. From 7:00 until 17:00, the occupants should be at the university attending classes. Therefore, the residential building is not required to be heated. However, the desired building is 22 °C at 18:00, which is when the occupants should arrive back from classes.

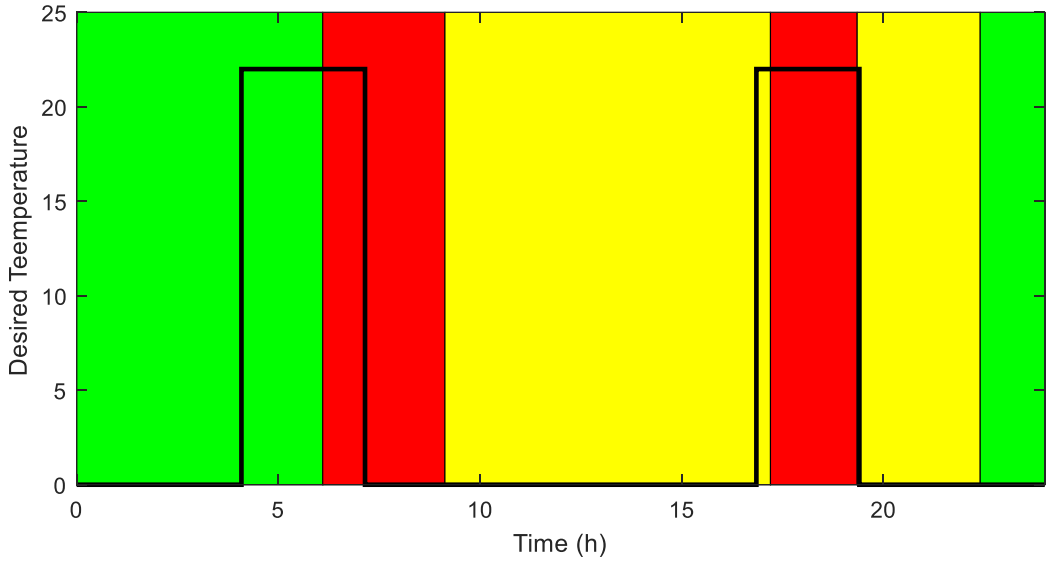

Fig. 3.7: Desired temperature of the residential building during winter

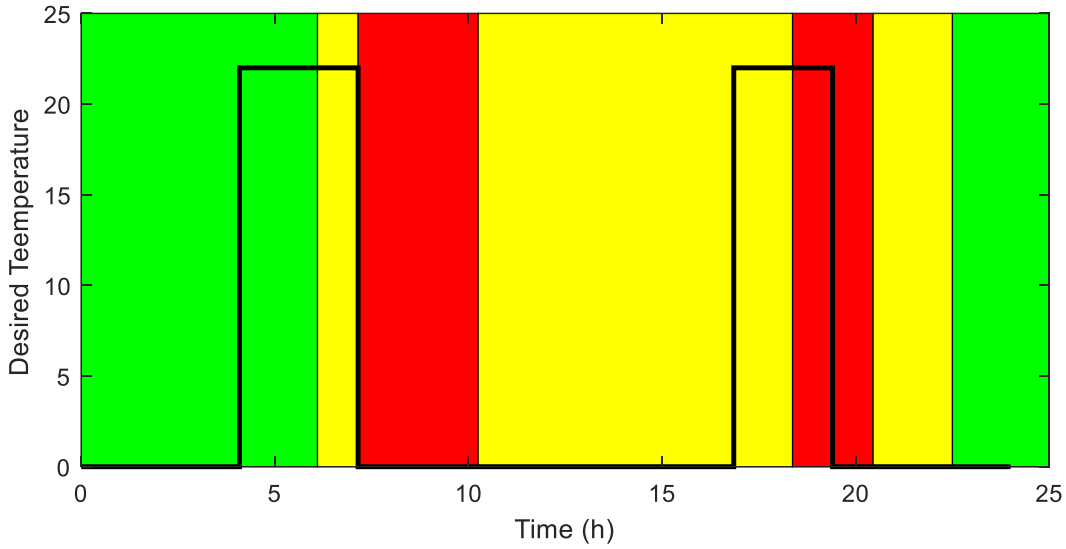

Fig. 3.8: Desired temperature of the residential building during summer

Table 3.3 depicts the input parameters, which are used perform the simulation of the developed model linked to the selected case study. Furthermore, the TOU tariffs for both high demand season (winter) and low demand season (summer), are depicted in the table below.

Table 3.3: Simulation parameters [101]

Parameter description	Value
Sampling time (t_s)	30 min
Optimization interval (hours)	24 h
ϱ_p (low season peak tariff)	0.092 USD/kWh
ϱ_o (low season off-peak tariff)	0.054 USD/kWh
ϱ_s (low season standard tariff)	0.063 USD/kWh
ϱ_p (high season peak tariff)	0.189 USD/kWh
ϱ_o (high season off-peak tariff)	0.088 USD/kWh
ϱ_s (high season standard tariff)	0.096 USD/kWh

3.4 SIMULATION RESULTS AND DISCUSSION

3.4.1 Baseline

There are various common techniques available to control an air-to-air heat pump. These techniques are quite inefficient, due to their simplicity in which they are controlling the air-to-air heat pump. In this Section, two different baselines are adopted, which are used to control the air-to-air heat pump, for the selected winter and summer cases.

The first baseline is the thermostat-based control technique, discussed in Sections 3.4.1.1 and 3.4.1.3, for the selected winter case and summer case, respectively. By making use of this technique, the air-to-air heat pump is switched on, once the minimum temperature set-point was reached and switched off once the maximum temperature set-point is reached. Thus, the heat pump is controlled, such that the temperature is kept within these boundary limits.

The second baseline is the timer with thermostat-based control technique, discussed in Sections 3.4.1.2 and 3.4.1.4, for the selected winter case and summer case, respectively. By making use of this technique, the air-to-air heat pump is further switched, such that the temperature is retained within a maximum and minimum set-point, as well as, the use of a timer, which ensures the desired temperatures set by the end-user, is achieved.

The optimal switching control of an air-to-air heat pump is discussed in Section 3.4.2. This model optimally controls the switching of an air-to-air heat pump, where it ensured that the desired temperature set-points were achieved, whilst consuming the least amount of energy. The optimal switching control model is thoroughly evaluated against the two baselines, to evaluate the effectiveness thereof.

3.4.1.1 Winter case thermostat-based control (winter baseline 1)

In this Section, the thermostat-based switching control of the air-to-air heat pump is adopted as the first baseline, in order to evaluate the economic feasibility of the optimal switching control model. The thermostat switching control is based on the switching of the air-to-air heat pump, ensuring the temperature of the residential building, is retained within the temperature limits, set by the end-user.

The thermostat switching control of the air-to-air heat pump is simulated, based on the parameters in Table 3.1, lighting load in Fig. 3.2, occupancy load in Fig. 3.3, heat pump parameters in Table. 3.2, ambient air temperature in Fig. 3.4 and simulation parameters in Table 3.3. The following sub-sections present the results from the thermostat-based switching control simulation (Figs. 3.9 - 3.10).

3.4.1.1 a) First off-peak pricing period 00h00 - 06h00 (green)

From Fig. 3.2, the lighting load may be observed, which occurs solely from 04h30 and from Fig. 3.3, it may be observed that there is an occupancy load during the entire first off-peak pricing period, where both of these loads are contributing towards heating the space of the residential building. From Fig. 3.4, the ambient temperature initially starts at 10 °C and decreases until 06h00, which is when the ambient temperature is at 4 °C.

In Figs. 3.9 and 3.10, the switching function of the air-to-air heat pump, as well as the temperature inside the residential building, are presented, respectively. Initially, the temperature inside the residential building starts at 18.2 °C, which is the final state of the

previous day. From 00h00 – 05h00, the building temperature increases, due to the air-to-air heat pump being switched on, as seen from Fig. 3.9. It may be observed that the air-to-air heat pump is switched on from 00h00 until 05h00, in order to reach the maximum temperature limit of 22 °C, due to the ambient temperature being initially low and decreasing further, during this time-period. From 05h00 – 06h00, the building temperature decreases, due to the air-to-air heat pump being switched off by means of the thermostat controller, as seen from Fig. 3.9.

3.4.1.1 b) First peak pricing period 06h00 - 09h00 (red)

From 06h00 – 09h00, the residential building temperature decreases, as seen in Fig. 3.10. This is due to the air-to-air heat pump being switched off, as seen from the switching function of the air-to-air heat pump, illustrated in Fig. 3.9. Furthermore, the residential building temperature continues to decrease, as the minimum temperature limit of 20 °C is not obtained at this instance in time.

3.4.1.1 c) First standard pricing period 09h00 - 17h00 (yellow)

From 09h00 – 16h00, the residential building temperature decreases, as seen in Fig. 3.10. The air-to-air heat pump is switched off, due to the minimum temperature limit of 20 °C is obtained at this instance in time, as seen from the switching function of the air-to-air heat pump, illustrated in Fig. 3.9. From 16h00 – 17h00, the residential building temperature begins to increase, as seen from Fig. 3.10, which is due to the air-to-air heat pump being switched on, by means of the thermostat controller.

3.4.1.1 d) Second peak pricing period 17h00 - 19h00 (red)

From 17h00 – 19h00, the residential building temperature increases until it reaches the maximum temperature limit of 22 °C, which is during the peak pricing period, as illustrated in Fig. 3.10.

3.4.1.1 e) Second standard pricing period 19h00-22h00 (yellow)

From 19h00 – 22h00, the residential building temperature continues to decrease, due to the air-to-air heat pump switched off, by means of the thermostat controller, as the minimum temperature limit of 20 °C is not obtained, which may be observed in Fig. 3.10.

3.4.1.1 f) Second off-peak pricing period 22h00 - 24h00 (green)

From 22h00 – 24h00, the residential building temperature continues to decrease, as seen in Fig. 3.10. The residential building temperature decreases, due to the air-to-air heat pump being switched off during this period, as seen in Fig. 3.9. The air-to-air heat pump is not required to be switched on, due to the minimum temperature limit not reached yet at 24h00.

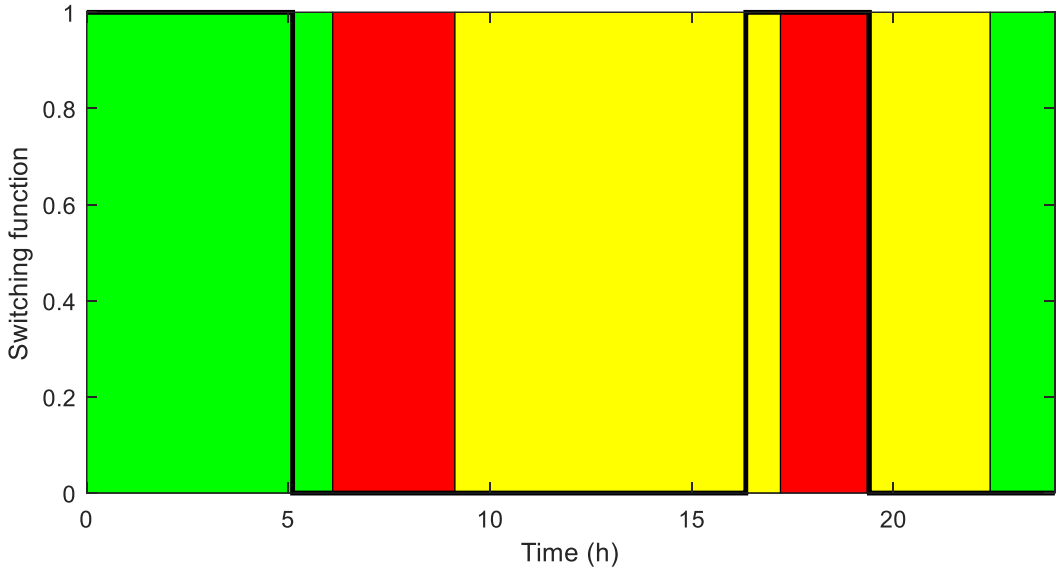

Fig. 3.9: Winter baseline 1 – Switching function of the air-to-air heat pump

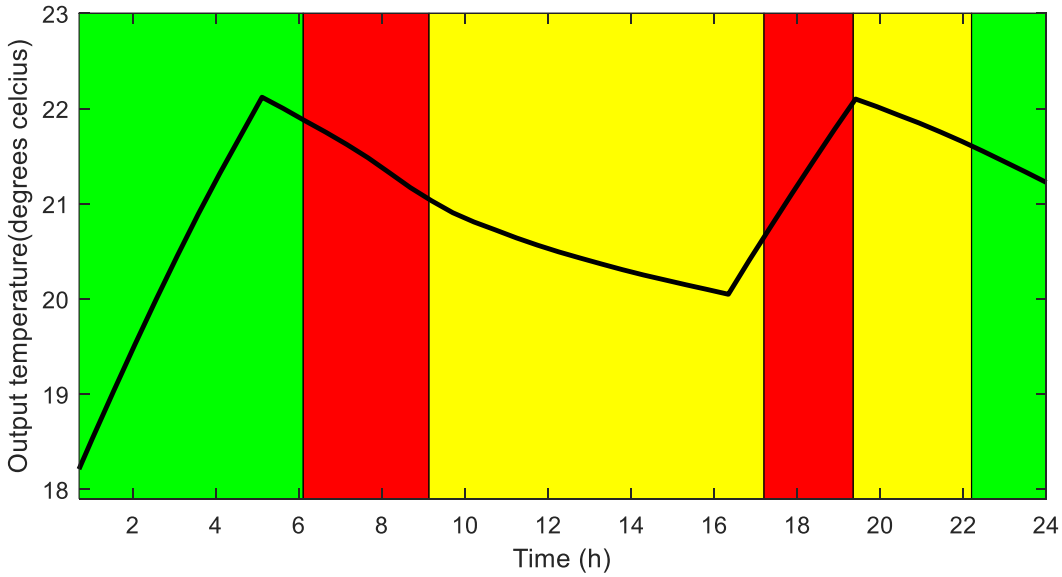

Fig. 3.10: Winter baseline 1 – Residential building temperature

3.4.1.2 Winter case timer with thermostat-based control (winter baseline 2)

In this section, the timer with thermostat-based switching control of the air-to-air heat pump, was adopted, as the second baseline, in order to evaluate the economic feasibility of

the optimal switching control model. The timer with thermostat switching control is based on the switching of the air-to-air heat pump, ensuring that the temperature of the residential building is retained within the temperature limits, as well as the use of a timer, which ensures the desired temperatures set by the end-user, is achieved.

The timer with thermostat switching control of the air-to-air heat pump, is simulated, based on the parameters in Table 3.1, lighting load in Fig. 3.2, occupancy load in Fig. 3.3, heat pump parameters in Table. 3.2, ambient air temperature in Fig. 3.4 and simulation parameters in Table. 3.3. The following sub-sections present the results from the timer, with a thermostat-based switching control simulation (Figs. 3.11 - 3.12).

3.4.1.2 a) First off-peak pricing period 00h00 - 06h00 (green)

From Fig. 3.2, the lighting load may be observed, which occurs solely from 04h30 and, from Fig. 3.3, it may be observed that there is an occupancy load during the entire first off-peak pricing period, where both of these loads are contributing towards heating the space of the residential building. From Fig. 3.4, the ambient temperature initially starts at 10 °C and decreases until 06h00, which is when the ambient temperature is at 4 °C.

In Fig. 3.12, the temperature inside the residential building, heated by the air-to-air heat pump, is presented. Initially, the temperature inside the residential building, starts at 18.2 °C, which is the final state of the previous day. From 00h00 – 05h00, the building temperature increases, due to the air-to-air heat pump being switched on. It may be observed that the air-to-air heat pump is switched on from 00h00 until 05h00, in order to reach the maximum temperature limit of 22 °C, due to the ambient temperature being initially low and further decreasing, during this time-period. From 05h00 – 06h00, the building temperature decreases further, as the air-to-air heat pump is switched off, by means of the thermostat controller, as seen from Fig. 3.11.

3.4.1.2 b) First peak pricing period 06h00 - 09h00 (red)

From 06h00 – 06h30, the residential building temperature decreases, as seen in Fig. 3.12. This is due to the air-to-air heat pump being switched off, as seen from the switching function of the air-to-air heat pump, illustrated in Fig. 3.11. From 06h30 – 07h00, the residential building temperature increases, as the air-to-air heat pump is switched on by means of the timer, as seen from Fig. 3.11. From 07h00 – 09h00, the residential building temperature decreases, as the air-to-air heat pump is switched off, by means of the thermostat controller, as seen from Fig. 3.11. Furthermore, the residential building temperature continues to decrease, as the minimum temperature limit of 20 °C is not obtained at this instance in time.

3.4.1.2 c) First standard pricing period 09h00 - 17h00 (yellow)

From 10h00 – 15h00, the residential building temperature decreases, as seen in Fig. 3.12, due to the air-to-air heat pump being switched off. From 15h00 – 17h00, the residential building temperature begins to increase, as seen from Fig. 3.12, due to the air-to-air heat pump being switched on, by means of the timer, in order to achieve the desired temperature.

3.4.1.2 d) Second peak pricing period 17h00 - 19h00 (red)

From 17h00 – 18h30, the residential building temperature continues to decrease, due to the air-to-air heat pump being switched off, as illustrated in Fig. 3.11. From 18h30 – 19h00, the residential building temperature begins to increase, due to the air-to-air heat pump that is switched on, by means of the timer, in order to achieve the desired temperature, as seen from Fig. 3.12.

3.4.1.2. e) Second standard pricing period 19h00 - 22h00 (yellow)

From 19h00 – 22h00, the residential building temperature continues to decrease, due to the air-to-air heat pump switched off by means of the thermostat controller, as the minimum temperature limit of 20 °C is not obtained, which may be observed in Fig. 3.12.

3.4.1.2 f) Second off-peak pricing period 22h00 - 24h00 (green)

From 22h00 – 24h00, the residential building temperature continues to decrease, as seen in Fig. 3.12. The residential building temperature decreases, due to the air-to-air heat pump switched off during this period, as seen in Fig. 3.11. The air-to-air heat pump is not required to be switched on, due to the minimum temperature limit is not yet reached at 24h00.

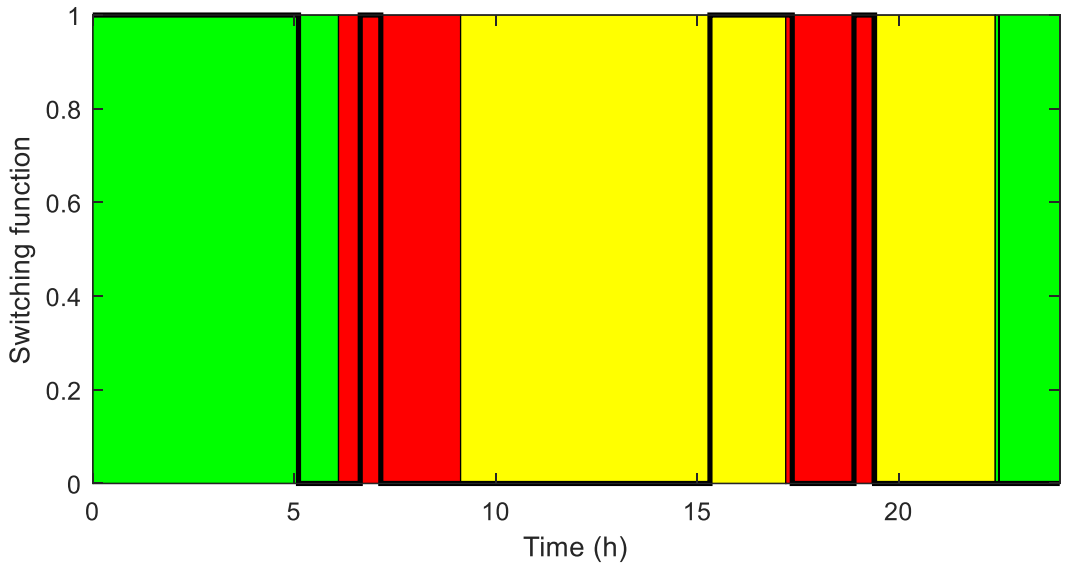

Fig. 3.11: Winter baseline 2 – Switching function of the air-to-air heat pump

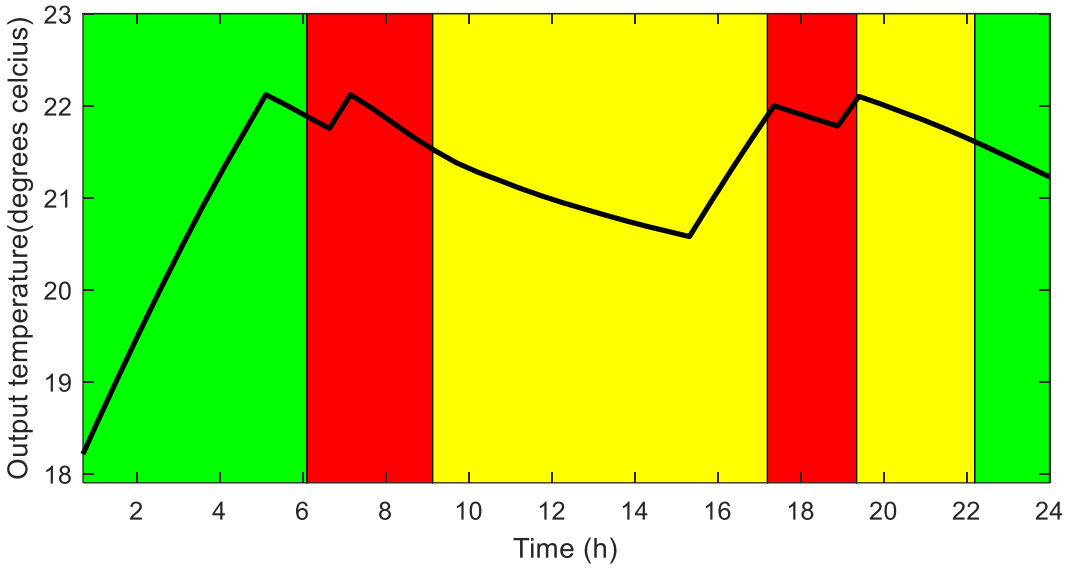

Fig. 3.12: Winter baseline 2 – Residential building temperature

3.4.1.3 Summer thermostat-based control (summer baseline 1)

In this Section, thermostat-based switching control of the air-to-air heat pump, is adopted as the first baseline, in order to evaluate the economic feasibility of the optimal switching control model. The thermostat switching control is based on the switching of the air-to-air heat pump, ensuring the temperature of the residential building is retained within the temperature limits, set by the end-user.

The thermostat switching control of the air-to-air heat pump is simulated, based on the parameters in Table 3.1, lighting load in Fig. 3.2, occupancy load in Fig. 3.3, heat pump parameters in Table. 3.2, ambient air temperature in Fig. 3.5, and simulation parameters in Table. 3.3. The following sub-sections present the results from the thermostat-based switching control simulation (Figs. 3.13 - 3.14.).

3.4.1.3 a) First off-peak pricing period 00h00 - 06h00 (green)

From Fig. 3.2, the lighting load may be observed which occurs solely from 04h00 and from Fig. 3.3, it may be observed that there is an occupancy load during the entire first off-

peak pricing period, where both of these loads contribute towards heating the space of the residential building. From Fig. 3.5, the ambient temperature initially starts at 22.5 °C and decreases until 06h00, which is when the ambient temperature is at 16 °C.

In Figs. 3.13 and 3.14, the switching function of the air-to-air heat pump, as well as the temperature inside the residential building, are presented, respectively. Initially, the temperature inside the residential building starts at 25.5 °C, which is the final state of the previous day. From 00h00 – 06h00, the building temperature decreases, due to the air-to-air heat pump being switched on, as seen from Fig. 3.13. It may be observed that the air-to-air heat pump is switched on from 00h00 until 06h00, in order to reach the minimum temperature limit of 22 °C.

3.4.1.3 b) First standard pricing period 06h00 - 07h00 (yellow)

From 06h00 – 06h30, the residential building temperature continues to decrease, as the air-to-air heat pump is switched on during this period, as seen from Figs. 3.13 and 3.14. The air-to-air heat pump is switched on during this period, until to the minimum temperature limit of 22 °C is achieved. From 06h30 – 07h00, the residential building temperature increases, due to the air-to-air heat pump being switched off, as seen from Fig. 3.13.

3.4.1.3 c) First peak pricing period 07h00 - 10h00 (red)

From 07h00 – 10h00, the residential building temperature continues to increase, as seen in Fig. 3.14. This is due to the air-to-air heat pump being switched off, until the maximum temperature limit of 24 °C, is achieved.

3.4.1.3 d) Second standard pricing period 10h00 - 18h00 (yellow)

From 10h00 – 16h00, the residential building temperature continues to increase, as seen in Fig. 3.14. The air-to-air heat pump is switched off, due to the maximum temperature limit

of 24 °C being achieved, as seen from the switching function of the air-to-air heat pump, illustrated in Fig. 3.13. From 16h00 – 18h00, the residential building temperature begins to decrease, as seen from Fig. 3.13, which is due to the air-to-air heat pump being switched on, by means of the thermostat controller.

3.4.1.3 e) Second peak pricing period 18h00 - 20h00 (red)

From 18h00 – 20h00, the residential building temperature continues to decrease, until it reaches the minimum temperature limit of 22 °C, which is during the peak pricing period, as illustrated in Fig. 3.14.

3.4.1.3 f) Third standard pricing period 20h00 - 22h00 (yellow)

From 20h00 – 22h00, the residential building temperature continues to increase, due to the air-to-air heat pump is switched off, by means of the thermostat controller, as the maximum temperature limit of 24 °C is not obtained, which may be observed in Fig. 3.14.

3.4.1.3 g) Second off-peak pricing period 22h00 - 24h00 (green)

From 22h00 – 24h00, the residential building temperature continues to increase, as seen in Fig. 3.14. The residential building temperature increases, due to the air-to-air heat pump switched off during this period, as seen in Fig. 3.13. The air-to-air heat pump is not required to be switched on, as the maximum temperature limit has not yet reached 24h00.

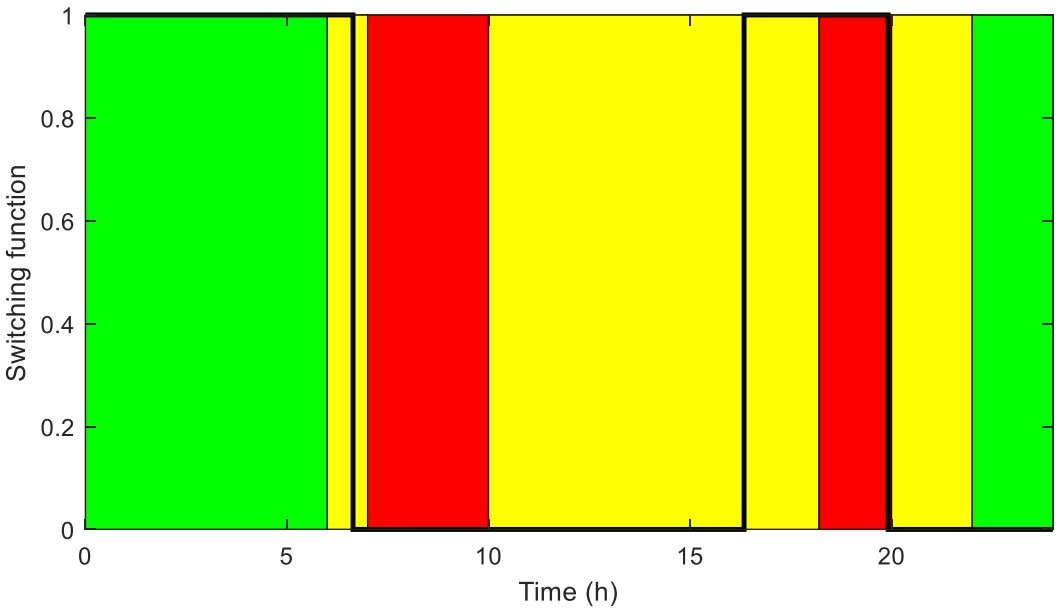

Fig. 3.13: Summer baseline 1 – Switching function of the air-to-air heat pump

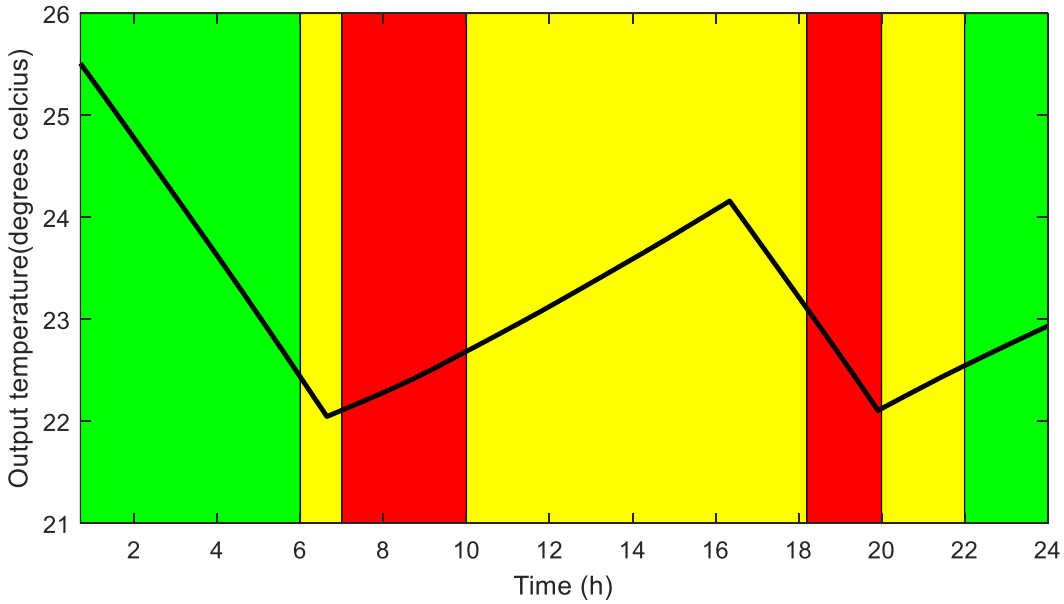

Fig. 3.14: Summer baseline 1 – Residential building temperature

3.4.1.4 Summer case timer with thermostat-based control (summer baseline 2)

In this Section, thermostat-based switching control of the air-to-air heat pump is adopted as the first baseline, in order to evaluate the economic feasibility of the optimal switching control model. The thermostat switching control is based on the switching of the air-to-air heat pump, ensuring the temperature of the residential building is retained within the temperature limits, set by the end-user.

The thermostat switching control of the air-to-air heat pump is simulated, based on the parameters in Table 3.1, lighting load in Fig. 3.2, occupancy load in Fig. 3.3, heat pump parameters in Table. 3.2, ambient air temperature in Fig. 3.5 and simulation parameters in Table. 3.3. The following sub-sections present the results from the thermostat-based switching control simulation (Figs. 3.15 - 3.16).

3.4.1.4 a) First off-peak pricing period 00h00 - 06h00 (green)

From Fig. 3.2, the lighting load may be observed, which occurs solely from 04h00 and, from Fig. 3.3, it may be observed that there is an occupancy load during the entire first off-peak pricing period, where both of these loads contribute towards heating the space of the residential building. From Fig. 3.5, the ambient temperature initially starts at 22.5 °C and decreases until 06h00, which is when the ambient temperature is at 16 °C.

In Figs. 3.15 and 3.16, the switching function of the air-to-air heat pump, as well as the temperature inside the residential building, are presented, respectively. Initially, the temperature inside the residential building starts at 25.5 °C, which is the final state of the previous day. From 00h00 – 06h00, the building temperature decreases, due to the air-to-air heat pump being switched on, as seen from Fig. 3.15. It may be observed that the air-to-air heat pump is switched on from 00h00 until 06h00, in order to reach the minimum temperature limit of 22 °C.

3.4.1.4 b) First standard pricing period 06h00 - 07h00 (yellow)

From 06h00 – 06h30, the residential building temperature continues to decrease, as the air-to-air heat pump is switched on during this period, as seen from Figs. 3.15. and 3.16. The air-to-air heat pump is switched on during this period, until the minimum temperature limit of 22 °C is achieved. From 06h30 – 07h00, the residential building temperature increases, due to the air-to-air heat pump being switched off, as seen in Fig. 3.15.

3.4.1.4 c) First peak pricing period 07h00 - 10h00 (red)

From 07h00 – 10h00, the residential building temperature continues to increase, as seen in Fig. 3.16. This is due to the maximum temperature limit of 24 °C not being achieved during this period.

3.4.1.4. d) Second standard pricing period 10h00 - 18h00 (yellow)

From 10h00 – 13h30, the residential building temperature continues to increase, as seen in Fig. 3.16, due to the air-to-air heat pump being switched off. From 13h30 – 16h30, the residential building temperature begins to decrease, as seen from Fig. 3.15, which is due to the air-to-air heat pump being switched on, by means of the timer, in order to achieve the desired temperature. From 16h30 – 18h00, the residential building begins to increase, due to the air-to-air being switched off, as seen in Fig. 3.15.

3.4.1.4 e) Second peak pricing period 18h00 - 20h00 (red)

From 18h00 – 18h30, the residential building temperature begins to decrease, due to the air-to-air heat pump being switched on again, by means of the timer, to achieve the desired temperature set-point during the peak pricing region of the TOU tariff structure, as illustrated in Fig. 3.16. From 18h30 – 19h00, the residential building temperature begins to

increase, due to the air-to-air heat pump, that is switched off by means of the thermostat controller, as the minimum temperature of 22 °C, is achieved.

3.4.1.4 f) Third standard pricing period 20h00 - 22h00 (yellow)

From 20h00 – 22h00, the residential building temperature continues to increase, due to the air-to-air heat pump is switched off by means of the thermostat controller, as the maximum temperature limit of 24 °C is not obtained, seen in Fig. 3.16.

3.4.1.4 g) Second off-peak pricing period 22h00 - 24h00 (green)

From 22h00 – 24h00, the residential building temperature continues to increase, as seen in Fig. 3.16. The residential building temperature increases, due to the air-to-air heat pump switched off during this period, as seen in Fig. 3.15. The air-to-air heat pump is not required to be switched on, due to the maximum temperature limit still not being reached at 24h00.

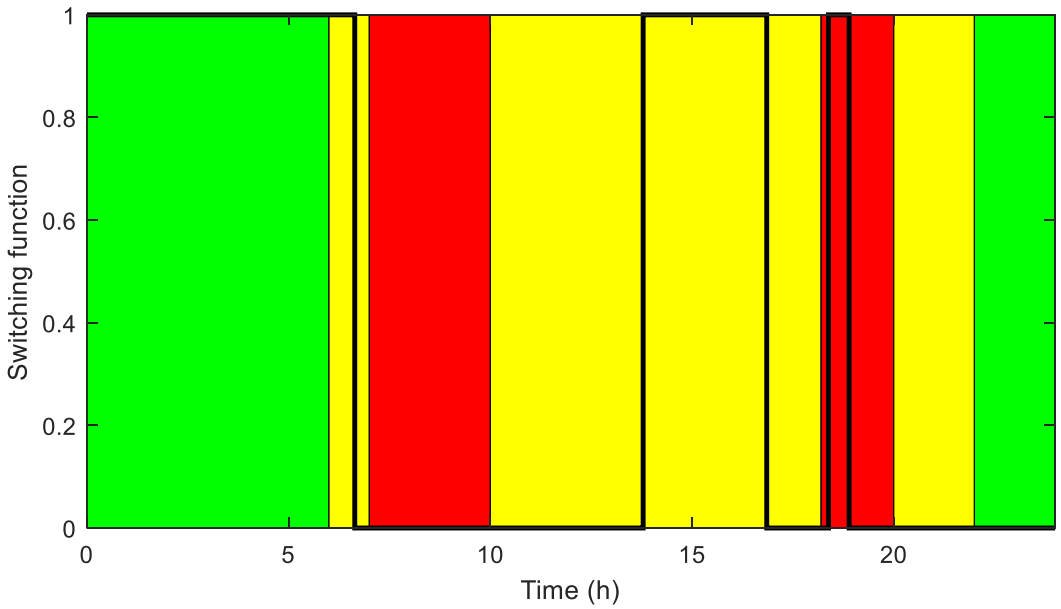

Fig. 3.15: Summer baseline 2 – Switching function of the air-to-air heat pump

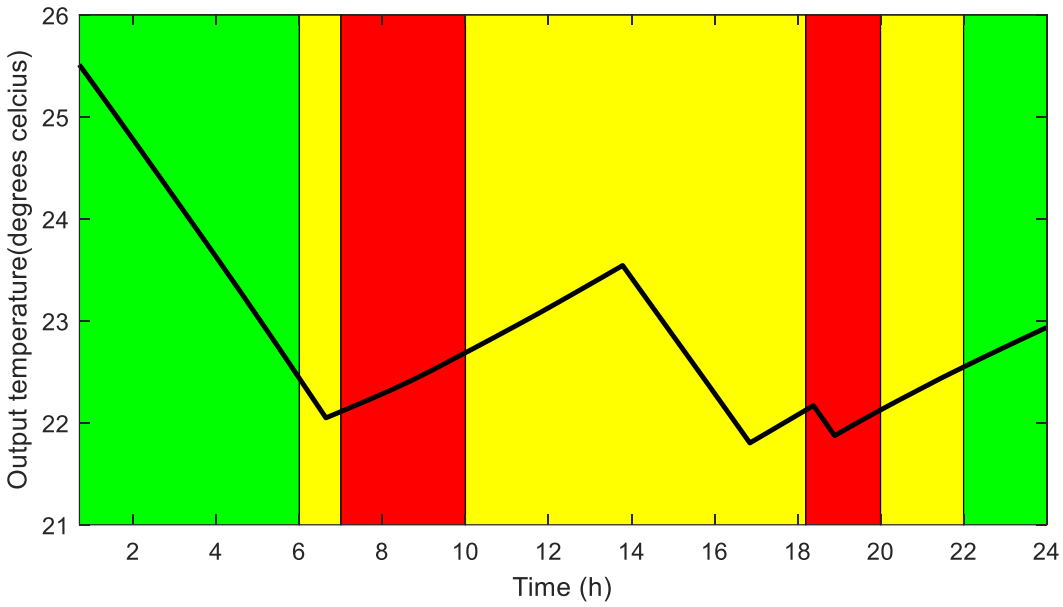

Fig. 3.16: Summer baseline 2 – Residential building temperature

3.4.2 Optimal control case

In this Section, the optimal switching control of the air-to-air heat pump is simulated, using the SCIP solver in the optimization toolbox of MATLAB. The main objective, was to minimize the space heating and space cooling level of discomfort for the occupants and whilst minimizing the running energy cost of the air-to-air heat pump, under time-based pricing. Two weighting factors are adopted to differentiate whether the operating energy cost of the heat pump has priority over the level of discomfort to the consumer, or vice versa. The first weighting factor, W_1, is used for the operating energy cost of the heat pump and the second weighting factor, W_2, is used for the level of discomfort.

The optimal switching control of the air-to-air heat pump is simulated based on the parameters in Table 3.1, the lighting load in Fig. 3.2, the occupancy load in Fig. 3.3, heat pump parameters in Table. 3.2, ambient air temperature profiles in Figs. 3.4 and 3.5 and simulation parameters in Table. 3.3. The following sub-sections present the results from the optimal switching control simulation (Figs. 3.17 - 3.18.).

3.4.2.1 Winter case

3.4.2.1 a) First off-peak pricing period 00h00 - 06h00 (green)

From Fig. 3.2, the lighting load may be observed, which occurs solely from 04h00 and from Fig. 3.3 it may be observed that there is an occupancy load during the entire first off-peak pricing period, where both of these loads are contributing towards heating the space of the residential building. From Fig. 3.4, the ambient temperature initially starts at 10 °C and decreases until 06h00, which is when the ambient temperature is at 4 °C.

In Fig. 3.18, the temperature inside the residential building, heated by the air-to-air heat pump, is presented. Initially, the temperature inside the residential building starts at 18.2 °C, which is the final state of the previous day. From 00h00 – 03h00, the building temperature increases to reach 22 °C, which is the morning desired temperature set-point. From 03h00 – 03h30, the building temperature decreases, which may be observed in Fig. 3.18, due to the air-to-air heat pump being switched off. From 03h30 – 04h00, the building temperature begins to increase again, as seen in Fig. 3.18, until the desired temperature of 22 °C, is obtained. From 04h00 – 04h30, the building temperature begins to decrease, which is due to air-to-air heat pump being switched off, as seen from Fig. 3.17. From 04h30 – 06h00, the building temperature increases, which is due to air-to-air heat pump being switched on, which is when the desired temperature set-point is achieved.

3.4.2.1 b) First peak pricing period 06h00 - 09h00 (red)

From 06h00 – 09h00, the residential building temperature decreases, as seen in Fig. 3.18. This is due to the air-to-air heat pump being switched off, as seen from the switching function of the air-to-air heat pump, illustrated in Fig. 3.17. The main reasons for the air-to-air heat pump being switched off, is due to the peak pricing period, as well as the residential building which is not required to be heated, as most of the occupants are not present during this period.

3.4.2.1 c) First standard pricing period 09h00 - 17h00 (yellow)

From 09h00 – 13h00, the residential building temperature continues to decrease, as seen in Fig. 3.18. From 13h00 – 13h30, the residential building temperature begins to increase, due to the air-to-air heat pump being switched on, as seen in Fig. 3.18, ensuring the least amount of energy is consumed. From 13h30 – 15h00, the residential building temperature begins to decrease, due to the air-to-air heat pump being switched off, as seen in Fig. 3.17. From 15h00 – 17h00, the air-to-air heat pump is switched on, as seen in Fig. 3.17, as the desired temperature is achieved.

3.4.2.1 d) Second peak pricing period 17h00 - 19h00 (red)

From 17h00 – 19h00, the residential building temperature decreases from 22 °C to 21.6 °C, as seen in Fig. 3.18. The residential building temperature decreases, due to the air-to-air heat pump switching off during the peak pricing period, as seen in Fig. 3.17.

3.4.2.1 e) Second standard pricing period 19h00 - 22h00 (yellow)

From 19h00 – 22h00, the residential building temperature decreases from 21.6 °C to 21.2 °C, as seen in Fig. 3.18. The residential building temperature decreases, due to the air-to-air heat pump switched off during the standard pricing period, as seen in Fig. 3.17. The air-to-air heat pump is not required to be switched on, due to the evening desired temperature set-point having passed.

3.4.2.1 f) Second off-peak pricing period 22h00 - 24h00 (green)

From 22h00 – 24h00, the residential building temperature decreases from 21.2 °C to 20.8 °C, as seen in Fig. 3.18. The residential building temperature decreases, due to the air-to-air heat pump switching off during this period, as seen in Fig. 3.17. The air-to-air heat pump is not required to be switched on, due to no evening desired temperature set-point that is required for the remainder of the evening.

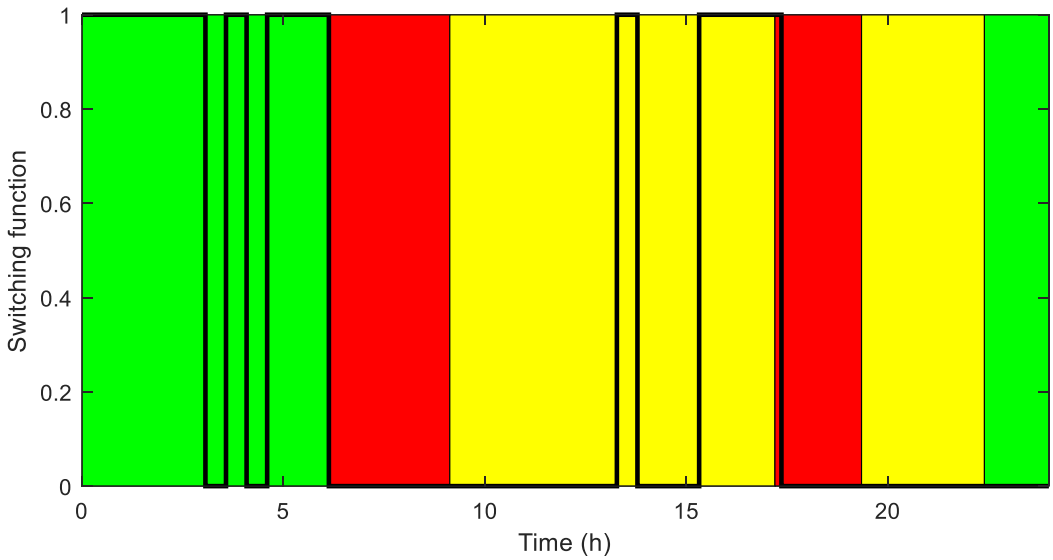

Fig. 3.17: Optimal switching function of the air-to-air heat pump during winter

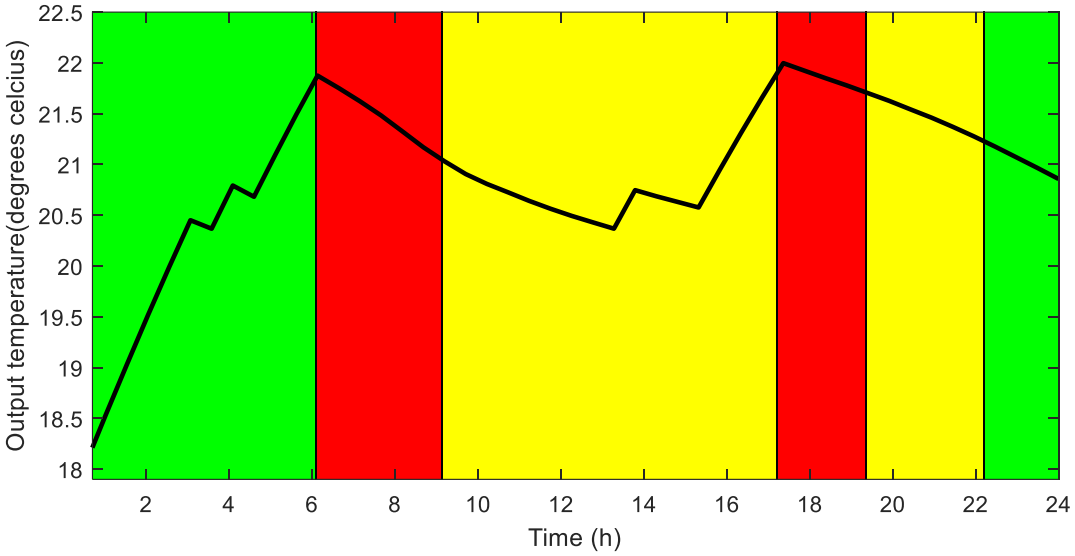

Fig. 3.18: Residential building temperature during winter

3.4.2.2 Summer case

3.4.2.2 a) First off-peak pricing period 00h00 - 06h00 (green)

From Fig. 3.2, the lighting load may be observed which occurs solely from 04h00 and from Fig. 3.3, it may be observed that there is an occupancy load during the entire first off-peak pricing period, where both of these loads are contributing towards heating the space of the residential building. From Fig. 3.5, the ambient temperature initially starts at 22.5 °C and decreases until 06h00, which is when the ambient temperature is at 16 °C.

In Figs. 3.19 and 3.20, the switching function of the air-to-air heat pump, as well as the temperature inside the residential building, are presented, respectively. Initially, the temperature inside the residential building starts at 25.5 °C, which is the final state of the previous day. From 00h00 – 06h00, the building temperature decreases, due to the air-to-air heat pump being switched on, as seen from Fig. 3.19. It may be observed that the air-to-air heat pump is switched on from 00h00 until 06h00, in order to reach the minimum temperature set-point of 22 °C.

3.4.2.2 b) First standard pricing period 06h00 - 07h00 (yellow)

From 06h00 – 06h30, the residential building temperature continues to decrease, as the air-to-air heat pump is switched on during this period, as seen in Figs. 3.19. and 3.20. The air-to-air heat pump is switched on during this period until to the desired temperature set-point of 22 °C is achieved. From 06h30 – 07h00, the residential building temperature increases, due to the air-to-air heat pump being switched off, as seen from Fig. 3.19.

3.4.2.2 c) First peak pricing period 07h00 - 10h00 (red)

From 07h00 – 10h00, the residential building temperature increases as seen in Fig. 3.20. This is due to the air-to-air heat pump being switched off, as seen from the switching function of the air-to-air heat pump, illustrated in Fig. 3.19. Furthermore, the residential building temperature continues to increase during the peak pricing region of the TOU tariff structure.

3.4.2.2 d) Second standard pricing period 10h00 - 18h00 (yellow)

From 10h00 – 12h00, the residential building temperature increases, as seen in Fig. 3.20, due to the air-to-air heat pump is still switched off, illustrated in Fig. 3.19. From 12h00 – 12h30, the residential building temperature begins to decrease, as seen in Fig. 3.20, which is due to the air-to-air heat pump being switched on. From 12h30 – 13h00, the residential building temperature increases, due to the air-to-air heat pump being switched off, as seen from Fig. 3.19. From 13h00 – 13h30, the temperature inside the residential building decreases, as the air-to-air heat pump is switched on, as seen from Fig. 3.19, ensuring the least amount of energy is consumed. From 13h30 – 16h00, the temperature inside the residential building begins to increase, as seen from Fig. 3.20. From 16h00 – 18h00, the air-to-air heat pump is switched on again, in order to achieve the desired temperature set-point, as seen in Fig. 3.19.

3.4.2.2 e) Second peak pricing period 18h00 - 20h00 (red)

From 18h00 – 20h00, the residential building temperature begins to increase, due to the air-to-air heat pump being switched off, as illustrated in Fig. 3.19. The air-to-air heat pump is switched off, as this is the second peak pricing region of the TOU tariff structure.

3.4.2.2 f) Third standard pricing period 20h00 - 22h00 (yellow)

From 20h00 – 22h00, the residential building temperature increases from 22.5 °C to 22.9 °C, as seen in Fig. 3.20. The residential building temperature increases, due to the air-to-air heat pump switched off during the standard pricing period, as seen in Fig. 3.19. The air-to-air heat pump is not required to be switched on, due to the evening desired temperature set-point having passed.

3.4.2.2 g) Second off-peak pricing period 22h00 - 24h00 (green)

From 22h00 – 24h00, the residential building temperature increases from 22.9 °C to 23.3 °C, as seen in Fig. 3.20. The residential building temperature increases, due to the air-to-air heat pump switching off during this period, as seen in Fig. 3.19. The air-to-air heat pump is not required to be switched on, due to no evening desired temperature set-point being required for the remainder of the evening.

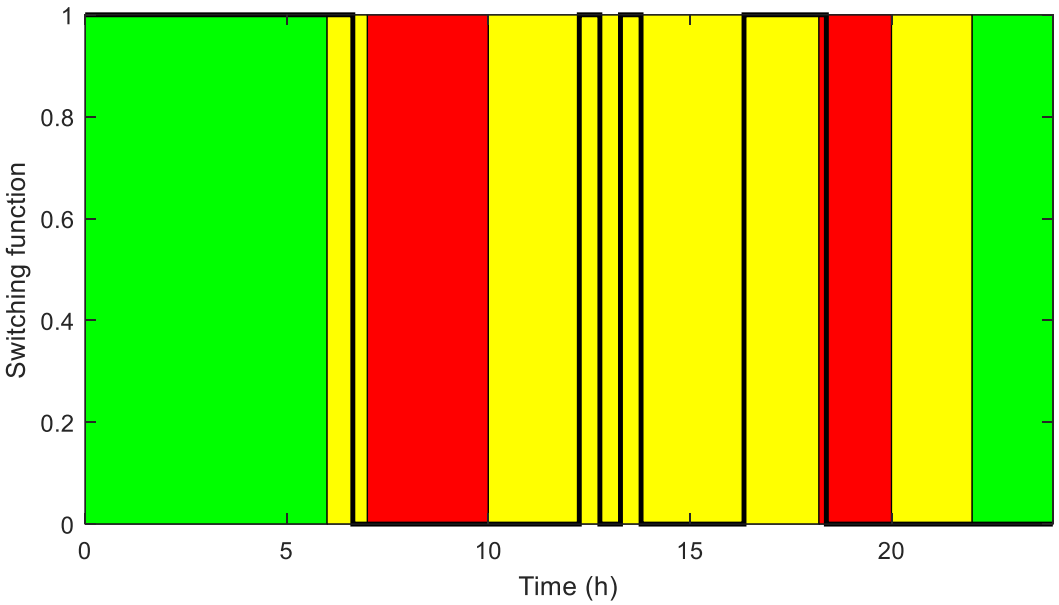

Fig. 3.19: Optimal switching function of the air-to-air heat pump during summer

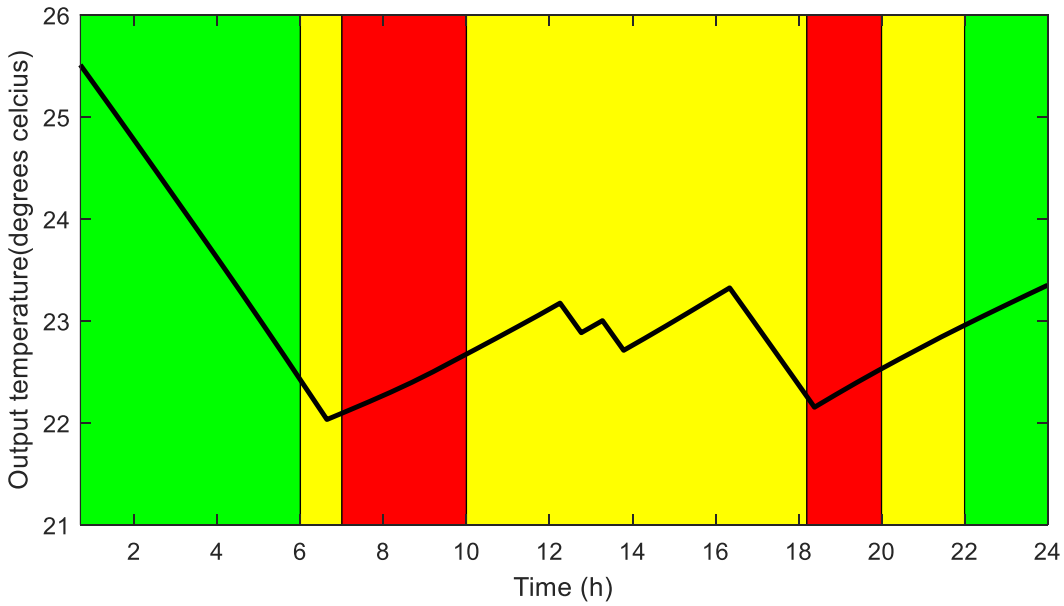

Fig. 3.20: Residential building temperature during summer

3.4.3 Daily economic analysis

The optimal switching control model should be evaluated from an economic feasibility standpoint, against the two baselines, to evaluate the effectiveness, thereof. The economic feasibility study comprised of a daily economic analysis, which is due to the major cost contributing equipment that is required by the first baseline, second baseline and the optimal control model, are precisely the same. Therefore, in this case, a comprehensive economic analysis may not be required.

The daily operating energy cost of each space heating system is calculated, by making use of the following Eq. (3.23), as illustrated in sub-section 3.2.4.

The daily operating energy cost is calculated, based on the simulation results of each control method. Table 3.4 illustrates the daily operating energy cost of the first baseline, second baseline and the optimal control model. Furthermore, the daily operating energy cost savings of the optimal control model is evaluated against the first baseline, as well as the second baseline.

Table 3.4 Daily operating energy cost savings of the optimal control model against baseline 1 and baseline 2

Strategy	Energy cost (USD/day)	Saving (%)
Baseline		
Winter - Thermostat-based control (Baseline 1)	440.04	/
Winter - Timer with thermostat-based control (Baseline 2)	373.46	/
Summer - Thermostat-based control (Baseline 1)	263.22	/
Summer - Timer with thermostat-based control (Baseline 2)	249.36	/
Optimal control		
Optimal control - Winter	318.45	
Winter - Optimal control against Baseline 1	/	27.63
Winter - Optimal control against Baseline 2	/	14.73
Optimal control - Summer	218.7	
Summer - Optimal control against Baseline 1	/	16.91
Summer - Optimal control against Baseline 2	/	12.30

The results in Table 3.4 presented the daily operating energy cost of the thermostat-based control strategy, timer with thermostat-based control strategy and the optimal control strategy during the winter, as well as summer. Furthermore, the optimal control strategy was evaluated against the first baseline and the second baseline. The simulation results, in conjunction with the daily economic analysis, of the proposed space heating model, yielded a daily operating energy cost saving of 27.63 % and 14.73 %, as compared to the thermostat-based control strategy and the timer with thermostat-based control strategy, during the selected winter day, respectively. The simulation results of the proposed space cooling model yielded a daily operating energy cost saving of 16.91 % and 12.30 %, compared to the

thermostat-based control strategy and the timer, with thermostat-based control strategy, during the selected summer day, respectively.

3.5 CONCLUSIONS AND RECOMMENDATIONS

In this chapter, the optimal switching control strategy was evaluated, based on relevant literature. The optimal switching control of the space heating and space cooling system has been mathematically modelled, after which the multi-objective function and the various constraints have been outlined in detail. Actual and accurate data, presented in Section 3.3, has been adopted to conduct effective and accurate simulations, which were outlined in Section 3.4.

The optimal switching control strategy was evaluated, by comparing it against the thermostat-based control strategy (Baseline 1), as well as against the timer with thermostat-based control strategy (Baseline 2) through simulations, for a typical winter and summer day.

The simulation results, in conjunction with the daily economic analysis, of the proposed space heating model yielded a daily operating energy cost saving of 27.63 % and 14.73 %, compared to the thermostat-based control strategy and the timer with thermostat-based control strategy, during the selected winter day, respectively. The simulation results of the proposed space cooling model yielded a daily operating energy cost saving of 16.91 % and 12.30 %, compared to the thermostat-based control strategy and the timer with thermostat-based control strategy, during the selected summer day, respectively.

The simulation results also revealed that for both the space heating and space cooling system, has successfully heated and cooled the residential building within acceptable limits of the desired temperature, solely when the occupants were present, respectively. Thus, the optimal control model ensured the air-to-air heat pump is switched off when space heating and space cooling is not required, respectively.

The other fragment of the multi-objective function was to minimize the operating energy cost of the space heating and space cooling system, where it successfully operated, taking the TOU tariff structure into account. Furthermore, the optimal switching control model has

adapted to the various exogenous disturbances, such as the building transmission losses, the number of occupants present at each moment in time and the number of lights switched on, at each moment in time.

CHAPTER IV: OPTIMAL HEAT RECOVERY DURING POLYMER ELECTROLYTE MEMBRANE ELECTROLYSIS

Various improvements in the operational performance of a PEMWE and further recently applied energy management strategies are reviewed, followed by identifying the requirement of the study. Therefore, this chapter further presents the proposed hydrogen PEMWE water heating system. A mathematical model is developed for the proposed optimal switching control of a hydrogen PEMWE water heating system, with the main aim of maximizing the heat transfer from the PEMWE to the HWST, whilst ensuring a stable hydrogen production rate.

Section 4.1 introduces the chapter, with various relevant literature on optimization techniques applied to a PEMWE, to improve the operational performance, thereof. Section 4.2, presents the PEMWE water heating model; Section 4.3 presents the case study description. The simulation results and discussion are presented in Section 4.4. Lastly, in Section 4.5, the Conclusion is presented.

4.1 INTRODUCTION

The severe reduction in the global fossil fuels supply, caused by the increase in the global energy demand, highlights the need to make more use of renewable energy resources (RER), such as solar PV modules, wind turbines, hydro-turbines, etc [102]. The energy produced by these RER, is not harmful to the environment and is regarded as a promising, environmentally sustainable alternative to fossil fuel resources. Hydrogen may be seen as a possible alternative fuel, which may be produced from renewable energy, as mentioned and a promising contender, in the energy storage domain. Furthermore, hydrogen is regarded as a clean fuel, as the product of the chemical reaction is water (H_2O) and heat, as the by-product [103]. An electrolyser harnesses the energy produced by the RER, to produce hydrogen,

which could be stored in its current form, to be used at a later stage, to generate electrical energy, by means of a fuel cell [104]. The generated heat influences the performance of the hydrogen electrolyser, meaning that its performance could be enhanced, by increasing the operating temperature, to certain extent [105]. However, this enhanced performance comes at a price, which cannot be ignored, causing a reduction in the lifespan of the membrane itself [106].

Various authors have attempted to improve the performance of an electrolyser, by effectively controlling the operating temperature, thereof. However, few authors have considered developing an optimal control model, with the main objective of maximizing the heat transfer from the Proton exchange membrane (PEM) H_2 electrolyser to the HWST and a secondary objective, to ensure a stable H_2 production.

The authors in Reference [64], proposed a hybrid Photovoltaic/Proton Exchange Membrane Electrolyser. The water temperature of the electrolyser was controlled using fuzzy logic control, improving its efficiency. The efficiency of the hybrid system was verified by maximising the Proton Exchange Membrane Electrolyser hydrogen flow and the PV captured energy.

The authors in Reference [41], have developed a mathematical model to analyse the performance of a PEMWE and the effect of operating temperature, cathode pressure, membrane thickness, width and height of channel and current density. The developed model was validated, with experimental data, where the results indicated that, when increasing the current density, the voltage of the electrolyser increased, the energy and exergy efficiencies decrease. When the operating temperature of the electrolyser was increased from 313 °K to 353 °K and the decrease of cathode pressure from 40 bar to 1 bar, the energy and exergy efficiencies increased between 2 % and 6 % of the operating range of the electrolyser.

In Reference [107], the authors developed a mathematical model of a PEMWE powered by solar PV cells to analyse how temperature influences the various parameters, thereof. Simulations were conducted using the MATLAB/Simulink software, to evaluate whether this type of system would be feasible in desert areas, such as Adrar. The simulation results

illustrated that the PEMWE powered by solar PV cells, would benefit from desert areas, such as Adrar, due to its high average solar irradiance and high average air temperature.

In Reference [108], the authors developed an optimization control model of a hybrid Electrolyser-Fuel cell system, of which the main purpose was to produce hydrogen and fresh water from seawater. The optimal control model calculates the optimal operation of the hybrid system, by making use of GAMS/BARON, based on the operating temperature, current density of the Electrolyser, the thickness of the electrodes and the humidity factor. A techno-economic feasibility study was conducted, which yielded a 41.2 % for the power conversion efficiency and 48.2 % freshwater recovery rate.

The authors in Reference [109], have developed a mathematical model of an advanced alkaline Electrolyser, to investigate how temperature influences the performance of the Electrolyser in terms of the current-voltage curve, over-voltage, hydrogen flow rate and energy efficiency. Simulations were conducted, using MATLAB/Simulink, at various temperatures between 20 °C and 100 °C, which illustrated that the operating temperature does not influence the hydrogen flow rate. However, the simulation results have further presented that the operating temperature, significantly influences the current and voltage, over-voltage and the energy efficiency.

In Reference [110], the authors have conducted a numerical analysis on a PEMWE, to examine as to how the operating temperature affects the performance, thereof. In this study, it was expected that the higher operating temperature should reduce the activation over-voltages. However, this study further predicted that, if the operating temperature surpasses the saturation temperature, it should reduce the water content available for the reaction and in effect, increase the over-voltages. This problem was overcome, by increasing the operating pressure from 0.13 to 0.22 MPa, which, thereafter, enables the operating temperature to be increased from 100 °C to 120 °C. Therefore, the cell overvoltage was effectively reduced, from 1.57 to 1.51 V.

The authors in Reference [105], have developed a mathematical model of the PEMWE system, to optimize its performance, by finding the optimal electric current density. Furthermore, various parameters, such as the inlet water flow rate, membrane thickness,

operating temperature and efficiency of heat exchangers, were analysed, to evaluate the performance of the system. The simulation results validated that the redunNt heat, which is generated during Electrolysis, was successfully absorbed and fed back to the PEMWE, for the improved overall performance, thereof.

In Reference [111], the authors presented a PEMWE integrated with a low temperature waste gas, from a small coal fired power plant driven advanced absorption power-cycle, producing hydrogen and oxygen. The results of the proposed integrated system, illustrated a daily hydrogen production of 1.15 kg and 4.59 kg of oxygen. Furthermore, the results showed to be promising, compared to conventional electrolysers, in terms of hydrogen production cost.

The authors in Reference [112], have presented a mathematical model of an alkaline electrolyser, to illustrate the hydrogen production, changes in operating temperature and state transitions. Furthermore, the optimal dispatch of the electrolyser model was evaluated, based on a practical of a hybrid wind/electrolyser system. The simulation results revealed that the alkaline electrolyser model may successfully capture the link between the thermal and electrical dynamics, as well as switching the electrolyser on and off. Furthermore, the flexible strategy of operation, adopted by this model, yielded a substantial increase in daily revenues, in terms of electricity.

The authors in Reference [106], developed a model of a PEMWE, to evaluate the influence of temperature and current density on the degradation of the membrane. Furthermore, the developed model was used to study the time it takes for the membrane thickness to degrade to 50 %, at certain membrane temperatures, from which the membrane degradation occurs non-linearly. The results indicated the membrane thickness for a time period of 4.39 years, to degrade to 50 %, operating at 60 °C, whereas a time period of 1 year to degrade to 50 % at 80 °C. Therefore, operating the PEMWE at a higher temperature, drastically reduces the membrane thickness, which leads to membrane failure.

From the literature review conducted, it may be observed that various authors have developed optimal control models, to improve the performance of a PEMWE, by increasing the operating temperature through various means. These authors mainly focused on

recovering heat from various thermal processes, to increase the operating temperature of the PEMWE. However, in this study, the generated heat during the Electrolysis process, was recovered from the PEMWE and transferred this generated heat to an integrated water heating system.

After evaluating the reviewed literature and the research gap, the main objective and contribution of this study, is to propose a comprehensive optimal switching control model of a PEMWE, which could maximize the heat recovery from the PEMWE by the HWST, whilst ensuring that sufficient hydrogen is produced. The recovered heat could be utilized, to form part of an integrated water heating system effectively, to minimize the operational energy cost of the main water heating source, such as an air-to-water heat pump.

The second additional contribution, could be the optimal control model, which may further yield a prolonged membrane lifespan of the PEMWE, by controlling its operating temperature, which is one of the highest cost items in this type of system [106].

4.2 METHODOLOGY

4.2.1 Dynamic model of hydrogen PEMWE water heating system

Fig. 4.1 illustrates the schematic of the proposed supplementary water heating system, for a university residential building, in which 270 occupants reside. The PEMWE is used to convert solar energy into hydrogen gas, which may be stored for later use, such as converting hydrogen gas back into usable electrical energy. During the electrolysis process, heat is further generated, which is transferred to the HWST. Thus, the PEMWE serves as the input to the HWST, which can provide water heating to the residential building. This model ensures that majority of heat being generated during the Electrolysis process, is transferred to the HWST, whilst ensuring stable hydrogen production.

4.2.2 Proposed hydrogen PEMWE water heating system

In this Section, a mathematical model of this system is developed for simulation purposes, which negates the necessity of conducting physical experiments. The control variable and state variable, forming part of the proposed model, are as follows:

- U_A : Discrete switching function of the PEMWE;
- Ts : HWST temperature;

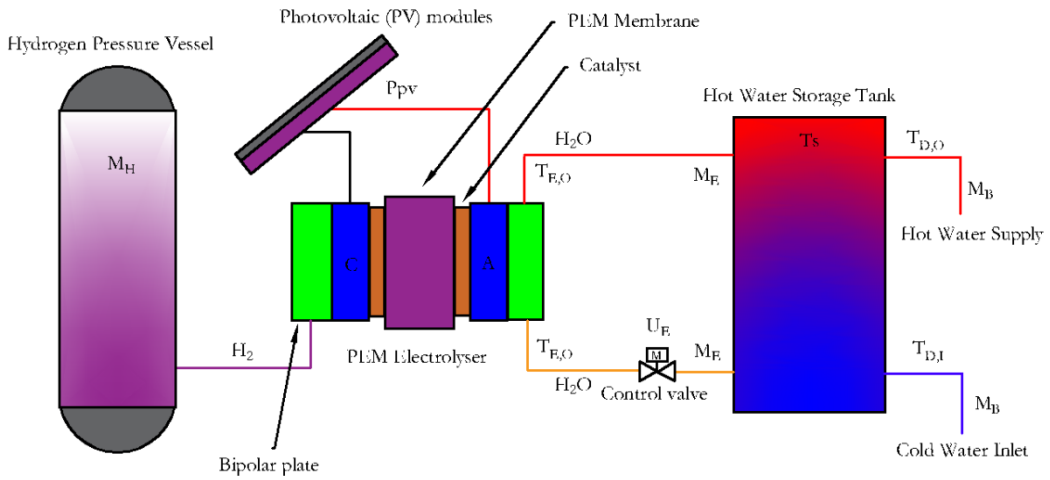

Fig. 4.1: Schematic of the PEM electrolyser model

The first law of thermodynamics, is applied to the circulation fluid storage tank, to obtain the energy balance in the tank. The following equation describes the change in the internal energy (energy within HWST), which relates to the difference in heat entering and leaving the HWST. Eq. (4.1) describes the energy balance equation derived from change in internal energy within the HWST. Q_{IN} is the useful heat gained by the thermodynamic system, Q_{LOAD} is the heat removed from the tank to the load, Q_{CW} is the heat removed from the tank through the addition of cold water at a flow rate of $\dot{M}_B$ and Q_{LOSS} is the heat lost in the tank,

due to its thermal properties. The heat losses, due to the connecting pipes, are neglegted [60]:

$$M.C.\frac{dT_S}{dt} = Q_{IN} - Q_{LOAD} + Q_{CW} - Q_{LOSS} \tag{4.1}$$

The useful heat gain, is described in Eq. (4.2), which is the heat transfer from the electrolyser to the HWST. $\dot{M}_E$ is the mass flow rate of the circulation fluid at the electrolyser, C is the specific heat capacity of the circulation fluid, $T_{E,O}$ and $T_{E,I}$ are the outlet and inlet temperatures of the electrolyser, respectively.

$$Q_{IN} = \dot{M}_E.C.(T_{E,O} - T_{E,I}) \tag{4.2}$$

The heat transfer from the HWST to the load, is defined in Eq. (4.3). $\dot{M}_B$ is the mass flow rate of the circulation fluid at the load (consumer); $T_{D,O}$ is the demand outlet water temperature at the consumer's side. The heat removed from the tank through the addition of cold water at a flow rate of $\dot{M}_B$, is described in Eq. (4.4), where $T_{D,I}$ is the demand inlet water temperature at the supply side.

$$Q_{LOAD} = \dot{M}_B.C.T_{D,O} \tag{4.3}$$

$$Q_{CW} = \dot{M}_B.C.T_{D,I} \tag{4.4}$$

The heat losses in the tank, due to its thermal properties, are stated in Eq. (4.5). T_S is the temperature within the HWST, T_a is ambient air temperature, A_S is surface area of the HWST, Δx is the thickness of selected insulation layer, K is the thermal conductivity coefficient of the selected material and h is the heat transfer coefficient of the surface of the tank.

$$Q_{LOSS} = \frac{(T_s - T_a).A_s}{\frac{\Delta x}{K} + \frac{1}{h}} \tag{4.5}$$

Where: $\beta = \frac{A_s}{\frac{\Delta x}{K} + \frac{1}{h}}$ (4.6)

By substituting Eqs. (4.2), (4.3), (4.4), (4.5) and (4.6) into Eq. (4.1) yields equation (4.7):

$$M.C.\frac{dT_s}{dt} = \dot{M}_E.C.(T_{E,O} - T_{E,I}) - \dot{M}_B.C.T_{D,O} + \dot{M}_B.C.T_{D,I} - \beta.(T_s - T_a) \tag{4.7}$$

The heat gain of an electrolyser, during the electrolysis process, is described in Eq. (4.8). I_E is the electrical current consumed by the electrolyser. V_{act} is the activation over-potential, which is the energy required to activate the chemical reactions at the electrodes. V_{ohm} is the ohmic over-potential, which is the resistance of the membrane and the charge transfer resistance, when electrons pass from/to the electrodes surface to/from the membrane. V_{con} is the concentration over-potential, which is the mass transfer limitation of the cell causing bubbles, which form on the surface of the electrodes [105, 111].

$$Q_{IN} = I_E.(V_{act} + V_{ohm} + V_{con}) \tag{4.8}$$

The activation over-potential, which is the energy required to activate the chemical reactions at the anode and cathode, is stated in Eq. (4.9). a_a and a_c is the anode charge transfer coefficient and the cathode charge transfer coefficient, R is the universal gas constant, T_E is the operating temperature of the electrolyser, F is the Faraday's constant, J is the current density and J_O is the exchange current density.

$$V_{act} = \left(\frac{\alpha_a + \alpha_c}{\alpha_a . \alpha_c} \right) . \frac{R.T_E}{2.F} . ln \left(\frac{J}{J_O} \right) \tag{4.9}$$

The ohmic over-potential, stated in Eq. (4.10), is the resistance caused by the electrons transferring through the membrane, electrodes, and plates. t_{mem} is the membrane thickness and σ_{mem} is the conductivity of the membrane.

$$V_{ohm} = J . \frac{t_{mem}}{\sigma_{mem}} \tag{4.10}$$

The concentration over-potential, described in Eq. (4.11), is the mass transfer limitation of the cell, which causes bubbles to form on the surface of the electrodes. This type of over-potential losses becomes more significant during high limiting current conditions, denoted as J_L.

$$V_{con} = \frac{R.T_E}{2.F} . ln \left(\frac{1 + \frac{1}{J_L}}{1 - \frac{1}{J_L}} \right) \tag{4.11}$$

By substituting Eqs. (4.9), (4.10) and (4.11) into Eq. (4.8) yields Eq. (4.12):

$$Q_{IN} = I_E . \left(\left(\frac{\alpha_a + \alpha_c}{\alpha_a . \alpha_c} \right) . \frac{R.T_E}{2.F} . ln \left(\frac{J}{J_O} \right) + J . \frac{t_{mem}}{\sigma_{mem}} + \frac{R.T_E}{2.F} . ln \left(\frac{1 + \frac{1}{J_L}}{1 - \frac{1}{J_L}} \right) \right) \tag{4.12}$$

Multiplying the current consumed by the electrolyser (I_E), with each of the previously mentioned over-potentials, is described in Eq. (4.13):

$$Q_{IN} = I_E.\left(\frac{\alpha_a + \alpha_c}{\alpha_a.\alpha_c}\right).\frac{R.T_E}{2.F}.ln\left(\frac{J}{J_O}\right) + I_E.J.\frac{t_{mem}}{\sigma_{mem}} + I_E.\frac{R.T_E}{2.F}.ln\left(\frac{1+\frac{1}{J_L}}{1-\frac{1}{J_L}}\right) \tag{4.13}$$

Combining Eq. (4.2) and Eq. (4.14) yields:

$$\dot{M}_E.C.\left(T_{E,O} - T_{E,I}\right) = I_E.\left(\frac{\alpha_a + \alpha_c}{\alpha_a.\alpha_c}\right).\frac{R.T_E}{2.F}.ln\left(\frac{J}{J_O}\right) + I_E.J.\frac{t_{mem}}{\sigma_{mem}} + I_E.\frac{R.T_E}{2.F}.ln\left(\frac{1+\frac{1}{J_L}}{1-\frac{1}{J_L}}\right) \tag{4.14}$$

Where: $T_E = T_{E,O} - T_{E,I}$;

$$\dot{M}_E.C.\left(T_{E,O} - T_{E,I}\right) = \left(T_{E,O} - T_{E,I}\right).\left(\frac{\alpha_a + \alpha_c}{\alpha_a.\alpha_c}\right).\frac{R.I_E}{2.F}.ln\left(\frac{J}{J_O}\right) + \frac{I_E.J.t_{mem}}{\sigma_{mem}}$$
$$+\left(T_{E,O} - T_{E,I}\right).\frac{R.I_E}{2.F}.ln\left(\frac{1+\frac{1}{J_L}}{1-\frac{1}{J_L}}\right) \tag{4.15}$$

Moving the like-terms, which contain the temperature difference of the electrolyser to the left-hand side of the equation, is illustrated in Eq. (4.16).

$$\dot{M}_E.C.\left(T_{E,O} - T_{E,I}\right) - \left(T_{E,O} - T_{E,I}\right).\left(\frac{\alpha_a + \alpha_c}{\alpha_a.\alpha_c}\right).\frac{R.I_E}{2.F}.ln\left(\frac{J}{J_O}\right) - \left(T_{E,O} - T_{E,I}\right).\frac{R.I_E}{2.F}.ln\left(\frac{1+\frac{1}{J_L}}{1-\frac{1}{J_L}}\right) \tag{4.16}$$

Factoring out the temperature difference of the Electrolyser and, thereafter, rearranging the equation, yields Eq. (4.17):

$$T_{E,O} = \frac{\frac{I_E.J.t_{mem}}{\sigma_{mem}}}{\dot{M}_E.C - \left(\frac{\alpha_a + \alpha_c}{\alpha_a.\alpha_c}\right).\frac{R.I_E}{2.F}.ln\left(\frac{J}{J_O}\right) - \frac{R.I_E}{2.F}.ln\left(\frac{1+\frac{1}{J_L}}{1-\frac{1}{J_L}}\right)} + T_{E,I} \quad (4.17)$$

$$T_{E,O} - T_{E,I} = \frac{\frac{I_E.J.t_{mem}}{\sigma_{mem}}}{\dot{M}_E.C - \left(\frac{\alpha_a + \alpha_c}{\alpha_a.\alpha_c}\right).\frac{R.I_E}{2.F}.ln\left(\frac{J}{J_O}\right) - \frac{R.I_E}{2.F}.ln\left(\frac{1+\frac{1}{J_L}}{1-\frac{1}{J_L}}\right)} \quad (4.18)$$

By substituting (4.18) into (4.7), yields:

$$M.C.\frac{dTs}{dt} = \dot{M}_E.C.\left(\frac{\frac{I_E.J.t_{mem}}{\sigma_{mem}}}{\dot{M}_E.C - \left(\frac{\alpha_a + \alpha_c}{\alpha_a.\alpha_c}\right).\frac{R.I_E}{2.F}.ln\left(\frac{J}{J_O}\right) - \frac{R.I_E}{2.F}.ln\left(\frac{1+\frac{1}{J_L}}{1-\frac{1}{J_L}}\right)}\right) \quad (4.19)$$

$$-\dot{M}b.C.Ts + \dot{M}b.C.Td,i - \beta.Ts + \beta.Ta$$

Factoring out more like-terms yields Eq. (4.20):

$$M.C.\frac{dTs}{dt} = \dot{M}_E.C.\left(\frac{\frac{I_E.J.t_{mem}}{\sigma_{mem}}}{\dot{M}_E.C - \left(\frac{\alpha_a+\alpha_c}{\alpha_a.\alpha_c}\right).\frac{R.I_E}{2.F}.ln\left(\frac{J}{J_O}\right) - \frac{R.I_E}{2.F}.ln\left(\frac{1+\frac{1}{J_L}}{1-\frac{1}{J_L}}\right)}\right) - T_s\left(\dot{M}_B.C+\beta\right)+T_{D,I}\left(\dot{M}_B.C\right)+T_a\left(\beta\right) \quad (4.20)$$

Dividing both sides of the expression, with the product of *M.C*, is illustrated in Eq. (4.21):

$$\frac{dTs}{dt} = \frac{\dot{M}_E.C.}{M.C}\left(\frac{\frac{I_E.J.t_{mem}}{\sigma_{mem}}}{\dot{M}_E.C - \left(\frac{\alpha_a+\alpha_c}{\alpha_a.\alpha_c}\right).\frac{R.I_E}{2.F}.ln\left(\frac{J}{J_O}\right) - \frac{R.I_E}{2.F}.ln\left(\frac{1+\frac{1}{J_L}}{1-\frac{1}{J_L}}\right)}\right) - T_s\left(\frac{\dot{M}_B.C+\beta}{M.C}\right)+T_{D,I}\left(\frac{\dot{M}_B.C}{M.C}\right)+T_a\left(\frac{\beta}{M.C}\right) \quad (4.21)$$

The general state space representation, illustrated in Eq. (3.12), Section 3.2.2, is applied to the proposed model. $\dot{X}(t)$, the state variable, is the temperature of the HWST, *A* is known as the state matrix, *B* is the input matrix and α is the disturbances to the system.

Then, applying (3.12) to (4.21), yields:

$$\dot{\mathrm{T}}(t)=\left(\frac{\frac{I_E.J.t_{mem}}{\sigma_{mem}}}{\dot{M}_E.C-\left(\frac{\alpha_a+\alpha_c}{\alpha_a.\alpha_c}\right).\frac{R.I_E}{2.F}.ln\left(\frac{J}{J_O}\right)-\frac{R.I_E}{2.F}.ln\left(\frac{1+\frac{1}{J_L}}{1-\frac{1}{J_L}}\right)}\right).X(t)$$
$$+T_s(t).\left(\frac{\dot{M}_B.C+\beta}{M.C}\right)+T_{D,I}\left(\frac{\dot{M}_B}{M}\right)+T_a\left(\frac{\beta}{M.C}\right) \quad (4.22)$$

The state matrix, A, is stated in Eq. (4.23), *B*, the input matrix, is illustrated in Eq. (4.24) and α, the disturbances to the system, is stated in Eq. (4.25).

$$A=-\left(\frac{\dot{M}_B.C+\beta}{M.C}\right) \quad (4.23)$$

$$B=\left(\frac{\frac{I_E.J.t_{mem}}{\sigma_{mem}}}{\dot{M}_E.C-\left(\frac{\alpha_a+\alpha_c}{\alpha_a.\alpha_c}\right).\frac{R.I_E}{2.F}.ln\left(\frac{J}{J_O}\right)-\frac{R.I_E}{2.F}.ln\left(\frac{1+\frac{1}{J_L}}{1-\frac{1}{J_L}}\right)}\right) \quad (4.24)$$

$$\alpha=T_{D,I}\left(\frac{\dot{M}_B}{M}\right)+T_a\left(\frac{\beta}{M.C}\right) \quad (4.25)$$

So that, the final state space equation, may be written as in Eq. (4.26).

$$\dot{\mathrm{T}}(t)=A(t).Ts(t)+B(t).U(t)+\alpha(t) \quad (4.26)$$

4.2.3 Discretized hot water storage tank temperature

The general discretized temperature equation known as Eq. (3.22), derived in Chapter III, sub-section 3.2.3, is applied to the proposed PEMWE water heating model, as follows:

$$T_{k+1} = T_0.\prod_{j=0}^{k}\left(1+t_s.A_j\right)+t_s.\sum_{j=0}^{k}B_j.U_j\prod_{i=j+1}^{k}\left(1+t_s.A_i\right)+t_s.\sum_{j=0}^{k}\alpha_j\prod_{i=j+1}^{k}\left(1+t_s.A_i\right) \tag{4.27}$$

4.2.4 Objective function

4.2.4.1 Electolyser hydrogen production

The theoretical open-circuit voltage of an electrolyser cell, is calculated by making use of Eq. (4.28) [110]. 1.2583 V is the standard voltage of a cell at equilibrium, P_{H2O} is the partial pressure of water, P_{H2} is the partial pressure of hydrogen and P_{O2} is the partial pressure of oxygen.

$$E_{OC} = \left[1.2583+\frac{R.T_E}{2.F}ln\left(\frac{P_{H_2O}}{P_{H_2}.P_{O_2}{}^{0.5}}\right)\right] \tag{4.28}$$

The voltage of the electrolyser is calculated using Eq. (4.29) [105]. V_{act}, V_{ohm} and V_{con}, have been discussed and explained previously.

$$V_{el} = E_{OC}+V_{act}+V_{ohm}+V_{con} \tag{4.29}$$

By substituting (4.9), (4.10), (4.11) and (4.28), into (4.29), yields:

$$V_{el} = \left[1.2583 + \frac{R.T_E}{2.F} ln\left(\frac{P_{H_2O}}{P_{H_2}.P_{O_2}^{0.5}}\right)\right] + \left(\frac{\alpha_a + \alpha_c}{\alpha_a.\alpha_c}\right).\frac{R.T_E}{2.F}.ln\left(\frac{J}{J_O}\right) + J.\frac{t_{mem}}{\sigma_{mem}} + \frac{R.T_E}{2.F}.ln\left(\frac{1+\frac{1}{J_L}}{1-\frac{1}{J_L}}\right) \quad (4.30)$$

Factoring out the temperature of the electrolyser, T_E, is conducted with all of the terms that contains it, is illustrated in Eq. (4.31).

$$V_{el} = 1.2583 + J.\frac{t_{mem}}{\sigma_{mem}} + T_E\left[\frac{R}{2.F} ln\left(\frac{P_{H_2O}}{P_{H_2}.P_{O_2}^{0.5}}\right) + \left(\frac{\alpha_a + \alpha_c}{\alpha_a.\alpha_c}\right).\frac{R}{2.F}.ln\left(\frac{J}{J_O}\right) + \frac{R}{2.F}.ln\left(\frac{1+\frac{1}{J_L}}{1-\frac{1}{J_L}}\right)\right] \quad (4.31)$$

Where: $T_E = T_{E,O} - T_{E,O}$. The electrical power of the electrolyser may be calculated using the following equation:

$$P_{el} = 1.2583.I_E + \frac{I_E.J.t_{mem}}{\sigma_{mem}} + T_E\left[\frac{R.I_E}{2.F} ln\left(\frac{P_{H_2O}}{P_{H_2}.P_{O_2}^{0.5}}\right) + \left(\frac{\alpha_a + \alpha_c}{\alpha_a.\alpha_c}\right).\frac{R.I_E}{2.F}.ln\left(\frac{J}{J_O}\right) + \frac{R.I_E}{2.F}.ln\left(\frac{1+\frac{1}{J_L}}{1-\frac{1}{J_L}}\right)\right] \quad (4.32)$$

By substituting (4.17) into (4.32), yields:

$$P_{el} = 1.2583.I_E + \frac{I_E.J.t_{mem}}{\sigma_{mem}} + \left[\frac{\frac{I_E.J.t_{mem}}{\sigma_{mem}}}{\dot{M}_E.C - \left(\frac{\alpha_a + \alpha_c}{\alpha_a.\alpha_c}\right).\frac{R.I_E}{2.F}.ln\left(\frac{J}{J_O}\right) - \frac{R.I_E}{2.F}.ln\left(\frac{1+\frac{1}{J_L}}{1-\frac{1}{J_L}}\right)} \right] \left[\frac{R.I_E}{2.F} ln\left(\frac{P_{H_2O}}{P_{H_2}.P_{O_2}^{0.5}}\right) + \left(\frac{\alpha_a + \alpha_c}{\alpha_a.\alpha_c}\right).\frac{R.I_E}{2.F}.ln\left(\frac{J}{J_O}\right) + \frac{R.I_E}{2.F}.ln\left(\frac{1+\frac{1}{J_L}}{1-\frac{1}{J_L}}\right) \right] \quad (4.33)$$

Therefore, the first objective function for the hydrogen production is as follows:

$$maxJ_e = \sum_{k=1}^{N} \left(1.2583.I_E + \frac{I_E.J.t_{mem}}{\sigma_{mem}} + \left[\frac{\frac{I_E.J.t_{mem}}{\sigma_{mem}}}{\dot{M}_E.C - \left(\frac{\alpha_a + \alpha_c}{\alpha_a.\alpha_c}\right).\frac{R.I_E}{2.F}.ln\left(\frac{J}{J_O}\right) - \frac{R.I_E}{2.F}.ln\left(\frac{1+\frac{1}{J_L}}{1-\frac{1}{J_L}}\right)} \right] \left[\frac{R.I_E}{2.F} ln\left(\frac{P_{H_2O}}{P_{H_2}.P_{O_2}^{0.5}}\right) + \left(\frac{\alpha_a + \alpha_c}{\alpha_a.\alpha_c}\right).\frac{R.I_E}{2.F}.ln\left(\frac{J}{J_O}\right) + \frac{R.I_E}{2.F}.ln\left(\frac{1+\frac{1}{J_L}}{1-\frac{1}{J_L}}\right) \right] \right) \quad (4.34)$$

Where: M_E is the control variable, which is the mass flow rate of water to the electrolyser.

4.2.4.2 Thermal discomfort level

A load profile is obtained, known as the function *F(t)*. This is a function of time and defined as the desired output temperature of the consumer. The thermal comfort level of the consumer is addressed, where the difference between the output temperature *T(t)* of the hot water storage tank and the desired temperature *F(t)*, should not be excessive. That is, the value of $(T(t)-F(t))^2$ should be minimized. The function *L(t)* in Eq. (4.35), denotes the thermal discomfort level, which is the second objective function to be minimized [92].

$$L(t) = W_2 \sum_{k=1}^{N} \left(T(k) - F(k)\right)^2 .t_s \tag{4.35}$$

The output temperature *T(t)*, is known as the discrete differential temperature equation and is shown in the following equation:

$$T_{k+1} = \prod_{j=0}^{k} \left(1 + t_s.A_j\right) + \sum_{j=0}^{k} B_j.U_j \prod_{i=j+1}^{k} \left(1 + t_s.A_i\right) + \sum_{j=0}^{k} \alpha_j \prod_{i=j+1}^{k} \left(1 + t_s.A_i\right) \tag{4.36}$$

The final objective function, containing both objective functions, is expressed as follows:

$$J = J_e + \mu.L \tag{4.37}$$

Where : μ is the weighting factor for the final objective function.

Therefore, substituting Eq. (4.35) and Eq. (4.36), into Eq. (4.37), yields the final objective function:

$$J=\sum_{k=1}^{N}\left(\begin{array}{l}1.2583.I_E+\dfrac{I_E.J.t_{mem}}{\sigma_{mem}}\\ +\left[\dfrac{\dfrac{I_E.J.t_{mem}}{\sigma_{mem}}}{\dot{M}_E.C-\left(\dfrac{\alpha_a+\alpha_c}{\alpha_a.\alpha_c}\right).\dfrac{R.I_E}{2.F}.ln\left(\dfrac{J}{J_O}\right)-\dfrac{R.I_E}{2.F}.ln\left(\dfrac{1+\dfrac{1}{J_L}}{1-\dfrac{1}{J_L}}\right)}\right]\\ \left[\dfrac{R.I_E}{2.F}ln\left(\dfrac{P_{H_2O}}{P_{H_2}.P_{O_2}^{\ 0.5}}\right)+\left(\dfrac{\alpha_a+\alpha_c}{\alpha_a.\alpha_c}\right).\dfrac{R.I_E}{2.F}.ln\left(\dfrac{J}{J_O}\right)+\dfrac{R.I_E}{2.F}.ln\left(\dfrac{1+\dfrac{1}{J_L}}{1-\dfrac{1}{J_L}}\right)\right]\\ +W_2\sum_{k=1}^{N}\left(T(k)-F(k)\right)^2.t_s\end{array}\right) \tag{4.38}$$

Where:

W_1 is the weighting factor, to set priority to maximize the hydrogen production of the Electrolyser

W_2 is the weighting factor to set priority, to maximize the storage tank temperature

4.2.5 Constraints

The discrete switching function, U_k, which is used to switch the PEMWE system, may either be 1 or 0. This is illustrated below:

$$U_k \in \{0,1\} \tag{4.39}$$

The control variable may either be 1 or 0, which is the upper bound and lower bound of the switch. This is shown in the following equation:

$$lb \le x \le ub \tag{4.40}$$

The lower boundary and upper boundary are expressed as follows:

$$lb = zeros(1, N), \tag{4.41}$$

$$ub = ones(1, N). \tag{4.42}$$

4.2.6 Proposed optimization solver

The objective function, as shown in Eq. (4.38), is a non-linear function, with an integer binary control variable, that should be solved, to obtain the optimal switching status of the PEMWE system. This problem is a mixed integer nonlinear optimization problem (MINLP) and may be solved using the SCIP solver, in the optimization toolbox of MATLAB, as illustrated in Eq. (4.43). The main reasons for using SCIP as the solver, is due to its fast-solving capabilities, as well as that it is capable of solving non-linear optimization problems, by controlling a binary integer decision variable, which is required to switch PEMWE system.

$$\begin{aligned} &min_x\, f(x) \\ &subject\,to: A.x \le b \\ &A_{eq}.x \le b_{eq} \\ &lb \le x \le ub \\ &x_j \in \{0,1\} \end{aligned} \tag{4.43}$$

Where: $f(x)$ is the objective function, which is a scalar function, $A.x \leq b$ is the linear inequality constraint, $lb \leq x \leq ub$ is the lower boundary and upper boundary of the decision variable, x_j is a decision variable that solely takes binary values.

4.3 CASE STUDY DESCRIPTION

In this Section, the optimal switching control of the PEMWE water heating system is simulated using the SCIP solver, in the optimization toolbox of MATLAB. The main objective is to maximize the heat transfer to the HWST, during the hydrogen production process.

A case study is conducted using meteorological data, obtained at the University of Free State, Bloemfontein, South Africa, on an air-to-air heat pump [94]. The heat transferred to the HWST may be used, to assist the main water heating source for a university residential building, in which 270 occupants are residing. The sampling time, t_s = 30 minutes, is implemented, to simplify the simulations.

4.3.1 Data representation

Table 4.1 shows the parameters of the HWST for a University residential building, in which 270 occupants reside [113-115]. A_s is the surface area of the tank, M is the volume of the tank, C is the specific heat capacity of water, h is the surface, k is the thermal conductivity and dx is the insulation thickness.

Table 4.1: HWST parameters

Parameters	Symbol	Value	Unit
Tank surface area	A_s	32	m^2
Tank volume	M	10 000	L
Specific heat capacity	C	4 186	J/kgK
Surface heat transfer coefficient	h	11.3	W/m^2K
Thermal conductivity	k	50	W/mK
Thickness of insulation	dx	0.07	m

Table 4.2 shows the parameters of the PEMWE used for the hydrogen production [105, 110, 116, 117]. The exchange current densities at the anode and cathode are identical, due to the anode exchange being the most dominant of the two current densities [118]. A solar PV module, rated at 435 W of power, making up a total array power of 287.1 kW, is used in this study, to supply the electrical energy required by the PEM electrolyser [119]. a_a and a_c is the anode and cathode charge transfer coefficients, respectively. R is the universal gas constant, F is the Faraday constant, J is the current density, J_0 is the exchange current density, t_{mem} is the membrane thickness, σ_{mem} is the membrane conductivity and J_L is the limiting current density. ϱ_{H20} is the partial pressure of water. ϱ_H and ϱ_O is the partial pressure of hydrogen and oxygen, respectively.

Table 4.2: PEM Electrolyser parameters

Parameters	**Symbol**	**Value**	**Unit**
Anode transfer coefficient	a_a	0.5	-
Cathode transfer coefficient	a_c	0.5	-
Universal gas constant	R	8.314	J/mol.K
Faraday constant	F	96 485	C/mol
Current density	J	1	A/cm^2
Exchange current density	J_o	0.00000173	A/cm^2
Membrane thickness	t_{mem}	0.0178	cm
Membrane conductivity	σ_{mem}	0.0001	S/cm
Limiting current density	J_L	2	A/cm^2
Partial pressure of water	ϱ_{H20}	101 325	Pa
Partial pressure of hydrogen	ϱ_H	101 325	Pa
Partial pressure of oxygen	ϱ_0	101 325	Pa

Fig. 4.2 presents the ambient temperature in degrees Celsius, during a typical winter day in Bloemfontein, Free State, South Africa. The ambient air temperatures have been retrieved from the radiometric station, situated at the University of Free State, forming part of the South African Universities Radiometric Network (SAURAN) [94].

The inlet water and ambient temperature profile during summer, is further illustrated in Fig. 4.3.

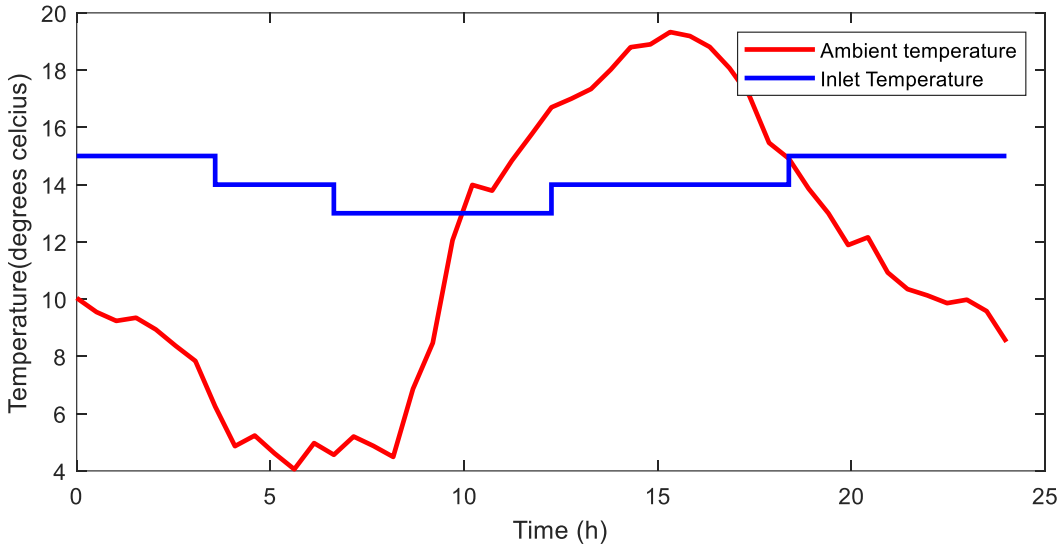

Fig. 4.2: Ambient and inlet water temperature during winter

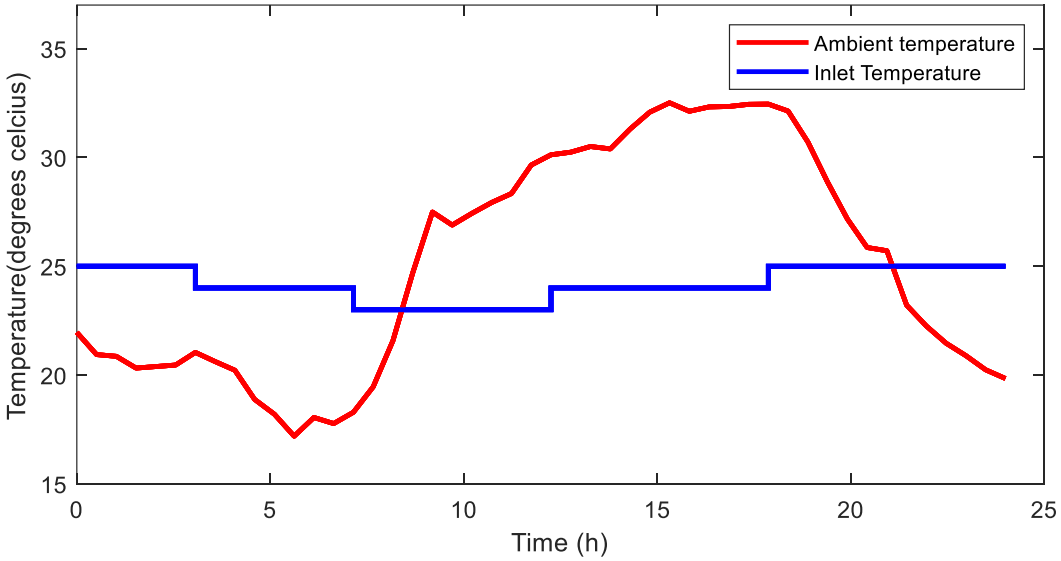

Fig. 4.3: Ambient and inlet water temperature during summer

Fig. 4.4 presents the electrical energy produced by the PV array in kW during winter, which is used to supply the PEMWE with energy, which is responsible of hydrogen gas production.

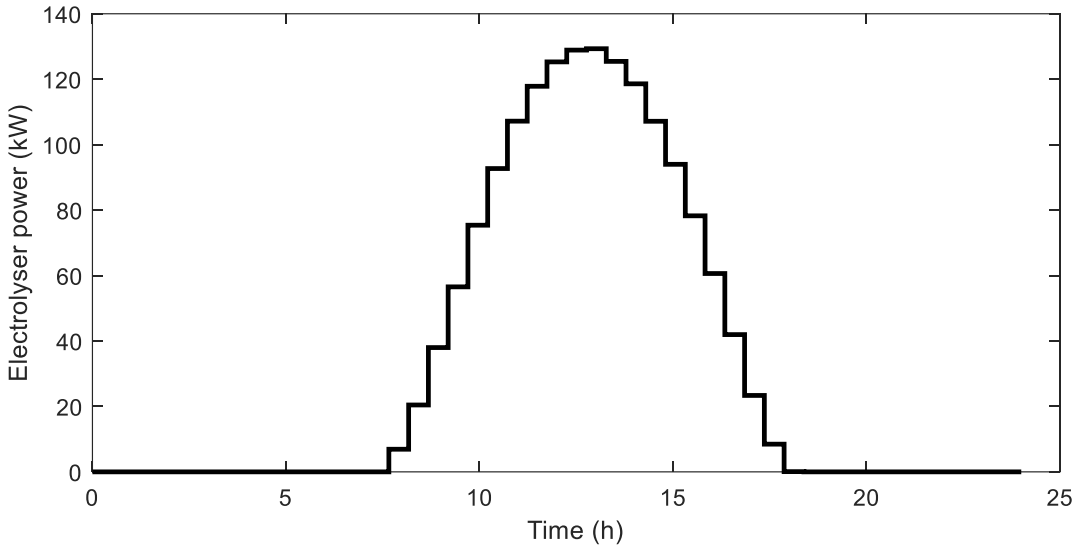

Fig. 4.4: Solar PV power production during winter

Fig. 4.5 presents the electrical energy produced by the PV array in kW during summer, which is used to supply the PEMWE with energy, which is responsible of hydrogen gas production.

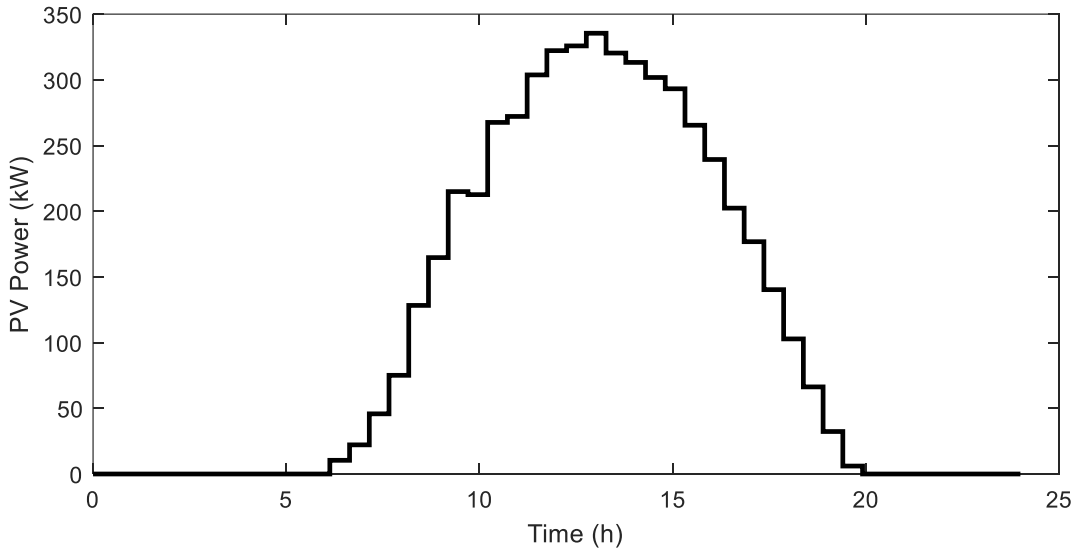

Fig. 4.5: Solar PV power production during summer

Table 4.3 depicts the input parameters, which were used perform the simulation of the developed model linked to the selected case study.

Table 4.3: Simulation parameters

Parameters	description	Value
t_s	Sampling time	30 min
Hours	Optimization interval	24 h

4.4 SIMULATION RESULTS AND DISCUSSION

The proposed optimal control model is evaluated against a standard PEMWE system, which generates heat as a by-product, during the electrolysis process. The generated heat is not recovered and, is therefore, absorbed by the electro-chemical process. The optimal switching control of a PEMWE water heating system, is discussed in Section 4.2.1. This model optimally controls the switching of the PEMWE, where it attempts to maximize the hydrogen production rate, whilst absorbing the maximum amount of undesired heat from the PEMWE. The undesired heat negatively influences the lifespan of the PEMWE, as mentioned in Section 4.1. However, the main objective is to recover the most amount of heat from the PEMWE as possible. The optimal switching control of the PEMWE, is evaluated against a standard PEMWE system (baseline), during winter and summer periods.

4.4.1 Baseline

4.4.1.1 Winter case standard PEMWE system

From Fig. 4.6, the power produced by the PEMWE is observed. From 00h00 to 07h30, the power is zero, as no electrical energy is produced via the solar PV modules, as seen from Fig. 4.4. The power production begins to gradually increase to a maximum of 126.3 kW, at 13h00, after which it corresponds to the electrical energy production of the solar PV

modules. From 13h00, the power produced by the PEMWE, begins to decrease, until it is unable to consume any electrical energy at 18h00, which is when the electrical energy produced via the solar PV modules is not available for the remainder of the day, due to the absence of solar irradiance.

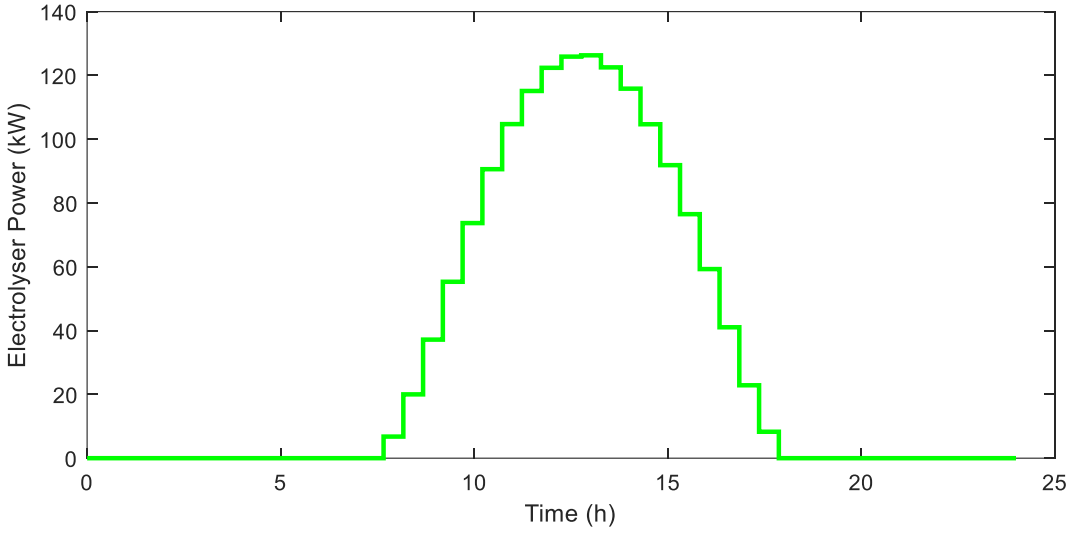

Fig. 4.6: PEM Electrolyser power production during winter

The hydrogen storage level, produced by the PEMWE, is illustrated in Fig. 4.7. From 00h00 to 07h30, the hydrogen storage level remains at 0 kg, due to the PEMWE not being in operation. From 07h30 to 19h30, the hydrogen storage level begins to gradually increase, until the hydrogen storage level reaches 13.98 kg. From 18h00 to 24h00, the hydrogen storage level remains unchanged, due to any further hydrogen being produced, as a result of the absence of solar irradiance.

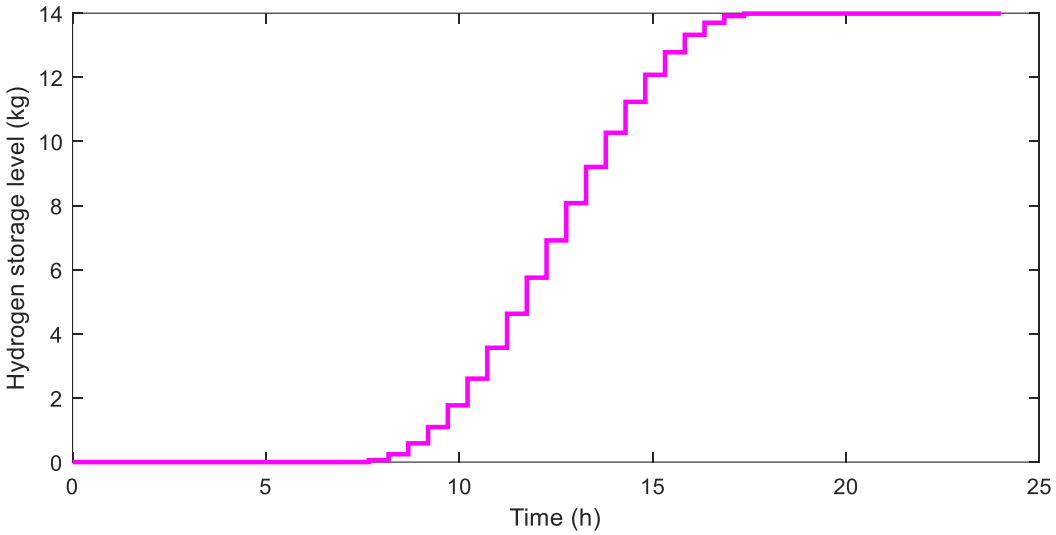

Fig. 4.7: Hydrogen storage level during winter

From Fig. 4.8, the water storage tank (WST) temperature is initially 60 °C at 00h00, after which it begins to decrease. The WST temperature decreases significantly until 10h00, due to the decrease in the ambient air temperature, as seen from Fig. 4.2. From 10h00 to 17h00, the WST temperature decreases further at a less steep rate, which is due to a gradual increase in the ambient air temperature. From 17h00 to 24h00, the temperature begins to significantly decrease, until it reaches a minimum temperature of 47.78 °C, which is due to the significant reduction in the ambient air temperature observed during this time period.

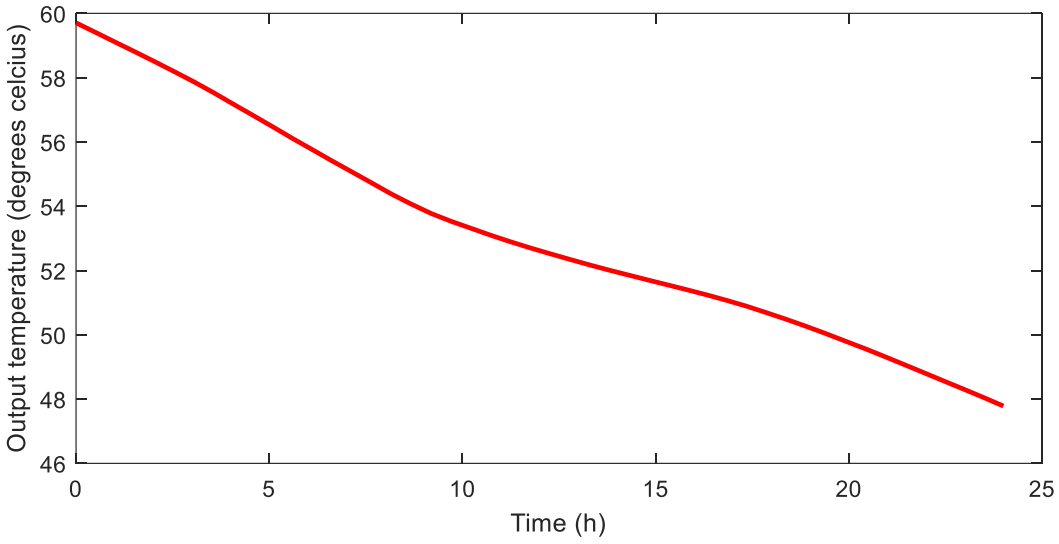

Fig. 4.8: Water storage tank temperature during winter

The cumulative energy production of the PEMWE during winter, is illustrated in Fig. 4.9. From 00h00 to 07h30, the energy consumption is at zero, due to the absence of solar radiation. From 07h30, the PEMWE begins to produce energy, which is when solar radiation becomes available. It may be observed that the rate of energy production gradually increases, until 13h00, which is when the solar radiation peaks, after which the rate begins to gradually decrease, until 18h00, which is when solar radiation is no longer available for the remainder of the day. The total energy produced by the PEMWE during winter, reached a total of 801.24 kWh.

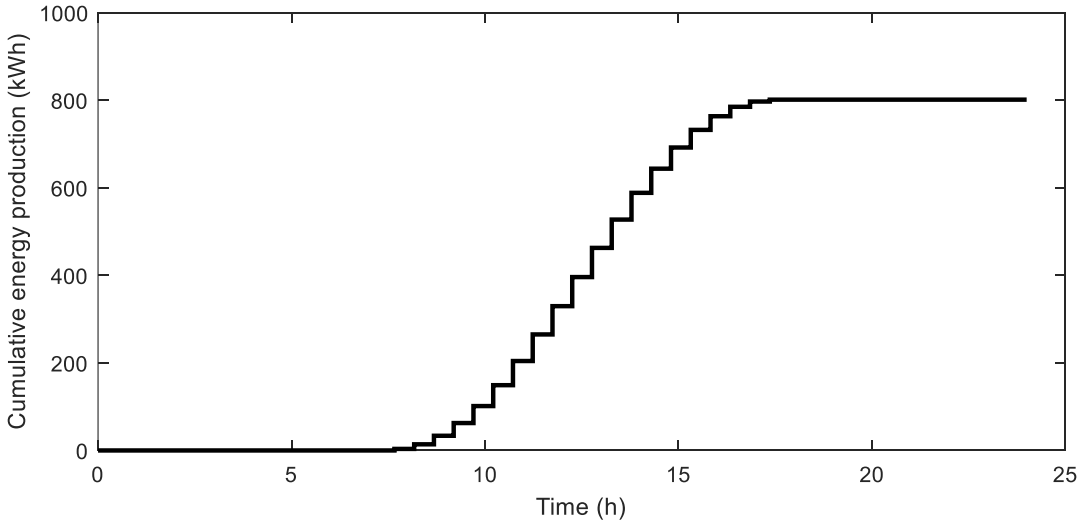

Fig. 4.9: Electrolyser cumulative energy production during winter

4.4.1.2 Summer case standard PEMWE system

From Fig. 4.10, the power produced by the PEMWE is observed. From 00h00 to 06h00, the power is at zero, as no electrical energy is produced via the solar PV modules, as seen from Fig. 4.5. The power production begins to gradually increase to a maximum of 258.55 kW, at 13h00, after which it corresponds to the electrical energy production of the solar PV modules. From 13h30, the power produced by the PEMWE, begins to decrease, until it is unable to consume any electrical energy at 19h30, which is when the electrical energy produced via the solar PV modules, is not available for the remainder of the day, due to the absence of solar irradiance.

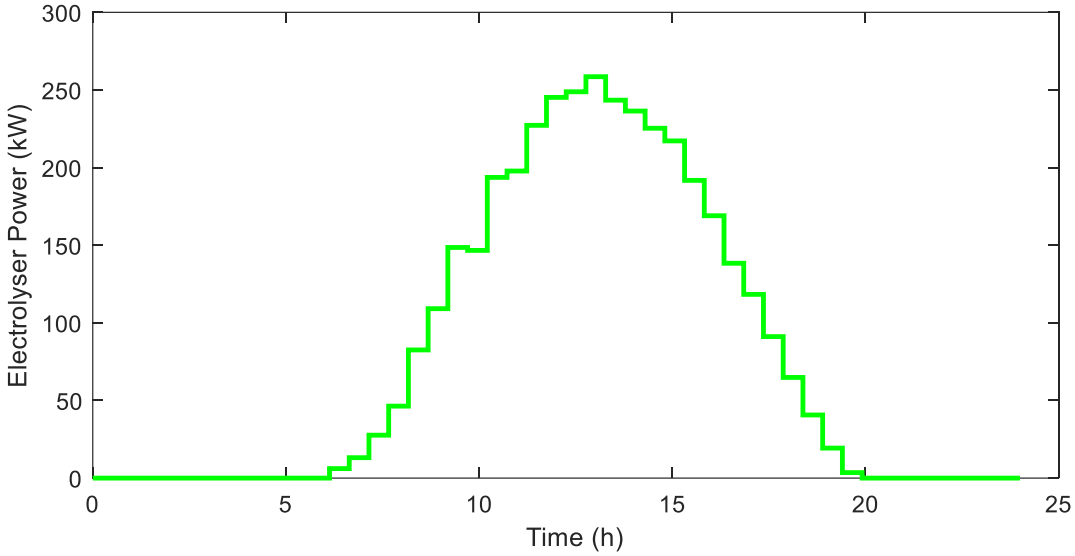

Fig. 4.10: PEM Electrolyser power production during summer

The hydrogen storage level, produced by the PEMWE, is illustrated in Fig. 4.11. From 00h00 to 06h00, the hydrogen storage level remains at 0 kg, due to the PEMWE not being in operation. From 06h00 to 19h30, the hydrogen storage level begins to gradually increase, until it reaches 34.31 kg. From 19h30 to 24h00, the hydrogen storage level remains unchanged, due to any further hydrogen being produced, a result of the absence of solar irradiance.

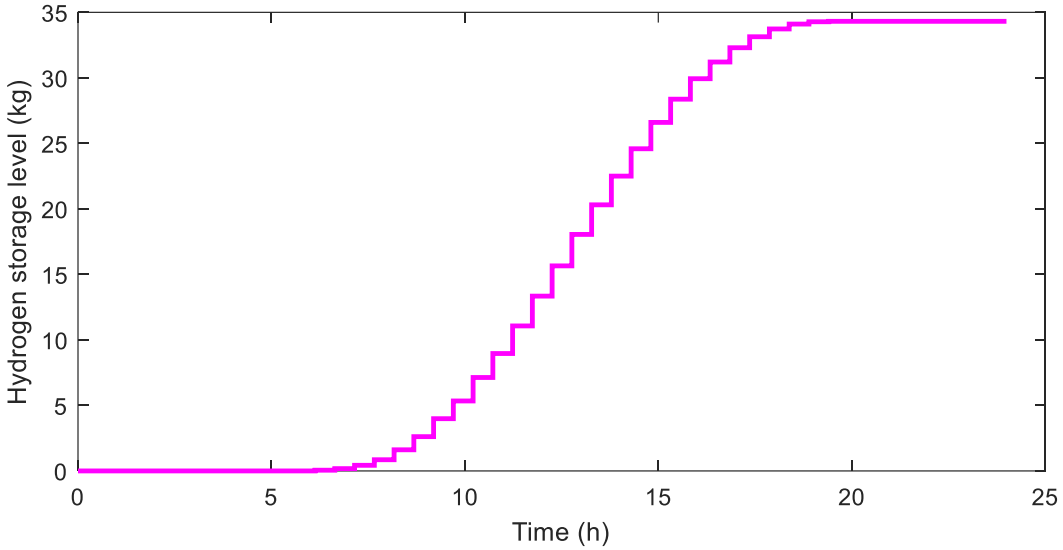

Fig. 4.11: Hydrogen storage level during summer

From Fig. 4.12, the WST temperature is initially 60 °C, at 00h00, after which it begins to decrease. The WST temperature decreases significantly, until 07h00, due to the decrease in the ambient air temperature, as seen from Fig. 4.3. From 07h00 to 14h30, the WST temperature decreases further at a less steep rate, due to a gradual increase in the ambient air temperature. From 14h30 to 18h30, the WST temperature remains rather stable, at approximately 56.35 °C. From 18h30 to 24h00, the temperature begins to significantly decrease, until it reaches a minimum temperature of 54.71 °C, due to a significant reduction in the ambient air temperature, during this time period.

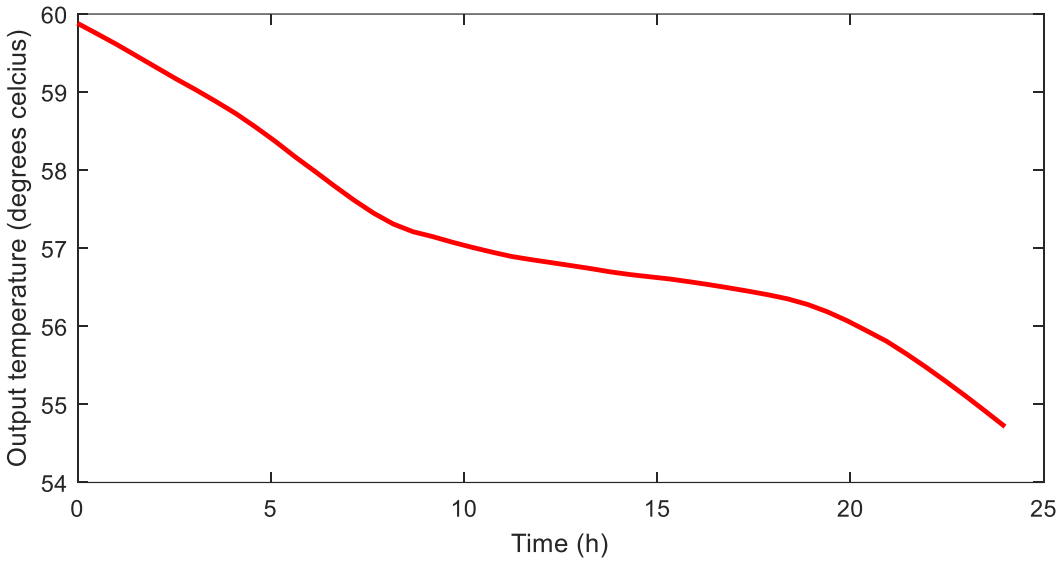

Fig. 4.12: Water storage tank temperature during summer

The cumulative energy production of the PEMWE, is illustrated in Fig. 4.13. From 00h00 to 06h00, the energy consumption is at zero, due to the absence of solar radiation. From 06h00, the PEMWE begins to produce hydrogen energy, which is when solar radiation becomes available. It may be observed that, the rate of energy production gradually increases until 13h00, which is when the solar radiation peaks, after which, the rate begins to gradually decrease until 19h30, which is when solar radiation is no longer available, for the remainder of the day. The total energy produced by the PEMWE, reached a total of 1 965.74 kWh.

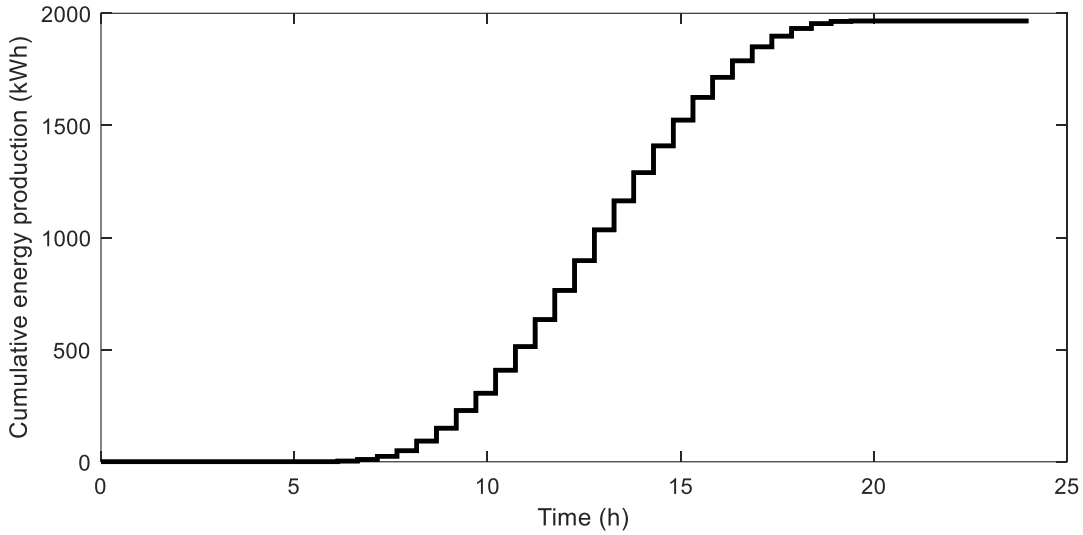

Fig. 4.13: Electrolyser cumulative energy production during summer

4.4.2 Optimal control case

4.4.2.1 Winter

From Fig. 4.14, the hydrogen power production of the PEMWE and the switching function, thereof, may be observed. From 00h00 to 07h30, the PEMWE is switched off, due to the absence of electrical energy supplied, via the solar PV modules, as seen from Fig. 4.4. The hydrogen power production begins to increase to a maximum of 129.32 kW, at 13h00, due to the solar PV modules producing at maximum power during these weather conditions, as seen from Fig. 4.4. From 13h00, the power production of the PEMWE begins to decrease, until it cannot consume electrical energy at 18h00, which is when the electrical energy produced via the solar PV modules is not available, for the remainder of the day.

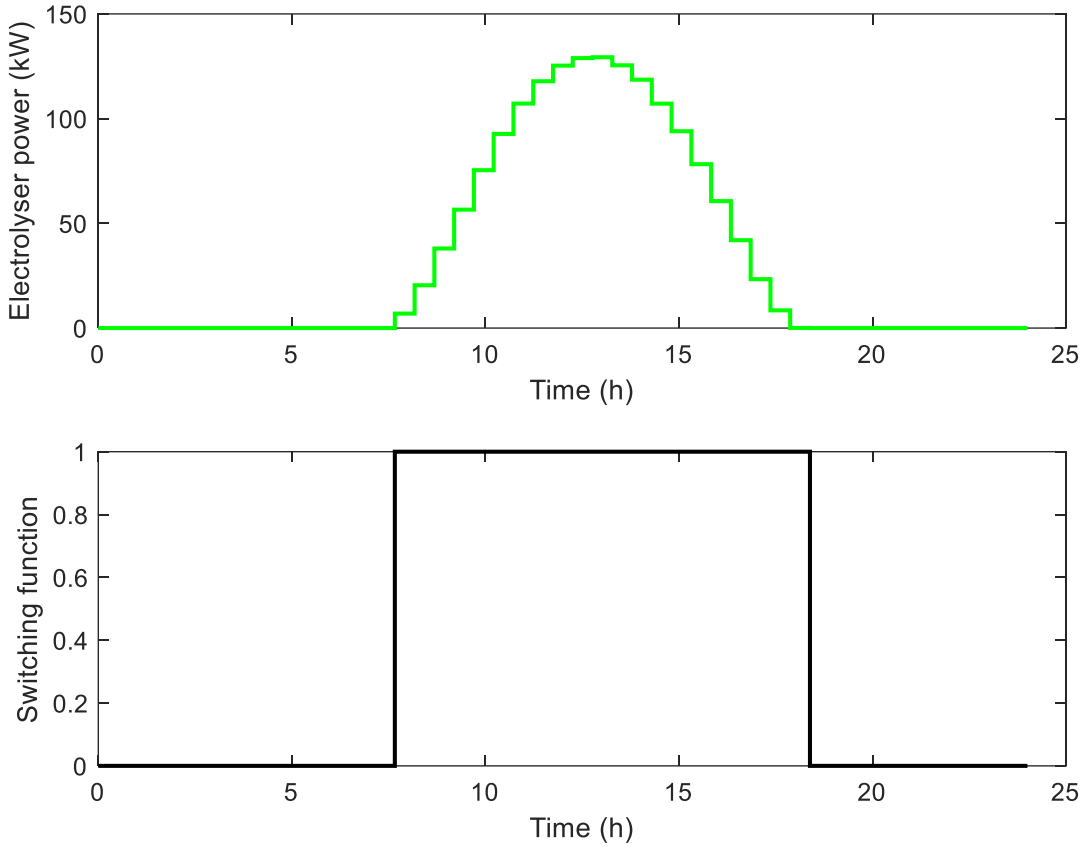

Fig. 4.14: PEM Electrolyser power production and switching function during winter

The hydrogen storage level and the HWST temperature, are illustrated in Fig. 4.15. From 00h00 to 07h30, the hydrogen storage level remains 0 kg, which is due to the PEMWE not operating. From 07h30, the hydrogen storage begins to increase until 13h00, which corresponds to the results observed from Fig. 4.14. From 13h00 to 18h00, the slope of the increase in the hydrogen storage level, begins to steadily decrease, as observed by the power production of the PEMWE, until the hydrogen storage level reaches a maximum of 13.72 kg.

From Fig. 4.15, the HWST temperature is initially 60 °C at 00h00, after which it begins to decrease. The HWST temperature decreases to 53.77 °C, until 10h00, due to the significant decrease in the ambient air temperature, as seen from Fig. 4.2. From 10h00, the HWST temperature begins to increase, due to the heat produced by the PEMWE, during hydrogen

production. The HWST temperature increases until it reaches 54.58 °C at 15h00, after which it begins to decrease. This is due to the significant reduction in the ambient air temperature, outweighs the much lower heat, produced by the PEMWE during this time period, causing the HWST temperature to reach a minimum of 50.55 °C.

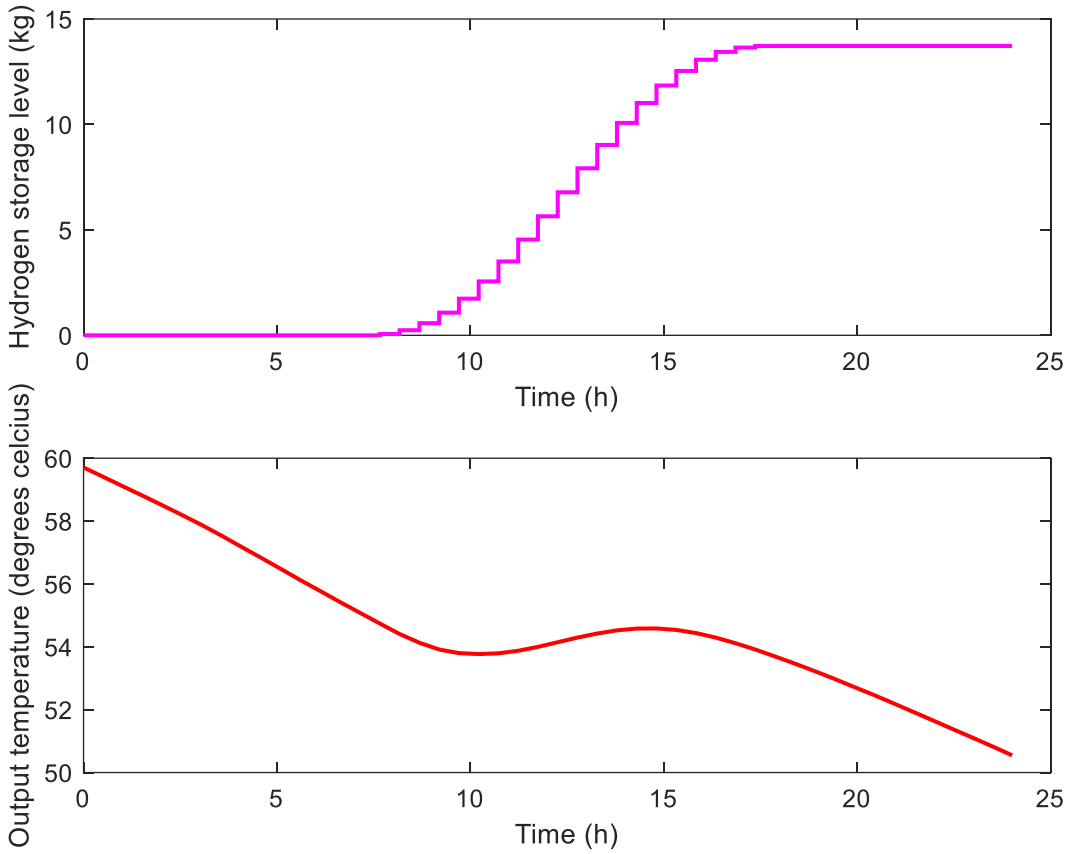

Fig. 4.15: Hydrogen storage level and HWST temperature during winter

In Fig. 4.16, the cumulative thermal energy recovered by the HWST, is illustrated. Initially, the cumulative heat gain is at zero and decreases until 10h00 to -234 723 kJ, as the thermal energy is lost to the ambient air. After 10:00, the thermal energy gained inside the HWST, begins to increase, as the PEMWE is in production of hydrogen, resulting in heat generation. The thermal energy gain increases to -204 017 kJ at 15h00. Thereafter, the

thermal energy recovery decreases until 24h00, reaching an overall heat loss of -345 379 kJ to the environment, equivalent to 95.94 kWh.

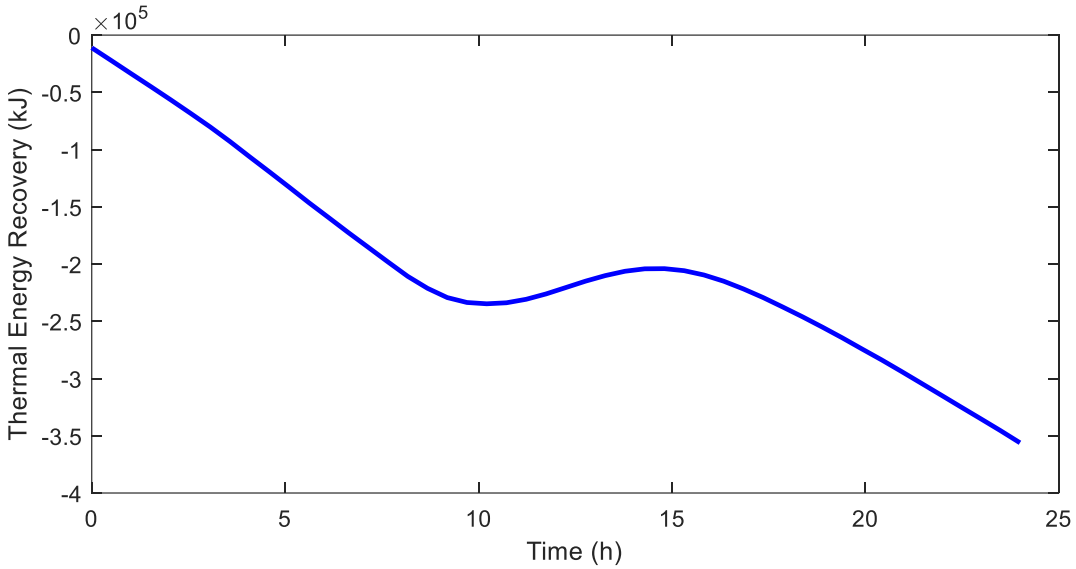

Fig. 4.16: Thermal energy recovery during winter

The cumulative energy production of the PEMWE is illustrated in Fig. 4.17. From 00h00 to 07h30, the energy production is at zero, due to the absence of solar radiation. From 07h30, the PEMWE begins to produce energy, which is when solar radiation becomes available during the winter period. It may be observed that the rate of energy production gradually increases until 13h00, which is when the solar radiation peaks, after which the rate begins to gradually decrease until 18h00, when solar radiation is no longer available for the remainder of the day. The total energy produced by the PEMWE, reached a total of 778.19 kWh.

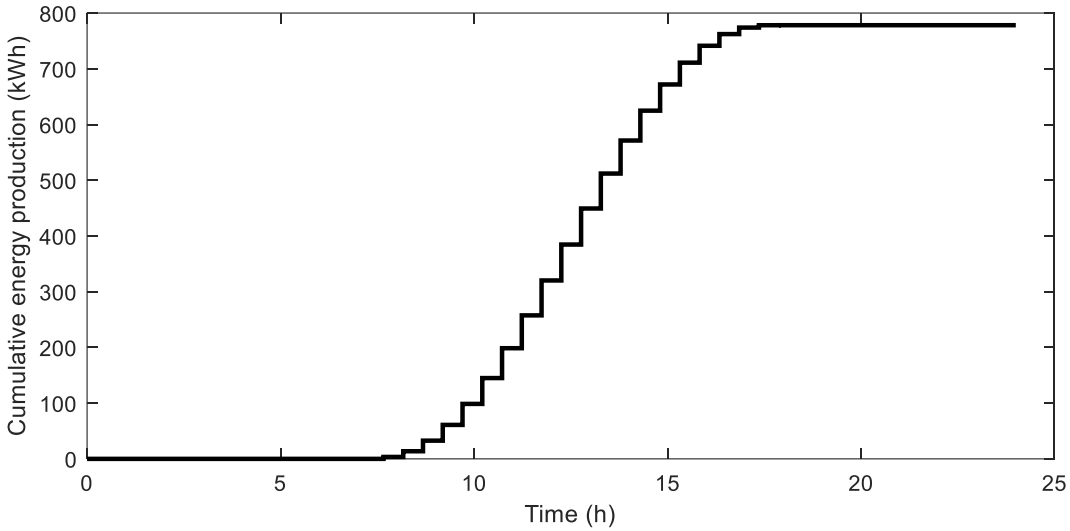

Fig. 4.17: Electrolyser cumulative energy production during winter

4.4.2.2 Summer

From Fig. 4.18, the hydrogen power production of the PEMWE and the switching function, thereof, may be observed. From 00h00 to 06h00, the PEMWE is switched off, due to the absence of electrical energy supplied via the solar PV modules, as seen from Fig. 4.5. The hydrogen power production begins to increase, progressively, to 265.48 kW at 13h00, after which is corresponds to the electrical energy production of the solar PV modules, due to the PEMWE being switched on. From 13h00, the hydrogen power production of the PEMWE begins to decrease, until it is unable to consume electrical energy at 19h30, when the electrical energy produced via the solar PV modules is not available for the remainder of the day. Therefore, meaning that the PEMWE remains switched off during this time period, as seen from Fig. 4.18.

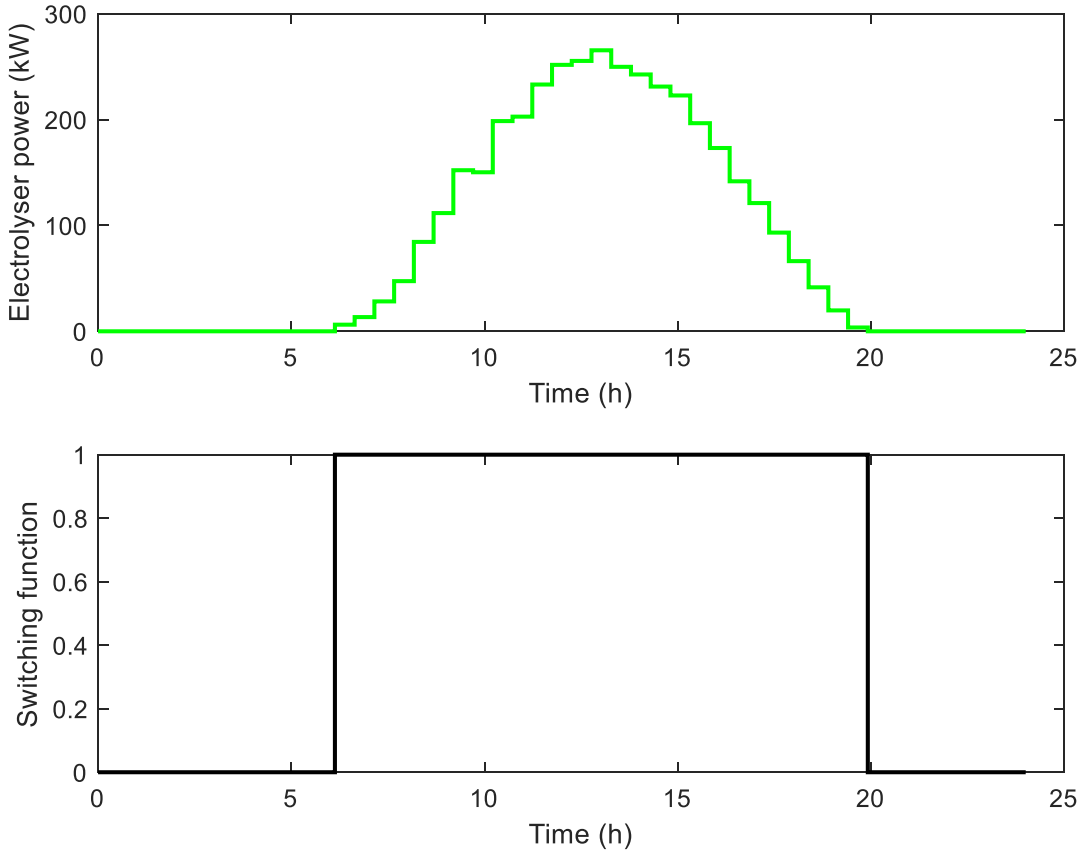

Fig. 4.18: PEM Electrolyser power production and switching function during summer

The hydrogen storage level and the HWST temperature, are illustrated in Fig. 4.19. From 00h00 to 06h00, the hydrogen storage level remains 0 kg, due to the PEMWE not being in operation. From 06h00, the hydrogen storage begins to increase, progressively, until 13h00, which corresponds to the results observed from Fig. 4.18. From 13h00 to 19h30, the increase in the hydrogen storage level, begins to steadily decrease, as observed by the power production of the PEMWE, until the hydrogen storage level reaches 33.54 kg.

From Fig. 4.19, the HWST temperature is initially 60 °C at 00h00, after which it begins to decrease. The HWST temperature decreases until 05h30, due to the significant decrease in the ambient air temperature, as seen from Fig. 2. From 08h00, the HWST temperature begins to increase, which is due to the heat produced by the PEMWE, during hydrogen production. The HWST temperature increases until it reaches a maximum 69.12 °C, at

17h30, after which it begins to decrease. This is due to the significant reduction in the ambient air temperature, which outweighs the much lower heat produced by the PEMWE, during this time period.

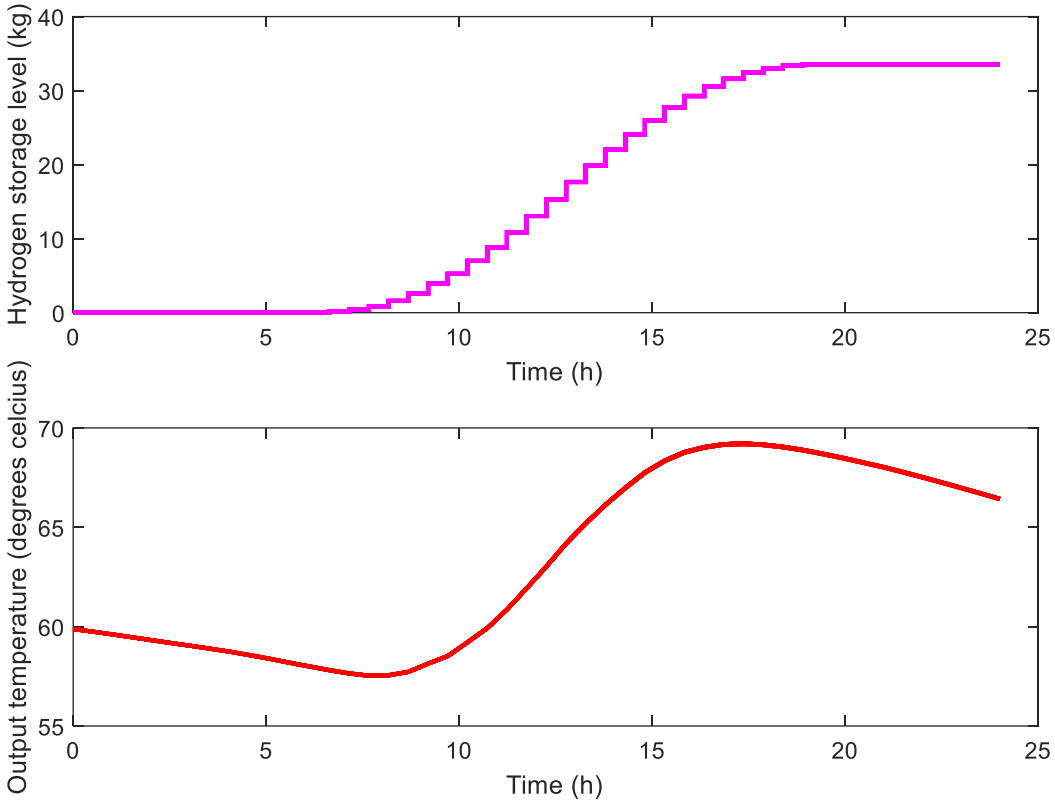

Fig. 4.19: Hydrogen storage level and HWST temperature during summer

In Fig. 4.20, the cumulative thermal energy, recovered by the HWST, is illustrated. Initially, the cumulative heat gain is at zero and decreases until 08h00 to -92 319 kJ, as the thermal energy is lost to the ambient air. After 08:00, the thermal energy gained inside the HWST begins to increase, as the PEMWE is in production of hydrogen, resulting in heat generation. The thermal energy gain increased to a maximum of 347 323 kJ at 17h00. Afterwards, the thermal energy recovery decreased until 24h00, reaching an overall heat gain of 242 354 kJ, which is equivalent to 67.32 kWh.

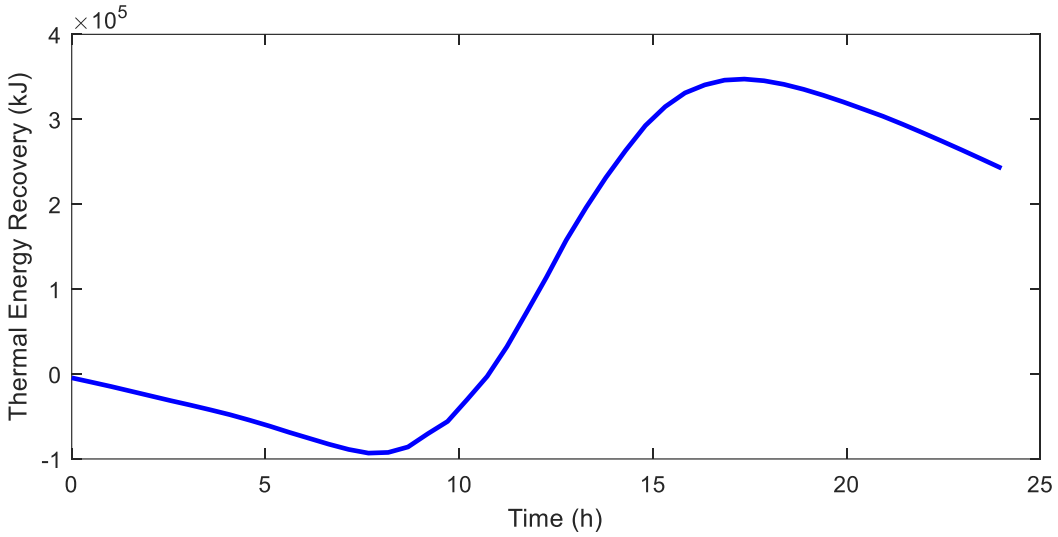

Fig. 4.20: Thermal energy recovery during summer

The cumulative energy production of the PEMWE, is illustrated in Fig. 4.21. From 00h00 to 06h00, the energy consumption is at zero, due to the absence of solar radiation. From 06h00, the PEMWE begins to produce energy, when solar radiation becomes available. It may be observed that the rate of energy production gradually increased until 13h00, which is when the solar radiation peaks, after which the rate begins to gradually decrease, until 19h30, when solar radiation is no longer available for the remainder of the day. The total energy produced by the PEMWE, reached a total of 1 902.36 kWh.

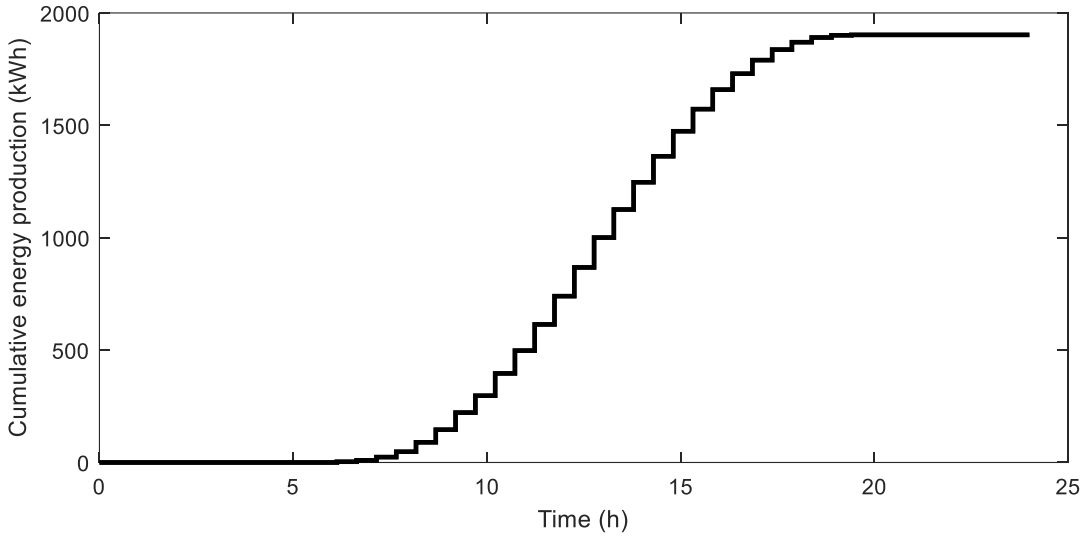

Fig. 4.21: Electrolyser cumulative energy production during summer

4.5 CONCLUSIONS AND RECOMMENDATIONS

In this chapter, relevant and recent literature was used, to evaluate the optimal switching control technique. The optimal switching control of the PEMWE water heating system, was firstly mathematically modelled, and the multi-objective function with the associated constraints of the system, was thereafter outlined in Section 4.2. The simulations, which were conducted in this study, used accurate and actual data, purely for the effectiveness and accuracy, thereof.

The optimal switching control of the PEMWE was compared against a standard PEMWE system, to evaluate the proposed model. The simulation results of the proposed optimal switching control model, yielded the PEMWE produced 778.19 kWh of energy during winter, which corresponds to 13.72 kg of hydrogen production. However, during summer, the PEMWE produced 1 902.36 kWh which corresponds to 33.54 kg of hydrogen. Most importantly, a daily maximum of 67.32 kWh of thermal energy was recovered during summer, by absorbing the maximum amount of thermal energy, generated during the electrolysis process and transferring it to the HWST.

The standard PEMWE system (baseline) without any cooling, produced 801.24 kWh of energy during winter, which corresponds to 13.98 kg of hydrogen. However, the standard PEMWE system produced 1 965.74 kWh during summer, which corresponds to 34.31 kg of hydrogen.

The simulation results revealed that, by removing the generated heat from the PEMWE, which were generated during the electrolysis process, could slightly decrease the energy production of the PEMWE, resulting in slightly less hydrogen being produced. In contrary, when the PEMWE retained the generated heat, slightly higher energy could be produced, which could result in a slightly higher hydrogen production, compared to the optimal control model. However, the main objective of this proposed model, was to recover the maximum amount of available thermal energy, compromising a slight reduction in the amount of hydrogen production.

Furthermore, by recovering the generated heat from the PEMWE, the time period for the membrane to degrade to a thickness of 50 %, could be prolonged by 1.02 years, by means of the interpolation of the simulation results, obtained from Reference [106]. Therefore, when the membrane goes beyond 50 %, the membrane degradation occurs non-linearly.

The main aim of this study, was to develop an optimal switching control technique of a PEMWE system, to recover the maximum amount of thermal energy from the process, where further research may be conducted on obtaining an optimal mass flow rate at each sampling interval, may be used instead of the current proposed optimal switching control technique.

Further research may further be conducted on more advanced control techniques, such as MPC, which has the ability to adapt to any changes to its external environment.

CHAPTER V: OPTIMAL ELECTRICAL AND THERMAL ENERGY MANAGEMENT OF A RESIDENTIAL ENERGY HUB INTEGRATING RENEWABLE ENERGY, DEMAND RESPONSE AND ENERGY STORAGE SYSTEM

5.1 INTRODUCTION

In residential buildings space heating (SH), space cooling (SC) and water heating, account for approximately 61.2 % [2] of the total energy consumption, which highlights the requirement to investigate methods of improving the efficiency, thereof. Therefore, in this chapter, a mathematical model for an optimal heat recovery and power dispatch of hybrid renewable energy system, connected to space heating and water heating systems in large residential buildings, is presented.

Hydrogen may be seen as a possible alternative fuel, which may be produced from renewable energy, as mentioned and a promising contender in the energy storage domain. Furthermore, hydrogen is regarded as a clean fuel, as the product of the chemical reaction is water (H_2O) and heat as the by-product [103]. An electrolyser harnesses the energy produced by the RER, in this specific case, the solar PV modules, to produce hydrogen, which may be stored in its current form, to be used by a fuel cell to generate electrical energy. The electrical energy generated by the fuel cell, may be supplied primarily to the space heating, space cooling and water heating equipment [104], to reduce the energy consumption from the electrical grid and the energy cost during the peak pricing regions of the TOU tariff structure. Furthermore, the heat generated from the solar PV modules, PEMWE and PEMFC, may be recovered, by transferring the generated heat to a HWST, which could reduce the burden on the air-to-water heat pump, to maintain the hot water demand.

The main objective of the proposed system, is to propose a comprehensive optimal control strategy of a residential energy hub, forming part of a hybrid renewable energy micro-grid system connected to the utility grid, which may maximize the heat recovery from the PEMWE and PEMFC by the HWST, whilst maximizing the electrical energy supplied from the solar PV modules to the electrical load. Thirdly, the operating energy cost of the utility grid, may further be minimized, from a power dispatch perspective. The final additional contribution, may be the optimal control model, which may further yield a prolonged membrane lifespan of the PEMWE and PEMFC, by controlling its operating temperature, which are two of the highest cost items in this type of system [106].

The development of the mathematical model is outlined in Section 5.2, whilst the case study is discussed in Section 5.3. The simulation results are presented in Section 5.4. In Section 5.5, the economic analysis is discussed and, lastly, in Section 5.6, the chapter is concluded.

5.2 METHODOLOGY

5.2.1 Dynamic model of residential energy hub integrating renewable energy, demand response and energy storage system

The proposed residential energy hub, integrated with renewable energy and the utility grid, is illustrated in Fig. 5.1.

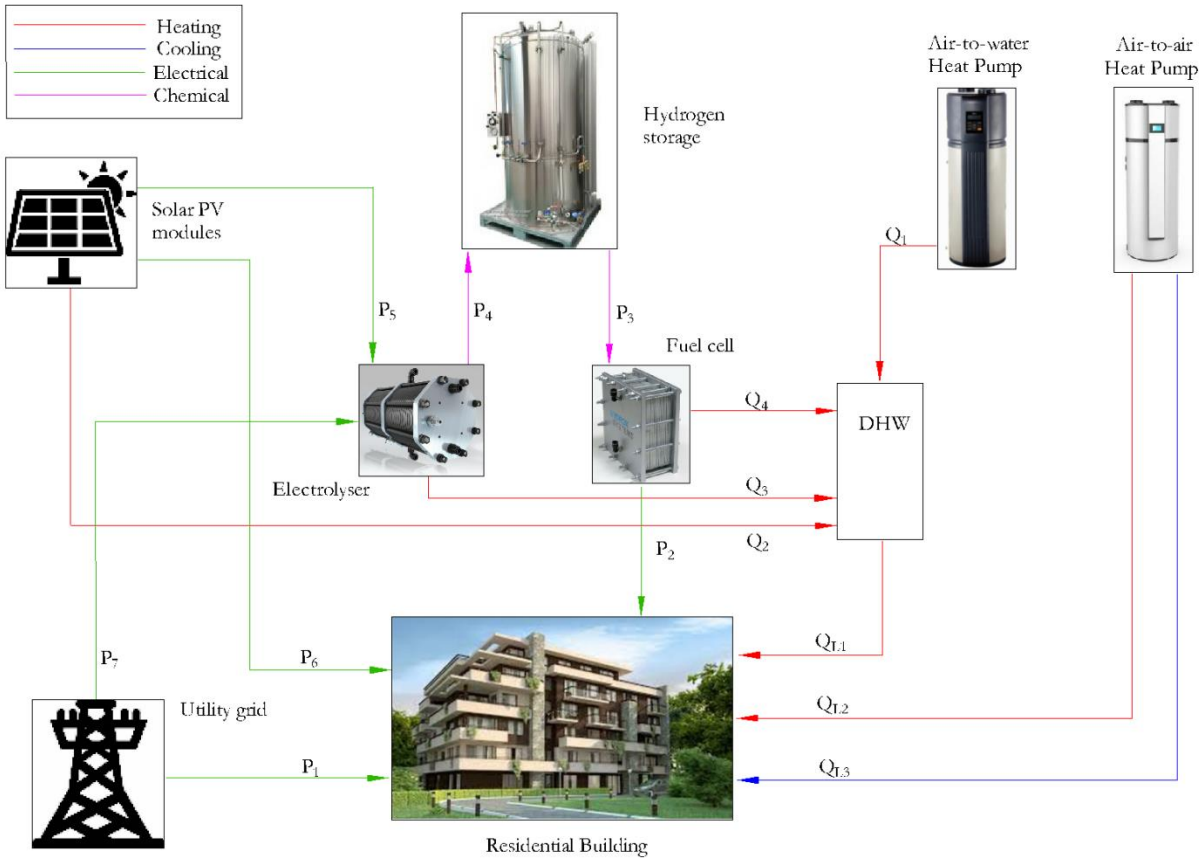

Fig. 5.1: Schematic of the proposed residential energy hub integrated with renewable energy

The PEMWE utilizes solar PV energy and the utility grid, to generate hydrogen, which is stored in a hydrogen storage tank. The hydrogen storage tank supplies hydrogen to the PEMFC. The PEMFC, solar PV modules and the utility grid, are supplied the load. The air-to-air heat pump and the air-to-water heat pump are supplied by both the utility grid and the integrated renewable energy system. When H_2 is generated, it is stored in the hydrogen storage tank and is ideally utilized by the PEMFC, during the high-cost regions of the TOU tariff structure, under which the utility grid is confined to. The electrical power flows and thermal energy flows, presented in Fig. 2, are defined as follows:

- P_1: Electrical power supplied to the load from the utility grid;

- P_2: Electrical power supplied from the PEMFC to the load;
- P_3: Hydrogen power supplied to PEMFC from hydrogen storage tank;
- P_4: Hydrogen power supplied to hydrogen storage tank from PEMWE;
- P_5: Electrical power supplied to the PEMWE from PV modules;
- P_6: Electrical power supplied to the load from PV modules;
- P_7: Electrical power supplied to the PEMWE from the utility grid;
- Q_1: Thermal energy supplied to the HWST from the air-to-water heat pump;
- Q_2: Thermal energy supplied to the HWST from the solar PV modules;
- Q_3: Thermal energy supplied to the HWST from the PEMWE;
- Q_4: Thermal energy supplied to the HWST from the PEMFC;
- Q_{L1}: Hot water supplied to the load;
- Q_{L2}: Heated air supplied to the load;
- Q_{L3}: Cooled air supplied to the load.

5.2.2 Sub-models

5.2.2.1 Hot water storage tank temperature

The first law of thermodynamics is applied to the circulation fluid storage tank, to obtain the energy balance in the tank. The following equation describes the change in the internal energy (energy within HWST), which relates to the difference in heat entering and leaving the HWST. Eq. (5.1) describes the energy balance equation derived from change in internal energy within the HWST. Q_1 is the input heat from the air-to-water heat pump to the HWST, Q_2 is the heat recovered from the solar PV modules, Q_3 is the heat recovered from the PEMWE, as discussed in Chapter 4 and Q_4 is the heat recovered from the PEMFC, similar to Q_4. Q_{L1} is the heat removed from the tank to the load, Q_{CW} is the heat removed from the tank through the addition of cold water at a flow rate of $\dot{M}_B$ and Q_{LOSS} is the heat

lost in the tank, due to its thermal properties. The heat losses, due to the connecting pipes, are neglegted [60]:

$$M.C.\frac{dT_S}{dt} = Q_1 + Q_2 + Q_3 + Q_4 - Q_{L1} + Q_{CW} - Q_{LOSS} \tag{5.1}$$

The useful heat gain inside the HWST is described in Eq. (5.2). V_W is the volumetric flow rate of the circulation fluid, which is water in this case. ϱ_W is the density of water, $T_{W,O}$ and $T_{W,I}$ are the outlet and inlet temperatures of the air-to-water heat pump.

$$Q_1 = V_w.\rho_w.C.(T_{W,O} - T_{W,I}) \tag{5.2}$$

The heat recovered from the solar PV modules is described in Eq. (5.3), which is the heat transfer from the solar PV modules to the HWST. $\dot{M}_W$ is the mass flow rate of the circulation fluid, C is the specific heat capacity of the circulation fluid, $T_{P,O}$ and $T_{P,I}$ are the outlet and inlet temperatures of the solar PV modules, respectively.

$$Q_2 = \dot{M}_W.C.(T_{P,O} - T_{P,I}) \tag{5.3}$$

The heat recovered from the PEMWE is described in Eq. (5.4), which is the heat transfer from the PEMFC to the HWST. $\dot{M}_W$ is the mass flow rate of the circulation fluid, $T_{E,O}$ and $T_{E,I}$ are the outlet and inlet temperatures of the PEMWE, respectively.

$$Q_3 = \dot{M}_W.C.(T_{E,O} - T_{E,I}) \tag{5.4}$$

The heat recovered from the PEMFC is described in Eq. (5.5), which is the heat transfer from the PEMFC to the HWST. $\dot{M}_W$ is the mass flow rate of the circulation fluid, $T_{F,O}$ and $T_{F,I}$ are the outlet and inlet temperatures of the PEMFC, respectively.

$$Q_4 = \dot{M}_W.C.(T_{F,O} - T_{F,I}) \tag{5.5}$$

The heat transfer from the HWST to the load, is defined in Eq. (5.6). $\dot{M}_B$ is the mass flow rate of the circulation fluid at the load (consumer) and $T_{D,O}$ is the demand outlet water temperature at the consumer's side. The heat removed from the tank through the addition of cold water at a flow rate of $\dot{M}_B$, is described in Eq. (5.7), where $T_{D,I}$ is the demand inlet water temperature, at the supply side.

$$Q_{L1} = \dot{M}_B.C.T_{D,O} \tag{5.6}$$

$$Q_{CW} = \dot{M}_B.C.T_{D,I} \tag{5.7}$$

The heat losses in the tank, due to its thermal properties are stated in Eq. (5.8). T_S is the temperature within the HWST, T_a is ambient air temperature, A_S is the surface area of the HWST, Δx is the thickness of the selected insulation layer, K is the thermal conductivity coefficient of the selected material and h is the heat transfer coefficient of the surface of the tank.

$$Q_{LOSS} = \frac{(T_s - T_a).A_s}{\frac{\Delta x}{K} + \frac{1}{h}} \tag{5.8}$$

Where: $\beta = \frac{A_s}{\frac{\Delta x}{K} + \frac{1}{h}}$ (5.9)

By substituting Eqs. (5.2), (5.3), (5.4), (5.5), (5.6), (5.7), (5.8) and (5.9), into Eq. (5.1), yields Eq (5.10):

$$M.C.\frac{dT_s}{dt} = V_W.\rho_W.C.(T_{W,O} - T_{W,I}) + \dot{M}_W.C.(T_{P,O} - T_{P,I}) + \dot{M}_E.C.\left(T_{E,O} - T_{E,I}\right) + \dot{M}_W.C.(T_{F,O} - T_{F,I}) - \dot{M}_B.C.T_{D,O} + \dot{M}_B.C.T_{D,I} - \beta.\left(T_s - T_a\right) \quad (5.10)$$

The COP, of an air-to-water heat pump, is calculated, by making use of Eq. (5.11) [90]. P_W is the rated power of the air-to-water heat pump.

$$COP = \frac{Q_{IN}}{P_W} \quad (5.11)$$

Combining Eq. (5.11) and Eq. (5.2), yield:

$$P_W.COP = V_W.\rho_W.C.(T_{W,O} - T_{W,I}) \quad (5.12)$$

Eq. (5.12), may be re-written as follows:

$$(T_{W,O} - T_{W,O}) = \frac{P_W.COP}{V_W.\rho_W.C} \quad (5.13)$$

Eq. (5.14), obtained from Siecker et al [61], is used to illustrate the heat generated from the solar PV modules to the HWST. A_c is the area of the collector, Fr is the collector heat removal factor, τ and a_P are the transmittance and absorbance factors, G is the global irradiance and U_l is the collector overall heat loss coefficient.

$$(T_{P,O} - T_{P,O}) = \frac{A_C.F_R.\tau.\alpha_P.G}{\dot{M}_W.C + A_C.F_R.U_L} \quad (5.14)$$

Eq. (5.15), obtained from Siecker et al [120], as well as Section 4.2.2, describes the generated heat from the PEMWE to the HWST.

$$T_{E,O} - T_{E,I} = \frac{\frac{I_E . J . t_{mem}}{\sigma_{mem}}}{\dot{M}_W . C - \left(\frac{\alpha_a + \alpha_c}{\alpha_a . \alpha_c} \right) . \frac{R . I_E}{2 . F} . ln\left(\frac{J}{J_O} \right) - \frac{R . I_E}{2 . F} . ln\left(\frac{1 + \frac{1}{J_L}}{1 - \frac{1}{J_L}} \right)} \quad (5.15)$$

Eq. (5.16), obtained from Siecker et al [120], as well as Section 4.2.2, describes the generated heat from the PEMFC to the HWST.

$$T_{F,O} - T_{F,I} = \frac{\frac{I_F . J . t_{mem}}{\sigma_{mem}}}{\dot{M}_W . C - \left(\frac{\alpha_a + \alpha_c}{\alpha_a . \alpha_c} \right) . \frac{R . I_F}{2 . F} . ln\left(\frac{J}{J_O} \right) - \frac{R . I_F}{2 . F} . ln\left(\frac{1 + \frac{1}{J_L}}{1 - \frac{1}{J_L}} \right)} \quad (5.16)$$

By substituting Eqs. (5.13), (5.14), (5.15) and (5.16), into Eq. (5.10), yields Eq (5.17):

$$M.C.\frac{dT_s}{dt} = V_W.\rho_W.C.\left(\frac{P_W.COP}{V_W.\rho_W.C}\right) + \dot{M}_W.C.\left(\frac{A_C.F_R.\tau.\alpha_P.G}{\dot{M}_W.C + A_C.F_R.U_L}\right) +$$

$$\dot{M}_W.C.\left(\dot{M}_E.C.\frac{\frac{I_E.J.t_{mem}}{\sigma_{mem}}}{\dot{M}_W.C - \left(\frac{\alpha_a+\alpha_c}{\alpha_a.\alpha_c}\right).\frac{R.I_E}{2.F}.ln\left(\frac{J}{J_O}\right) - \frac{R.I_E}{2.F}.ln\left(\frac{1+\frac{1}{J_L}}{1-\frac{1}{J_L}}\right)}\right) +$$

$$\dot{M}_W.C.\left(\dot{M}_W.C.\frac{\frac{I_F.J.t_{mem}}{\sigma_{mem}}}{\dot{M}_W.C - \left(\frac{\alpha_a+\alpha_c}{\alpha_a.\alpha_c}\right).\frac{R.I_F}{2.F}.ln\left(\frac{J}{J_O}\right) - \frac{R.I_F}{2.F}.ln\left(\frac{1+\frac{1}{J_L}}{1-\frac{1}{J_L}}\right)}\right)$$

$$-\dot{M}_B.C.T_{D,O} + \dot{M}_B.C.T_{D,I} - \beta.\left(T_s - T_a\right) \qquad (5.17)$$

It could be assumed that temperature of the water to the load, is equal to the temperature inside the storage tank, that is $T_{D,O} = T_s$. Furthermore, some like-terms are cancelled out.

$$M.C.\frac{dT_s}{dt} = P_W.COP + \dot{M}_W.C.\left(\frac{A_C.F_R.\tau.\alpha_p.G}{\dot{M}_W.C + A_C.F_R.U_L}\right) +$$

$$\dot{M}_W.C.\left(\dot{M}_E.C.\frac{\frac{I_E.J.t_{mem}}{\sigma_{mem}}}{\dot{M}_W.C - \left(\frac{\alpha_a + \alpha_c}{\alpha_a.\alpha_c}\right).\frac{R.I_E}{2.F}.ln\left(\frac{J}{J_O}\right) - \frac{R.I_E}{2.F}.ln\left(\frac{1+\frac{1}{J_L}}{1-\frac{1}{J_L}}\right)}\right) +$$

$$\dot{M}_W.C.\left(\dot{M}_W.C.\frac{\frac{I_F.J.t_{mem}}{\sigma_{mem}}}{\dot{M}_W.C - \left(\frac{\alpha_a + \alpha_c}{\alpha_a.\alpha_c}\right).\frac{R.I_F}{2.F}.ln\left(\frac{J}{J_O}\right) - \frac{R.I_F}{2.F}.ln\left(\frac{1+\frac{1}{J_L}}{1-\frac{1}{J_L}}\right)}\right) \qquad (5.18)$$

$$-\dot{M}_B.C.T_s + \dot{M}_B.C.T_{D,I} - \beta.T_s + \beta.T_a$$

Factoring out more like-terms, yield Eq. (5.19).

$$M.C.\frac{dT_s}{dt} = P_W.COP + \dot{M}_W.C.\left(\frac{A_C.F_R.\tau.\alpha_p.G}{\dot{M}_W.C + A_C.F_R.U_L}\right) +$$
$$\dot{M}_W.C.\left(\dot{M}_E.C.\frac{\frac{I_E.J.t_{mem}}{\sigma_{mem}}}{\dot{M}_W.C - \left(\frac{\alpha_a+\alpha_c}{\alpha_a.\alpha_c}\right).\frac{R.I_E}{2.F}.ln\left(\frac{J}{J_O}\right) - \frac{R.I_E}{2.F}.ln\left(\frac{1+\frac{1}{J_L}}{1-\frac{1}{J_L}}\right)}\right) +$$
$$\dot{M}_W.C.\left(\dot{M}_W.C.\frac{\frac{I_F.J.t_{mem}}{\sigma_{mem}}}{\dot{M}_W.C - \left(\frac{\alpha_a+\alpha_c}{\alpha_a.\alpha_c}\right).\frac{R.I_F}{2.F}.ln\left(\frac{J}{J_O}\right) - \frac{R.I_F}{2.F}.ln\left(\frac{1+\frac{1}{J_L}}{1-\frac{1}{J_L}}\right)}\right)$$
$$-T_s\left(\dot{M}_B.C+\beta\right)+T_{D,I}\left(\dot{M}_B.C\right)+T_a\left(\beta\right) \qquad (5.19)$$

Dividing both sides of the expression, with the product of *M.C*, with the result, is illustrated in Eq. (5.20).

$$\frac{dT_s}{dt}=\left(\frac{P_W.COP}{M.C}\right)+\frac{\dot{M}_W}{M}.\left(\frac{A_C.F_R.\tau.\alpha_P.G}{\dot{M}_W.C+A_C.F_R.U_L}\right)+$$

$$\frac{\dot{M}_W}{M}.\left(\dot{M}_E.C.\frac{\frac{I_E.J.t_{mem}}{\sigma_{mem}}}{\dot{M}_W.C-\left(\frac{\alpha_a+\alpha_c}{\alpha_a.\alpha_c}\right).\frac{R.I_E}{2.F}.ln\left(\frac{J}{J_O}\right)-\frac{R.I_E}{2.F}.ln\left(\frac{1+\frac{1}{J_L}}{1-\frac{1}{J_L}}\right)}\right)+$$

$$\frac{\dot{M}_W}{M}.\left(\dot{M}_W.C.\frac{\frac{I_F.J.t_{mem}}{\sigma_{mem}}}{\dot{M}_W.C-\left(\frac{\alpha_a+\alpha_c}{\alpha_a.\alpha_c}\right).\frac{R.I_F}{2.F}.ln\left(\frac{J}{J_O}\right)-\frac{R.I_F}{2.F}.ln\left(\frac{1+\frac{1}{J_L}}{1-\frac{1}{J_L}}\right)}\right)$$

$$-T_s\left(\frac{\dot{M}_B.C+\beta}{M.C}\right)+T_{D,I}\left(\frac{\dot{M}_B.}{M}\right)+T_a\left(\frac{\beta}{M.C}\right) \qquad (5.20)$$

The general state space representation, illustrated in Eq. (3.12), Section 3.2.2, is applied to the proposed model. $\dot{\mathrm{X}}(t)$, the state variable, is the temperature of the HWST, A is known as the state matrix, B is the input matrix and α is the disturbances to the system.

Then, applying Eq. (3.12), in Section 3.2.2, to Eq. (5.20), yields:

$$\dot{T}(t)=\left(\frac{P_W.COP}{M.C}\right).U(t)+T_s(t).\left(\frac{\dot{M}_B.C+\beta}{M.C}\right)+T_{D,I}\left(\frac{\dot{M}_B}{M}\right)+T_a\left(\frac{\beta}{M.C}\right)$$
$$+\frac{\dot{M}_W}{M}.\left(\frac{A_C.F_R.\tau.\alpha_P.G}{\dot{M}_W.C+A_C.F_R.U_L}\right)+$$
$$\frac{\dot{M}_W}{M}.\left(\dot{M}_E.C.\frac{\frac{I_E.J.t_{mem}}{\sigma_{mem}}}{\dot{M}_W.C-\left(\frac{\alpha_a+\alpha_c}{\alpha_a.\alpha_c}\right).\frac{R.I_E}{2.F}.ln\left(\frac{J}{J_O}\right)-\frac{R.I_E}{2.F}.ln\left(\frac{1+\frac{1}{J_L}}{1-\frac{1}{J_L}}\right)}\right)+$$
$$\frac{\dot{M}_W}{M}.\left(\dot{M}_W.C.\frac{\frac{I_F.J.t_{mem}}{\sigma_{mem}}}{\dot{M}_W.C-\left(\frac{\alpha_a+\alpha_c}{\alpha_a.\alpha_c}\right).\frac{R.I_F}{2.F}.ln\left(\frac{J}{J_O}\right)-\frac{R.I_F}{2.F}.ln\left(\frac{1+\frac{1}{J_L}}{1-\frac{1}{J_L}}\right)}\right) \quad (5.21)$$

The state matrix, A, is stated in Eq. (5.22), *B*, the input matrix, is illustrated in Eq. (5.23) and α, the disturbances to the system, is stated in Eq. (5.24).

$$A=-\left(\frac{\dot{M}_B.C+\beta}{M.C}\right) \quad (5.22)$$

$$B=\left(\frac{P_W.COP}{M.C}\right) \quad (5.23)$$

$$\alpha = T_{D,I}\left(\frac{\dot{M}_B}{M}\right) + T_a\left(\frac{\beta}{M.C}\right) + \frac{\dot{M}_W}{M}.\left(\frac{A_C.F_R.\tau.\alpha_P.G}{\dot{M}_W.C + A_C.F_R.U_L}\right) +$$

$$\frac{\dot{M}_W}{M}.\left(\dot{M}_E.C.\frac{\frac{I_E.J.t_{mem}}{\sigma_{mem}}}{\dot{M}_W.C - \left(\frac{\alpha_a+\alpha_c}{\alpha_a.\alpha_c}\right).\frac{R.I_E}{2.F}.ln\left(\frac{J}{J_O}\right) - \frac{R.I_E}{2.F}.ln\left(\frac{1+\frac{1}{J_L}}{1-\frac{1}{J_L}}\right)}\right) +$$

$$\frac{\dot{M}_W}{M}.\left(\dot{M}_W.C.\frac{\frac{I_F.J.t_{mem}}{\sigma_{mem}}}{\dot{M}_W.C - \left(\frac{\alpha_a+\alpha_c}{\alpha_a.\alpha_c}\right).\frac{R.I_F}{2.F}.ln\left(\frac{J}{J_O}\right) - \frac{R.I_F}{2.F}.ln\left(\frac{1+\frac{1}{J_L}}{1-\frac{1}{J_L}}\right)}\right) \quad (5.24)$$

So that the final state space equation may be written as in Eq. (5.25).

$$\dot{T}(t) = A(t).Ts(t) + B(t).U(t) + \alpha(t) \quad (5.25)$$

5.2.2.2 Residential building temperature

Please refer to what was developed in Chapter III, sub-section 3.2.2.

5.2.2.3 Hydrogen storage

The hydrogen storage dynamics, E_{H2}, is illustrated in Eq. (5.26), which is essentially the difference between the hydrogen power supplied to the hydrogen storage tank, from the PEM electrolyser, P_4 and the hydrogen power supplied from the hydrogen storage tank to

the PEM fuel cell, P_3. The PEM electrolyser receives electrical energy directly from the solar PV modules. η_{EL} is the efficiency of the PEM electrolyser and η_{FC} is the efficiency of the PEM fuel cell.

$$E_{H_2} = \eta_{EL}.P_4 - \frac{1}{\eta_{FC}}.P_3 \tag{5.26}$$

The mass of the hydrogen stored at any given moment, is expressed in Eq. (5.27). HHV_H, is the higher heating value of hydrogen [73].

$$M_{H_2} = \frac{E_{H_2}}{HHV_H} \tag{5.27}$$

5.2.2.4 Utility grid power

The utility grid power, P_1 may supply the load, whenever the PEM fuel cell power, P_2 used in the renewable energy micro-grid and the solar PV power, P_6, are incapable of performing the task. During this study, the model is subjected to the TOU tariff structure, from the main electrical power supplier, Eskom. The pricing of the TOU tariff structure is denoted as $\varrho(t)$, which may be sub-categorized as off-peak $\varrho(op)$, standard $\varrho(s)$ and peak $\varrho(p)$.

5.2.2.5 Power balance

The power balance at the load (P_{load}), is expressed in Eq. (5.28), which includes the power from the utility grid, PEMFC and solar PV modules.

$$P_{load} = P_1 + P_2 + P_6 \tag{5.28}$$

5.2.3 Discrete sub-models formulation

5.2.3.1 Discrete residential building temperature

Refer to Eq. (3.22), developed in Chapter III, sub-section 3.2.3.

5.2.3.2 Discrete hot water storage tank temperature

Furthermore, refer to Eq. (3.22) developed in Chapter III, sub-section 3.2.3, used and applied to the proposed water heating sub-model.

5.2.3.3 Discrete hydrogen storage level

The discretized expression of Eq. (5.26), in terms of the k^{th} hydrogen storage level, is illustrated in Eq. (5.29). t_s is known as the sampling time.

$$M_{H_2}(k+1) = M_{H_2}(k) + \eta_{EL}.t_s.P_4(k) - \frac{t_s}{\eta_{FC}}.P_3(k) \tag{5.29}$$

The state variable, known as $M_{H2}(k+1)$, should be expressed in terms of its initial value, $M_{H2}(0)$, is derived as follows:

$$M_{H_2}(1) = M_{H_2}(0) + \eta_{EL}.t_s.P_4(0) - \frac{t_s}{\eta_{FC}}.P_3(0);$$

$$M_{H_2}(2) = M_{H_2}(1) + \eta_{EL}.t_s.P_4(1) - \frac{t_s}{\eta_{FC}}.P_3(1);$$

$$M_{H_2}(3) = M_{H_2}(2) + \eta_{EL}.t_s.P_4(2) - \frac{t_s}{\eta_{FC}}.P_3(2).$$

The general discretized hydrogen storage level is illustrated as follows:

$$M_{H_2}(k+1) = M_{H_2}(0) + \eta_{EL}.t_s.\sum_{k=1}^{N} P_4(k) - \frac{t_s}{\eta_{FC}}.\sum_{k=1}^{N} P_3(k) \tag{5.30}$$

5.2.4 Objective function

The first objective, f_1, of the proposed optimal control model, is to minimize the daily operational energy cost of the utility grid, resulting from the various power flows, by taking the TOU tariff structure into account, illustrated in Eq. (5.31). ρ_c is the electricity pricing tariff, P_1 is the electrical power supplied to the load by the utility grid, P_7 is the electrical power supplied to the PEMWE by the utility grid and t_s is the sampling time.

$$f_1 = \sum_{k=1}^{N} [\rho_C (P_1(k) + P_7(k))].t_s \tag{5.31}$$

The second objective is to maximize the electrical energy supplied from the solar PV modules to the electrical load, which is depicted in Eq. (5.32):

$$f_2 = \sum_{k=1}^{N} [(P_6(k)].t_s \tag{5.32}$$

The thermal comfort level of the consumer is addressed, where the difference between the output temperature $T_W(k)$ of the HWST temperature and the desired temperature $F_W(k)$, should not be excessive. That is, the value of $(T_W(k)-F_W(k))^2$, should be minimized. The function f_3, in Eq. (5.33), denotes the thermal discomfort level, which is the third objective function to be minimized [105]:

$$f_3 = \sum_{k=1}^{N} \left[(T_W(k) + F_W(k))^2 \right].t_s \tag{5.33}$$

The same principle is applied for the space heating and space cooling of the residential building. Therefore, the thermal comfort level of the consumer is addressed, where the difference between the output temperature $T_B(k)$, of the HWST temperature and the desired temperature $F_B(k)$, should not be excessive. That is, the value of $(T_B(k)-F_B(k))^2$ should be minimized. The function f_4 in Eq. (5.34), denotes the thermal discomfort level, which is the fourth and last objective function to be minimized [105]:

$$f_4 = \sum_{k=1}^{N} \left[(T_B(k) + F_B(k))^2 \right] . t_s \tag{5.34}$$

The final multi-objective function, is shown in Eq. (5.35), which contains the minimization of the operating energy cost from the utility grid, the maximization of the electrical power produced by the PEM fuel cell and the minimization of the level of discomfort of the HWST temperature.

$$f = \min \left(W_1 . f_1 - W_2 . f_2 + W_3 . f_3 + W_4 . f \right)_4 \tag{5.35}$$

Where: W_1 is the weighting factor for the first objective, W_2 is the weighting factor for the second objective, W_3 is the weighting factor for the third objective and W_4 is the weighting factor for the fourth objective.

5.2.5 Variable constraints

5.2.5.1 Equality constraints

5.2.5.1 a) Load power balance

The variables, which are involved in supplying power to the load, are depicted in the load power balance expression, as illustrated in Eq. (5.36). The power from the utility grid to the load, is P_1, P_2, as defined previously, is the power from the PEMFC to the load and, P_6, is the power from the solar PV modules to the load.

$$P_1(k) + P_2(k) + P_6(k) = P_{load}(k) \tag{5.36}$$

5.2.5.1 b) Electrolyser power balance

The variables which are involved in supplying power to the PEMWE, are depicted in the electrolyser power balance expression, as illustrated in Eq. (5.37). The power from the utility grid to the PEMWE, is P_7, P_5, the power from the solar PV modules to the PEMWE, P_4, which is the hydrogen power from the PEMWE to the hydrogen storage tank and, $P_{EL}{}^{max}$, is the maximum acceptable power supplied to the PEMWE.

$$P_5(k) + P_7(k) - P_4(k) = P_{EL}{}^{\max}(k) \tag{5.37}$$

5.2.5.2 Inequality constraints

5.2.5.2 a) Hydrogen storage

The hydrogen storage dynamics, are depicted in Eq. (5.38), with the minimum and maximum boundary constraints. $M_{H2}(0)$ is the initial mass within the hydrogen storage tank.

$M_{H2}{}^{min}$ is the minimum allowable limit of the hydrogen storage level and, $M_{H2}{}^{max}$, is the maximum allowable limit of the hydrogen storage level. η_{EL} and η_{FC} is the efficiency of the PEMWE and the PEMFC, respectively. HHV_H is the higher heating value of hydrogen, which is 39.7 kWh/kg [73].

$$M_{H_2}{}^{min}(k) \le M_{H_2}(0) + \eta_{EL}.t_s.\sum_{k=1}^{N}\frac{P_4(k)}{HHV_{H_2}} - \frac{t_s}{\eta_{FC}}.\sum_{k=1}^{N}\frac{P_2(k)}{HHV_H} \le M_{H_2}{}^{max}(k) \tag{5.38}$$

5.2.5.2 b) Utility grid

The sum of the power from the utility grid, P_1 to the load and the power from the utility grid to the PEMWE, P_7, should be less than or equal to the maximum power supplied from the utility grid, as illustrated in Eq. (5.39):

$$P_1(k) + P_7(k) = P_G{}^{max}(k) \tag{5.39}$$

5.2.5.2 c) Solar PV power

The sum of the power from the solar PV modules to the load, P_6 and the power to the PEMWE, P_5, should be less than or equal to the maximum power supplied from the solar PV modules, as illustrated in Eq. (5.40):

$$P_5(k) + P_6(k) \le P_{PV}{}^{max}(k) \tag{5.40}$$

5.2.5.3 Control variable limits

The limits of each control variable are implemented, as a safety precautionary measure to protect each of the equipment from unwanted damage. These limits consist of a minimum

lower boundary limit and a maximum upper boundary limit. The first control variable limit, is P_1, which is the safe limit set for the utility grid, as illustrated in Eq. (5.41):

$$0 \leq P_1 \leq P_1^{max} \tag{5.41}$$

The second control variable limit is P_2 which is the safe limits set for the PEM fuel cell, as illustrated in Eq. (5.42):

$$0 \leq P_2 \leq P_2^{max} \tag{5.42}$$

5.2.5.4 Solar PV electrical power production

The production of electrical energy from solar PV modules, is calculated in Eq. (5.43). $P_{PV,STC}$ rated power of a solar PV module, under standard test conditions, N_{PVP} is the number of solar PV modules connected in parallel, N_{PVS} is the number of solar PV modules connected in series, G is the global solar irradiance, γ is known as the power temperature coefficient and Tj is known as the temperature of the solar PV module [3].

$$P_{PV} = P_{PV,STC} N_{PV_P} N_{PV_S} \frac{G(k)}{1000}\left[1-\alpha(T_j(k)-25)\right] \tag{5.43}$$

The temperature of the solar PV modules, is described, using Eq. (5.44). T_{NOC} is known as the nominal operating cell temperature of a solar PV module [121].

$$T_j = T_a + \frac{G(k)}{800}\left(T_{NOC} - 20\right) \tag{5.44}$$

5.2.5.5 Exclusive power flows

Hydrogen power supplied from the PEMWE to the hydrogen storage tank and the hydrogen power supplied from the hydrogen storage tank to the PEMFC, are unable to occur simultaneously, as the flow of hydrogen power is solely limited to one direction, illustrated in Eq. (5.45). Furthermore, the same principle should be applied to the PEMWE to ensure that power flows solely in one direction. Therefore, the product of the hydrogen power from the PEMWE, and the sum of the input power to the PEMWE, which is P_5 and P_7, should be zero, as depicted in Eq. (5.46).

$$P_3(k) \times P_4(k) = 0 \tag{5.45}$$

$$\left(P_5(k) + P_7(k)\right) \times P_4(k) = 0 \tag{5.46}$$

5.2.5.6 Fixed-final state condition

The final state of the hydrogen storage tank, should be the same as the initial state, to ensure that the proposed optimal control model may be computed over several control horizons. In this case, the proposed optimal control model, should ensure that the following day begins at the same initial state at which the initial state of the current day, expressed in Eq. (5.47) [93]:

$$\sum_{k=1}^{N} \left(P_4(k) - P_3(k)\right) = 0 \tag{5.47}$$

5.2.5.7 Proposed optimization solver

The objective function, as shown in Eq. (5.35), is a mixed integer nonlinear optimization problem (MINLP) and may be solved using the SCIP solver, in the optimization toolbox of

MATLAB, as illustrated in Eq. (5.48). The main reason for using SCIP as the solver is, due to its fast solving capabilities and that it may solve non-linear optimization problems, by controlling integer decision variables, as well as binary integer decision variables [122].

$$\begin{aligned} & min_x f(x) \\ & subject\,to: A.x \le b \\ & A_{eq}.x \le b_{eq} \\ & lb \le x \le ub \\ & x_j \in \{0,1\} \end{aligned} \tag{5.48}$$

5.3 CASE STUDY DESCRIPTION

In this section, the proposed optimal control strategy of residential energy hub integrating renewable energy, demand response and the energy storage system, is using the SCIP solver, in the optimization toolbox of MATLAB. The objectives, are to minimize the operating energy costs of the utility grid to the load and to the PEMWE, as well as maximize the supply of the electrical power generated by the solar PV modules to the load. Further objectives, are to minimize the level of discomfort for the hot water requirements, as well as the space heating and space cooling requirements.

A case study is conducted, using meteorological data obtained at the University of Free State, Bloemfontein, South Africa, on the residential energy hub integrating renewable energy, demand response and energy storage system [94]. The main purpose of the residential energy hub is to provide space heating, space cooling and water heating for 270 occupants. This is achieved, by supplying power from the residential energy hub, to mainly the air-to-air heat pump and air-to-water heat pump. The sampling time, t_s = 30 minutes, may be implemented, to simplify the simulations.

5.3.1 Data representation

In this study, optimal system sizing is not conducted, as this does not form part of the main focus of the study. However, sizing of the air-to-air and air-to-water heat pump, required for space heating, space cooling and water heating, are conducted, to a certain level.

The air-to-air heat pump selected for this study, is precisely the same air-to-air heat pump that was previously sized in Chapter III, in Section 3.3.1. Therefore, in this Section, the sizing of the air-to-water heat pump, responsible for the water heating requirements, is conducted for the worst-case scenario, which is during the winter. The first step in the sizing of the air-to-water heat pump, is to determine the hot water load demand, for the residential building. In this case, it is assumed that the peak hot water demand on average, per occupant, is 45 l/h [123], which calculates to a maximum of 12 150 l/h, for the entire residential building. It is further assumed that a maximum of 60 % of the occupants would consume hot water simultaneously, which is calculated to a peak demand consumption of 7 290 l/h. The thermal power required to heat the water, is calculated, by making use of Eq. (3.2), in Section 3.2.1, based on the calculated peak hot water demand and is calculated to be 1.22 x 10^9 J, which relates to 339.07 kW of thermal power. Therefore, the required calculated power, as well as the calculated hot water peak demand flow, are used to determine the required air-to-water heat pump system used in this study, which is depicted in Table 5.1 [124].

In this Section, the sizing of the HWST is further conducted, based on the required storage capacity, determined through the simulations. Furthermore, Table 5.1 further shows the parameters of the HWST, for a University residential building, in which 270 occupants reside [113-115]. A_s is the surface area of the tank, M is the volume of the tank, C is the specific heat capacity of water, h is the surface, k is the thermal conductivity and dx is the insulation thickness.

Table 5.1: Hot water storage tank (HWST) and air-to-water heat pump parameters

Parameters	Symbol	Value	Unit
Tank surface area	A_s	32	m^2
Tank volume	M	10 000	L
Specific heat capacity	C	4 186	J/kgK
Surface heat transfer coefficient	h	11.3	W/m^2K
Thermal conductivity	k	50	W/mK
Thickness of insulation	dx	0.07	m
Electrical Power	P_W	94.15	kW
Thermal Power	P_{QW}	367.2	kW
COP	COP_W	3.9	-

In this section, the sizing of the required PEMFC was conducted, which is primarily based on the largest energy consuming equipment, which is the air-to-air heat pump and the air-to-water heat pump. The electrical power required for the air-to-air heat pump, during space heating and the electrical power required for the air-to-water heat pump, are mainly considered. The main reason that the space heating electrical power is solely considered, is due to it consuming considerably more electrical power, compared to the space heating electrical power. The electrical power required from the PEMFC, is a combination of the electrical power required for space heating, as shown in Table 3.2 and the electrical power required for water heating, which equates to 233.16 kW. Therefore, the selected PEMFC, based on the electrical power required from the major energy consuming equipment, is rated at 250 kW [125].

Table 5.2 shows the parameters of the PEMFC used for producing electrical energy [105, 110, 116, 117]. The exchange current densities at the anode and cathode are identical, due to the anode exchange being the dominant of the two current densities [118]. a_a and a_c is the anode and cathode charge transfer coefficients, respectively. R is the universal gas constant, F is the Faraday constant, J is the current density, J_0 is the exchange current density, t_{mem} is the membrane thickness, σ_{mem} is the membrane conductivity and J_L is the limiting current

density. ϱ_{H20} is the partial pressure of water. ϱ_H and ϱ_O is the partial pressure of hydrogen and oxygen, respectively.

Table 5.2: PEMFC parameters

Parameters	**Symbol**	**Value**	**Unit**
Anode transfer coefficient	a_a	0.5	-
Cathode transfer coefficient	a_c	0.5	-
Universal gas constant	R	8.314	J/mol.K
Faraday constant	F	96 485	C/mol
Current density	J	1	A/cm^2
Exchange current density	J_o	0.00000173	A/cm^2
Membrane thickness	t_{mem}	0.0178	cm
Membrane conductivity	σ_{mem}	0.0001	S/cm
Limiting current density	J_L	2	A/cm^2
Partial pressure of water	ϱ_{H20}	101 325	Pa
Partial pressure of hydrogen	ϱ_H	101 325	Pa
Partial pressure of oxygen	ϱ_0	101 325	Pa

Figs. 5.2 and 5.3, illustrate the load demand of the typical University residential building, purely for the air-to-air heat pump and air-to-water heat pump during winter and summer, respectively. The regions of the TOU tariff structure are further indicated. The off-peak regions are illustrated by the green areas, the standard regions are illustrated by the yellow areas and the red regions are illustrated by the red areas.

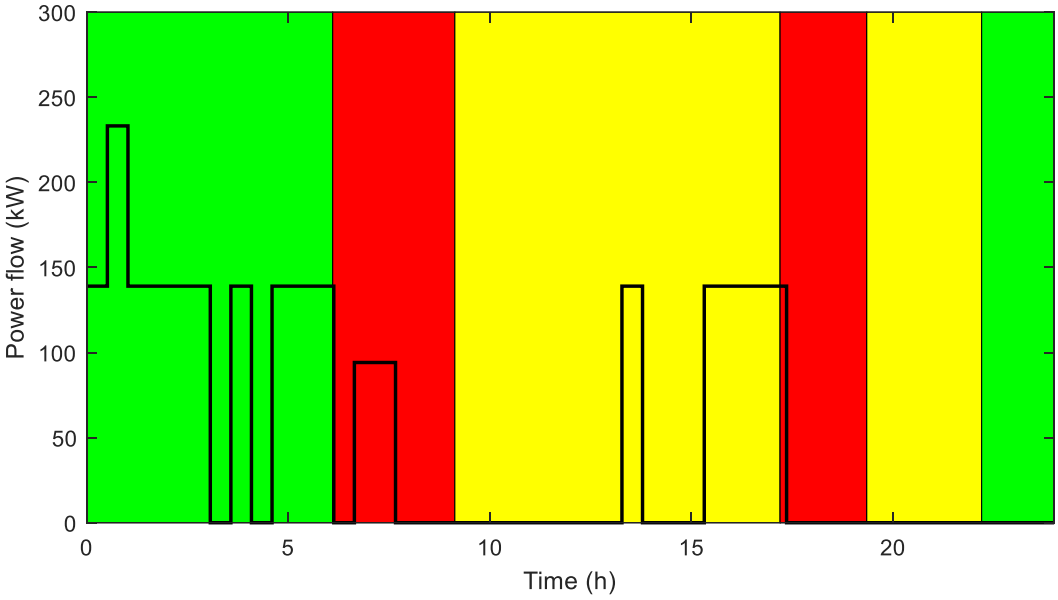

Fig. 5.2: Electrical load profile of the residential building during winter

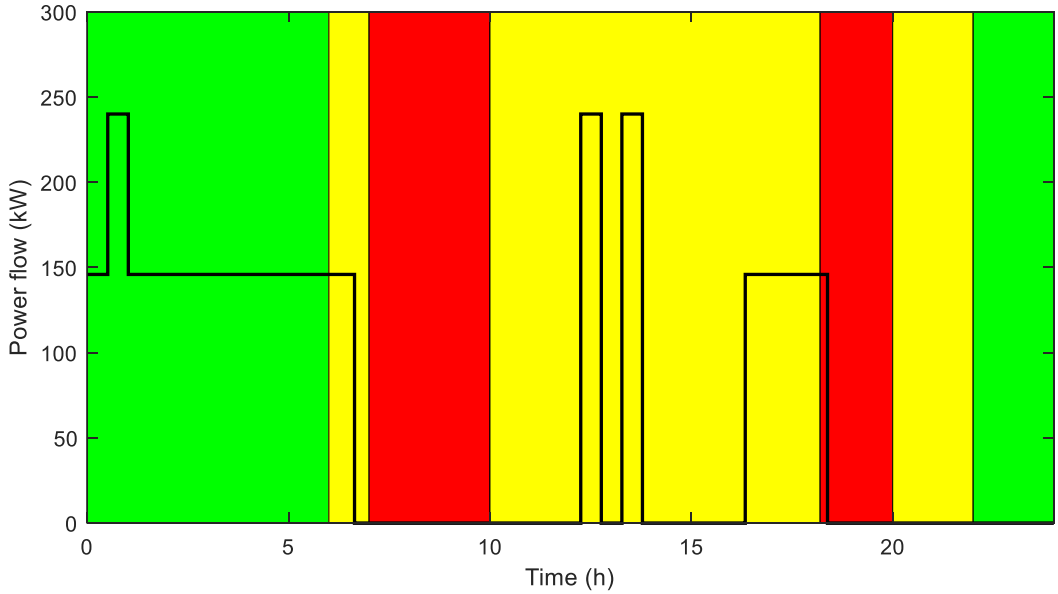

Fig. 5.3: Electrical load profile of the residential building during summer

Referring to Chapter IV, sub-section 4.3.1, the ambient air and inlet water temperature profiles during a selected winter day, as well as a summer day, used in this section, have been illustrated in Figs. 4.2 and 4.3. Furthermore, referring to Chapter IV, sub-section 4.3.1, the

electrical energy produced by the solar PV array in kW, during a selected winter day and summer day, are, illustrated and described in Figs. 4.4 and 4.5.

Furthermore, the hot water demand profile, is illustrated in Fig. 5.4.

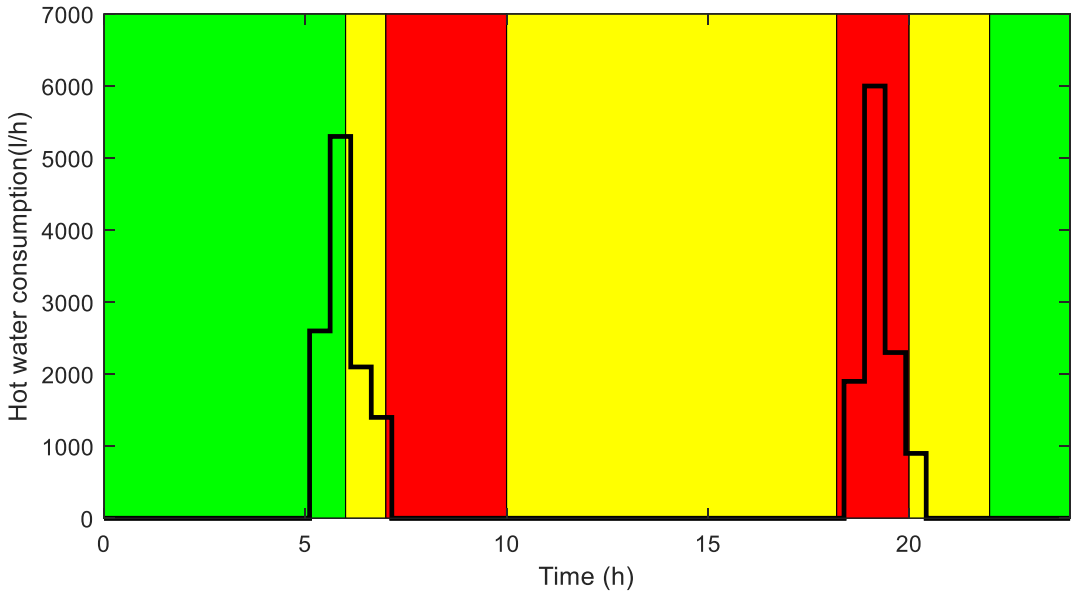

Fig. 5.4: Hot water demand profile

Table 5.3 depicts the input parameters, which are used perform the simulation of the developed model linked to the selected case study.

Table 5.3: Simulation parameters

Parameters	**description**	**Value**
t_s	Sampling time	30 min
Hours	Optimization interval	24 h

5.4 SIMULATION RESULTS AND DISCUSSION

The proposed optimal control model is evaluated against two baselines, of which conventional control philosophies are used to control the air-to-air heat pump, as well as the

air-to-water heat pump. The first control technique (Baseline 1) utilizes a thermostat-based controller, to control the air-to-air heat pump and, a further thermostat-based controller, to control the air-to-water heat pump. The second control technique (Baseline 2) utilizes a timer with a thermostat-based controller, to control the air-to-air heat pump and, a further timer with a thermostat-based controller, to control the air-to-water heat pump.

The optimal control of a residential energy hub integrating renewable energy, demand response and energy storage system, is discussed in Section 5.4.2. This model optimally controlled the switching of the air-to-air heat pump and the air-to-water heat pump, based on the optimal power flow of the integrated renewable energy system. The optimal power flow of the residential energy hub, integrating renewable energy, demand response and energy storage, is further presented in Section 5.4.2. This optimal control model attempts to firstly minimize the grid electrical energy cost, supplied to the residential energy hub and the PEMWE and, secondly, to maximize the electrical energy supplied from the solar PV modules to the electrical load and, thereafter, to the PEMWE. The level of discomfort is further minimized between the residential building temperature and the desired building temperature, of which is the responsibility of the air-to-air heat pump. Furthermore, the level of discomfort is minimized between the HWST temperature and the desired building temperature, which is the responsibility of the air-to-water heat pump. The burden on the air-to-water heat pump is further reduced, as the thermal energy is recovered from the solar PV modules, PEMWE and the PEMFC. This is mainly due to heat being generated during the nature of their operation, as mentioned before.

The proposed optimal control model is evaluated against these two previously mentioned baselines, during the selected winter and summer days.

5.4.1 Baseline

There are various common techniques available to control an air-to-air heat pump. These techniques are particularly inefficient, due to their simplicity in which they control the air-to-air heat pump and the air-to-water heat pump. In this Section, two different baselines are

adopted, which are used to control the air-to-air heat pump, for the selected winter and summer cases, as well as the air-to-water heat pump, for the selected winter and summer cases.

The first baseline is the thermostat-based control technique, discussed in Sections 5.4.1.1 and 5.4.1.5. By making use of this technique, the air-to-air heat pump and the air-to-water heat pump are switched on once the minimum temperature set-point is reached and switched off, once the maximum temperature set-point is reached. Thus, the heat pumps are controlled such that the temperature is maintained within these boundary limits.

The second baseline is the timer with a thermostat-based control technique, discussed in Sections 5.4.1.3 and 5.4.1.7. With this technique, the air-to-air heat pump and air-to-water heat pump are further switched, such that the residential building temperature is retained within a maximum and minimum set-points, as well as the use of a timer, ensuring the desired temperatures set by the end-user, is achieved.

The optimal control of a residential energy hub integrating renewable energy, demand response and energy storage system, discussed in Section 5.4.2, are thoroughly evaluated against the two baselines, to evaluate the effectiveness, thereof.

5.4.1.1 Winter case thermostat-based control (winter Baseline 1)

In this Section, thermostat-based switching control of the air-to-air heat pump and air-to-water heat pump, are adopted as the first baseline, in order to evaluate the economic feasibility of the optimal switching control model. The thermostat switching control is based on the switching of the air-to-air heat pump and the air-to-water heat pump, ensuring the temperature of the residential building, as well as the HWST are retained within their temperature limits, set by the end-user.

Referring to Chapter III, sub-section 3.3.1, the thermostat switching control of the air-to-air heat pump, was simulated, based on the parameters in Table 3.1, lighting load in Fig. 3.2, occupancy load in Fig. 3.3, heat pump parameters in Table. 3.2, ambient air temperature in Fig. 3.4 and simulation parameters in Table. 3.3. The following sub-sections, present the

results from the thermostat-based switching control simulation for the air-to-air heat pump (Figs. 5.5 - 5.6).

The thermostat switching control of the air-to-water heat pump is simulated, based on the parameters in Table 5.1, hot water demand profile in Fig. 5.4, heat pump parameters in Table. 5.1, ambient air temperature in Fig. 3.4 and simulation parameters in Table. 5.3. The following sub-sections present the results from the thermostat-based switching control simulation, for the air-to-water heat pump (Figs. 5.7 - 5.8).

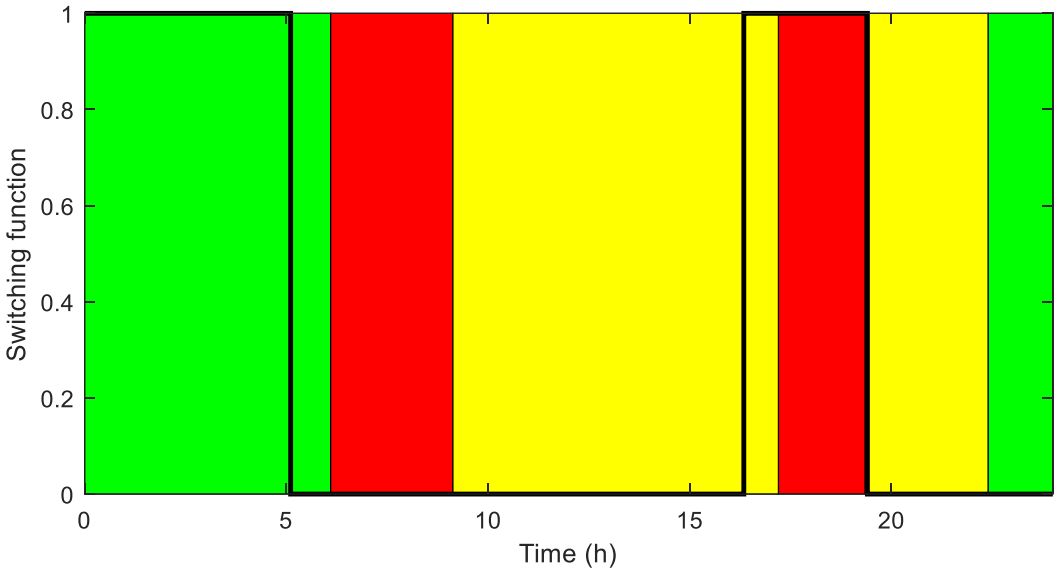

Fig. 5.5: Winter Baseline 1 – Switching function of the air-to-air heat pump

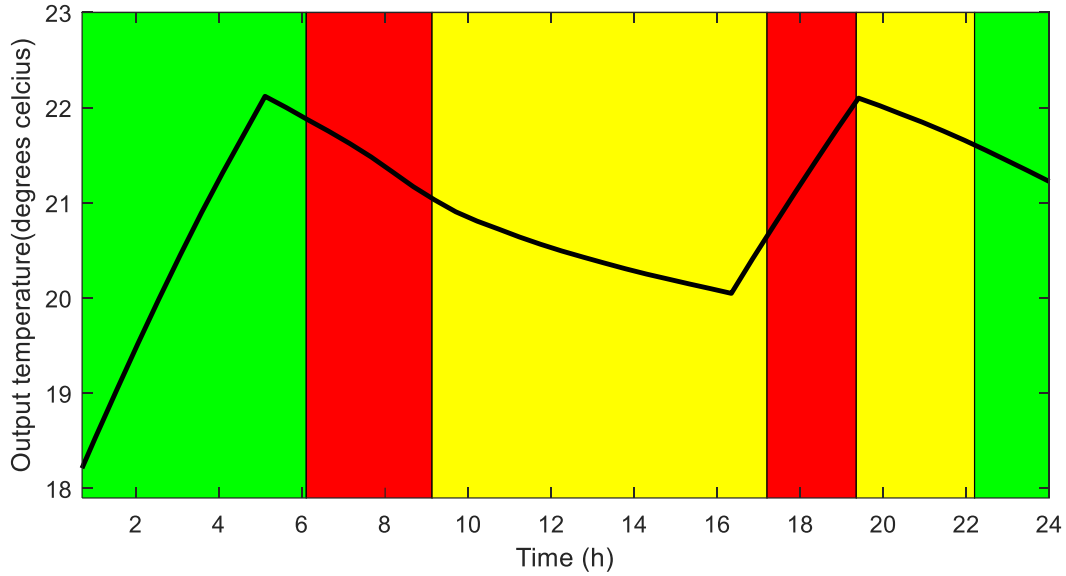

Fig. 5.6: Winter Baseline 1 – Residential building temperature

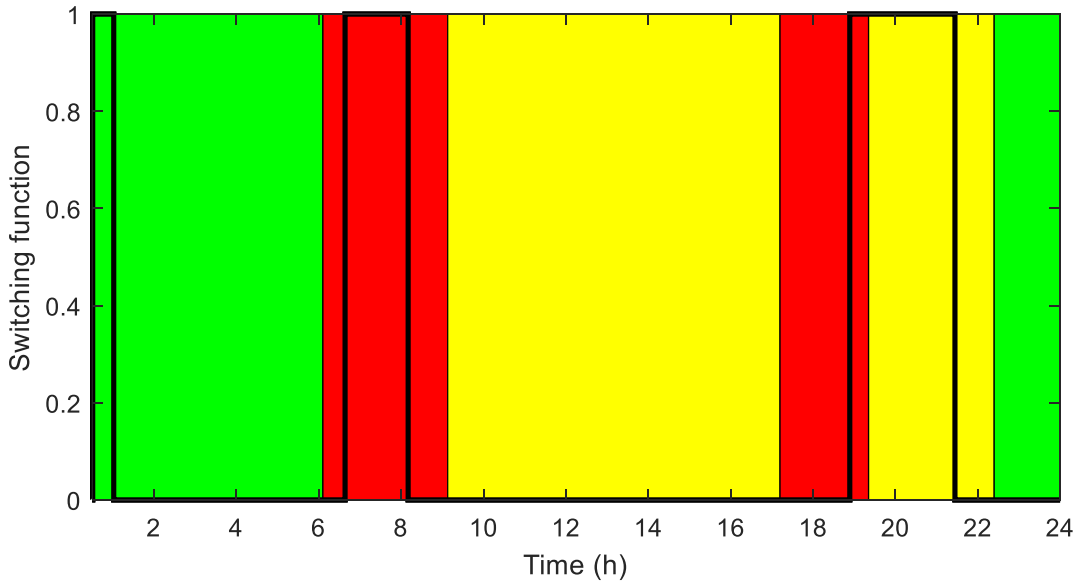

Fig. 5.7: Winter Baseline 1 – Switching function of the air-to-water heat pump

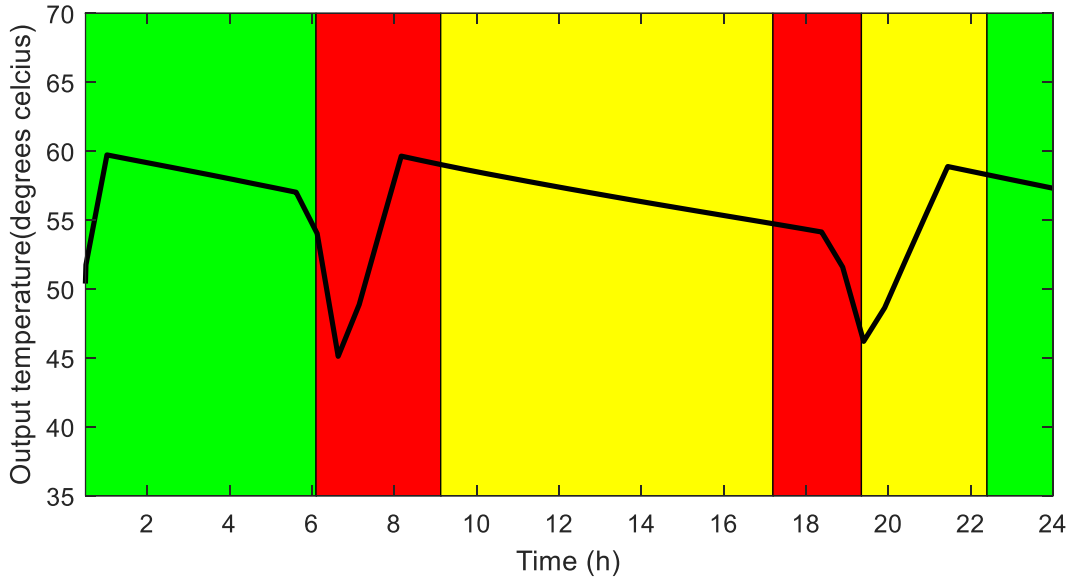

Fig. 5.8: Winter Baseline 1 – HWST temperature

5.4.1.2 Winter case thermostat-based control (winter Baseline 1) discussion

5.4.1.2 a) First off-peak pricing period 00h00 - 06h00 (green)

In Figs. 5.5 and 5.6, the switching function of the air-to-air heat pump, as well as the temperature inside the residential building, were presented, respectively. Initially, the temperature inside the residential building starts at 18.2 °C, which was the final state from the previous day. From 00h00 – 05h00, the building temperature increases, due to the air-to-air heat pump being switched on, as seen from Fig. 5.5. It may be observed that the air-to-air heat pump was switched on from 00h00 until 05h00, in order to reach the maximum temperature limit of 22 °C, due to the ambient temperature being initially low and decreased further, during this time-period. From 05h00 – 06h00, the building temperature decreased, due to the air-to-air heat pump being switched off, by means of the thermostat controller, as seen in Fig. 5.5.

In Figs. 5.7 and 5.8, the switching function of the air-to-water heat pump, as well as the HWST temperature, were presented, respectively. Initially, the temperature of the HWST,

begins at 50 °C, which was the final state of the previous day. From 00h00 – 00h30, the temperature of the HWST increases, until it reaches 60 °C, as seen from Fig. 5.8. The air-to-water heat pump was switched off, due to the temperature limit of the thermostat controller of 60 °C, is achieved, as seen from Fig. 5.7. From 00h30 – 05h30, the temperature of the HWST decreased gradually, due to standby losses experienced by the HWST. From, 05h30 – 06h00, the temperature started to decrease significantly, due to the hot water demand during this period, as seen from Fig. 5.4.

5.4.1.2 b) First peak pricing period 06h00 - 09h00 (red)

From 06h00 – 09h00, the residential building temperature decreased, as seen in Fig. 5.6. This is due to the air-to-air heat pump being switched off, as seen from the switching function of the air-to-air heat pump, illustrated in Fig. 5.5. Furthermore, the residential building temperature continued to decrease, as the minimum temperature limit of 20 °C was not obtained, at this instance in time.

From 06h00 – 06h30, the temperature inside the HWST continued to decrease significantly, as seen from Fig. 5.4, until it reached the minimum temperature limit of 45 °C, which may be observed from Fig. 5.8. From 06h30 – 08h00, the temperature started to increase, as the air-to-water heat pump was switched, as seen in Fig. 5.7. From 08h00 – 09h00, the temperature of the HWST started to decrease as the maximum temperature limit of 60 °C was achieved, as seen from Fig. 5.8.

5.4.1.2. c) First standard pricing period 09h00 - 17h00 (yellow)

From 09h00 – 16h00, the residential building temperature decreased, as seen in Fig. 5.6. The air-to-air heat pump is switched off, due to the minimum temperature limit of 20 °C is obtained, at this instance in time, as seen from the switching function of the air-to-air heat pump, illustrated in Fig. 5.5. From 16h00 – 17h00, the residential building temperature

started to increase, as seen from Fig. 5.6, due to the air-to-air heat pump being switched on, by means of the thermostat controller.

From 09h00 – 17h00, the residential building temperature continued to gradually decrease, as seen in Fig. 5.8. The air-to-water heat pump remained switched off, due to the minimum temperature limit of 45 °C not yet achieved, illustrated in Fig. 5.7.

5.4.1.2 d) Second peak pricing period 17h00 - 19h00 (red)

From 17h00 – 19h00, the residential building temperature increased, until it reached the maximum temperature limit of 22 °C, which was during the peak pricing period, as illustrated in Fig. 5.6.

From 17h00 – 18h00, the temperature of the HWST continued to gradually decrease, due to the standby losses experienced by the HWST, as seen from Fig. 5.8. From 18h00 – 19h00, the temperature of the HWST started to decrease significantly, due to the hot water being demanded during this period, as seen from Fig. 5.4, until it reached the minimum temperature limit of 45 °C, during the peak pricing period, as illustrated in Fig. 5.8.

5.4.1.2 e) Second standard pricing period 19h00-22h00 (yellow)

From 19h00 – 22h00, the residential building temperature continued to decrease, due to the air-to-air heat pump being switched off, by means of the thermostat controller, as the minimum temperature limit of 20 °C was not obtained, which may be observed in Fig. 5.6.

From 19h00 – 21h00, the temperature of the HWST started to increase, due to the air-to-water heat pump being switched on, as seen from Fig. 5.8. This was due to the minimum temperature limit of 45 °C being reached. From 21h00 – 22h00, the temperature of the HWST started to decrease, as seen from Fig. 5.8. This was due to the air-to-water heat pump was switched off, by means of the thermostat controller, as the maximum temperature limit of 60 °C was achieved, which may be observed in Fig. 5.7.

5.4.1.2 f) Second off-peak pricing period 22h00 - 24h00 (green)

From 22h00 – 24h00, the residential building temperature continued to decrease, as seen in Fig. 5.6. The residential building temperature decreased, due to the air-to-air heat pump being switched off during this period, as seen in Fig. 5.5. The air-to-air heat pump was not required to be switched on, due to the minimum temperature limit not yet reached at 24h00.

From 22h00 – 24h00, the temperature of the HWST continued to decrease, as seen in Fig. 5.8. The temperature continued to decrease, due to the air-to-water heat pump being switched off during this period, as seen in Fig. 5.7. This was due to the fact that the minimum temperature limit was not yet reached and there was no demand during this period, as seen from Fig. 5.4.

5.4.1.3 Winter case timer with thermostat-based control (winter Baseline 2)

In this Section, the timer with thermostat-based switching control of the air-to-air heat pump and air-to-water heat pump, is adopted as the second baseline, in order to evaluate the economic feasibility of the optimal switching control model. The timer, with thermostat switching control, is based on the switching of the air-to-air heat pump and the air-to-water heat pump, ensuring the temperature of the residential building, as well as the temperature of the HWST are retained within their temperature limits, as well as the use of a timer, which ensures that the desired temperatures set by the end-user, is achieved.

The timer with thermostat switching control of the air-to-air heat pump is simulated, based on the parameters in Table 3.1, lighting load in Fig. 3.2, occupancy load in Fig. 3.3, heat pump parameters in Table. 3.2, ambient air temperature in Fig. 3.4 and simulation parameters in Table. 3.3. The following sub-sections present the results from the timer, with thermostat-based switching control simulation (Figs. 5.9 – 5.10).

The timer with thermostat switching control of the air-to-water heat pump, is simulated, based on the parameters in Table 5.1, hot water demand profile in Fig. 5.4, heat pump parameters in Table. 5.1, ambient air temperature in Fig. 3.4 and simulation parameters in

Table. 5.3. The following sub-sections present the results from the thermostat-based switching control simulation, for the air-to-air heat pump (Figs. 5.11 - 5.12).

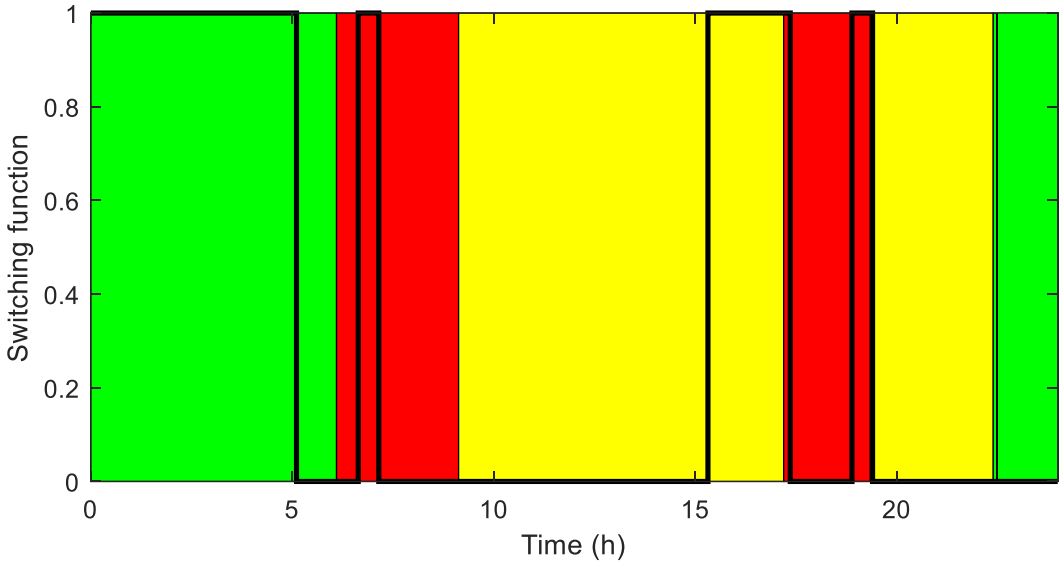

Fig. 5.9: Winter Baseline 2 – Switching function of the air-to-air heat pump

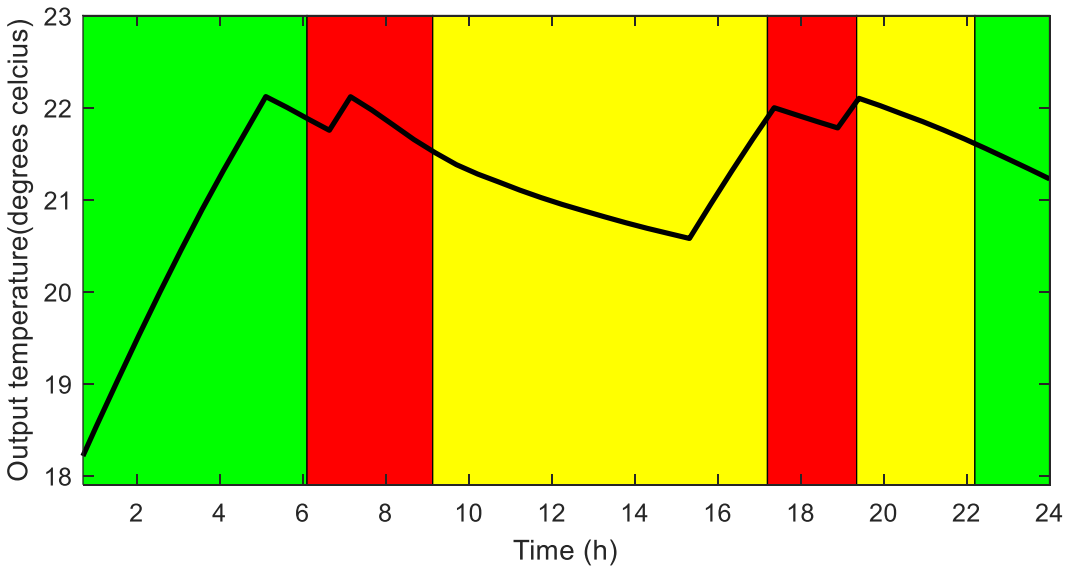

Fig. 5.10: Winter Baseline 2 – Residential building temperature

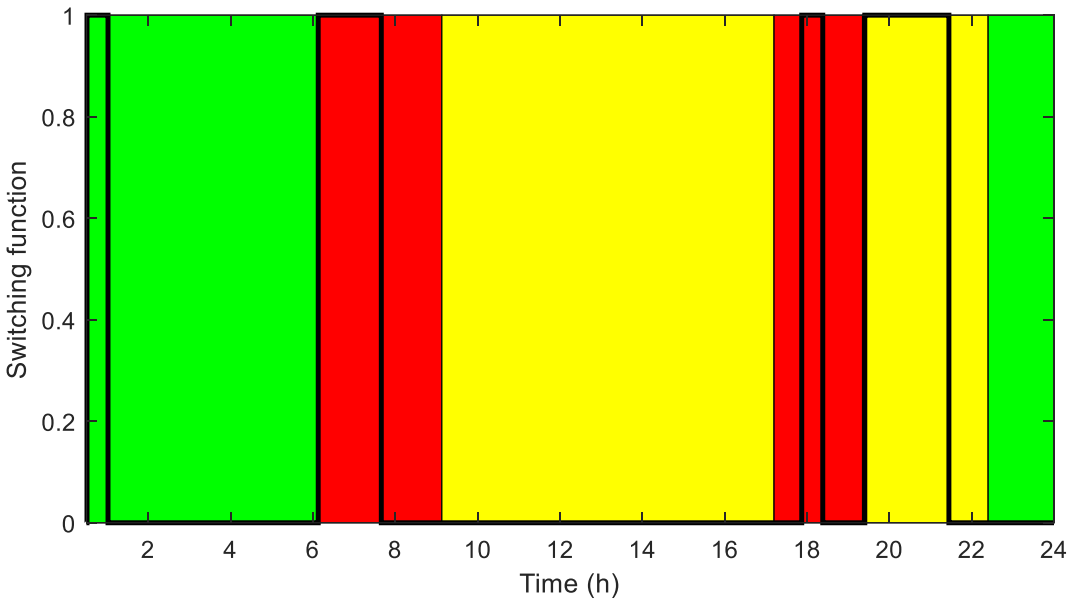

Fig. 5.11: Winter Baseline 2 – Switching function of the air-to-water heat pump

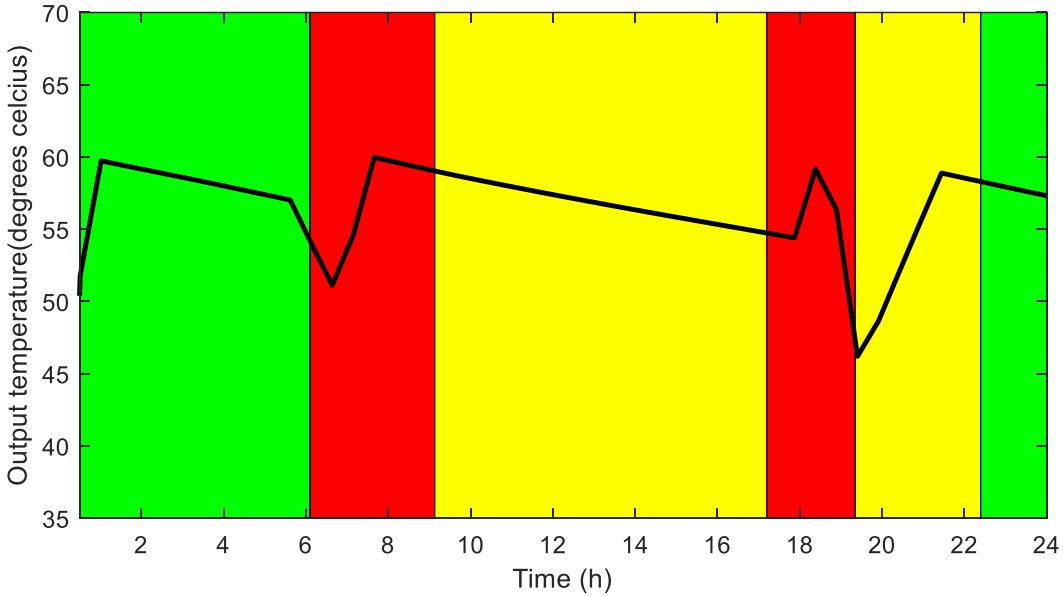

Fig. 5.12: Winter Baseline 2 – HWST temperature

5.4.1.4 Winter case timer with thermostat-based control (winter Baseline 2) discussion

5.4.1.4 a) First off-peak pricing period 00h00 - 06h00 (green)

In Fig. 5.10, the temperature inside the residential building, heated by the air-to-air heat pump, was presented. Initially, the temperature inside the residential building, started at 18.2 °C, which was the final state of the previous day. From 00h00 – 05h00, the building temperature increased, due to the air-to-air heat pump being switched on. It may be observed that the air-to-air heat pump was switched on from 00h00 until 05h00, in order to reach the maximum temperature limit of 22 °C, due to the ambient temperature being initially low and decreasing further, during this time-period. From 05h00 – 06h00, the building temperature decreased, as the air-to-air heat pump was switched off, by means of the thermostat controller, as seen from Fig. 5.9.

In Figs. 5.11 and 5.12, the switching function of the air-to-water heat pump, as well as the HWST temperature, were presented, respectively. Initially, the temperature of the HWST begins at 50 °C, which was the final state of the previous day. From 00h00 – 00h30, the temperature of the HWST increased, until it reached 60 °C, as seen from Fig. 5.12. The air-to-water heat pump was switched off, due to the temperature limit of the thermostat controller of 60 °C, being achieved, as seen from Fig. 5.11. From 00h30 – 05h30, the temperature of the HWST decreased gradually, due to standby losses, experienced by the HWST. From 05h30 – 06h00, the temperature started to decrease significantly, due to the hot water demand during this period, as seen from Fig. 5.4.

5.4.1.4 b) First peak pricing period 06h00 - 09h00 (red)

From 06h00 – 06h30, the residential building temperature decreased, as seen in Fig. 5.10. This was due to the air-to-air heat pump being switched off, as seen from the switching function of the air-to-air heat pump, illustrated in Fig. 5.9. From 06h30 – 07h00, the residential building temperature increased, as the air-to-air heat pump was switched on by

means of the timer, as seen from Fig. 5.9. From 07h00 – 09h00, the residential building temperature decreased, as the air-to-air heat pump was switched off, by means of the thermostat controller, as seen from Fig. 5.9. Furthermore, the residential building temperature continued to decrease, as the minimum temperature limit of 20 °C was not obtained at this time.

From 06h00 – 06h30, the temperature inside the HWST continued to decrease significantly, as seen from Fig. 5.12. From 06h30 – 07h30, the temperature of the HWST started to increase, as the air was switched on by means of the timer, to meet the hot water demand during this period, as seen from Figs. 5.11 and 5.12. From 07h30 – 10h00, the temperature of the HWST started to decrease, due to the maximum temperature limit of 60 °C being achieved, as seen from Fig. 5.12.

5.4.1.4 c) First standard pricing period 09h00 - 17h00 (yellow)

From 10h00 – 15h00, the residential building temperature decreased, as seen in Fig. 5.10, due to the air-to-air heat pump being switched off. From 15h00 – 17h00, the residential building temperature started to increase, as seen from Fig. 5.10, which was due to the air-to-air heat pump being switched on, by means of the timer, in order to achieve the desired temperature.

From 09h00 – 17h00, the residential building temperature continued to gradually decrease, as seen in Fig. 5.12. The air-to-water heat pump remained switched off, due to the minimum temperature limit of 45 °C, not yet achieved, illustrated in Fig. 5.11.

5.4.1.4 d) Second peak pricing period 17h00 - 19h00 (red)

From 17h00 – 18h30, the residential building temperature continued to decrease, due to the air-to-air heat pump being switched off, as illustrated in Fig. 5.9. From 18h30 – 19h00, the residential building temperature started to increase, due to the air-to-air heat pump being

switched on, by means of the timer, in order to achieve the desired temperature, as seen from Fig. 5.10.

From 17h00 – 17h30, the temperature of the HWST continued to gradually decrease, due to the standby losses experienced by the HWST, as seen from Fig. 5.12. From 17h30 – 18h00, the temperature of the HWST started to increase, as the air-to-water heat pump was switched on by means of the timer, to achieve the desired temperature during this period. From 18h00 – 19h00, the temperature of the HWST started to decrease significantly, due to the demand for hot water during this period, as seen from Fig. 5.4, until it reached the minimum temperature limit of 45 °C, which was during the peak pricing period, as illustrated in Fig. 5.12.

5.4.1.4 e) Second standard pricing period 19h00 - 22h00 (yellow)

From 19h00 – 22h00, the residential building temperature continued to decrease, due to the air-to-air heat pump being switched off by means of the thermostat controller, as the minimum temperature limit of 20 °C was not obtained, which may be observed in Fig. 5.10.

From 19h00 – 21h00, the temperature of the HWST started to increase, due to the air-to-water heat pump being switched on by means of the thermostat controller, as the minimum temperature limit of 45 °C was obtained, which may be observed in Fig. 5.12. From 21h00 – 22h00, the temperature started to gradually decrease, as the maximum temperature limit of 60 °C was obtained, as seen from Fig. 5.12.

5.4.1.4 f) Second off-peak pricing period 22h00 - 24h00 (green)

From 22h00 – 24h00, the residential building temperature continued to decrease, as seen in Fig. 5.10. The residential building temperature decreased, due to the air-to-air heat pump switched off during this period, as seen in Fig. 5.9. The air-to-air heat pump was not required to be switched on, due to the minimum temperature limit not yet reached at 24h00.

From 22h00 – 24h00, the temperature of the HWST continued to decrease, as seen in Fig. 5.12. The temperature decreased, due to the air-to-water heat pump switched off during this period, as seen in Fig. 5.11. The air-to-water heat pump was not required to be switched on, due to the minimum temperature limit still not being reached at 24h00.

5.4.1.5 Summer thermostat-based control (summer Baseline 1)

In this Section, thermostat-based switching control of the air-to-air heat pump and air-to-water heat pump are adopted as the first baseline, in order to evaluate the economic feasibility of the optimal switching control model. The thermostat switching control is based on the switching of the air-to-air heat pump, as well as the air-to-water heat pump, ensuring the temperatures of the residential building and HWST, are retained within the temperature limits, set by the end-user.

The thermostat switching control of the air-to-air heat pump is simulated, based on the parameters in Table 3.1, lighting load in Fig. 3.2, occupancy load in Fig. 3.3, heat pump parameters in Table. 3.2, ambient air temperature in Fig. 3.5 and simulation parameters in Table. 3.3, obtained in Chapter III. The following sub-sections present the results from the thermostat-based switching control simulation, for the air-to-air heat pump (Figs. 5.13 - 5.14).

The thermostat switching control of the air-to-water heat pump, is simulated, based on the parameters in Table 5.1, hot water demand profile in Fig. 5.4, heat pump parameters in Table. 5.1, ambient air temperature in Fig. 3.5 and simulation parameters in Table. 5.3. The following sub-sections present the results from the thermostat-based switching control simulation for the air-to-air heat pump (Figs. 5.15 - 5.16).

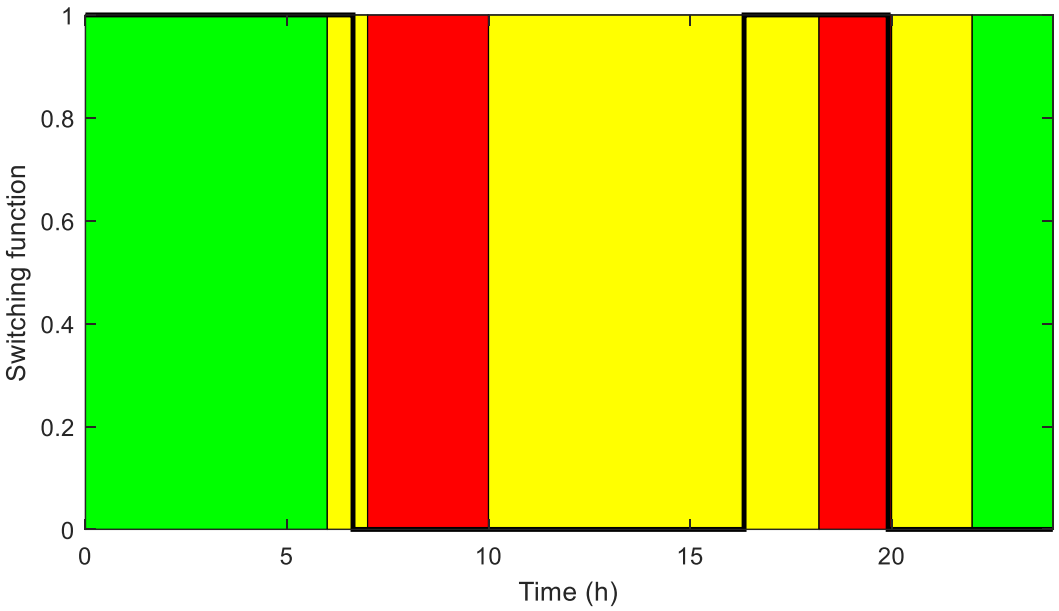

Fig. 5.13: Summer Baseline 1 – Switching function of the air-to-air heat pump

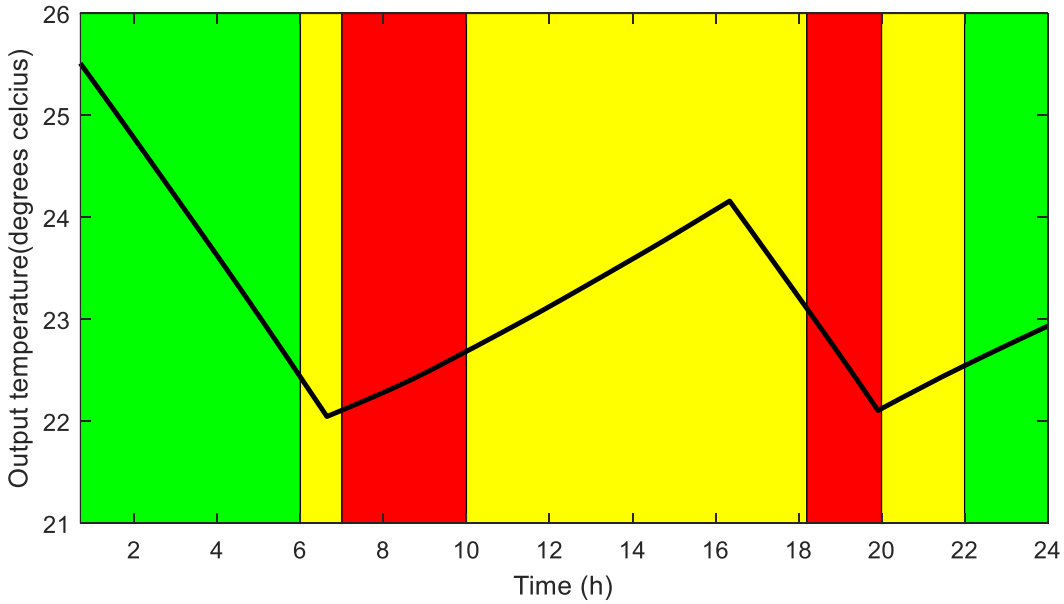

Fig. 5.14: Summer Baseline 1 – Residential building temperature

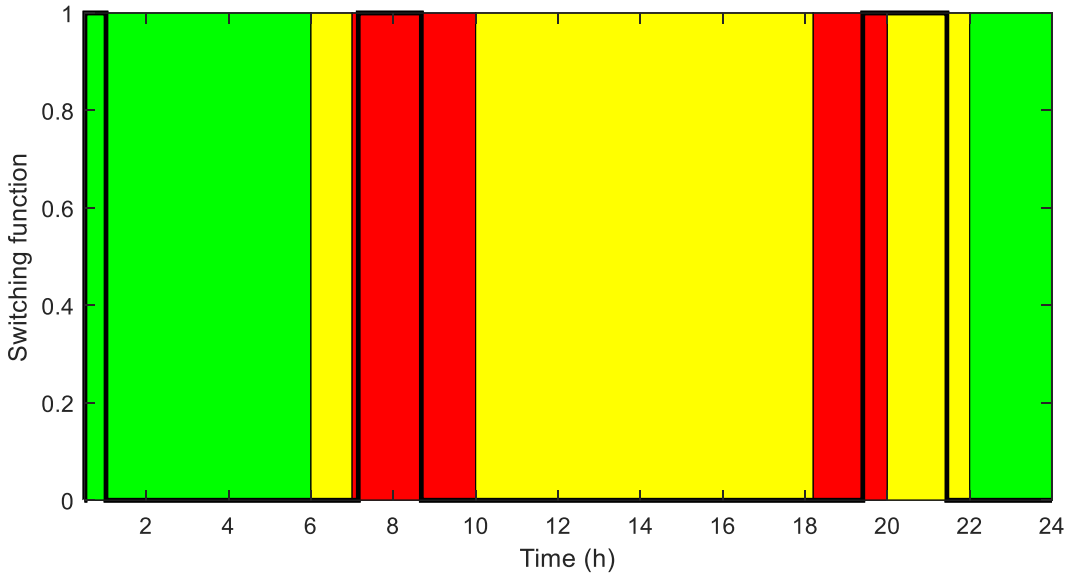

Fig. 5.15: Summer Baseline 1 – Switching function of the air-to-water heat pump

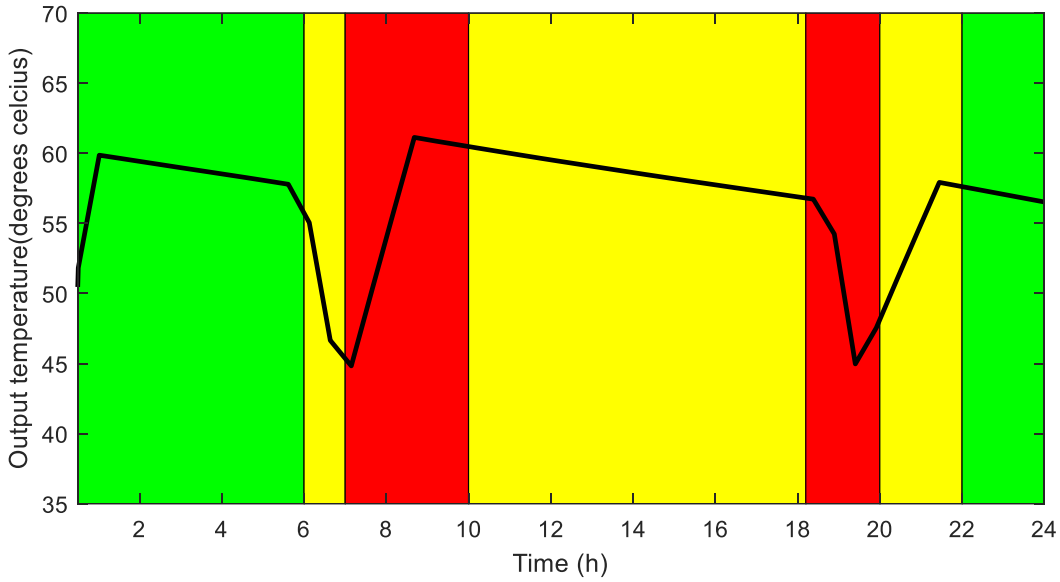

Fig. 5.16: Summer Baseline 1 – HWST temperature

5.4.1.6 Summer thermostat-based control (summer Baseline 1) discussion

5.4.1.6 a) First off-peak pricing period 00h00 - 06h00 (green)

In Figs. 5.13 and 5.14, the switching function of the air-to-air heat pump, as well as the temperature inside the residential building, were presented, respectively. Initially, the temperature inside the residential building started at 25.5 °C, which was the final state of the previous day. From 00h00 – 06h00, the building temperature decreases, due to the air-to-air heat pump being switched on, as seen from Fig. 5.13. It may be observed that the air-to-air heat pump was switched on from 00h00 until 06h00, in order to reach the minimum temperature limit of 22 °C.

In Figs. 5.15 and 5.16, the switching function of the air-to-water heat pump, as well as the HWST temperature, were presented, respectively. Initially, the temperature of the HWST begins at 50 °C, which was the final state of the previous day. From 00h00 – 00h30, the temperature of the HWST increased until it reached 60 °C, as seen from Fig. 5.16. The air-to-water heat pump was switched off, due to the temperature limit of the thermostat controller of 60 °C was achieved, as seen from Fig. 5.15. From 00h30 – 05h30, the temperature of the HWST decreased gradually, due to standby losses experienced by the HWST. From 05h30 – 06h00, the temperature started to decrease significantly, which was due to hot water demanded during this period, as seen from Fig. 5.4.

5.4.1.6 b) First standard pricing period 06h00 - 07h00 (yellow)

From 06h00 – 06h30, the residential building temperature continued to decrease, as the air-to-air heat pump was switched on during this period, as seen from Figs. 5.13 and 5.14. The air-to-air heat pump was switched on during this period, until to the minimum temperature limit of 22 °C, was achieved. From 06h30 – 07h00, the residential building temperature increased, due to the air-to-air heat pump being switched off, as seen from Fig. 5.13.

From 06h00 – 07h00, the temperature inside the HWST continued to decrease significantly, as seen from Fig. 5.4, until it reached the minimum temperature limit of 45 °C, which may be observed from Fig. 5.16. The air-to-water heat pump remained switched off during this period, due to the minimum temperature limit reached solely at the end of this period.

5.4.1.6 c) First peak pricing period 07h00 - 10h00 (red)

From 07h00 – 10h00, the residential building temperature continued to increase, as seen in Fig. 5.14. This was due to the air-to-air heat pump being switched off until the maximum temperature limit of 24 °C, was achieved.

From 07h00 – 08h30, the temperature of the HWST increased, until it reached the maximum temperature limit of 60 °C, after which the air-to-water heat pump was switched off by the thermostat controller, as seen from Figs. 5.15 and 5.16. From 08h30 – 10h00, the temperature of the HWST decreased gradually, as seen from Fig. 5.16. This was due to the air-to-water heat pump being switched off during this period.

5.4.1.6 d) Second standard pricing period 10h00 - 18h00 (yellow)

From 10h00 – 16h00, the residential building temperature continued to increase, as seen in Fig. 5.14. The air-to-air heat pump was switched off, due to the maximum temperature limit of 24 °C being achieved, as seen from the switching function of the air-to-air heat pump, illustrated in Fig. 5.13. From 16h00 – 18h00, the residential building temperature started to decrease, as seen from Fig. 5.13, due to the air-to-air heat pump being switched on by means of the thermostat controller.

From 10h00 – 18h00, the residential building temperature continued to gradually decrease, as seen in Fig. 5.16. The air-to-water heat pump remained switched off, due to the minimum temperature limit of 45 °C was still not achieved, illustrated in Fig. 5.15.

5.4.1.6 e) Second peak pricing period 18h00 - 20h00 (red)

From 18h00 – 20h00, the residential building temperature continued to decrease, until it reached the minimum temperature limit of 22 °C, which was during the peak pricing period, as illustrated in Fig. 5.14.

From 18h00 – 19h30, the temperature of the HWST decreased significantly, due to the hot water being demanded during this period, as seen from Fig. 5.4, until it reached the minimum temperature limit of 45 °C, which was during the peak pricing period, as illustrated in Fig. 5.16. From 19h30 – 20h00, the temperature started to increase, as a result of the air-to-water heat pump switched on by means of the thermostat controller, as seen from Figs. 5.15 and 5.16.

5.4.1.6 f) Third standard pricing period 20h00 - 22h00 (yellow)

From 20h00 – 22h00, the residential building temperature continued to increase, due to the air-to-air heat pump being switched off by means of the thermostat controller, as the maximum temperature limit of 24 °C was not obtained, which may be observed in Fig. 5.14.

From 20h00 – 21h30, the temperature of the HWST continued to increase, due to the air-to-water heat pump being switched on, as seen from Fig. 5.16. From 21h30 – 22h00, the temperature of the HWST started to decrease, as seen from Fig. 5.16. This was due to the air-to-water heat pump was switched off by means of the thermostat controller, as the maximum temperature limit of 60 °C was achieved, observed in Fig. 5.15.

5.4.1.6 g) Second off-peak pricing period 22h00 - 24h00 (green)

From 22h00 – 24h00, the residential building temperature continued to increase, as seen in Fig. 5.14. The residential building temperature increased, due to the air-to-air heat pump switched off during this period, as seen in Fig. 5.13. The air-to-air heat pump was not

required to be switched on, due to the maximum temperature limit not yet being reached at 24h00.

From 22h00 – 24h00, the temperature of the HWST continued to decrease, as seen in Fig. 5.16. The temperature continued to decrease, due to the air-to-water heat pump switched off during this period, as seen in Fig. 5.15. This was due to the minimum temperature limit was not yet reached and no further hot water was demanded during this period, as seen from Fig. 5.4.

5.4.1.7 Summer case timer with thermostat-based control (summer Baseline 2)

In this Section, the timer with thermostat-based switching control of the air-to-air heat pump is adopted as the second baseline, in order to evaluate the economic feasibility of the optimal switching control model. The thermostat switching control, is based on the switching of the air-to-air heat pump, as well as the air-to-water heat pump, ensuring the temperatures of the residential building and HWST, are retained within the temperature limits, set by the end-user.

The timer with thermostat switching control of the air-to-air heat pump, is simulated, based on the parameters in Table 3.1, lighting load in Fig. 3.2, occupancy load in Fig. 3.3, heat pump parameters in Table. 3.2, ambient air temperature in Fig. 3.5 and simulation parameters in Table. 3.3, Chapter III. The following sub-sections present the results from the thermostat-based switching control simulation for the air-to-air heat pump (Figs. 5.17 - 5.18).

The timer with thermostat switching control of the air-to-water heat pump is simulated, based on the parameters in Table 5.1, hot water demand profile in Fig. 5.4, heat pump parameters in Table. 5.1, ambient air temperature in Fig. 3.5 and simulation parameters in Table. 5.3. The following sub-sections present the results from the thermostat-based switching control simulation for the air-to-air heat pump (Figs. 5.19 - 5.20).

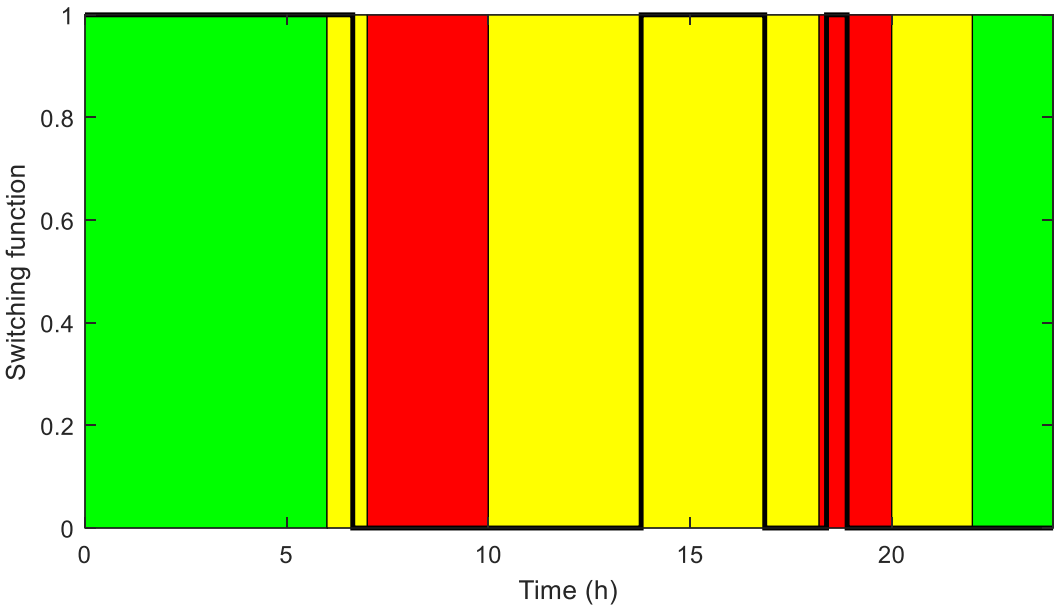

Fig. 5.17: Summer Baseline 2 – Switching function of the air-to-air heat pump

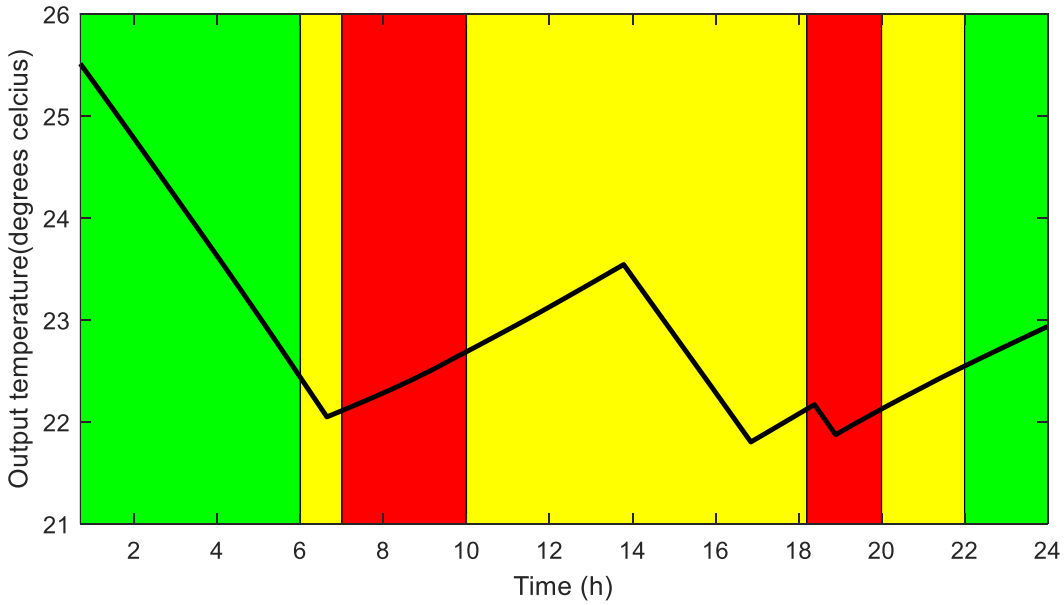

Fig. 5.18: Summer Baseline 2 – Residential building temperature

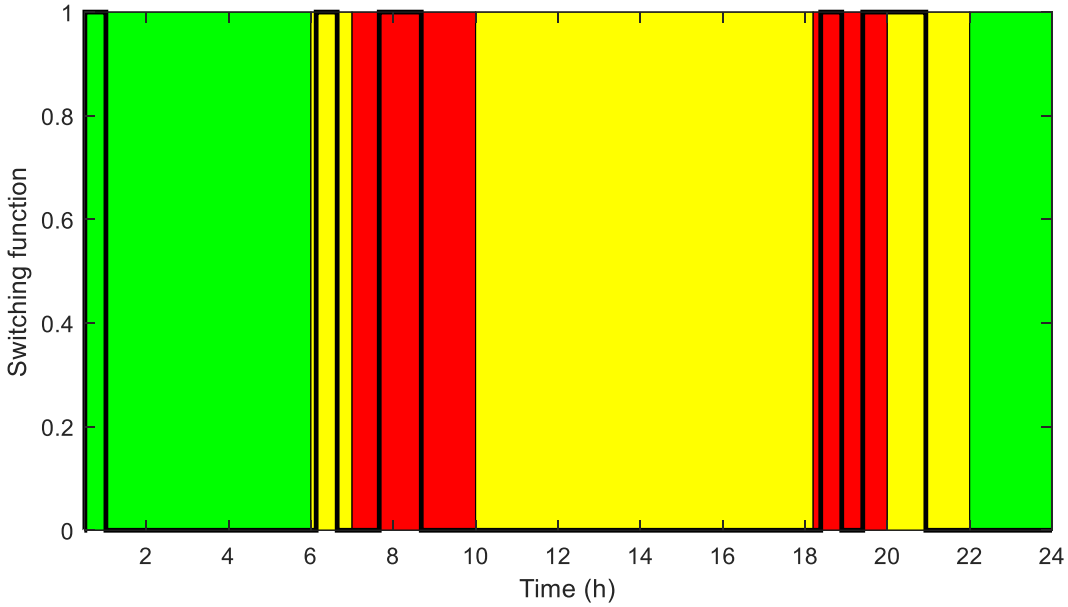

Fig. 5.19: Summer Baseline 2 – Switching function of the air-to-water heat pump

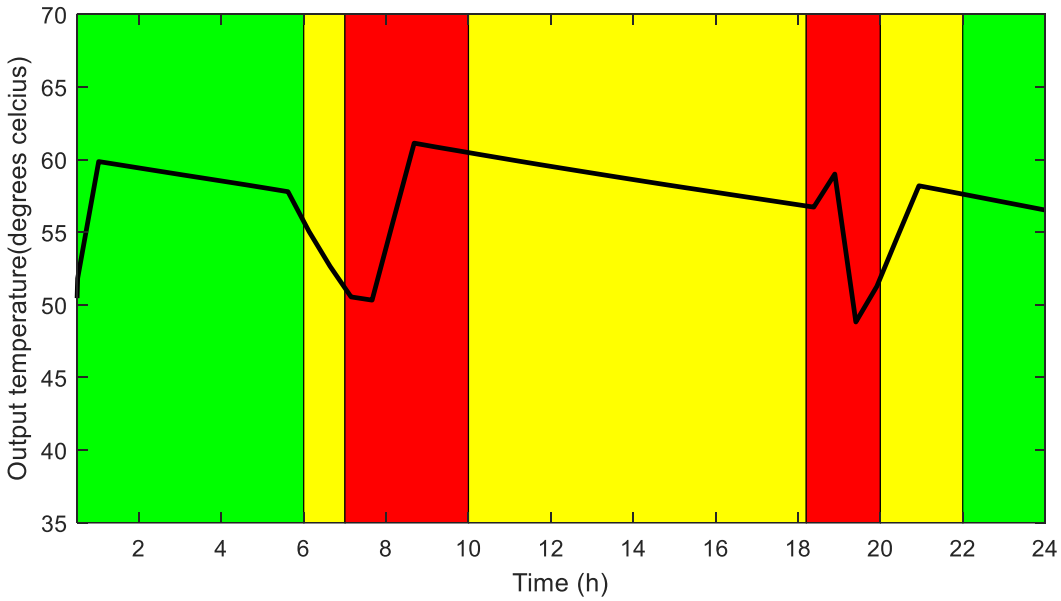

Fig. 5.20: Summer Baseline 2 – HWST temperature

5.4.1.8 Summer case timer with thermostat-based control (summer Baseline 2) discussion

5.4.1.8 a) First off-peak pricing period 00h00 - 06h00 (green)

In Figs. 5.17 and 5.18, the switching function of the air-to-air heat pump, as well as the temperature inside the residential building, were presented, respectively. Initially, the temperature inside the residential building started at 25.5 °C, which was the final state of the previous day. From 00h00 – 06h00, the building temperature decreased, due to the air-to-air heat pump being switched on, as seen from Fig. 5.17. It may be observed that the air-to-air heat pump was switched on from 00h00 until 06h00, in order to reach the minimum temperature limit of 22 °C.

In Figs. 5.19 and 5.20, the switching function of the air-to-water heat pump, as well as the HWST temperature, were presented, respectively. Initially, the temperature of the HWST begins at 50 °C, which was the final state of the previous day. From 00h00 – 00h30, the temperature of the HWST increased, until it reached 60 °C, as seen from Fig. 5.20. The air-to-water heat pump was switched off, due to the temperature limit of the thermostat controller of 60 °C being achieved, as seen from Fig. 5.19. From 00h30 – 05h30, the temperature of the HWST decreased gradually, due to standby losses experienced by the HWST. From, 05h30 – 06h00, the temperature begins to decrease significantly, due to the demand of hot water during this period, as seen from Fig. 5.4.

5.4.1.8 b) First standard pricing period 06h00 - 07h00 (yellow)

From 06h00 – 06h30, the residential building temperature continued to decrease, as the air-to-air heat pump was switched on during this period, seen from Figs. 5.17 and 5.18. The air-to-air heat pump was switched on during this period, until to the minimum temperature limit of 22 °C, was achieved. From 06h30 – 07h00, the residential building temperature increased, due to the air-to-air heat pump being switched off, as seen from Fig. 5.17.

From 06h00 – 07h00, the temperature inside the HWST, continued to decrease significantly, as seen from Fig. 5.4, until it reached the minimum temperature limit of 45 °C, which may be observed from Fig. 5.20. The air-to-water heat pump remained switched off during this period, due to the minimum temperature limit being reached solely at the end of this period.

5.4.1.8 c) First peak pricing period 07h00 - 10h00 (red)

From 07h00 – 10h00, the residential building temperature continued to increase, as seen in Fig. 5.18. This is due to the maximum temperature limit of 24 °C not being achieved during this period.

From 07h00 – 07h30, the temperature of the HWST decreased, as seen from Fig. 5.20, due to the air-to-water heat pump was switched off, as seen from Fig. 5.19. From 07h30 – 08h30, the temperature of the HWST started to increase, as seen from Fig. 5.20. This was due to the air-to-water heat pump being switched on, by means of the timer, to achieve the desired temperature. From 08h30 – 10h00, the temperature of the HWST started to decrease, due to the maximum temperature limit of 60 °C being reached, as seen from Fig. 5.20. Therefore, the air-to-water heat pump was switched off, which caused the temperature to decrease, as seen from Fig. 5.19.

5.4.1.8 d) Second standard pricing period 10h00 - 18h00 (yellow)

From 10h00 – 13h30, the residential building temperature continued to increase, as seen in Fig. 5.18, due to the air-to-air heat pump being switched off. From 13h30 – 16h30, the residential building temperature started to decrease, as seen from Fig. 5.17, which was due to the air-to-air heat pump being switched on by means of the timer, in order to achieve the desired temperature. From 16h30 – 18h00, the residential building started to increase, due to the air-to-air being switched off, as seen from Fig. 5.17.

From 10h00 – 18h00, the residential building temperature continued to gradually decrease, as seen in Fig. 5.20. The air-to-water heat pump remained switched off, due to the minimum temperature limit of 45 °C not yet achieved, illustrated in Fig. 5.19.

5.4.1.8 e) Second peak pricing period 18h00 - 20h00 (red)

From 18h00 – 18h30, the residential building temperature started to decrease, due to the air-to-air heat pump being switched on again, by means of the timer, to achieve the desired temperature set-point during the peak pricing region of the TOU tariff structure, as illustrated in Fig. 5.18. From 18h30 – 19h00, the residential building temperature started to increase, due to the air-to-air heat pump that was switched off, by means of the thermostat controller, as the minimum temperature of 22 °C was achieved.

From 18h00 – 18h30, the temperature of the HWST started to increase, until it reached the maximum temperature limit of 60 °C, which was during the peak pricing period, as illustrated in Fig. 5.20. From 18h30 – 19h30, the temperature started to decrease, because of the air-to-water heat pump switched off by means of the thermostat controller, as seen from Figs. 5.19 and 5.20. From 19h30 – 20h00, the temperature of the HWST started to increase, due to the minimum temperature limit of 45 °C being achieved, as seen from Fig. 5.20.

5.4.1.8 f) Third standard pricing period 20h00 - 22h00 (yellow)

From 20h00 – 22h00, the residential building temperature continued to increase, due to the air-to-air heat pump being switched off, by means of the thermostat controller, as the maximum temperature limit of 24 °C was not obtained, which may be observed in Fig. 5.18.

From 20h00 – 21h00, the temperature of the HWST continued to increase, due to the air-to-water heat pump being switched on, as seen from Fig. 5.20. From 21h00 – 22h00, the temperature of the HWST started to decrease, as seen from Fig. 5.20. This was due to the air-to-water heat pump being switched off by means of the thermostat controller, as the maximum temperature limit of 60 °C was achieved, observed in Fig. 5.19.

5.4.1.8 g) Second off-peak pricing period 22h00 - 24h00 (green)

From 22h00 – 24h00, the residential building temperature continued to increase, as seen in Fig. 5.18. The residential building temperature increased, due to the air-to-air heat pump being switched off during this period, as seen in Fig. 5.17. The air-to-air heat pump was not required to be switched on, due to the maximum temperature limit not yet being reached at 24h00.

From 22h00 – 24h00, the temperature of the HWST continued to decrease, as seen in Fig. 5.20. The temperature continued to decrease, due to the air-to-water heat pump switched off during this period, as seen in Fig. 5.19. This was due to the minimum temperature limit not yet being reached and there was no further demand for hot water during this period, as seen from Fig. 5.4.

5.4.2 Optimal control case

The optimal control of a residential energy hub integrating renewable energy, demand response and energy storage system, is discussed in Section 5.2.1. This model optimally controls the switching of the air-to-air heat pump and the air-to-water heat pump, based on the optimal power flow of the integrated renewable energy system. The optimal power flow of the residential energy hub, integrating renewable energy, demand response and energy storage, is further presented in Section 5.4.2. Furthermore, this optimal control model attempts to minimize the grid electrical energy cost supplied to the residential energy hub and the PEMWE, as well as maximize the electrical energy supplied from the solar PV modules to the electrical load and thereafter to the PEMWE. The level of discomfort is minimized, further between the residential building temperature and the desired building temperature, which is the responsibility of the air-to-air heat pump. Furthermore, the level of discomfort is minimized between the HWST temperature and the desired building temperature, which is the responsibility of the air-to-water heat pump. The burden on the air-to-water heat pump is further reduced, as the thermal energy is recovered from the solar

PV modules, PEMWE and the PEMFC. This is mainly due to heat being generated during the nature of their operation, as mentioned before.

In this Section, the optimal control of a residential energy hub integrating renewable energy, demand response and energy storage system is simulated, using the SCIP solver, in the optimization toolbox of MATLAB. This model optimally controls the switching of the air-to-air heat pump and the air-to-water heat pump, based on the optimal power flow of the integrated renewable energy system. The optimal power flow of the residential energy hub, integrating renewable energy, demand response and energy storage, is further presented in Section 5.4.2. Furthermore, this optimal control model attempts to minimize the grid electrical energy cost, supplied to the residential energy hub and the PEMWE and, to maximize the electrical energy supplied from the solar PV modules to the electrical load as well as, thereafter, to the PEMWE. The level of discomfort is minimized further between the residential building temperature and the desired building temperature, which is the responsibility of the air-to-air heat pump. Furthermore, the level of discomfort is minimized between the HWST and desired building temperatures, which is the responsibility of the air-to-water heat pump. The burden on the air-to-water heat pump is further reduced, as the thermal energy is recovered from the solar PV modules, PEMWE and the PEMFC. This is mainly due to heat being generated during the nature of their operation, as mentioned before.

The optimal control of a residential energy hub integrating renewable energy, demand response and energy storage system, is simulated, based on three categorized parameters.

The first category is, the parameters used for space heating and space cooling, which was adopted from Chapter III. In Table 3.1, the residential building parameters are presented and the lighting load is illustrated in Fig. 3.2, the occupancy load is illustrated in Fig. 3.3, the heat pump parameters are presented in Table. 3.2, the ambient air temperature is illustrated in Fig. 3.4 and simulation parameters are illustrated in Table. 3.3.

The second category is the parameters used for water heating. In Table 5.1 the parameters of the HWST and the air-to-water heat pump, the PEMFC parameters is presented in Table. 5.2, the hot water demand profile is illustrated in Fig. 5.4, heat pump

parameters in Table. 5.1, the ambient air temperature during winter and summer, are illustrated in Figs. 3.4 and 3.5, depicted in Chapter II, respectively, as well as simulation parameters in Table. 5.3.

The third category is the parameters used for the integrated renewable energy, demand response and energy storage system portion of the residential energy hub. In Fig. 5.2, the electrical load during winter was illustrated, the electrical load during a selected summer day was illustrated and the simulation parameters are presented in Table. 5.3.

In this Section, the simulation results of the optimal control case during a selected summer day, was illustrated. In Figs. 5.21 and 5.22, the optimal switching function of the air-to-air heat pump and the residential building temperature are illustrated, respectively.

The optimal switching function of the air-to-water heat pump and the HWST temperature, depicted in Figs. 5.23 and 5.24, are illustrated.

The thermal energy recoveries, with respect to the solar PV module, PEMWE and PEMFC, are illustrated in Figs. 5.25 – 5.27, respectively.

In Fig. 5.28, the electrical power flows to the electrical load, was illustrated to satisfy the electrical load demand, as illustrated in Fig. 5.2. Fig. 5.29, depicts the electrical power flows to the PEMWE, to supply the hydrogen storage tank with hydrogen, as seen from Fig. 5.30.

5.4.2.1 Winter case

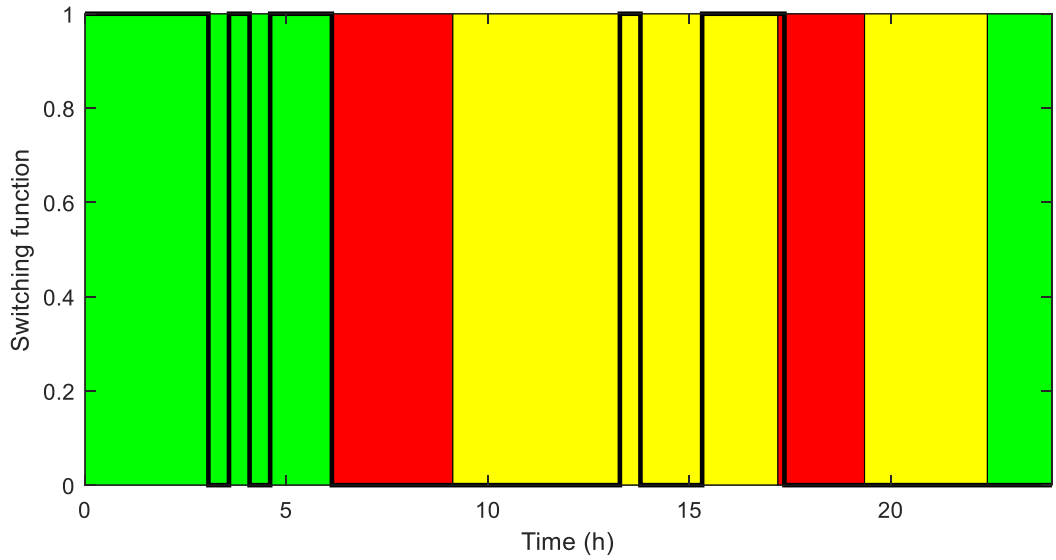

Fig. 5.21: Optimal switching function of the air-to-air heat pump during winter

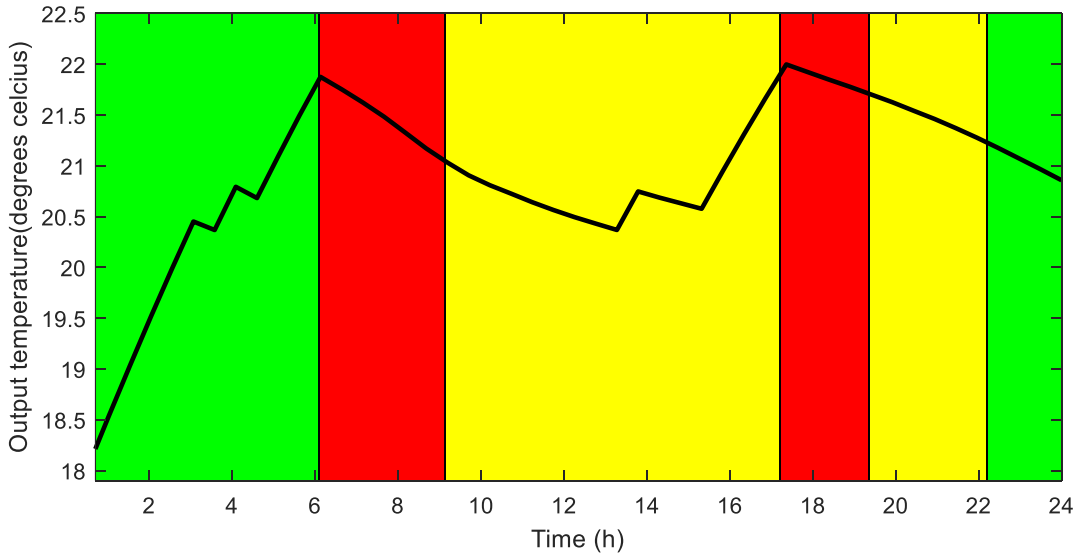

Fig. 5.22: Residential building temperature during winter

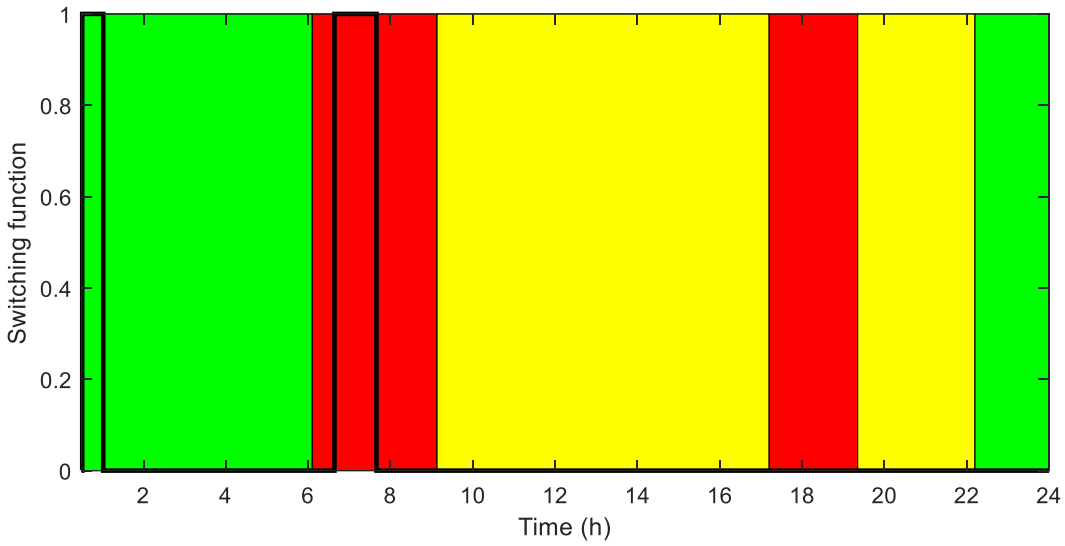

Fig. 5.23: Optimal switching function of the air-to-water heat pump during winter

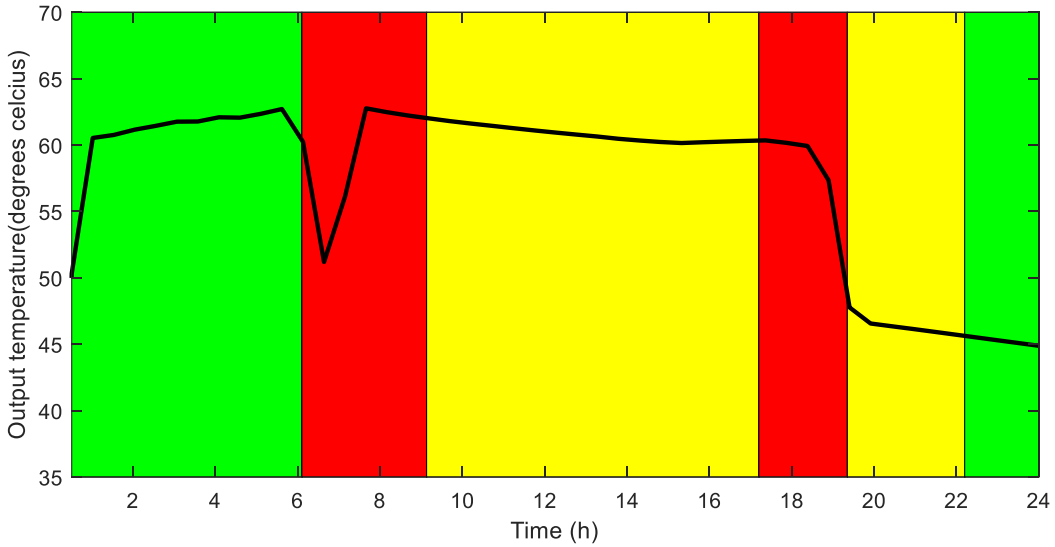

Fig. 5.24: HWST temperature during winter

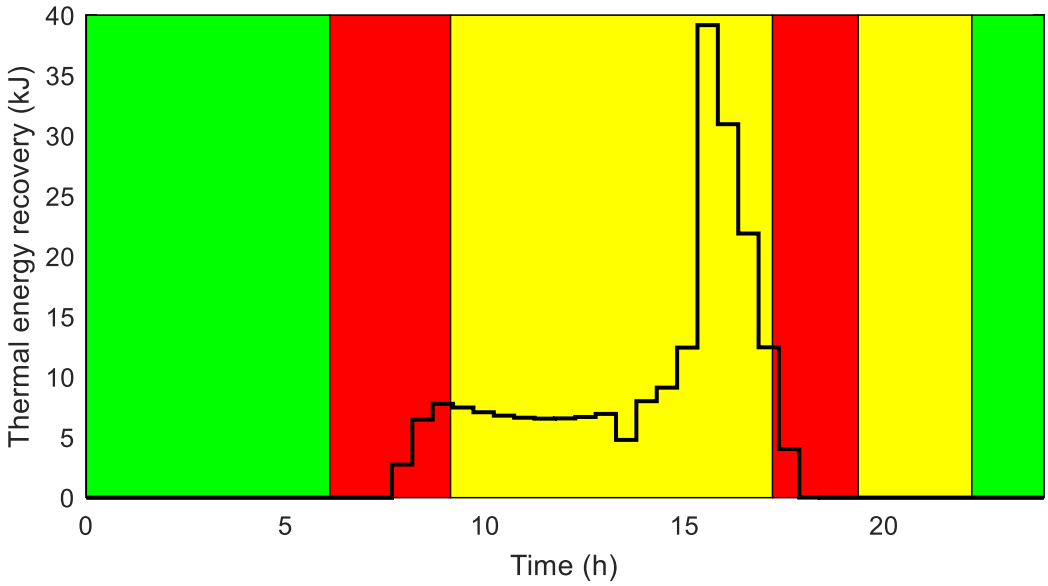

Fig. 5.25: PV thermal energy recovery during winter

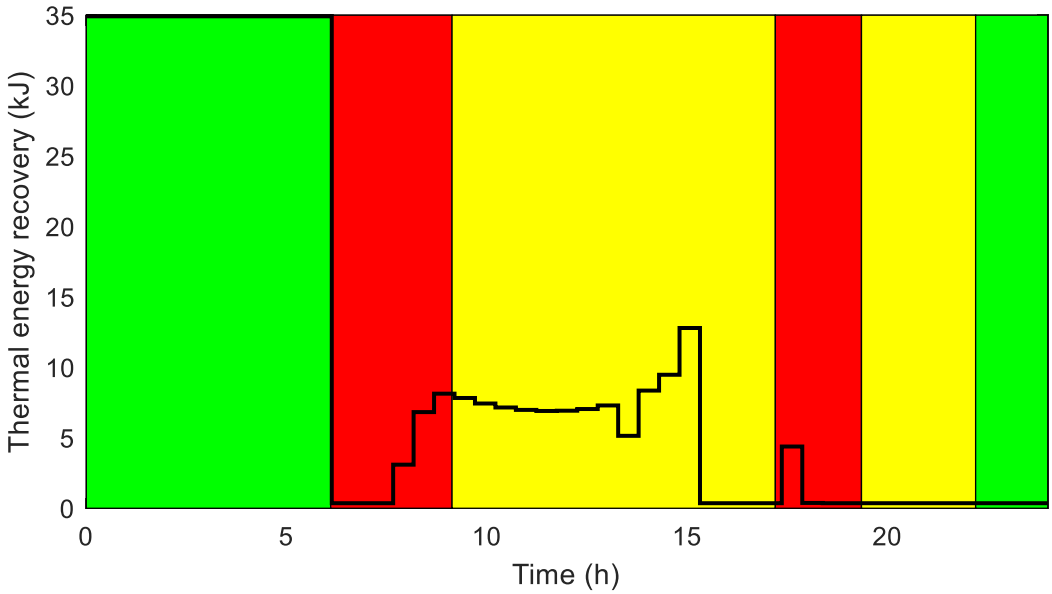

Fig. 5.26: PEMWE thermal energy recovery during winter

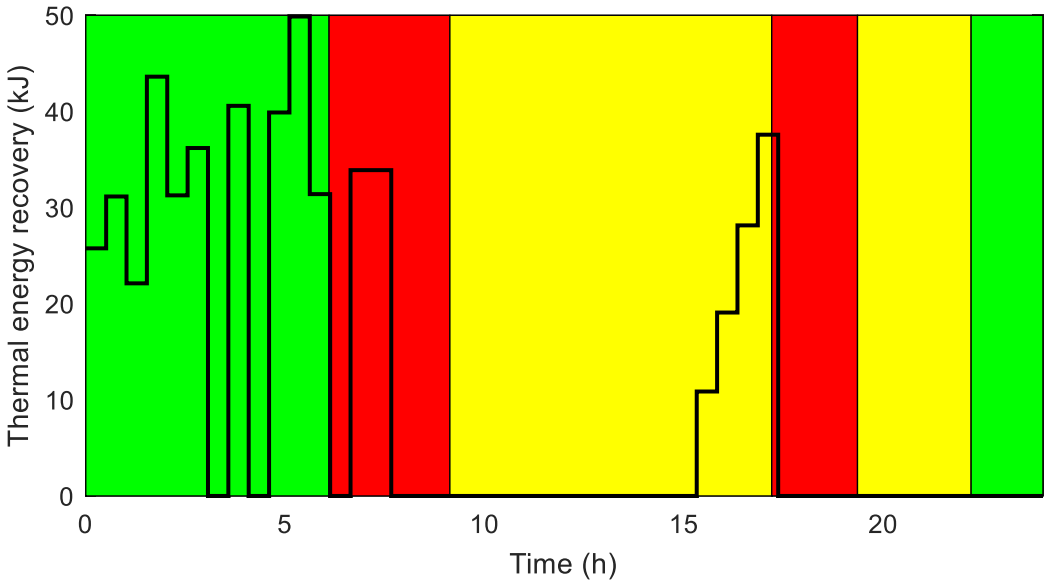

Fig. 5.27: PEMFC thermal energy recovery during winter

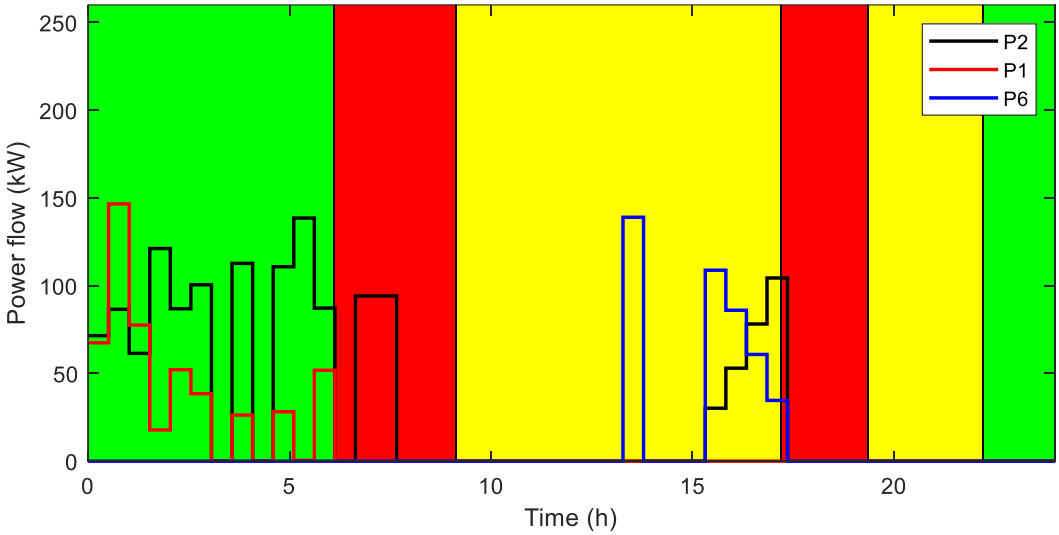

Fig. 5.28: Electrical power flows to load during winter

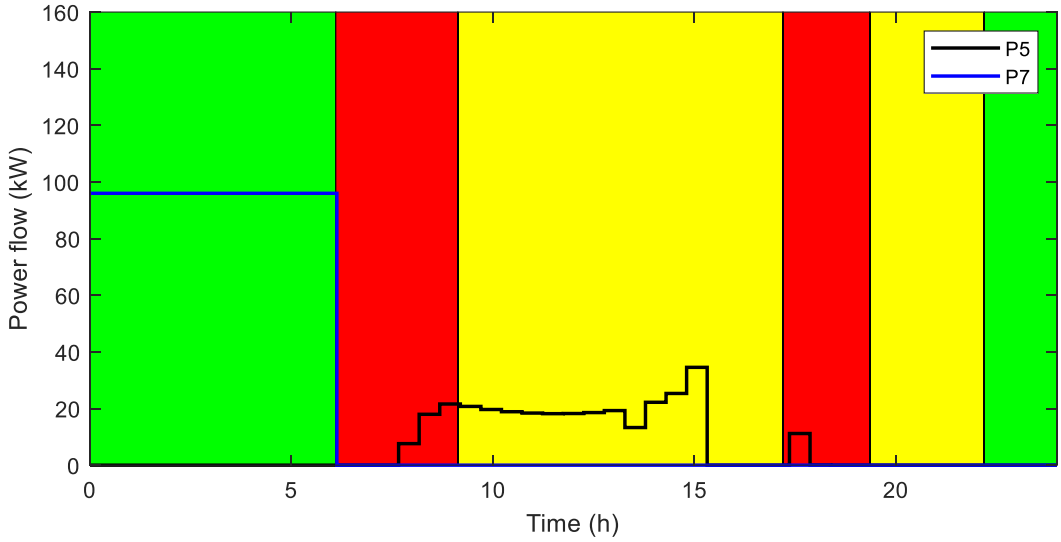

Fig. 5.29: Electrical power flows to PEMWE during winter

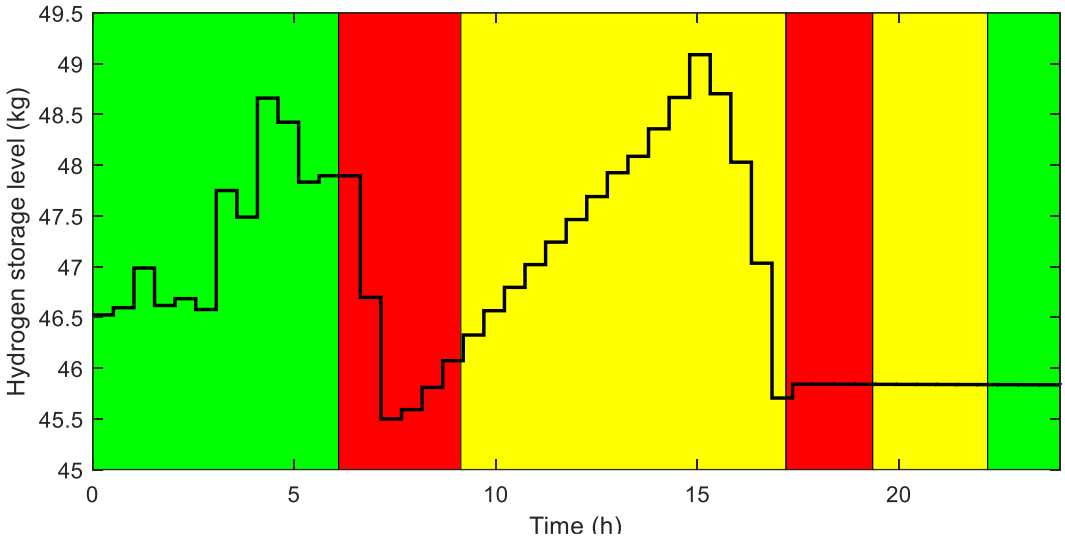

Fig. 5.30: Hydrogen storage tank dynamics during winter

5.4.2.2 Winter case discussion

5.4.2.2 a) First off-peak pricing period 00h00 - 06h00 (green)

From Fig. 3.2, the lighting load may be observed, which occurs solely from 04h00 and, from Fig. 3.3, it may be observed that there was an occupancy load during the entire first off-peak pricing period, where both of these loads were contributing towards heating the space of the residential building. From Fig. 3.4, the ambient temperature initially started at 10 °C and decreases until 06h00, which was when the ambient temperature is at 4 °C.

In Fig. 5.22, the temperature inside the residential building, heated by the air-to-air heat pump, was presented. Initially, the temperature inside the residential building started at 18.2 °C, which was the final state of the previous day. From 00h00 – 03h00, the building temperature increased, in order to reach 22 °C, which was the morning desired temperature set-point. From 03h00 – 03h30, the building temperature decreased, which may be observed from Fig. 5.22, due to the air-to-air heat pump being switched off. From 03h30 – 04h00, the building temperature started to increase again, as seen from Fig. 5.22, until the desired temperature of 22 °C was obtained. From 04h00 – 04h30, the building temperature started to decrease, due to air-to-air heat pump being switched off, as seen from Fig. 5.21. From 04h30 – 06h00, the building temperature increased, due to air-to-air heat pump being switched on, which was when the desired temperature set-point was achieved.

From 00h00 - 00h30, the temperature of the HWST increased to 60.53 °C, due to the air-to-water heat pump being switched on, to achieve the desired temperature during the morning, as seen from Figs. 5.23 and 5.24. From 00h30 – 05h30, the air-to-water heat pump was switched off, as seen from Fig. 5.23. However, the residential building temperature continued to increase, due to the HWST recovering thermal energy from the PEMWE and PEMFC, as seen from Fig. 5.26 and 5.27, respectively. From 05h30 – 06h00, the HWST temperature has decreased, as seen from Fig. 5.24, which was due to the presence of the hot water demand, as seen from Fig. 5.4.

From 00h00 – 06h00, electrical power was flowing from the utility grid, P_1, and the PEMFC, P_2, to the load, purely supplying the air-to-air heat pump and air-to-water heat pump, as seen from Fig. 5.28.

From 00h00 – 06h00, the utility grid, P_7, was purely supplying power to the PEMWE during this period for hydrogen production, as seen from Fig. 5.29.

From 00h00 – 03h00, the hydrogen storage tank level remained stable at 46.58 kg, as seen from Fig.5.30. During this period, the PEMFC utilized the hydrogen, whilst the PEMWE was supplying the hydrogen storage tank with hydrogen, as seen from Figs. 5.28 – 5.30. From 03h00 – 03h30, the hydrogen storage level decreased slightly, due to the PEMFC requiring hydrogen, to supply the electrical load with electrical energy, which was higher than the amount of hydrogen power supplied to the hydrogen storage tank, as seen from Figs. 5.28 – 5.30. From 03h30 – 04h00, the hydrogen storage level increased to 47.75 kg, due to the PEMWE supplying the hydrogen storage tank and, the PEMFC was not in operation during this period, as seen from Figs. 5.28 – 5.30. From 04h00 – 06h00, the hydrogen storage tank level decreased, due to the PEMFC required to supply electrical energy to the electrical load which was higher than what the PEMWE was supplying hydrogen to the hydrogen storage tank, as seen from Figs. 5.28 – 5.30.

5.4.2.2 b) First peak pricing period 06h00 - 09h00 (red)

From 06h00 – 09h00, the residential building temperature decreased, as seen in Fig. 5.22. This was due to the air-to-air heat pump being switched off, as seen from the switching function of the air-to-air heat pump, illustrated in Fig. 5.21. The main reasons for the air-to-air heat pump being switched off, was due to the peak pricing period, as well as the residential building, which was not required to be heated, as few occupants were present in this period.

From 06h00 – 06h30, the temperature of the HWST continued to decrease, due to the air-to-water heat pump switched off, as seen from Figs. 5.23 and 5.24. However, the main reason the temperature decreased, was due to the hot water demand being present during

this time, as seen from Fig. 5.4. From 06h30 – 07h30, the temperature of the HWST started to increase, due to the air-to-water heat pump being switched on during this period, as seen from Figs. 5.23 and 5.24. From 07h30 – 09h00, the temperature of the HWST, started to decrease slightly.

From 06h00 – 06h30, none of the electrical energy sources supplied electrical energy to the electrical load, as seen from Fig. 5.28. From 06h30 – 07h30, the PEMFC supplied electrical energy to the electrical load, as seen from Fig. 5.28, as the utility grid and the solar PV modules were incapable of supplying electrical energy demanded from the electrical load, due to this time being the peak pricing period of the TOU tariff structure. From 07h30 – 09h00, none of the electrical energy sources were required to supply electrical energy to the electrical load, as seen from Fig. 5.28

From 06h00 – 07h30, neither the utility grid nor the solar PV modules, supplied electrical energy to the PEMWE, as seen from Fig. 5.29. However, from 07h30 – 09h00, the solar PV modules started to supply electrical energy to the PEMWE, as seen from Fig. 5.29.

From 06h00 – 07h00, the hydrogen storage tank decreased significantly to 45.5 kg, due to the PEMFC supplied electrical energy to the electrical load, as seen from Figs. 5.28 and 5.30. The reason for the PEMFC being in operation, was due to the utility grid failing to supply supplying the electrical load during the peak pricing region of the TOU tariff structure. From 07h00 – 09h00, the hydrogen storage level started to gradually increase, due to the PEMWE supplying the hydrogen storage tank, by means of the solar PV modules, as seen from Figs 5.29 – 5.30. Furthermore, the electrical load did not demand electrical power, as seen from Fig. 5.2.

5.4.2.2 c) First standard pricing period 09h00 - 17h00 (yellow)

From 09h00 – 13h00, the residential building temperature continued to decrease, as seen from Fig. 5.22. From 13h00 – 13h30, the residential building temperature started to increase, due to the air-to-air heat pump being switched on, as seen from Fig. 5.22, ensuring that the least amount of energy was consumed. From 13h30 – 15h00, the residential building

temperature started to decrease, due to the air-to-air heat pump being switched off, as seen from Fig. 5.21. From 15h00 – 17h00, the air-to-air heat pump was switched on, as seen in Fig. 5.21, as the desired temperature was achieved.

From 09h00 – 15h30, the temperature of the HWST continued to decrease slightly, due to the air-to-water heat pump being switched off during this period, as seen from Figs. 5.23 and 5.24. From 15h30 - 17h00, the temperature of the HWST stabilized, as a result of the thermal energy recovered, mainly from the solar PV modules and the PEMFC, as seen from Figs. 5.25 and 5.27.

From 09h00 – 13h00, the electrical load did not demand electrical power, as seen from Figs. 5.2 and 5.28. From 13h00 – 13h30, the solar PV modules, P_6, were supplied electrical energy to the electrical load, as seen from Fig. 5.28. From 13h30 - 15h00, the electrical load did not require electrical power, as seen from Figs. 5.2 and 5.28. From 15h00 – 17h00, the solar PV modules, P_6 and the PEMFC, P_2, supplied electrical power to the electrical load, as seen from Fig. 5.28.

From 09h00 – 15h00, the solar PV modules, P_5, supplied electrical energy to the PEMWE, as seen from Fig. 5.29. From 15h00 – 17h00, the PEMWE was not supplied with electrical power during this period, as seen from Fig. 5.29.

From 09h00 – 15h30, the hydrogen storage tank increased from 46.33 kg to 49.09 kg, as seen from Fig. 5.30. This was due to the solar PV modules that supplied electrical energy to the PEMWE for hydrogen production, as seen from Fig. 5.29. From 15h30 – 17h00, the hydrogen storage level decreased significantly from 49.09 kg to 45.7 kg, as seen from Fig. 5.30, due to the PEMFC supplying electrical energy to the electrical load, as seen from Fig. 5.28.

5.4.2.2 d) Second peak pricing period 17h00 - 19h00 (red)

From 17h00 – 19h00, the residential building temperature decreased from 22 °C to 21.6 °C, as seen in Fig. 3.18. The residential building temperature decreased, due to the air-to-air heat pump being switched off during the peak pricing period, as seen in Fig. 3.17.

From 17h00 – 18h00, the temperature of the HWST was, even now, stabilized, due to the heat recovered from the solar PV modules and the PEMFC, as seen from Fig. 5.24. From 18h00 – 19h00, the temperature of the HWST decreased significantly to 47.77 °C, due to the hot water demand, as seen from Fig. 5.4.

From 17h00 – 19h00, none of the electrical energy sources supplied electrical energy to the electrical load, as seen from Fig. 5.28.

From 17h00 – 17h30, the solar PV modules, supplied electrical energy to the PEMWE, as seen from Fig. 5.29. From 17h30 – 19h00, none of the electrical energy sources supplied electrical energy to the PEMWE, as seen from Fig. 5.29.

From 17h00 – 17h30, the hydrogen storage level increased slightly to 45.84 kg, as seen from Fig. 5.30. From 17h30 – 19h00, the hydrogen storage level remained constant, as seen from Fig. 5.30, as the PEMWE did not supply hydrogen to the hydrogen storage tank and the PEMFC did not withdraw hydrogen power from the hydrogen storage, as seen from Fig. 5.28.

3.4.2.2 e) Second standard pricing period 19h00 - 22h00 (yellow)

From 19h00 – 22h00, the residential building temperature decreased from 21.6 °C to 21.2 °C, as seen in Fig. 5.22. The residential building temperature decreased, due to the air-to-air heat pump being switched off, during the standard pricing period, as seen in Fig. 5.21. The air-to-air heat pump was not required to be switched on, as the evening desired temperature set-point had passed.

From 19h00 – 22h00, the temperature of the HWST decreased slightly, due to the standby losses experienced by the HWST, as seen from 5.24. The air-to-water heat pump was not required to be switched on, as the evening desired temperature set-point had passed.

From 19h00 – 22h00, no further electrical energy was supplied to the electrical load from the PEMFC and the PEMWE did not supply hydrogen power to the hydrogen storage tank, as seen from Figs. 5.28 – 5.30.

5.4.2.2 f) Second off-peak pricing period 22h00 - 24h00 (green)

From 22h00 – 24h00, the residential building temperature decreased from 21.2 °C to 20.8 °C, as seen in Fig. 5.22. The residential building temperature decreased, due to the air-to-air heat pump being switched off during this period, as seen in Fig. 5.21. The air-to-air heat pump was not required to be switched on, due to the evening desired temperature set-point not being required, for the remainder of the evening.

From 22h00 – 24h00, the temperature of the HWST continued to decrease, as seen in Fig. 5.24. The temperature of the HWST decreased, due to the air-to-air heat pump being switched off during this period, as seen in Fig. 5.23. The air-to-air heat pump was not required to be switched on, as the evening desired temperature set-point was not required for the remainder of the evening.

From 22h00 – 24h00, no further electrical energy was supplied to the electrical load from the PEMFC, and the PEMWE did not supply hydrogen power to the hydrogen storage tank, as seen from Figs. 5.28 – 5.30.

5.4.2.3 Summer case

In this section, the simulation results of the optimal control case, during a selected summer day, is illustrated. In Figs. 5.31 and 5.32, the optimal switching function of the air-to-air heat pump and the residential building temperature, are illustrated, respectively.

The optimal switching function of the air-to-water heat pump and the HWST temperature, depicted in Figs. 5.33 and 5.34, are illustrated.

The thermal energy recoveries, with respect to the solar PV module, PEMWE and PEMFC, are illustrated in Figs. 5.35 – 5.37, respectively.

In Fig. 5.38, the electrical power flowing to the electrical load, is illustrated, to satisfy the electrical load demand, as illustrated in Fig. 5.3. Fig. 5.39 depicted the electrical power flows to the PEMWE, to supply the hydrogen storage tank with hydrogen, as seen from Fig. 5.40.

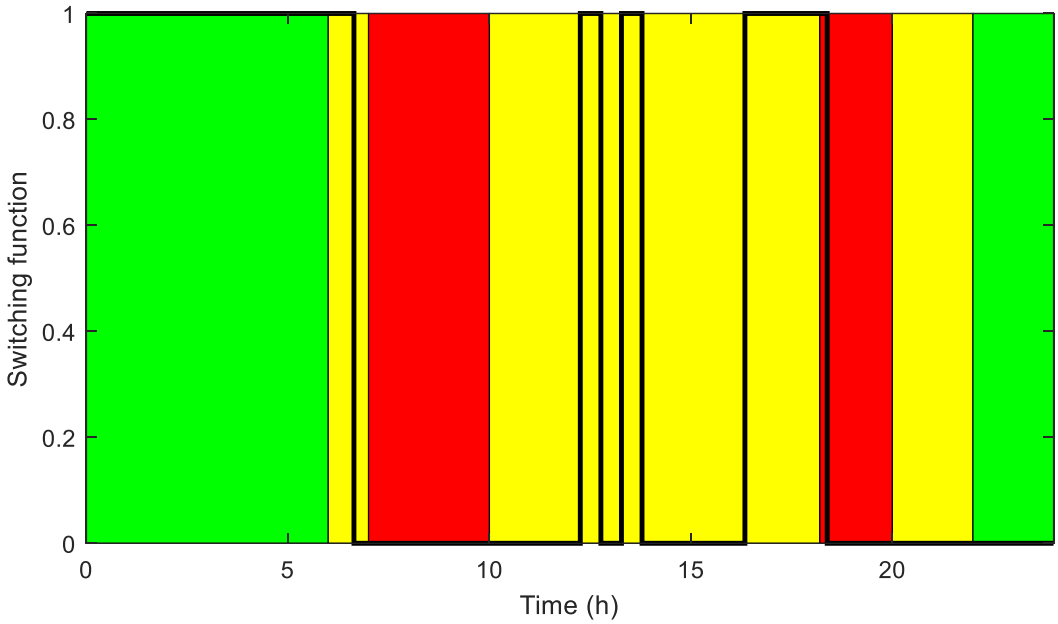

Fig. 5.31: Optimal switching function of the air-to-air heat pump during summer

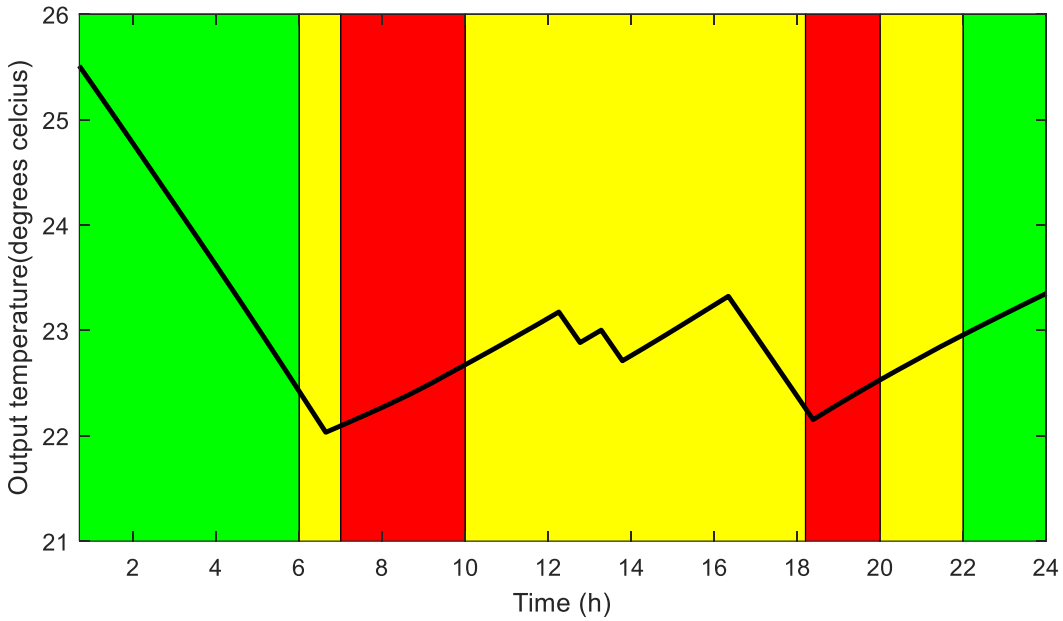

Fig. 5.32: Residential building temperature during summer

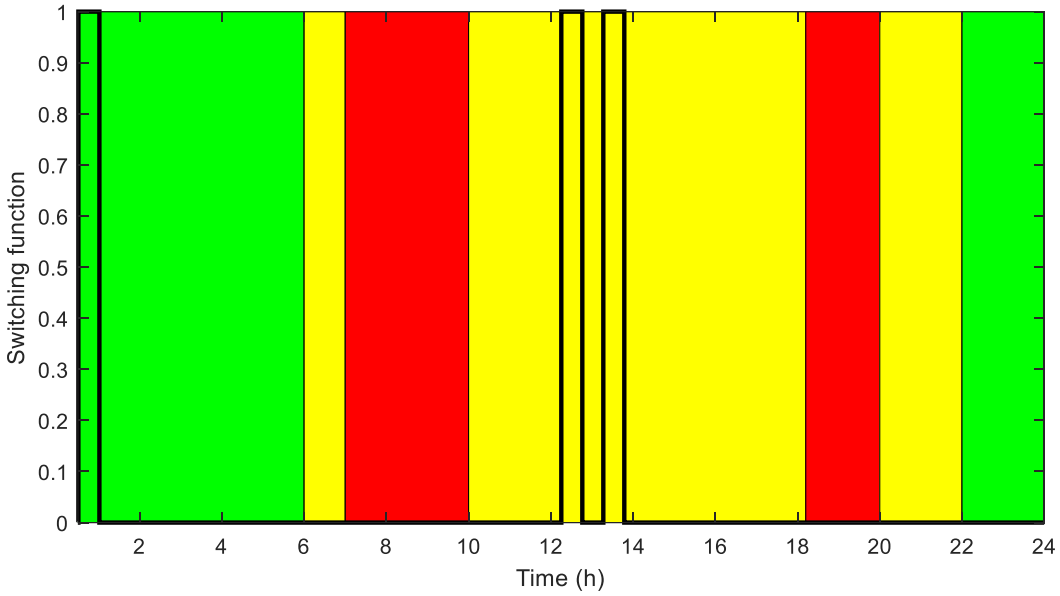

Fig. 5.33: Optimal switching function of the air-to-water heat pump during summer

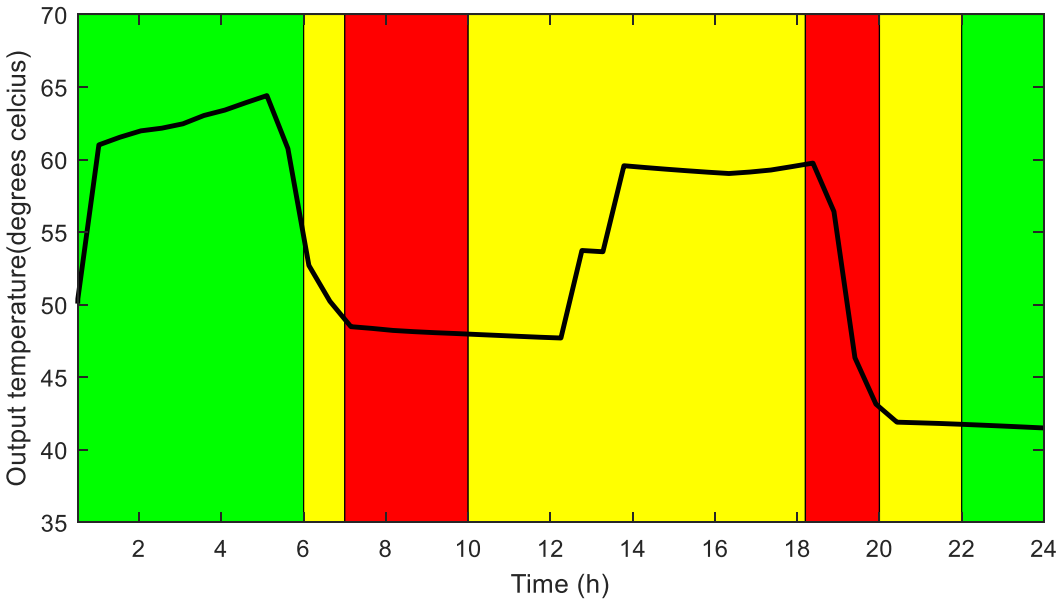

Fig. 5.34: HWST temperature during summer

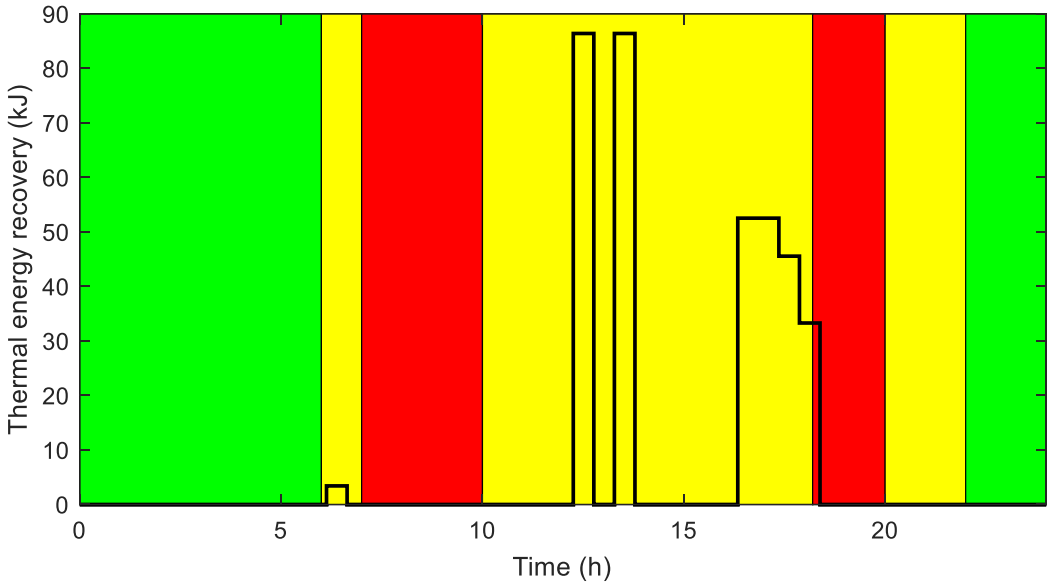

Fig. 5.35: PV thermal energy recovery during summer

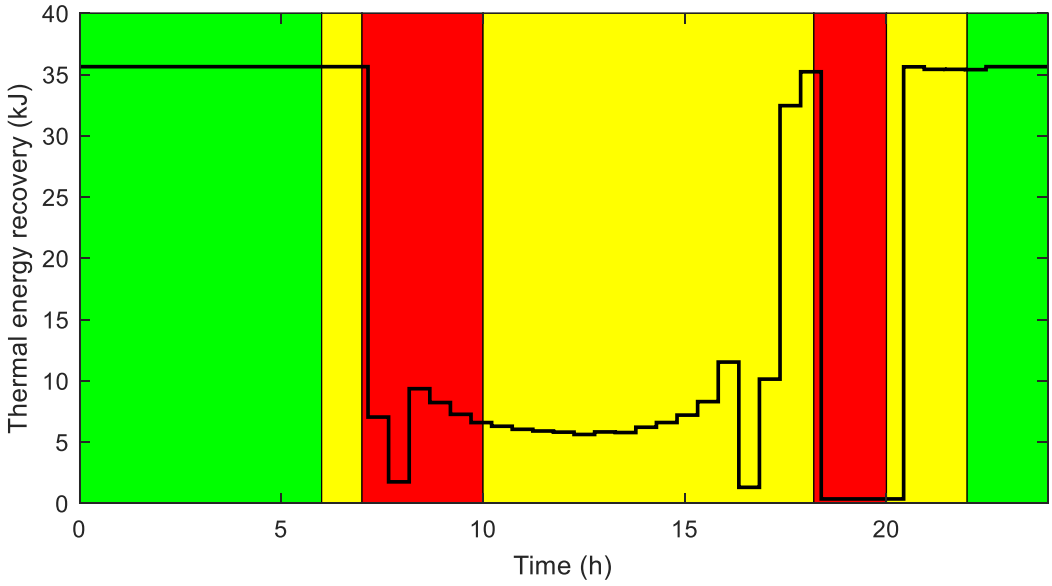

Fig. 5.36: PEMWE thermal energy recovery during summer

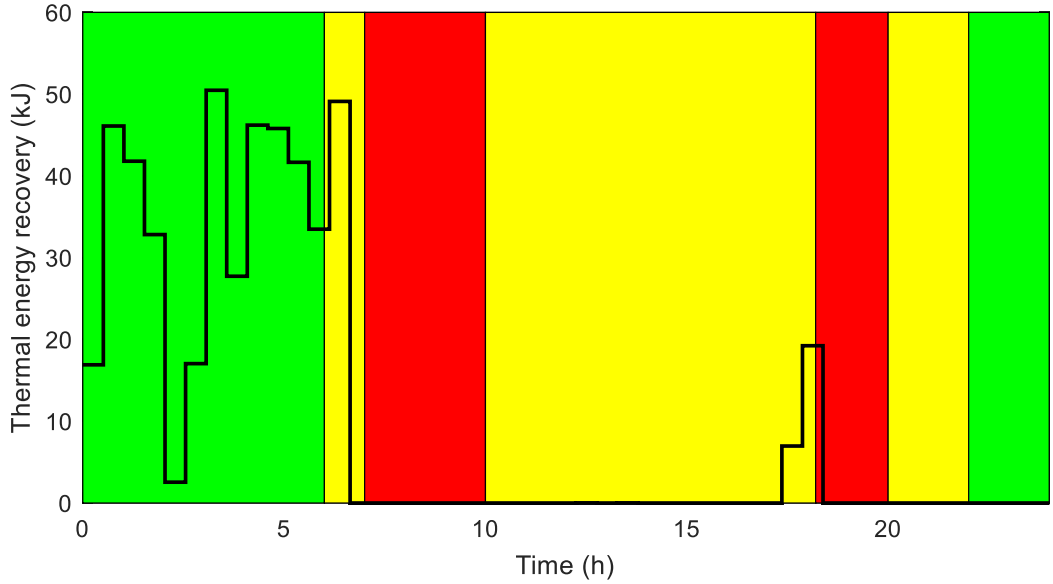

Fig. 5.37: PEMFC thermal energy recovery during summer

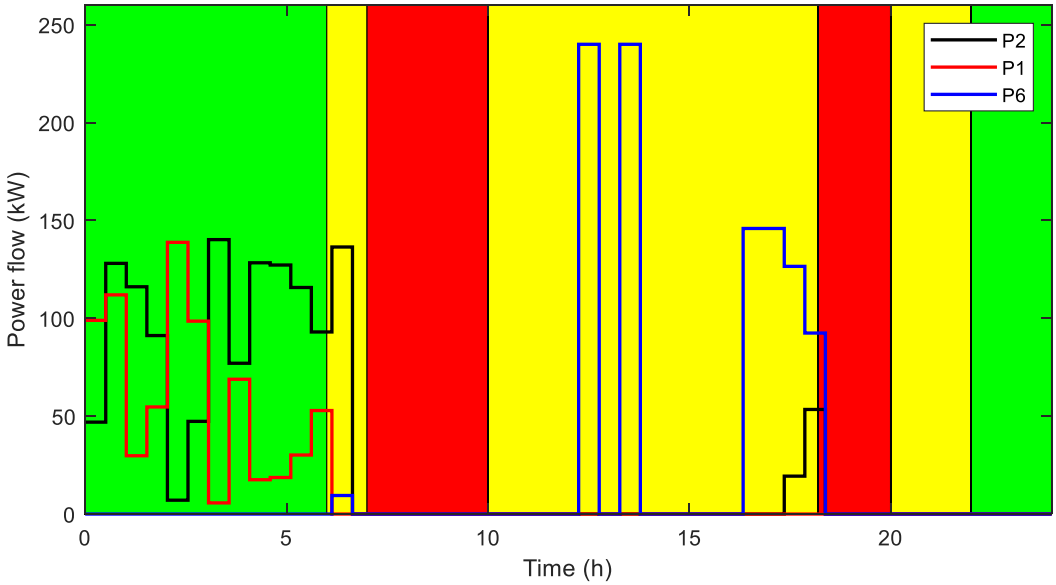

Fig. 5.38: Electrical power flows to load during summer

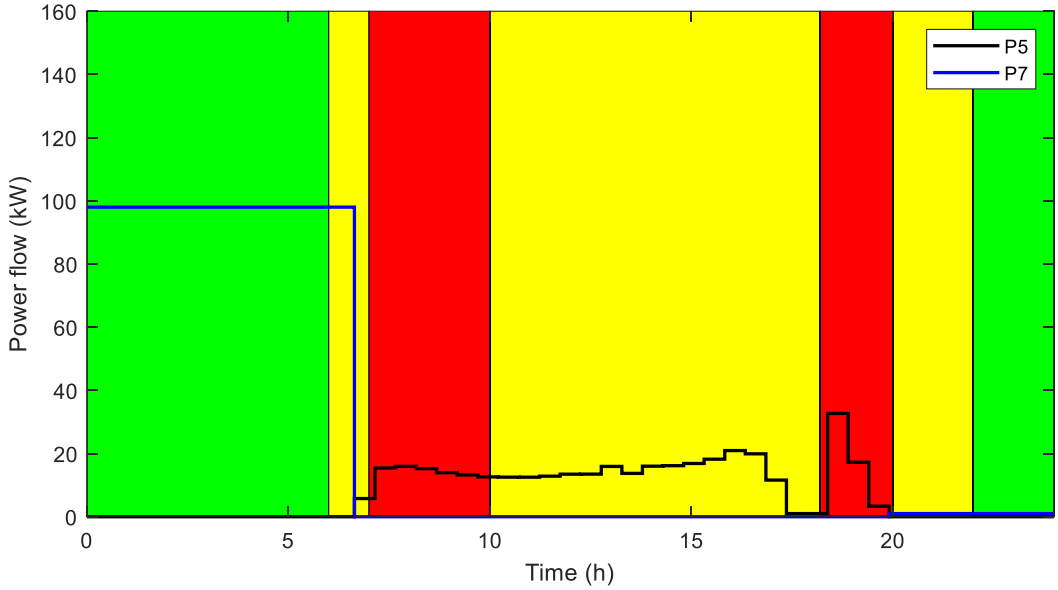

Fig. 5.39: Electrical power flows to PEMWE during summer

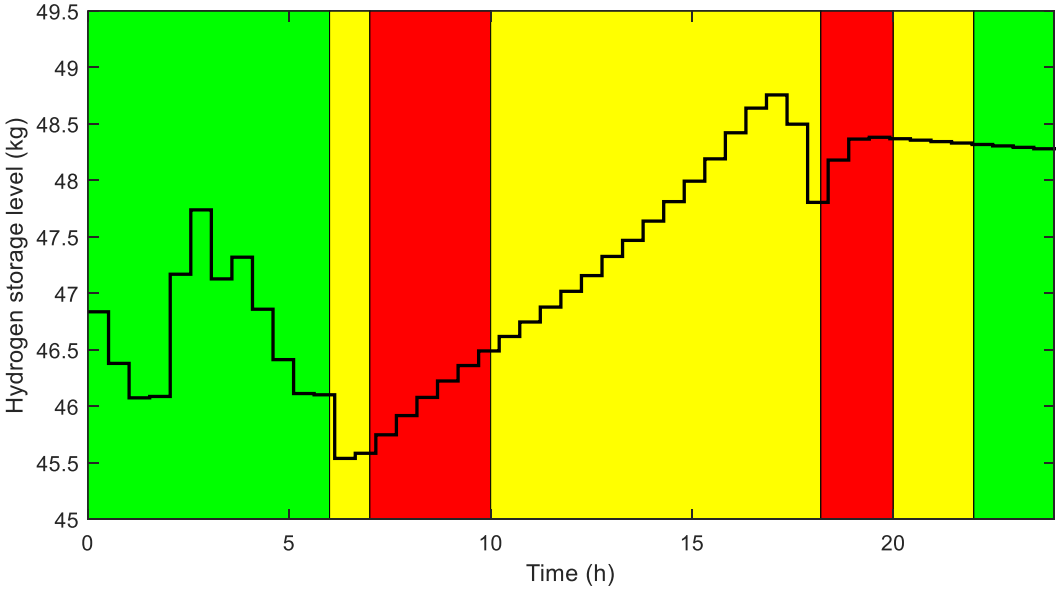

Fig. 5.40: Hydrogen storage tank dynamics during summer

5.4.2.4 Summer case discussion

5.4.2.4 a) First off-peak pricing period 00h00 - 06h00 (green)

In Figs. 5.31 and 5.32, the switching function of the air-to-air heat pump, as well as the temperature inside the residential building, were presented, respectively. Initially, the temperature inside the residential building started at 25.5 °C, which was the final state of the previous day. From 00h00 – 06h00, the building temperature decreased, due to the air-to-air heat pump being switched on, as seen from Fig. 5.31. It may be observed that the air-to-air heat pump was switched on from 00h00 until 06h00, in order to reach the minimum temperature set-point of 22 °C.

From 00h00 - 00h30, the temperature of the HWST increased to 60.95 °C, due to the air-to-water heat pump being switched on, to achieve the desired temperature during the morning, as seen from Figs. 5.33 and 5.34. From 00h30 – 05h00, the air-to-water heat pump was switched off, as seen from Fig. 5.33. However, the residential building temperature continued to increase, which is due to the HWST recovering thermal energy from the PEMWE and PEMFC, as seen from Fig. 5.38 and 5.39, respectively. From 05h00 – 06h00, the HWST temperature has decreased, as seen from Fig. 5.34, which was due to the presence of the hot water demand, as seen from Fig. 5.3.

From 00h00 – 06h00, electrical power flowed from the utility grid, P1 and the PEMFC, P2, to the load, purely supplying the air-to-air heat pump and air-to-water heat pump, as seen from Fig. 5.38.

From 00h00 – 06h00, the utility grid, P_7, was purely supplying power to the PEMWE during this period, for hydrogen production, as seen from Fig. 5.39.

From 00h00 – 02h00, the hydrogen storage tank level has decreased, due to the PEMFC, P_2, required hydrogen from the hydrogen storage tank, as seen from Figs. 5.40 and 5.38. During this time, the hydrogen drawn from the storage tank was higher than what the PEMWE was supplying, as seen from Fig. 5.39. From 02h00 – 03h00, the hydrogen storage tank level has increased, due to utility grid increasing the power supplied to the load, instead

of the PEMFC. From 03h00 – 06h00, the hydrogen storage level decreased, due to PEMFC, once again, taking over from the utility grid, as seen from Figs. 5.40 and 5.38, respectively.

5.4.2.4 b) First standard pricing period 06h00 - 07h00 (yellow)

From 06h00 – 06h30, the residential building temperature continued to decrease, as the air-to-air heat pump was switched on during this period, as seen from Figs. 5.31 and 5.32. The air-to-air heat pump was switched on during this period until the desired temperature set-point of 22 °C, was achieved. From 06h30 – 07h00, the residential building temperature increases, due to the air-to-air heat pump being switched off, as seen from Fig. 5.35.

From 06h00 – 07h00, the temperature of the HWST continued to decrease, as the air-to-water heat pump was switched off, as seen from Figs. 5.33 and 5.34. However, the main reason the temperature was decreasing, was due to the hot water demand being present during this time, as seen from Fig. 5.4.

From 06h00 – 07h00, electrical power was supplied to the load from the PEMFC and a small part of the PV electrical power, was further supplied to the load, as seen from Fig. 5.38.

The hydrogen storage level decreased as a result of the PEMFC, as seen from Fig. 5.40. However, the PEMWE supplied hydrogen to the hydrogen storage tank, however, at a lower rate than the amount that the PEMFC was demanding, as seen from Figs. 5.38 – 5.40.

5.4.2.4 c) First peak pricing period 07h00 - 10h00 (red)

From 07h00 – 10h00, the residential building temperature increased, as seen in Fig. 5.32. This was due to the air-to-air heat pump being switched off, as seen from the switching function of the air-to-air heat pump, illustrated in Fig. 5.31. Furthermore, the residential building temperature continued to increase, as this was during the peak pricing region of the TOU tariff structure.

From 07h00 – 10h00, the temperature of the HWST in Fig. 5.34 decreased slightly, as no hot water was required, as seen from Fig. 5.4 and the air-to-water heat pump was switched off, as seen from Fig. 5.33. Furthermore, barely only thermal energy was being recovered through the PEMWE, as seen from Fig. 5.39, which was the reason for the slight temperature decrease, during this period.

During this period, no electrical energy was supplied to the load, as seen from Fig. 5.38. This was due to electrical energy not being required, as seen from the electrical load demand, in Fig. 5.3. However, during this period, hydrogen was produced by the PEMWE, through the solar PV modules, P_6, which may be observed from the increase in the hydrogen storage level in Fig. 5.40 and the power delivered to the PEMWE, in Fig. 5.39.

5.4.2.4 d) Second standard pricing period 10h00 - 18h00 (yellow)

From 10h00 – 12h00, the residential building temperature increased, as seen in Fig. 5.32, as the air-to-air heat pump continued to be switched off, illustrated in Fig. 5.31. From 12h00 – 12h30, the residential building temperature started to decrease, as seen from Fig. 5.32, which was due to the air-to-air heat pump being switched on. From 12h30 – 13h00, the residential building temperature increased, as the air-to-air heat pump was switched off, as seen from Fig. 5.31. From 13h00 – 13h30, the temperature inside the residential building decreased, as the air-to-air heat pump was switched on, as seen from Fig. 5.31, ensuring that the least amount of energy was consumed. From 13h30 – 16h00, the temperature inside the residential building started to increase, as seen from Fig. 5.32. From 16h00 – 18h00, the air-to-air heat pump was switched on again, in order to achieve the desired temperature set-point, as seen from Fig. 5.31.

From 10h00 – 12h00, the temperature of the HWST continued to decrease slightly, as the air-to-water heat pump was switched off during this period, as seen from Figs. 5.33 and 5.34. From 12h00 - 13h30, the temperature of the HWST increased, as the air-to-water heat pump was switched on intermittently during this period, as seen from Fig. 5.33 and 5.34. From 13h30 – 16h00, the temperature of the HWST decreased slightly, as the air-to-water heat

pump was switched off during this period. The reason for the slight decrease in HWST temperature, was due to a low amount of thermal energy supplied from the PEMWE, as seen from Fig. 5.36. From 16h00 – 18h00, the temperature of the HWST increased slightly, as a result of the thermal energy recovered from the PV modules, PEMWE and PEMFC, as seen from Figs. 5.35 – 5.37.

From 10h00 – 12h00, the electrical load was not supplied with electricity, from any of the electrical energy supply sources, as seen from Fig. 5.38, as no electrical energy was demanded from the load, as seen from Fig. 5.3. From 12h00 – 13h30, the load was supplied with electrical energy from the solar PV modules, P_6, as seen from Fig. 5.38. From 13h30 – 16h00, none of the electrical energy supply sources supplied power to the electrical load, as seen from Fig. 5.38, as the load did not demand electrical energy during this period, as seen from Fig. 5.3. From 16h00 – 18h00, the solar PV modules and the PEMFC supplied power to the electrical load, as seen from Figs. 5.38 and 5.3.

From 10h00 – 17h00, the hydrogen storage level increased, until it reached 48.76 kg, as seen from Fig. 5.40. This was due to the PEMWE supplying hydrogen to the hydrogen storage tank, as seen from Fig. 5.39. From 17h00 – 18h00, the level of the hydrogen stored decreases, as seen from Fig. 5.40, as the PEMFC demanded hydrogen from the hydrogen storage tank, as seen from Fig. 5.38.

5.4.2.4 e) Second peak pricing period 18h00 - 20h00 (red)

From 18h00 – 20h00, the residential building temperature started to increase, as the air-to-air heat pump was switched off, as illustrated in Figs. 5.31 and 5.32.

From 18h00 – 20h00, the temperature of the HWST decreased significantly, due to the hot water demand during this period, as seen from Figs. 5.34 and 5.4. Furthermore, the air-to-water heat pump was further switched off during this period, as seen from Fig. 5.33.

It may be observed from Fig. 5.38, none of the power sources supplied electrical power to the load from 18h00 – 20h00, as there was no demand for electrical energy from the load, as seen from Fig. 5.3.

From 18h00 – 20h00, the solar PV modules supplied electrical energy to the PEMWE, to generate hydrogen, as seen from Fig. 5.39. Therefore, during this period, the hydrogen further correspondingly increased, as seen from Fig. 5.40.

5.4.2.4 f) Third standard pricing period 20h00 - 22h00 (yellow)

From 20h00 – 22h00, the residential building temperature increased from 22.5 °C to 22.9 °C, as seen in Fig. 5.32. The residential building temperature increased, as the air-to-air heat pump was switched off during this period, as seen in Fig. 5.31. The air-to-air heat pump was not required to be switched on, due to the evening desired temperature set-point having passed.

From 20h00 – 22h00, overall, the temperature of the HWST decreased overall slightly, as the air-to-water heat pump was switched off during this period, as seen from Figs. 5.33 and 5.34.

From 20h00 – 22h00, no power was supplied to the load and the PEMWE, during this period, as seen from Figs. 5.38 and 5.39, respectively. Therefore, the hydrogen storage level remained stable, as seen from Fig. 5.40.

5.4.2.4 g) Second off-peak pricing period 22h00 - 24h00 (green)

From 22h00 – 24h00, the residential building temperature increased from 22.9 °C to 23.3 °C, as seen in Fig. 5.32. The residential building temperature increased, as the air-to-air heat pump switched off during this period, as seen in Fig. 5.31. The air-to-air heat pump was not required to be switched on, as no evening desired temperature set-point was required, for the remainder of the evening.

From 22h00 – 24h00, the temperature of the HWST continued to decrease slightly, as seen from Fig. 5.34, as the air-to-water heat pump remained switched off during this period, as seen from Fig. 5.33.

From 22h00 – 24h00, no power was supplied to the load and the PEMWE, during this period, as seen from Figs. 5.38 and 5.39, respectively. Therefore, the hydrogen storage level remained stable, as seen from Fig. 5.40.

5.5 ECONOMIC ANALYSIS

5.5.1 Introduction

The feasibility of any project, should be economically validated, prior to the commencement thereof. In this case, the proposed optimal control of the residential energy hub integrating renewable energy, demand response and energy storage system, is economically evaluated, by comparing it against two baselines. These two baselines are described in sub-section 5.4.1. Well-known economic performance indicators exist, which may be utilized to evaluate the economic feasibility of the proposed optimal control system. These economic performance indicators include: simple payback period (SPP), benefits-to-cost ration (BCR), life cycle cost (LCC) and internal rate of return, amongst others [126]. Regarding the SPP, it is one of the simplest methods of determining the feasibility of a project. However, this technique has several flaws, with the main flaw being that it does not account for depreciation as a result of inflation, amongst other factors. Additionally, investors should be aware of the lifespan of the project in which they invest into. Therefore, the LCC analysis is used to evaluate the economic feasibility of the proposed system.

5.5.2 Annual energy cost-savings analysis

In this sub-section, the daily utility grid electrical energy cost of the first baseline, second baseline and the proposed optimal control model, is presented for the selected winter and summer days, where the TOU tariff structure is considered.

The calculated daily utility grid electrical energy costs, of the first baseline, the thermostat-based control of the air-to-air heat pump and the air-to-water heat pump, is

based on the simulation results obtained from sub-section 5.4.1, for the selected winter and summer days. The total daily energy consumption of the first baseline is 4 449.28 kWh and 4 715.6 kWh, during the selected winter and summer days, respectively. The calculated daily utility grid electrical energy consumption, is further used to calculate the daily utility grid electrical energy costs, depicted in Table 5.4.

The calculated daily utility grid electrical energy costs of the second baseline, which is the timer with thermostat-based control of the air-to-air heat pump and the air-to-water heat pump, are based on the simulation results obtained from sub-section 5.4.1, for the selected winter and summer days. The total daily energy of the second baseline, is 4 449.28 kWh and 4 715.6 kWh, during the selected winter and summer days, respectively. The calculated daily utility grid electrical energy consumption, is further used to calculate the daily utility grid electrical energy costs, depicted in Table 5.4.

The same process followed, to calculate the daily and annual utility grid electrical energy costs, applied to the proposed optimal control case, to determine the utility grid electrical energy cost-savings, compared to the first baseline, as well as the second baseline. The total daily utility grid energy consumption, for the selected winter and summer days, are calculated as 829.43 kWh and 1 004.8 kWh, respectively.

Table 5.4: Annual energy cost savings

Strategy	Energy cost (USD/day)	Energy cost (USD/annum)	Saving
Thermostat-based control (Baseline 1)			
Baseline 1 - winter	517.73 USD	517.73 x 92 days = 47 631.16 USD	/
Baseline 1 - summer	308.78 USD	308.78 x 273 days = 84 296.94 USD	
Baseline 1 - total net cost	/	131 928.1 USD	
Timer with thermostat-based control (Baseline 2)			
Baseline 2 - winter	470.94 kWh	470.94 x 92 days = 43 326.48 USD	
Baseline 2 - summer	291.27 kWh	291.27 x 273 days = 79 516.71 USD	
Baseline 2 - total net cost	/	122 843.19 USD	
Optimal control			
Optimal control-winter	72.98 kWh	72.98 x 92 days = 6 714.16 USD	
Optimal control-summer	54.73 kWh	54.73 x 273 days = 14 941.29 USD	
Optimal control-total net cost vs Baseline 1	/	21 655.45 USD	% 83.59
Optimal control-total net cost vs Baseline 2	/	21 655.45 USD	% 82.37

From Table 5.4, the total annual operational grid energy cost, amounted to 131 928.1 USD, for the first baseline and 122 843.19 USD, for the second baseline. The total annual

operational grid energy cost of the proposed optimal control model, amounted to 21 655.45 USD. The proposed optimal control model, achieved an annual operational grid energy cost-savings of 83.59 % and 82.37 %, compared to the first and second baseline, respectively.

5.5.3 Initial capital investment

In this sub-section, the initial capital investment for the two baselines, as well as for the proposed optimal control of a residential energy hub integrating renewable energy, demand response and energy storage system, are presented. The cost breakdown of each system is illustrated, based on the current South African trading rate, which is R 18.09 to the United States Dollar. The timer controller, as well as the thermostat controller, is excluded from the initial capital cost breakdown, as the cost of these two controllers are miniscule, compared to the other equipment. Therefore, the cost of these two controllers is negligible, for the sake of the study.

In Table 5.5, the initial capital cost breakdown of the first baseline, the air-to-air heat pump and the air-to-water heat pump, is controlled each by a thermostat-based controller [127, 128].

In Table 5.6, the initial capital cost breakdown of the second baseline, the air-to-air heat pump and the air-to-water heat pump, is controlled each by a timer with a thermostat-based controller [127, 128].

In Table 5.7, the initial capital cost breakdown of the proposed optimal control of a residential energy hub integrating renewable energy, demand response and energy storage system's purpose, purpose, is mainly to supply electrical energy to the air-to-air heat pump and the air-to-water heat pump, as well as thermal energy to the air-to-water heat pump [127-129].

Table 5.5: Initial capital cost breakdown of the first baseline

Component description	Quantity	Net price (R)	Net price (USD)
AWA PROZONE HDT C-H 2435 Z air-to-air heat pump	1	8 140 500	450 000
Midea 369 kW air-to-water heat pump	1	5 861 160	324 000
Labour	-	150 000	8 291.87
Total initial investment cost	-	14 151 660	782 291.87

Table 5.6: Initial capital cost breakdown of the second baseline

Component description	Quantity	Net price (R)	Net price (USD)
AWA PROZONE HDT C-H 2435 Z air-to-air heat pump	1	8 140 500	450 000
Midea 369 kW air-to-water heat pump	1	5 861 160	324 000
Labour	-	150 000	8 291.87
Total initial investment cost	-	14 151 660	782 291.87

Table 5.7: Initial capital cost breakdown of the proposed optimal control model

Component description	Quantity	Net price (R)	Net price (USD)
AWA PROZONE HDT C-H 2435 Z air-to-air heat pump	1	8 140 500	450 000
Midea 369 kW air-to-water heat pump	1	5 861 160	324 000
Solar PV modules	468	1 450 332	80 173.13
PEM electrolyser	1	3 618 000	200 000
Hydrogen storage tank	2	1 809 000	100 000
PEM fuel cell	1	3 618 000	200 000
Goodwe 250 kW Inverter	1	224 039	12 384.69
Labour	-	1 236 051.53	68 327.89
Total initial investment cost	-	25 957 082.53	1 434 885.71

5.5.4 Life cycle cost analysis

Prior the commencement of any project, an economic feasibility study is required, which, in this case, a LCC analysis is used, as for the reasons stipulated in Section 5.5.1.

The costs involved in implementing the control techniques of the two baselines, as well as the optimal control model, are neglected, for the purpose of this study, due to the costs being insignificant, in comparison to the main equipment forming part of this study.

The project lifetime is chosen as a 20 year period for the first baseline, second baseline, as well as the proposed optimal control model, whilst a year-on-year electricity increase of 10 % is assumed, an average annualised inflation rate of 5 % and maintenance cost of 1 % are considered for the purpose of this study [93]. The annual operating energy cost of the first baseline, second baseline and the proposed optimal control model, are illustrated in Table. 5.4. The initial capital investment of the two baselines and the proposed optimal control model, are presented in Tables 5.5 – 5.7.

In Fig. 5.41, the life cycle cost of the first baseline, compared to the proposed optimal control model, is presented. This figure illustrates the total life cycle costs in USD, on the y-axis and the period in years, on the x-axis. The starting point of the first baseline and the proposed optimal control model, indicate the initial investment amount for each system, which illustrated that the proposed optimal control model, started at a significantly higher initial capital expenditure, compared to the first baseline. The point at which these two systems intersect, is known as the break-even point, which indicates as to when these two compared systems break-even. From Fig. 5.41, the break-even point of the first baseline and the proposed optimal control model, has appeared to be 5 years, at a total life cycle cost of 1 646 380 USD. Furthermore, the proposed optimal control case, over the projected lifetime, may potentially achieve a cost-saving of 5 640 043.28 USD, compared to the first baseline.

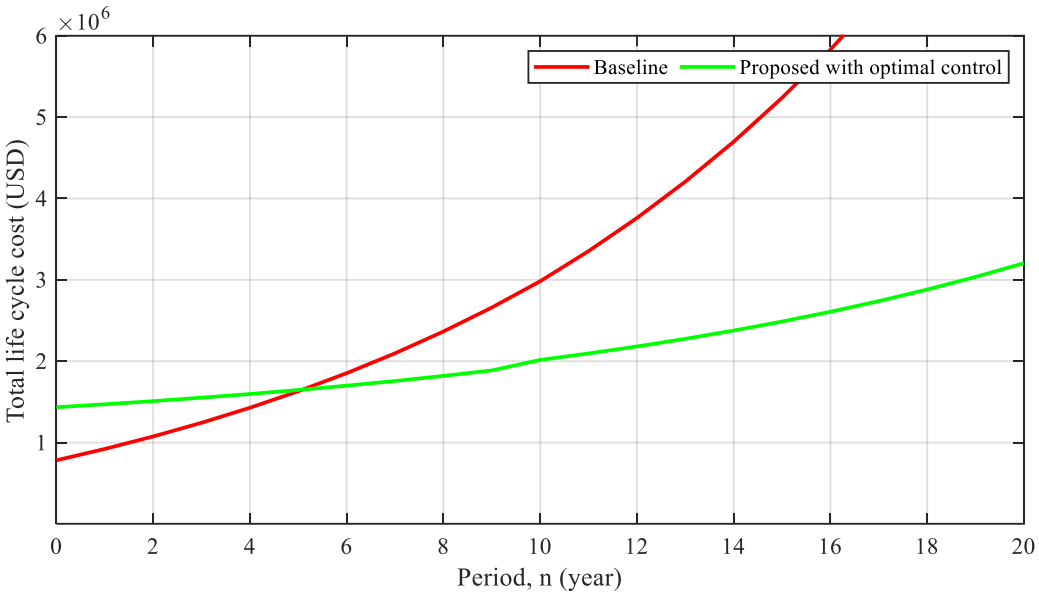

Fig. 5.41: Life cycle cost analysis of the first baseline compared to the proposed optimal control case

In Fig. 5.42, the life cycle cost of the first baseline, compared to the proposed optimal control model, are presented. From Fig. 5.42, the break-even point of the first baseline and the proposed optimal control model, has appeared to be 5.74 years, at a total life cycle cost of 1 672 975.64 USD. Furthermore, the proposed optimal control case, over the projected lifetime, may potentially achieve a cost-saving of 5 102 634.70 USD, compared to the first baseline.

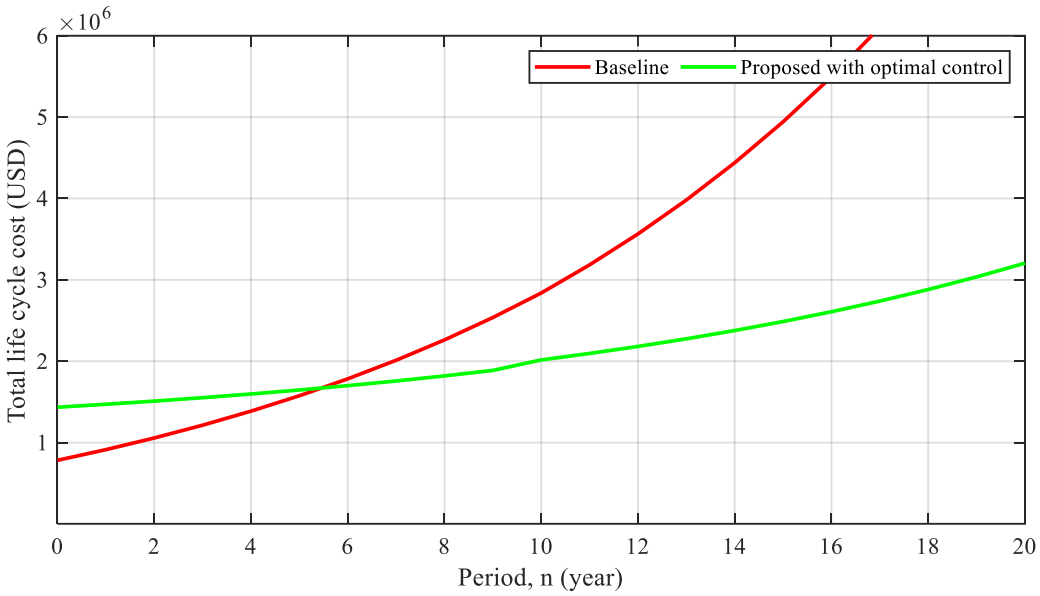

Fig. 5.42: Life cycle cost analysis of the second baseline and the proposed optimal control case

5.6 CONCLUSION

In this chapter, relevant and recent literature was used to evaluate the proposed optimal control case. The optimal control of the residential energy hub integrating renewable energy, demand response and energy storage system was, firstly, mathematically modelled and the multi-objective function, with the associated constraints of the system, was, thereafter, outlined in section 5.2.

The two baselines selected for this study, were well defined as well as simulated, to evaluate the optimal control approach.

The proposed optimal control of the residential energy hub integrating renewable energy, demand response and energy storage system was well outlined and simulated using actual and accurate data, purely for the effectiveness and accuracy, thereof.

The simulation results revealed the proposed optimal control approach, successfully minimized the operational energy costs, compared to the two baselines used in this study. A LCC analysis was conducted, to evaluate the feasibility of the proposed optimal control case against the first baseline, to establish a break-even point, as well as a potential cost saving

expanding over the lifetime of the project. The LCC analysis revealed a break-even point of 5 years, for the proposed optimal control case, compared to the first baseline, was illustrated, whilst a potential cost-saving of 5 640 043.28 USD, over a lifetime of 20 years for this project, was observed. Another LCC analysis was conducted, to evaluate the feasibility of the proposed optimal control case against the second baseline, to establish a break-even point, as well as a potential cost saving expanding over the lifetime of the project. The LCC analysis reveals a break-even point of 5.74 years for the proposed optimal control case, compared to the second baseline, was illustrated, whilst a potential cost-saving of 5 102 634.70 USD, over a lifetime of 20 years, for this project, was observed.

The proposed optimal control case was further evaluated, by comparing its annual operational grid energy consumption to the first and second baseline. Furthermore, the proposed optimal control model, achieved an annual operational grid energy cost-savings of 83.59 % and 82.37 %, compared to the first and second baseline, respectively.

CHAPTER VI: GENERAL CONCLUSION

6.1 CONCLUSION

In this chapter, all the research carried out throughout this study, building up to the proposed residential energy hub integrating renewable energy, demand response and energy storage system, was summarized.

The main concern of this study, was the contribution that the space heating, space cooling and water heating equipment have, towards the total energy consumption in large residential buildings. Therefore, a comprehensive review of hybrid renewable energy systems, connected to space heating, space cooling and water heating systems, was conducted, by applying the POET framework. This included a thorough literature survey, focusing on the operation and control philosophy of renewable energy arrangements with energy storage, space heating, space cooling and water heating equipment.

In Chapter III, the proposed optimal switching control model of an air-to-air heat pump, providing space heating and space cooling to a residential building, was presented. The proposed system was mathematically modelled, after which, the various constraints and the multi-objective function were developed and defined. Furthermore, a daily economic analysis was conducted, to evaluate the feasibility thereof, by comparing it with two baselines. The proposed space heating model, yielded a daily operating energy cost saving of 27.63 % and 14.73 %, compared to the thermostat-based control strategy and the timer with thermostat-based control strategy, during the selected winter day, respectively. The proposed space cooling model, yielded a daily operating energy cost saving of 16.91 % and 12.30 %, compared to the thermostat-based control strategy and the timer with thermostat-based control strategy, during the selected summer days, respectively.

In Chapter IV, an optimal switching control model of a solid polymer electrolyte membrane water electrolyser (PEMWE), to obtain optimal heat recovery to a HWST, was presented. A similar process to the previous Chapter was followed, which involved

mathematical model development. The various constraints and multi-objective function, were cautiously defined and developed. The simulations were conducted, to evaluate the feasibility of the proposed optimal switching control model, by comparing it to a conventional PEMWE system. The simulation results of the proposed optimal switching control model, revealed that the PEMWE produced 778.19 kWh of hydrogen energy during winter, which corresponds to 13.72 kg of hydrogen production, whereas, the PEMWE produced 1 902.36 kWh during summer, which corresponds to 33.54 kg of hydrogen. Most importantly, a daily maximum of 67.32 kWh of thermal energy was recovered during summer, by absorbing the maximum amount of thermal energy generated during the electrolysis process and transferring it to the HWST. The standard PEMWE system (baseline), without any cooling, produced 801.24 kWh of hydrogen energy during winter, which corresponds to 13.98 kg of hydrogen. However, the standard PEMWE system produced 1 965.74 kWh during summer, which corresponds to 34.31 kg of hydrogen. Furthermore, by recovering the generated heat from the PEMWE, the time period for the membrane to degrade to a thickness of 50 %, could be prolonged by 1.02 years.

In Chapter V, optimal control model for a residential energy hub integrating renewable energy, demand response and energy storage system, was presented. A comprehensive mathematical model was developed, as well as the multiple constraints to which the integrated system and the various sub-systems, are exposed to. Furthermore, the multi-objective function, was further developed and clearly described in Chapter V. The simulation results revealed the total daily energy consumption of the first baseline, is 4 449.28 kWh and 4 715.6 kWh, during the selected winter and summer days, respectively. The total daily energy of the second baseline was 4 449.28 kWh and 4 715.6 kWh, during the selected winter and summer days, respectively. The total daily utility grid energy consumption, of the proposed optimal control case, was 829.43 kWh and 1 004.8 kWh, during the selected winter and summer days, respectively. A thorough economic analysis was conducted, to evaluate the feasibility of the proposed optimal control model, by making use of the LCC analysis. The results of the proposed optimal control case, compared to the first baseline, revealed a break-even point of 5, years may be achieved, whilst a potential cost-saving of 5 640 043.28

USD, over a lifetime of 20 years for this project, was observed. The results of the proposed optimal control, case compared to the first baseline, reveal a break-even point of 5.74 years, may be achieved, whilst a potential cost-saving of 5 102 634.70 USD, over a lifetime of 20 years for this project, was observed. Furthermore, the proposed optimal control model achieved an annual operational grid energy cost-savings of 83.59 % and 82.37 %, compared to the first and second baseline, respectively.

The findings presented in this study of the proposed optimal control of a residential energy hub integrating renewable energy, demand response and energy storage system, presented significant potential energy improvements/reductions, as well as the associated operational energy cost improvements/reductions at a large residential building scale. These operational energy costs and energy efficiency improvements of the proposed model, may contribute significantly towards relieving the burden posed upon the national energy grid, as well as reducing the greenhouse gas emissions, thereof.

6.2 FURTHER RECOMMENDATIONS

Further research may include optimal temperature control of the residential energy hub integrating renewable energy, demand response and energy storage system, through applying a MPC technique. Therefore, the operating temperatures of the sub-systems, which are the solar PV modules, PEMWE and the PEMFC, should be predicted and then controlled co-dependently, to achieve a higher holistic operational efficiency. Furthermore, in the research conducted, open-loop optimal control, was considered, to evaluate the performance and economic feasibility of the residential energy hub integrating renewable energy, demand response and energy storage system. Closed-loop optimal control techniques, may be applied to the proposed system, which include fuzzy logic control, model predictive control and artificial neural networks.

REFERENCES

[1] M. M. Rahman, M. G. Rasul, and M. M. K. Khan, "Energy conservation measures in an institutional building in sub-tropical climate in Australia," *Applied Energy,* vol. 87, no. 10, pp. 2994-3004, 2010/10/01/ 2010, doi: https://doi.org/10.1016/j.apenergy.2010.04.005.

[2] F. Mancini, G. Lo Basso, and L. De Santoli, "Energy Use in Residential Buildings: Characterisation for Identifying Flexible Loads by Means of a Questionnaire Survey," *Energies,* vol. 12, no. 11, p. 2055, 2019. [Online]. Available: https://www.mdpi.com/1996-1073/12/11/2055.

[3] P. A. Hohne, K. Kusakana, and B. P. Numbi, "Model validation and economic dispatch of a dual axis pv tracking system connected to energy storage with grid connection: A case of a healthcare institution in South Africa," *Journal of Energy Storage,* vol. 32, p. 101986, 2020/12/01/ 2020, doi: https://doi.org/10.1016/j.est.2020.101986.

[4] M. A. Ancona, F. Catena, and F. Ferrari, "Optimal design and management for hydrogen and renewables based hybrid storage micro-grids," *International Journal of Hydrogen Energy,* 2022/11/12/ 2022, doi: https://doi.org/10.1016/j.ijhydene.2022.10.204.

[5] L. Yang *et al.*, "Advanced smart trigeneration energy system design for commercial building applications – Energy and cost performance analyses," *Energy,* vol. 259, p. 124890, 2022/11/15/ 2022, doi: https://doi.org/10.1016/j.energy.2022.124890.

[6] S. Şevik, "Techno-economic evaluation of a grid-connected PV-trigeneration-hydrogen production hybrid system on a university campus," *International Journal of*

Hydrogen Energy, vol. 47, no. 57, pp. 23935-23956, 2022/07/05/ 2022, doi: https://doi.org/10.1016/j.ijhydene.2022.05.193.

[7] R. Figaj, "Performance assessment of a renewable micro-scale trigeneration system based on biomass steam cycle, wind turbine, photovoltaic field," *Renewable Energy,* vol. 177, pp. 193-208, 2021/11/01/ 2021, doi: https://doi.org/10.1016/j.renene.2021.05.143.

[8] X. Xia and J. Zhang, "Energy Efficiency and Control Systems–from a POET Perspective," *IFAC Proceedings Volumes,* vol. 43, no. 1, pp. 255-260, 2010, doi: 10.3182/20100329-3-pt-3006.00047.

[9] P. A. Hohne, K. Kusakana, and B. P. Numbi, "Improving Energy Efficiency of Thermal Processes in Healthcare Institutions: A Review on the Latest Sustainable Energy Management Strategies," *Energies,* vol. 13, no. 3, p. 569, 2020. [Online]. Available: https://www.mdpi.com/1996-1073/13/3/569.

[10] X. Xia and J. Zhang, "Energy Audit-from a POET Perspective," 2010.

[11] A. Erdil, "An Evaluation on Lifecycle of Products in Textile Industry of Turkey through Quality Function Deployment and Pareto " presented at the 3rd World Conference on Technology, Innovation and Entrepreneurship (WOCTINE), 2019.

[12] X. Xia, J. Zhang, and W. Cass, "Energy management of commercial buildings – A case study from a POET perspective of energy efficiency," *Journal of Energy in Southern Africa,* vol. 23, no. 1, pp. 23-31, 2017, doi: 10.17159/2413-3051/2012/v23i1a3153.

[13] K. Vikhorev, R. Greenough, and N. Brown, "An advanced energy management framework to promote energy awareness," *Journal of Cleaner Production,* vol. 43, pp. 103-112, 2013, doi: 10.1016/j.jclepro.2012.12.012.

[14] V. Strezov, A. Evans, and T. J. Evans, "Assessment of the Economic, Social and Environmental Dimensions of the Indicators for Sustainable Development," *Sustainable Development,* vol. 25, no. 3, pp. 242-253, 2017, doi: https://doi.org/10.1002/sd.1649.

[15] J. Y. Yong, J. J. Klemeš, P. S. Varbanov, and D. Huisingh, "Cleaner energy for cleaner production: modelling, simulation, optimisation and waste management," *Journal of Cleaner Production,* vol. 111, pp. 1-16, 2016, doi: 10.1016/j.jclepro.2015.10.062.

[16] Gaonwe, Tsholofelo Priscilla, Kanzumba Kusakana, and Percy Andrew Hohne. "A review of solar and air-source renewable water heating systems, under the energy management scheme." Energy Reports 8 (2022): 1-10.

[17] *Energy Efficiency in Buildings–Evolution of a Standard Series,* SANS 204, 2010.

[18] A. Hepbasli and Y. Kalinci, "A review of heat pump water heating systems," *Renewable and Sustainable Energy Reviews,* vol. 13, no. 6-7, pp. 1211-1229, 2009, doi: 10.1016/j.rser.2008.08.002.

[19] A. Harris, M. Kilfoil, and E. Uken. "Domestic Energy Savings With Geyser Blankets." https://digitalknowledge.cput.ac.za/bitstream/11189/3457/1/Harris%2C_Domestic_2007.pdf (accessed 11 November, 2022).

[20] T. Hoyt, E. Arens, and H. Zhang, "Extending air temperature setpoints: Simulated energy savings and design considerations for new and retrofit buildings," *Building and Environment,* vol. 88, pp. 89-96, 2015, doi: 10.1016/j.buildenv.2014.09.010.

[21] Eskom. "Hot water and geyser management." https://lonehillresidents.co.za/wp-content/uploads/2021/01/Eskom-Hot-Water-management-Factsheet.pdf (accessed 11 November, 2021).

[22] I. Serban and C. Marinescu, "Battery energy storage system for frequency support in microgrids and with enhanced control features for uninterruptible supply of local loads," *International Journal of Electrical Power & Energy Systems,* vol. 54, pp. 432-441, 2014, doi: 10.1016/j.ijepes.2013.07.004.

[23] B. E. Ford, K. M. Fowler, and C. J. Anderson, *Using Metered Data for Energy and Water Evaluations*, U. S. D. o. Energy, ed., Pacific Northwest National Laboratory Batelle Memorial Institute, pp. 46-47.

[24] L. Schibuola, M. Scarpa, and C. Tambani, "Variable speed drive (VSD) technology applied to HVAC systems for energy saving: an experimental investigation," presented at the 3rd Conference of the Italian Thermal Machines Engineering Association (ATI 2018), Pisa, Italy, 2018.

[25] J. Wang, B. Wang, R. Wu, and H. Zhang, "On Unmanned Electric Power System and Its Development Strategy," presented at the oint International Advanced Engineering and Technology Research Conference, 2018.

[26] M. M. S. Dezfouli, S. Moghimi, F. Azizpour, S. Mat, and K. Sopian, "Feasibility of Saving Energy by Using VSD in HVAC System, A Case Study of Large Scale Hospital in Malaysia," *WSEAS TRANSACTIONS on ENVIRONMENT and DEVELOPMENT,* vol. 10, 2014.

[27] C. P. James, "Remote Generator Fuel Monitoring System," United States of America, 2006.

[28] H. M. Albeahdili, "Connecting Physical Infrastructure to the Cyber Space Using the Internet of Things (IOT) Devices," *Journal of Engineering and Applied Sciences,* vol. 14, pp. 117-130, 2019.

[29] M. Faschang *et al.*, "Provisioning, deployment, and operation of smart grid applications on substation level," *Comput. Sci.,* vol. 32, no. 1–2, pp. 117–130, 2017, doi: 10.1007/s00450-016-0311-x.

[30] Hohne, P. A., K. Kusakana, and B. P. Numbi. "Techno-economic comparison of timer and optimal switching control applied to hybrid solar electric water heaters." In 2018 International Conference on the Industrial and Commercial Use of Energy (ICUE), pp. 1-6. IEEE, 2018.

[31] S. K. Shah, L. Aye, and B. Rismanchi, "Simulated performance of a borehole-coupled heat pump seasonal solar thermal storage system for space heating in cold climate," *Solar Energy,* vol. 202, pp. 365-385, 2020/05/15/ 2020, doi: https://doi.org/10.1016/j.solener.2020.03.111.

[32] Y. Cai, D.-D. Zhang, D. Liu, F.-Y. Zhao, and H.-Q. Wang, "Air source thermoelectric heat pump for simultaneous cold air delivery and hot water supply: Full modeling and performance evaluation," *Renewable Energy,* vol. 130, pp. 968-981, 2019/01/01/ 2019, doi: https://doi.org/10.1016/j.renene.2018.07.007.

[33] N. Dai, S. Li, and Q. Ye, "Performance analysis on the charging and discharging process of a household heat pump water heater," *International Journal of Refrigeration,* vol. 98, pp. 266-273, 2019/02/01/ 2019, doi: https://doi.org/10.1016/j.ijrefrig.2018.10.009.

[34] X. Guo, Z. Ma, L. Ma, and J. Zhang, "Experimental Study of the Performance of a New Developed Heat Pump Water Heater with Frozen Evaporator," *Procedia*

Engineering, vol. 205, pp. 1600-1605, 2017/01/01/ 2017, doi: https://doi.org/10.1016/j.proeng.2017.10.284.

[35] A. R. Jordehi, "Parameter estimation of solar photovoltaic (PV) cells: A review," *Renewable and Sustainable Energy Reviews,* vol. 61, pp. 354-371, 2016/08/01/ 2016, doi: https://doi.org/10.1016/j.rser.2016.03.049.

[36] I. Pola, D. Chianese, L. Fanni, and R. Rudel, "Analysis of annealing and degradation effects on a-Si PV modules," in *23rd European photovoltaic solar energy conference*, 2008.

[37] A. Tijani and A. H. Abdol Rahim, *Numerical Modeling the Effect of Operating Variables on Faraday Efficiency in PEM Electrolyzer*. 2016.

[38] A. Salami Tijani, A. H. Abdol Rahim, and M. K. Badrol Hisam, "A STUDY OF THE LOSS CHARACTERISTIC OF A HIGH PRESSURE ELECTROLYZER SYSTEM FOR HYDROGEN PRODUCTION," *Jurnal Teknologi,* vol. 75, no. 8, 08/20 2015, doi: 10.11113/jt.v75.5213.

[39] M. F. Kaya, N. Demir, N. V. Rees, and A. El-Kharouf, "Improving PEM water electrolyser's performance by magnetic field application," *Applied Energy,* vol. 264, 2020, doi: 10.1016/j.apenergy.2020.114721.

[40] F. J. Wirkert, J. Roth, S. Jagalski, P. Neuhaus, U. Rost, and M. Brodmann, "A modular design approach for PEM electrolyser systems with homogeneous operation conditions and highly efficient heat management," *International Journal of Hydrogen Energy,* vol. 45, no. 2, pp. 1226-1235, 2020/01/06/ 2020, doi: https://doi.org/10.1016/j.ijhydene.2019.03.185.

[41] F. Moradi Nafchi, E. Afshari, E. Baniasadi, and N. Javani, "A parametric study of polymer membrane electrolyser performance, energy and exergy analyses," *International Journal of Hydrogen Energy,* 2019.

[42] S. Rau *et al.*, "Highly Efficient Solar Hydrogen Generation—An Integrated Concept Joining III–V Solar Cells with PEM Electrolysis Cells," *Energy Technology,* vol. 2, no. 1, pp. 43-53, 2014, doi: https://doi.org/10.1002/ente.201300116.

[43] R.-A. Felseghi, E. Carcadea, M. S. Raboaca, C. N. TRUFIN, and C. Filote, "Hydrogen Fuel Cell Technology for the Sustainable Future of Stationary Applications," *Energies,* vol. 12, no. 23, p. 4593, 2019. [Online]. Available: https://www.mdpi.com/1996-1073/12/23/4593.

[44] M. Ramezanizadeh, M. Alhuyi Nazari, M. Hossein Ahmadi, and L. Chen, "A review on the approaches applied for cooling fuel cells," *International Journal of Heat and Mass Transfer,* 2019.

[45] M. Arif, S. C. P. Cheung, and J. P. Andrews, "A systematic approach for matching simulated and experimental polarization curves for a PEM fuel cell," *International Journal of Hydrogen Energy,* vol. 45, pp. 2206-2223, 2020.

[46] E. Cho *et al.*, "Characteristics of the PEMFC Repetitively Brought to Temperatures below 0°C," *Journal of The Electrochemical Society,* vol. 150, 2003.

[47] M. J. Lees, J. Taylor, A. Chotai, P. C. Young, and Z. S. Chalabi, "DESIGN AND IMPLEMENTATION OF A PROPORTIONAL-INTEGRAL-PLUS (PIP) CONTROL SYSTEM FOR TEMPERATURE, HUMIDITY AND CARBON DIOXIDE IN A GLASSHOUSE," 1996: International Society for Horticultural Science (ISHS), Leuven, Belgium, 406 ed., pp. 115-124, doi:

10.17660/ActaHortic.1996.406.11. [Online]. Available: https://doi.org/10.17660/ActaHortic.1996.406.11

[48] M. J. Booysen, J. Engelbrecht, and A. Molinaro, *Proof of concept: Large-scale monitor and control of household water heating in near real-time*. 2013.

[49] "IBE Energy Savings From Maintenance." https://buildingefficiencyinitiative.org/resources/fact-sheet-ibe-energysavings-maintenance (accessed 20 December, 2019).

[50] G. Giebeler, H. Krause, R. Fisch, F. Musso, B. Lenz, and A. Rudolphi, *Refurbishment Manual: Maintenance, Conversions, Extensions*. Birkhäuser, 2012.

[51] S. A. Kalogirou and Y. Tripanagnostopoulos, "Hybrid PV/T solar systems for domestic hot water and electricity production," *Energy Conversion and Management,* vol. 47, no. 18, pp. 3368-3382, 2006/11/01/ 2006, doi: https://doi.org/10.1016/j.enconman.2006.01.012.

[52] W. A. N. W. Mohamed and M. H. M. Kamil, "Hydrogen preheating through waste heat recovery of an open-cathode PEM fuel cell leading to power output improvement," *Energy Conversion and Management,* vol. 124, pp. 543-555, 2016/09/15/ 2016, doi: https://doi.org/10.1016/j.enconman.2016.07.046.

[53] Hohne, P. A., K. Kusakana, and B. P. Numbi. "Operation cost minimisation of hybrid solar/electrical water heating systems: Model development." Advanced Science Letters 24, no. 11 (2018): 8076-8080.

[54] G. Li, "Parallel loop configuration for hybrid heat pump – gas fired water heater system with smart control strategy," *Applied Thermal Engineering,* vol. 138, pp. 807-818, 2018/06/25/ 2018, doi: https://doi.org/10.1016/j.applthermaleng.2018.04.087.

[55] A. Nguyen and P. Eslami-Nejad, "A transient coupled model of a variable speed transcritical CO2 direct expansion ground source heat pump for space heating and cooling," *Renewable Energy,* vol. 140, pp. 1012-1021, 2019/09/01/ 2019, doi: https://doi.org/10.1016/j.renene.2019.03.110.

[56] J. Allison, A. Cowie, S. Galloway, J. Hand, N. J. Kelly, and B. Stephen, "Simulation, implementation and monitoring of heat pump load shifting using a predictive controller," *Energy Conversion and Management,* vol. 150, pp. 890-903, 2017/10/15/ 2017, doi: https://doi.org/10.1016/j.enconman.2017.04.093.

[57] E. M. Wanjiru, S. M. Sichilalu, and X. Xia, "Optimal control of heat pump water heater-instantaneous shower using integrated renewable-grid energy systems," *Applied Energy,* vol. 201, pp. 332-342, 2017/09/01/ 2017, doi: https://doi.org/10.1016/j.apenergy.2016.10.041.

[58] E. M. Wanjiru, S. M. Sichilalu, and X. Xia, "Optimal Operation of Integrated Heat Pump-instant Water Heaters with Renewable Energy," *Energy Procedia,* vol. 105, pp. 2151-2156, 2017/05/01/ 2017, doi: https://doi.org/10.1016/j.egypro.2017.03.607.

[59] H. H. Ali, M. Ahmed, and A.-G. S.M., "Hybrid PV/T solar systems for domestic hot water and electricity production," *Energy Conversion and Management,* pp. 3368-3382, January 2006.

[60] S. Ntsaluba, B. Zhu, and X. Xia, "Optimal flow control of a forced circulation solar water heating system with energy storage units and connecting pipes," *Renewable Energy,* vol. 89, pp. 108-124, 2016/04/01/ 2016, doi: https://doi.org/10.1016/j.renene.2015.11.047.

[61] J. Siecker, K. Kusakana, and B. P. Numbi, "Optimal switching control of PV/T systems with energy storage using forced water circulation: Case of South Africa,"

Journal of Energy Storage, vol. 20, pp. 264-278, 2018/12/01/ 2018, doi: https://doi.org/10.1016/j.est.2018.09.019.

[62] Hohne, Percy A., Kanzumba Kusakana, and Bubele P. Numbi. "Optimal energy management and economic analysis of a grid-connected hybrid solar water heating system in bloemfontein." In 2018 IEEE PES/IAS PowerAfrica, pp. 515-520. IEEE, 2018.

[63] S.-Y. Wu, Q.-L. Zhang, L. Xiao, and F.-H. Guo, "A heat pipe photovoltaic/thermal (PV/T) hybrid system and its performance evaluation," *Energy and Buildings,* vol. 43, no. 12, pp. 3558-3567, 2011/12/01/ 2011, doi: https://doi.org/10.1016/j.enbuild.2011.09.017.

[64] A. Tabanjat, M. Becherif, M. Emziane, D. Hissel, H. S. Ramadan, and B. Mahmah, "Fuzzy logic-based water heating control methodology for the efficiency enhancement of hybrid PV–PEM electrolyser systems," *International Journal of Hydrogen Energy,* vol. 40, no. 5, pp. 2149-2161, 2015/02/09/ 2015, doi: https://doi.org/10.1016/j.ijhydene.2014.11.135.

[65] B. Paul and J. Andrews, "Optimal coupling of PV arrays to PEM electrolysers in solar–hydrogen systems for remote area power supply," *International Journal of Hydrogen Energy,* vol. 33, no. 2, pp. 490-498, 2008/01/01/ 2008, doi: https://doi.org/10.1016/j.ijhydene.2007.10.040.

[66] M. Lototskyy *et al.*, "A concept of combined cooling, heating and power system utilising solar power and based on reversible solid oxide fuel cell and metal hydrides," *International Journal of Hydrogen Energy,* vol. 43, no. 40, pp. 18650-18663, 2018/10/04/ 2018, doi: https://doi.org/10.1016/j.ijhydene.2018.05.075.

[67] S. Misbahuddin, M. Y. El-Sharkh, and S. Palanki, "Neural Network Controller for Regulation of a Water-Cooled Fuel Cell Stack," in *2016 15th IEEE International Conference on Machine Learning and Applications (ICMLA)*, 18-20 Dec. 2016 2016, pp. 1046-1049, doi: 10.1109/ICMLA.2016.0189.

[68] S. Strahl and R. Costa-Castelló, "Temperature control of open-cathode PEM fuel cells," *IFAC-PapersOnLine,* vol. 50, no. 1, pp. 11088-11093, 2017/07/01/ 2017, doi: https://doi.org/10.1016/j.ifacol.2017.08.2492.

[69] H. Lan, L. Yang, F. Zheng, C. Zong, S. Wu, and X. Song, "Analysis and optimization of high temperature proton exchange membrane (HT-PEM) fuel cell based on surrogate model," *International Journal of Hydrogen Energy,* vol. 45, no. 22, pp. 12501-12513, 2020/04/21/ 2020, doi: https://doi.org/10.1016/j.ijhydene.2020.02.150.

[70] S. Chen, M.-S. Chiu, and X. Wang, "Local control of fuel cell systems within hybrid renewable energy generation using model predictive control," *Energy Procedia,* vol. 145, pp. 333-338, 2018/07/01/ 2018, doi: https://doi.org/10.1016/j.egypro.2018.04.060.

[71] S. Sichilalu, T. Mathaba, and X. Xia, "Optimal control of a wind–PV-hybrid powered heat pump water heater," *Applied Energy,* vol. 185, pp. 1173-1184, 2017/01/01/ 2017, doi: https://doi.org/10.1016/j.apenergy.2015.10.072.

[72] S. M. Sichilalu and X. Xia, "Optimal energy control of grid tied PV–diesel–battery hybrid system powering heat pump water heater," *Solar Energy,* vol. 115, pp. 243-254, 2015/05/01/ 2015, doi: https://doi.org/10.1016/j.solener.2015.02.028.

[73] S. M. Sichilalu, H. Tazvinga, and X. Xia, "Integrated Energy Management of Grid-tied-PV-fuel Cell Hybrid System," *Energy Procedia,* vol. 103, pp. 111-116, 2016/12/01/ 2016, doi: https://doi.org/10.1016/j.egypro.2016.11.258.

[74] F. Brahman, M. Honarmand, and S. Jadid, "Optimal electrical and thermal energy management of a residential energy hub, integrating demand response and energy storage system," *Energy and Buildings,* vol. 90, pp. 65-75, 2015/03/01/ 2015, doi: https://doi.org/10.1016/j.enbuild.2014.12.039.

[75] M. Mohammadi, Y. Noorollahi, B. Mohammadi-ivatloo, M. Hosseinzadeh, H. Yousefi, and S. T. Khorasani, "Optimal management of energy hubs and smart energy hubs – A review," *Renewable and Sustainable Energy Reviews,* vol. 89, pp. 33-50, 2018/06/01/ 2018, doi: https://doi.org/10.1016/j.rser.2018.02.035.

[76] F. Jamalzadeh, A. Hajiseyed Mirzahosseini, F. Faghihi, and M. Panahi, "Optimal operation of energy hub system using hybrid stochastic-interval optimization approach," *Sustainable Cities and Society,* vol. 54, p. 101998, 2020/03/01/ 2020, doi: https://doi.org/10.1016/j.scs.2019.101998.

[77] A. A. Eladl, M. I. El-Afifi, M. A. Saeed, and M. M. El-Saadawi, "Optimal operation of energy hubs integrated with renewable energy sources and storage devices considering CO2 emissions," *International Journal of Electrical Power & Energy Systems,* vol. 117, p. 105719, 2020/05/01/ 2020, doi: https://doi.org/10.1016/j.ijepes.2019.105719.

[78] V. Davatgaran, M. Saniei, and S. S. Mortazavi, "Smart distribution system management considering electrical and thermal demand response of energy hubs," *Energy,* vol. 169, pp. 38-49, 2019/02/15/ 2019, doi: https://doi.org/10.1016/j.energy.2018.12.005.

[79] H. Saad, T. Ould-Bachir, J. Mahseredjian, C. Dufour, S. Dennetière, and S. Nguefeu, "Real-Time Simulation of MMCs Using CPU and FPGA," *IEEE Transactions on Power Electronics,* vol. 30, no. 1, pp. 259-267, 2015, doi: 10.1109/TPEL.2013.2282600.

[80] K. J. Chua, S. K. Chou, and W. M. Yang, "Advances in heat pump systems: A review," *Applied Energy,* vol. 87, no. 12, pp. 3611-3624, 2010/12/01/ 2010, doi: https://doi.org/10.1016/j.apenergy.2010.06.014.

[81] S. Hall, "9 - Boilers," in *Branan's Rules of Thumb for Chemical Engineers (Fifth Edition)*, S. Hall Ed. Oxford: Butterworth-Heinemann, 2012, pp. 166-181.

[82] M. J. McCourt. "Wall mounted panel heaters." (accessed 22 September, 2022).

[83] C. Xing, Q. ding, A. Jiang, W. Cheng, and D. Zhou, "Dynamic Operational Optimization of Air Source Heat Pump Heating System with the Consideration of Energy Saving," *IFAC-PapersOnLine,* vol. 48, no. 8, pp. 740-745, 2015/01/01/ 2015, doi: https://doi.org/10.1016/j.ifacol.2015.09.057.

[84] D. Marini, R. A. Buswell, and C. J. Hopfe, "Sizing domestic air-source heat pump systems with thermal storage under varying electrical load shifting strategies," *Applied Energy,* vol. 255, p. 113811, 2019/12/01/ 2019, doi: https://doi.org/10.1016/j.apenergy.2019.113811.

[85] Y. Qi, L. Du, Y. Mu, H. Jia, X. Wang, and G. Li, "Optimal dispatching of household air-source heat pump heating system considering thermal comfort," *Energy Procedia,* vol. 159, pp. 491-496, 2019/02/01/ 2019, doi: https://doi.org/10.1016/j.egypro.2018.12.035.

[86] C. Verhelst, D. Degrauwe, F. Logist, J. Van Impe, and L. Helsen, "Multi-objective optimal control of an air-to-water heat pump for residential heating," *Building Simulation,* vol. 5, 09/01 2012, doi: 10.1007/s12273-012-0061-z.

[87] J. Tang, C. Herman, and G. Gong, "A novel self-adaptive control strategy of frost prevention and retardation for air source heat pumps in winter conditions," *Applied*

Mathematical Modelling, vol. 83, pp. 284-300, 2020/07/01/ 2020, doi: https://doi.org/10.1016/j.apm.2020.02.027.

[88] A. Nagy, H. Kazmi, F. Cheaib, and J. Driesen, *Deep Reinforcement Learning for Optimal Control of Space Heating*. 2018.

[89] S. Gilani, E. Leriche, J. J. McArthur, P. Duez, A. Omidvar, and A. An, "Optimizing Energy with MachineLearning Grey-Box Models," presented at the SciX, 2019.

[90] Gaonwe, T. P., P. A. Hohne, and K. Kusakana. "Optimal energy management of a solar-assisted heat pump water heating system with a storage system." Journal of Energy Storage 56 (2022): 105885.

[91] "Transmission Heat Loss through Building Elements." Engineering ToolBox. https://www.engineeringtoolbox.com/heat-loss-transmission-d_748.html. (accessed 12 November, 2020).

[92] Hohne, P. A., K. Kusakana, and B. P. Numbi. "Scheduling and economic analysis of hybrid solar water heating system based on timer and optimal control." Journal of Energy Storage 20 (2018): 16-29.

[93] P. A. Hohne, K. Kusakana, and B. P. Numbi, "Optimal energy management and economic analysis of a grid-connected hybrid solar water heating system: A case of Bloemfontein, South Africa," *Sustainable Energy Technologies and Assessments,* vol. 31, pp. 273-291, 2019/02/01/ 2019, doi: https://doi.org/10.1016/j.seta.2018.12.027.

[94] "Southern African Universities Radiometric Network." http://www.sauran.net/ShowStation.aspx?station=7. (accessed 12 November, 2017).

[95] "Density of air (material)." aqua-calc. https://www.aqua-calc.com/page/density-table/substance/air. (accessed 24 September, 2022).

[96] "led-bulb-15-watt." Future light. https://www.futurelight.co.za/products/led-bulb-15-watt?variant=39375884167. (accessed 12 November, 2020).

[97] "Human body heat as a source for thermoelectric energy generation." Large.stanford.edu. http://large.stanford.edu/courses/2016/ph240/stevens1/ (accessed 13 November, 2020).

[98] "Awa Prozone HDT." https://technopartner.rs/PDF/INDUSTRIJA/CILERI%20-%20TOPLOTNE%20PUMPE/TOPLOTNE%20PUMPE/VAZDUH%20-%20VODA%20THERMOCOLD%20AWA%20PROZONE%20HDT.pdf (accessed 25 September, 2022).

[99] "Electricity tariffs." Centlec. https://centlec.co.za/Tariffs/TariffsDocuments (accessed 13 November, 2020).

[100] Hohne, P. A., K. Kusakana, and B. P. Numbi. "Operation cost and energy usage minimization of a hybrid solar/electrical water heating system." In 2018 international conference on the domestic use of energy (DUE), pp. 1-7. IEEE, 2018.

[101] Centlec. "Tariff Documents." Centlec. https://www.centlec.co.za/Tariffs/TariffsDocuments (accessed 10 October, 2022).

[102] Y. A. R. I. Mohamed, H. H. Zeineldin, M. M. A. Salama, and R. Seethapathy, "Seamless Formation and Robust Control of Distributed Generation Microgrids via Direct Voltage Control and Optimized Dynamic Power Sharing," *IEEE Transactions on Power Electronics,* vol. 27, no. 3, pp. 1283-1294, 2012, doi: 10.1109/TPEL.2011.2164939.

[103] J. Nowotny *et al.*, "Towards sustainable energy. Generation of hydrogen fuel using nuclear energy," *International Journal of Hydrogen Energy,* vol. 41, no. 30, pp. 12812-12825, 2016/08/10/ 2016, doi: https://doi.org/10.1016/j.ijhydene.2016.05.054.

[104] Z. Ural and M. T. Gencoglu, "Design and simulation of a solar-hydrogen system for different situations," *International Journal of Hydrogen Energy,* vol. 39, no. 16, pp. 8833-8840, 2014/05/27/ 2014, doi: https://doi.org/10.1016/j.ijhydene.2013.12.025.

[105] H. Zhang, S. Su, G. Lin, J. Chen, and 陈金灿, "Efficiency Calculation and Configuration Design of a PEM Electrolyzer System for Hydrogen Production," 2012.

[106] M. Chandesris, V. Médeau, N. Guillet, S. Chelghoum, D. Thoby, and F. Fouda-Onana, "Membrane degradation in PEM water electrolyzer: Numerical modeling and experimental evidence of the influence of temperature and current density," *International Journal of Hydrogen Energy,* vol. 40, no. 3, pp. 1353-1366, 2015/01/21/ 2015, doi: https://doi.org/10.1016/j.ijhydene.2014.11.111.

[107] B. Mohamed, B. Alli, and B. Ahmed, "Using the hydrogen for sustainable energy storage: Designs, modeling, identification and simulation membrane behavior in PEM system electrolyser," *Journal of Energy Storage,* vol. 7, pp. 270-285, 2016/08/01/ 2016, doi: https://doi.org/10.1016/j.est.2016.06.006.

[108] M. Singh, P. Mukoma, B. North, and T. Majozi, "A mathematical model for optimum design and synthesis of a hybrid electrolyser-fuel cell system: Production of hydrogen and freshwater from seawater," *Journal of Cleaner Production,* vol. 277, p. 123899, 2020/12/20/ 2020, doi: https://doi.org/10.1016/j.jclepro.2020.123899.

[109] M. Azuan, N. Z. Yahaya, A. Melinda, and M. Wasif Umar, "Effect of Temperature on Performance of Advanced Alkaline Electrolyser," *Science International (Lahore),* pp. 757 - 762, 2019.

[110] J. Kai, R. Saito, K. Terabaru, H. Li, H. Nakajima, and K. Ito, "Effect of Temperature on the Performance of Polymer Electrolyte Membrane Water Electrolysis: Numerical Analysis of Electrolysis Voltage Considering Gas/Liquid Two-Phase Flow," *Journal of The Electrochemical Society,* vol. 166, no. 4, pp. F246-F254, 2019, doi: 10.1149/2.0521904jes.

[111] S. Yosaf and H. Ozcan, "Exergoeconomic investigation of flue gas driven ejector absorption power system integrated with PEM electrolyser for hydrogen generation," *Energy,* vol. 163, pp. 88-99, 2018/11/15/ 2018, doi: https://doi.org/10.1016/j.energy.2018.08.033.

[112] Y. Zheng, S. You, H. W. Bindner, and M. Münster, "Optimal day-ahead dispatch of an alkaline electrolyser system concerning thermal–electric properties and state-transitional dynamics," *Applied Energy,* vol. 307, p. 118091, 2022/02/01/ 2022, doi: https://doi.org/10.1016/j.apenergy.2021.118091.

[113] "Commercial and Industrial Storage Vessels." ThermoWise. https://thermowise.co.za/products/storage-vessels/commercial-and-industrial-storage-vessels/ (accessed 06 October, 2022).

[114] "Gaonwe, T. P., K. Kusakana, and P. A. Hohne. "Walk-through Energy Audit and Savings opportunities: Case of Water Heaters at CUT Residential Buildings." In 2019 Open Innovations (OI), pp. 434-439. IEEE, 2019.

[115] J. Carvill, "3 - Thermodynamics and heat transfer," in *Mechanical Engineer's Data Handbook*, J. Carvill Ed. Oxford: Butterworth-Heinemann, 1993, pp. 102-145.

[116] K. Bareiß, C. de la Rua, M. Möckl, and T. Hamacher, "Life cycle assessment of hydrogen from proton exchange membrane water electrolysis in future energy systems," *Applied Energy,* vol. 237, pp. 862-872, 2019/03/01/ 2019, doi: https://doi.org/10.1016/j.apenergy.2019.01.001.

[117] M. Bernt, J. Schröter, M. Möckl, and H. A. Gasteiger, "Analysis of Gas Permeation Phenomena in a PEM Water Electrolyzer Operated at High Pressure and High Current Density," *Journal of The Electrochemical Society,* vol. 167, no. 12, p. 124502, 2020/01/09 2020, doi: 10.1149/1945-7111/abaa68.

[118] F. Barbir, *PEM Fuel Cells: Theory and Practice*. Science Direct, 2012.

[119] "Super High Bifacial PolyPerc Module." Canadian Solar Inc. https://www.canadiansolar.com/wp-content/uploads/2019/12/Canadian_Solar-Datasheet-BiHiKu_CS3W-PB-AG_High-Efficiency_1000V1500V_EN-2.pdf (accessed 06 October, 2022).

[120] J. Siecker, K. Kusakana, and B. P. Numbi, "Optimal heat recovery during polymer electrolyte membrane electrolysis," *International Journal of Hydrogen Energy,* vol. 47, no. 76, pp. 32692-32706, 2022/09/05/ 2022, doi: https://doi.org/10.1016/j.ijhydene.2022.07.169.

[121] S. Giglmayr, A. C. Brent, P. Gauché, and H. Fechner, "Utility-scale PV power and energy supply outlook for South Africa in 2015," *Renewable Energy,* vol. 83, pp. 779-785, 2015/11/01/ 2015, doi: https://doi.org/10.1016/j.renene.2015.04.058.

[122] P. A. Hohne, K. Kusakana, and B. P. Numbi, "Energy cost minimization of a multifarious water heating system with energy recovery: A case of a healthcare institution," *Journal of Energy Storage,* vol. 51, p. 104451, 2022/07/01/ 2022, doi: https://doi.org/10.1016/j.est.2022.104451.

[123] T. E. ToolBox. "Consumption of hot water per person or occupant." https://www.engineeringtoolbox.com/hot-water-consumption-person-d_91.html (accessed 13 October, 2022).

[124] "Commercial Applications." Midea. http://5.imimg.com/data5/AW/BX/EO/SELLER-18015862/jacuzzi-heating-pump.pdf (accessed 13 October, 2022).

[125] U. F. C. C. 2008. "Commercially Available Fuel Cell Products." https://www.hydrogen.energy.gov/pdfs/htac_fc_products.pdf (accessed 13 October, 2022).

[126] A. S. O. Ogunjuyigbe, T. R. Ayodele, and O. A. Akinola, "Optimal allocation and sizing of PV/Wind/Split-diesel/Battery hybrid energy system for minimizing life cycle cost, carbon emission and dump energy of remote residential building," *Applied Energy,* vol. 171, pp. 153-171, 2016/06/01/ 2016, doi: https://doi.org/10.1016/j.apenergy.2016.03.051.

[127] Alibaba. "AC digital temperature programmable thermostat hotel guest room thermostat." Alibaba. https://www.alibaba.com/product-detail/Ac-Thermostat-AC-Digital-Temperature-Programmable_62581267539.html?spm=a2700.drainage_lp_1.0.0.11974296XTwI1G&s=p (accessed 23 October, 2022).

[128] Alibaba. "Midea Domestic All In One New Energy Heat Pump Hot Water Heater." Alibaba. https://www.alibaba.com/product-detail/Midea-Domestic-All-In-One-New_1600423953760.html?spm=a2700.7724857.0.0.37dd879243IGu2 (accessed 23 October, 2022).

[129] Made-in-China. "Gas Generation Equipment and Parts." Made-in-China https://fr-fueldispenser.en.made-in-china.com/product/sZyTwkpKlEcU/China-Hydrogene-Generator-for-Car-100-Hho-Hydrogen-Generator.html (accessed 24 October, 2022).